University of Oxford

Department of Chemistry



Group four permethylindenyl-phenoxy (PHENI*) complexes for the synthesis of polyolefins

Clement G. Collins Rice

Jesus College

Hilary Term 2023

Thesis submitted in partial fulfilment of the requirements of the degree of Doctor of Philosophy

for L.C.F.

Preface

The work described in this thesis was carried out in the Chemistry Research Laboratory at the University of Oxford, U.K. between October 2019 and October 2022 under the supervision of Professor Dermot O'Hare. All work was performed by the author unless otherwise stated, and no part has previously been submitted for any other degree.



Clement Gregory Collins Rice

Jesus College

February 2023

Parts of the work contained in this thesis are published in the following journal articles:

C. G. Collins Rice, J.-C. Buffet, Z. R. Turner, and D. O'Hare, *Chem. Commun.*, 2021, **57**, 8600-8603,

C. G. Collins Rice, J.-C. Buffet, Z. R. Turner, and D. O'Hare, *Polym. Chem.*, 2022, **13**, 5597-5603,

and are covered by the following patent applications:

C. G. Collins Rice, J.-C. Buffet, Z. R. Turner, and D. O'Hare, UK Pat. Appl. PCT/GB2022/051160; WO-2022234292-A1.

C. G. Collins Rice, J.-C. Buffet, Z. R. Turner, and D. O'Hare, UK Pat. Appl. PCT/GB2022/051161; WO-2022234293-A1.

Presentations based on parts of the work contained in this thesis were accepted at the 49th World Polymer Congress (MACRO 2022, Winnipeg, Canada), and the 44th International Conference on Coordination Chemistry (ICCC 2022, Rimini, Italy). An invited presentation was given at the Organometallic and Main Group Seminar Series 2023 (Oxford, U.K.).

Abstract

Group four permethylindenyl-phenoxy (PHENI*) complexes for the synthesis of polyolefins

Clement G. Collins Rice **D.Phil. Thesis**

Jesus College **Hilary Term 2023**

This thesis discusses the synthesis and characterisation of *ansa*-bridged permethylindenyl-phenoxy (PHENI*) complexes and their applications in the synthesis of polyolefins. Efficient homogeneous and slurry-phase catalyst systems are developed for the homopolymerisation of ethylene and propylene, and a range of copolymerisations incorporating linear α-olefins.

A brief review of polyolefin materials, their synthesis and properties is presented, focussing on how the varied properties makes them suitable for a range of societally relevant applications. Traditional solid-state catalysts are contrasted with state-of-the-art molecular catalysts which offer exceptional control over polymer molecular weight and composition, enabling the production of novel materials while maintaining optimal catalytic efficiency. Constrained geometry and phenoxy-imine catalysts are highlighted as examples which offer outstanding performance and tunability for ethylene polymerisation and copolymerisations.

The synthesis and detailed characterisation of PHENI* complexes (^{Me,R}SB($^{R'R''}$ArO,I*)MX_2) is developed using a high-yielding adaptable procedure from low cost starting materials. A variety of metal centres, *ansa* bridge substituents, ancillary ligands, and phenoxide substitutions are presented with the influence of steric and electronic factors on structure, bonding, and reactivity explored. Structural trends are identified which help to rationalise the excellent catalytic performance of these complexes. The heterogenisation of PHENI* complexes on a range of solid supports is also discussed.

The homopolymerisation of ethylene and propylene using homogeneous and immobilised PHENI* catalysts was studied, with the effects of the ligand, support, and reaction conditions investigated extensively. Exceptional catalytic activities are reported under mild conditions for the synthesis of substantially disentangled ultra-high molecular weight polyethylene, and a novel elastomeric ultra-high molecular weight atactic polypropylene.

Supported PHENI* catalysts were finally investigated as a polyolefin platform technology, able to copolymerise a wide range of monomers efficiently. In all cases, random copolymers were produced in a monomer-agnostic fashion, with the composition determined simply by the concentration of monomers. This enables a significant degree of predictability and control, enabling the synthesis of designer copolymers through programmed synthesis.

Acknowledgements

Primarily I would like to thank Prof. Dermot O'Hare for the opportunity of studying in his research group, originally as a Part II, and for allowing me to continue my research. Dermot's advice, support, encouragement, and BBQs have been invaluable. Secondly, SCG Chemicals PLC for funding the project through a generous Oxford-SCG studentship.

This project owes its inception and completion to JC Buffet, Zoë Turner, and Louis Morris who have between them achieved the mammoth task of training me in the ways of organometallic chemistry, scientific writing, interacting with industry, and producing a thesis. This document simply would not exist were it not for the unbelievably hard work of Louis in proofreading and correcting well over a quarter of a million words of drafts – your suggestions have been invaluable, and your patience is honestly superhuman.

A large proportion of the results in this thesis owe their existence to others. Amber Thompson and Kirsten Christensen for teaching me the art of X-ray crystallography, and great uncle John Low for many discussions about interesting crystal structures. The satisfaction of seeing a set of pretty diffraction spots is truly something that will stay with me. Nick Rees, Caitlin Salter, and James Montgomery for their assistance with solid-state and polymer NMR. Liv Thobru, Sara Rund Herum, and Rita Jenssen at Norner for GPC. Thea Høibjerg Glittum, and Heidi Nornes Bryntesen at Norner for mechanical testing. Giovanni Santagiuliana at Nanoforce for microcompounding, and Prof. Clive Siviour and Nick Hawkins in the Engineering department for assistance with characterising polymers by DMTA. Joe Morford for assistance with the statistics. Alex Evans for TGA. Jingfang Yu for helping with rheology. Phil Kenyon for WAXS, many discussions about

UHMWPE, DSC, and entanglements, and a great deal of practical help in the lab. Luca Rongo, Roberta Cipullo, Christian Ehm, and the team at Xplore for high-throughput screening, and discussions surrounding the mechanism of polymerisation.

I would like to thank the members of the PHENI* subgroup (that's a thing, right?) – Justin Hayden, Peace Blake, Alex Evans, Joanna Bland, Issy Stephens, and Adam Hawkins have all at various points been landed with trying to replicate my synthesis. I owe many tweaks, optimisations, developments, and much of my understanding to these guys. Peace made the zirconium complex, Issy the scandium, and Adam the tantalum. Justin has contributed an enormous amount to the development of this ligand, and has produced complexes using yttrium, scandium, lanthanum, bismuth, aluminium, and lutetium so far. I have greatly enjoyed following all of your work on functionalised and renewable polymerisations and can't wait to see how far you're able to take it. I would like to thank my Part II students, Issy Stephens and Adam Hawkins, for being enthusiastic, committed researchers, fast learners, and for contributing immensely to our understanding of PHENI* chemistry. I wish you both the very best in all of your future endeavours.

Thanks are also due to the many DOH members over the years who have assisted in numerous ways with the chemistry, and for all of the pub trips, bowling adventures, tea breaks, and everything that makes the group such a delightful place to work. Perhaps most of all, to Justin Hayden for keeping S2 in order and full of good chat, and to Rebecca Jones for going through this wild DPhil together since day one – so nearly there now!

The chapel and choir at Merton has been a wonderful source of musical distraction for the best part of eight years, so thank you to Ben Nicholas and Simon Jones. Together, we

have performed repertoire spanning seven centuries at over a thousand services and concerts in seven countries across three continents. Singing the first ever Anglican evensong at St. Peter's Basilica in the Vatican is one of those magical experiences that I will always treasure. It's hard to know whether I've spent more time singing or doing chemistry at Oxford, and (un)fortunately I don't get to write a book about the MCC. The music-making has been tremendous, the appetite for the sesh *almost* unbelievable, the chat simply out of this world, the football enthusiastic, the Chapel Suppers legendary, and most importantly reliably the best group of people you could ever hope to meet.

Thank you too to my housemates, Victor Ajuwon, Seb Dows-Miller, Thomas Miller, and Joe Morford for teaching me more about birding, animal behaviour, and mediaeval French than I ever thought I needed. For the signature chilli nights, the uncountable G&Ts, the ambitious Christmas dinners, and for letting me turn our houses into botanical gardens.

Above all, thank you to my family. Grandma, your tales of chemistry are inspirational – I promise that I never tasted *any* of my samples. LucyAnne, thank you for putting up with my awkward plastic chat, and for always believing in me. At times, this project has been all-consuming and I'm so grateful for all your patience and support. I treasure our time together, and all the wonderful memories that we have made – the Half Moon has a lot to answer for. Mummy, Daddy, and Benedict, thank you for encouraging me at every stage of my life, and somehow always finding time for me. Getting this far has been a complete team effort, and I have no doubt that I couldn't have done it without you. I know none of you signed up to hear about polymers endlessly and am so appreciative of your love and support. Perhaps you'll find some nuggets in here for when people ask you what I do. . .

Abbreviations and nomenclature

[L], L_n	Ligand
[η]	Intrinsic viscosity
{^{1}H}	Proton decoupled
$^{3\text{-Ph}}$Ind$^{\#}$	3-phenyl-pentamethylindenyl
Å	Ångström, 10^{-10} m
A	Polymerisation activity
AB	*N*,*N*,-dimethylanilinium tetrakis(pentafluorophenyl)borate
acac	Acetylacetonate
Adm	Adamantyl, $C_{10}H_{16}$
AIM	Aqueous immiscible
Allyl	CH_2=CH_2CH_3
AMO	Aqueous miscible organic
*a*PP	Atactic polypropylene
Ar	Aryl
Ar^F	Perfluorophenyl, C_6F_5
atm	Standard atmosphere, 1 atm = 101.325 kPa
bar	1 bar = 100 kPa
BBI	Boron-bridged bis indenyl
BHT	3,5-di-*tert*-butyl-4-hydroxytoluene
Bn	Benzyl, CH_2Ph
c	Comonomer concentration
C12	1-dodecene
C18	1-octadecene
C4	1-butene
C6	1-hexene
C8	1-octene
CEF	Crystallisation elution fractionation
cent	Centroid
CGC	Constrained geometry complex
CGCI*	Permethylindenyl constrained geometry complex
COSY	Correlation spectroscopy

Cp	Cyclopentadienyl
C_p	Constant-pressure heat capacity
Cp*	Permethylcyclopentadienyl
CPMAS	Cross-polarisation magic angle spinning
Cp^{Me}	Methylcyclopentadienyl
Cumyl	CMe_2Ph
Cy	Cyclohexyl
Đ	Dispersity, PDI
Da	Dalton, g mol^{-1}
DEPT	Distortionless enhancement by polarisation transfer
DFS	Double frequency sweep
DFT	Density functional theory
Dipp	2,6-di*iso*propylphenyl
*dis*UHMWPE	Disentangled UHMWPE
DMTA	Dynamic mechanical thermal analysis
DPMAS	Direct polarisation magic angle spinning
DSC	Differential Scanning Calorimetry
DTG	Derivative thermogravimetry
E	Ethylene; Young's modulus
E'	Tensile elastic storage modulus
E''	Tensile elastic loss modulus
EB	Ethylene bridge, $–C_2H_4–$
EBI	Ethylene-bridged bis indenyl
ENB	5-ethylidene-2-norbornene
EPDM	Ethylene propylene diene terpolymer
EPM	Ethylene propylene rubber
ESD	Estimated standard deviation
Et	Ethyl, CH_2CH_3
EXAFS	Extended X-ray absorption fine structure
FI	Phenoxy-imine
Flu	Fluorenyl
G'	Shear elastic storage modulus

G''	Shear elastic loss modulus
GPC	Gel Permeation Chromatography
h	Hours
HD	1,4-hexadiene
HDPE	High Density Polyethylene
HMBC	Heteronuclear multiple bond correlation
HMWaPP	High molecular weight atactic polypropylene, M_w > 200 kDa
HSQC	Heteronuclear single-quantum coherence
^{i}Bu	*iso*-Butyl
Ind	Indenyl
Ind$^{\#}$, I$^{\#}$	Hexamethylindenyl
Ind*, I*	Permethylindenyl
*i*PP	Isotactic polypropylene
^{i}Pr	*iso*-Propyl
IR	Infrared
KHMDS	Potassium hexamethyldisilazide
LAO	Linear α-olefin
LDH	Layered double hydroxide
LDHMAO	MAO-modified LDH
LDPE	Low-density polyethylene
LLDPE	Linear low-density polyethylene
M	mol dm^{-3}
m	Meso
MAO	Polymethylaluminoxane
MBT	2-Mercaptobenzothiazole
Me	Methyl
MFI	Melt flow index
^{Me2}SB	Dimethylsilane bridged, –SiMe$_2$–
M_n	Number-average molecular weight
MOF	Metal organic framework
mol%	Percent by mole fraction
M_v	Viscosity-average molecular weight

M_w	Weight-average molecular weight
MWD	Molecular weight distribution
M_η	Viscosity-average molecular weight
n	Number of carbon atoms in LAO
N	Sample size
NBS	*N*-Bromosuccinimide
^{n}Bu	*n*-Butyl
Neosilyl	CH_2SiMe_3
NIR	Near infrared
NHC	*N*-Hetrocyclic carbene
NMR	Nuclear magnetic resonance
^{n}Pr	*n*-Propyl
NR	Natural rubber
P	Propylene
PDI	Polydispersity index; dispersity; Đ = M_w/M_n
PE	Polyethylene
Ph	phenyl
PHENI*	*ansa*-Permethylindenyl-phenoxy
PHENICS	Phenoxy-Induced Complex of Sumitomo
phr	Parts per hundred rubber
PO	Polyolefin
PP	Polypropylene
PPH	Poly(propylene-co-1-hexene)
ppm	Parts per million
PPR	Parallel pressure reactor
PSD	Particle size distribution
psi	Pound per square inch, 1 psi = 6.894757 kPa
PTFE	Polytetrafluoroethylene, Teflon®
QSAR	Quantitative structure-activity relationship
r, *rac*	Racemic
r_{M^+}	Ionic radius
rpm	Revolutions per minute

R_{tot}	Total reflectance
SB	Silyl bridged
SBI	Dimethylsilyl-bridged bis indenyl
SBI*	Dimethylsilyl-bridged bis permethylindenyl
SCB	Short-chain branching
SCB/1000TC	Short-chain branching per 1000 total carbon
SEM	Scanning electron microscopy
sMAO	Solid polymethylaluminoxane
*s*PP	Syndiotactic polypropylene
SSMAO	Silica-supported MAO
ssNMR	Solid-state nuclear magnetic resonance
STM	Scanning tunnelling microscopy
T_1	Spin-lattice relaxation time
T_a	Annealing temperature
TA’	Characteristic torsion angle
TB	Triphenylmethylium tetrakis(pentafluorophenyl)borate
TBP	2,2’-Thiobis(6-*tert*-butyl-4-methylphenoxy)
^{t}Bu	*tert*-Butyl
$^{t\text{Bu}_2}$Flu	2,7-Di-*tert*-butyl fluorenyl
$^{t\text{Bu}}$Cp	*Tert*-butyl cyclopentadienyl
TC	Total carbon
TCB	1,2,4-Trichlorobenzene
T_{diff}	Diffuse transmittivity
TEA	Triethylaluminium
T_g	Glass transition temperature
$T_{g,\infty}$	Glass transition temperature at infinite molecular weight
TGA	Thermogravimetric analysis
THF	Tetrahydrofuran
TIBA	Tri*iso*butyl aluminium
T_m	Melting point
TMA	Trimethylaluminium
TMEDA	Tetramethyl ethylenediamine

TMS	Trimethylsilyl
TOF	Turnover frequency
T_p	Temperature of polymerisation
TPE	Thermoplastic elastomer
T_{tot}	Total transmittivity
UHMWaPP	Ultra-high molecular weight atactic polypropylene
UHMWPE	Ultra-high molecular weight polyethylene
UV	Ultraviolet
V	Comonomer volume
*v*EPDM	Vulcanised ethylene propylene diene rubber
VH	4-Vinylcyclohexene
VT	Variable temperature
WAXS	Wide-angle x-ray scattering
wt%	Percentage by weight
x	Comonomer incorporation
Z'	Number of symmetry-independent molecules
ZN	Ziegler-Natta
α	Crystallinity
δ	Chemical shift; phase angle
$\Delta C_{p,Tg}$	Change in heat capacity at the glass transition
Δ_{M-C}	Ring-slip parameter
ε	Engineering strain
ε_B	Strain at break
λ	Wavelength
η^*	Complex viscosity
η^x	Hapticity
μ	Mean; bridging ligand
ρ	Density
σ	Engineering stress; standard deviation
σ_B	Stress at break
σ_y	Yield stress
ω	Angular frequency

Identification of Complexes

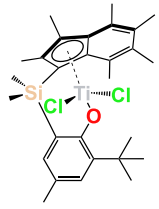

^{Me_2}SB(^{tBu,Me}ArO,I*)TiCl$_2$, **1**

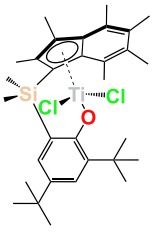

^{Me_2}SB(^{tBu_2}ArO,I*)TiCl$_2$, **2**

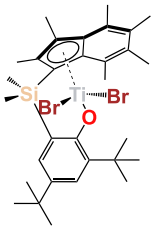

^{Me_2}SB(^{tBu_2}ArO,I*)TiBr$_2$, **3**

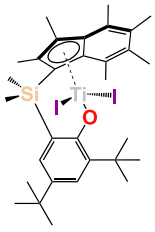

^{Me_2}SB(^{tBu_2}ArO,I*)TiI$_2$, **4**

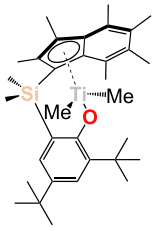

^{Me_2}SB(^{tBu_2}ArO,I*)TiMe$_2$, **5**

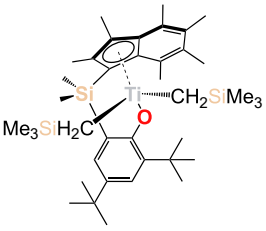

^{Me_2}SB(^{tBu_2}ArO,I*)Ti(CH$_2$SiMe$_3$)$_2$, **6**

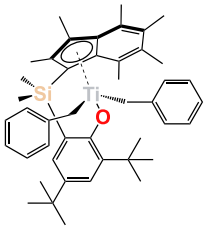

^{Me_2}SB(^{tBu_2}ArO,I*)TiBn$_2$, **7**



^{Me_2}SB(^{tBu_2}ArO,I*)Ti(NMe$_2$)$_2$, **8**

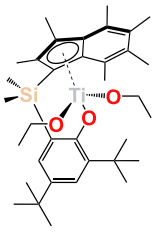

^{Me_2}SB(^{tBu_2}ArO,I*)Ti(OEt)$_2$, **9**

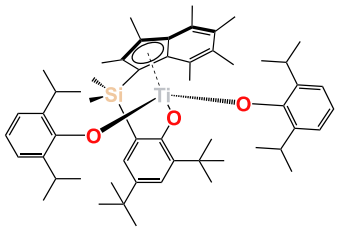

^{Me_2}SB(^{tBu_2}ArO,I*)Ti(O$^{2,6\text{-}iPr_2}$Ar)$_2$, **10**

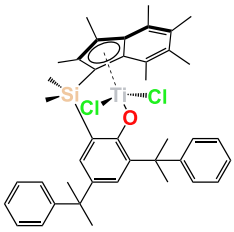

^{Me_2}SB(^{Cumyl_2}ArO,I*)TiCl$_2$, **11**

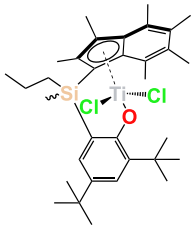

rac-^{Me,nPr}SB(^{tBu_2}ArO,I*)TiCl$_2$, **12**

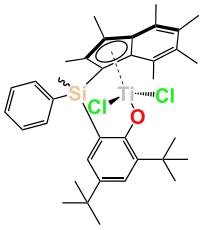

rac-^{Me,Ph}SB(^{tBu_2}ArO,I*)TiCl$_2$, **13**

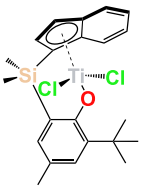

^{Me_2}SB(^{tBu,Me}ArO,Ind)TiCl$_2$, **14**

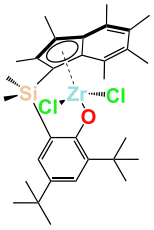

^{Me_2}SB(^{tBu_2}ArO,I*)ZrCl$_2$, **15**

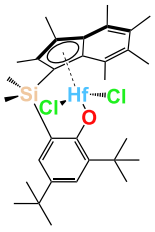

^{Me_2}SB(^{tBu_2}ArO,I*)HfCl$_2$, **16**

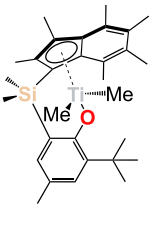

^{Me_2}SB(^{tBu,Me}ArO,I*)TiMe$_2$, **17**

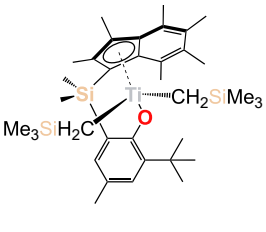

^{Me_2}SB(^{tBu,Me}ArO,I*)Ti(CH$_2$SiMe$_3$)$_2$, **18**

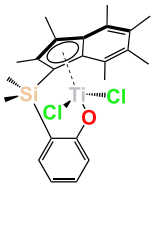

^{Me_2}SB(^{H_2}ArO,I*)Ti(OEt)$_2$, **19**

Table of Contents

Preface ... **iii**
Abstract ... **iv**
Acknowledgements ... **v**
Abbreviations and nomenclature ... **viii**
Identification of Complexes ... **xiv**
Table of Contents ... **xv**
Chapter 1 – Introduction ... **1**
1.1. Polyolefins ... 1
1.1.1. Polyethylene ... 1
1.1.1.1. Molecular weight distribution ... *2*
1.1.1.2. Ultra-high molecular weight polyethylene ... *3*
1.1.2. Polypropylene ... 4
1.1.2.1. Ultra-high molecular weight polypropylene ... *6*
1.1.3. Higher polyolefins ... 7
1.2. Olefinic copolymers ... 7
1.2.1.1. Ethylene linear α-olefin copolymers ... *8*
1.2.1.2. Thermoplastic polyolefin elastomers ... *9*
1.2.1.3. Ethylene propylene diene terpolymers ... *10*
1.3. Catalysts for the polymerisation of olefins ... 10
1.3.1. Heterogeneous catalysts ... 10
1.3.2. Homogeneous Kaminsky metallocenes ... 11
1.3.3. Supported single-site catalysts ... 12
1.3.3.1. Silica ... *13*
1.3.3.2. Layered double hydroxides ... *14*
1.3.3.3. Solid polymethylaluminoxane ... *15*
1.3.4. Polymerisation mechanism ... 16
1.3.5. Polymerisation conditions ... 18
1.3.5.1. Cocatalysts ... *18*
1.3.5.2. Scavengers ... *20*
1.4. Permethylindenyl chemistry ... 20
1.4.1. Cyclopentadienyl ligands ... 20
1.4.2. The indenyl effect ... 21
1.4.3. The *ansa* effect ... 23
1.5. Beyond metallocene catalysts ... 24
1.5.1. Constrained Geometry Catalysts ... 24

1.5.2. Phenoxy imine catalysts 27
1.5.3. Phenoxy-Induced Complexes of Sumitomo 29
1.5.4. Permethylindenyl post-metallocenes 30
1.6. Scope of thesis 31
1.7. References 32
Chapter 2 – Group four permethylindenyl-phenoxy (PHENI*) complexes 40
2.1. Introduction 40
2.1.1. Synthesis of PHENICS complexes 40
2.1.2. Permethylindenyl post-metallocenes 42
2.1.3. Chapter synopsis 42
2.1.4. Definition of geometric parameters 42
2.2. Synthesis of PHENI* complexes 43
2.2.1. Synthesis of proligands, $^{Me_2}SB(^{R_1,R_2}ArOAllyl,I^*)H$ 43
2.2.2. Synthesis of $^{Me_2}SB(^{R_1,R_2}ArO,I^*)TiCl_2$ 47
2.2.2.1. Synthesis of $^{Me_2}SB(^{R_1,R_2}ArO,I^*)Li_2$ 48
2.2.2.2. Characterisation of $^{Me_2}SB(^{R_1,R_2}ArO,I^*)TiCl_2$ 49
2.2.2.3. Attempted syntheses 53
2.2.3. Synthesis of $^{Me_2}SB(^{tBu,R_2}ArO,I^*)TiX_2$ (X = halide, alkyl, alkoxide, aryloxide, amide) 55
2.2.3.1. X = halide 55
2.2.3.2. X = alkyl 58
2.2.3.3. X = alkoxide, aryloxide, amide 60
2.2.4. Synthesis of *rac*-$^{Me,R_a}SB(^{tBu_2}ArO,I^*)TiCl_2$ (R_a = ^{n}Pr, Ph) 63
2.2.5. Synthesis of $^{Me_2}SB(^{tBu_2}ArO,I^*)MCl_2$ (M = Zr, Hf) 68
2.2.6. Attempted syntheses of dinuclear complexes 71
2.3. Formation of cationic reactive intermediates 72
2.3.1. Immobilisation of PHENI* complexes on sMAO 74
2.3.2. Immobilisation of PHENI* complexes on SSMAO and LDHMAO 77
2.4. Conclusions 79
2.5. References 80
Chapter 3 – Polymerisation of ethylene to *dis*UHMWPE 83
3.1. Introduction 83
3.1.1. Chapter synopsis 84
3.2. Homogeneous ethylene polymerisation 84
3.2.1. Influence of cocatalyst on solution-phase polymerisation 85

3.2.2. Polymer characterisation 86
3.3. Slurry-phase polymerisation 87
3.3.1. Variation of heterogeneous catalyst support 87
3.3.1.1. Polymer characterisation 89
3.3.2. Variation of the PHENI* ligands 91
3.3.2.1. Polymer characterisation 94
3.3.3. Variation of the ancillary ligand leaving group 95
3.3.3.1. Polymer characterisation 97
3.3.4. Variation of the group 4 metal 98
3.3.4.1. Polymer characterisation 100
3.3.5. Effect of reaction conditions 101
3.3.5.1. Variation of cocatalyst 101
3.3.5.2. Effect of the Al:Ti ratio 102
3.3.5.3. Effect of reaction scale and time 103
3.3.5.4. Hydrogen response 106
3.3.6. High pressure high-throughput screening 108
3.4. Characterisation of UHMWPE 110
3.4.1. Thermomechanical characterisation 110
3.4.2. Assessment of entanglement density 113
3.5. Polyethylene–polyethylene blends 116
3.5.1. LDPE/UHMWPE polymer blends 118
3.5.2. HDPE/UHMWPE polymer blend 120
3.6. Conclusions 122
3.7. References 123
Chapter 4 – Polymerisation of propylene to UHMWaPP 127
4.1. Introduction 127
4.1.1. Chapter synopsis 129
4.2. Polymerisation of propylene 129
4.2.1. The effect of reaction scale 133
4.2.2. The effect of cocatalyst loading 135
4.2.3. Thermal, optical, and mechanical properties of UHMWaPP 137
4.3. Chiral PHENI* complexes towards stereospecific polymerisation 142
4.3.1. Polypropylene microstructure 144
4.4. Conclusions 146
4.5. References 147

Chapter 5 – Copolymerisation of linear α-olefins 150
5.1. Introduction 150
5.1.1. Chapter synopsis 152
5.2. Copolymerisation of ethylene with propylene 152
5.2.1. The effect of temperature on E/P copolymerisation 156
5.3. Terpolymerisation of ethylene, propylene, and a diene 158
5.3.1. Characterisation of EPDM 159
5.3.2. Vulcanisation of EPDM 161
5.3.3. Characterisation of *v*EPDM 163
5.4. Copolymerisation of propylene and 1-hexene 165
5.4.1. Characterisation of PPH 166
5.5. Copolymerisation of ethylene with higher linear α-olefins 167
5.5.1. Copolymerisation of ethylene with 1-hexene 168
5.5.2. Characterisation of LLDPE-C6 169
5.5.3. Copolymerisation of ethylene with 1-octene 172
5.5.4. Characterisation of LLDPE-C8 173
5.5.5. Copolymerisation of ethylene with 1-dodecene 176
5.5.6. Characterisation of LLDPE-C12 177
5.5.7. Summary of E/LAO copolymerisation 179
5.6. Multivariate analysis of copolymerisation system 180
5.6.1. Introduction 180
5.6.2. Multivariate analysis 181
5.6.3. Multivariate linear regression modelling 183
5.6.4. Towards the synthesis of designer copolymers 187
5.7. Conclusions 191
5.8. References 192
Chapter 6 – Experimental details 195
6.1. General details and instrumentation 195
6.1.1. General procedures 195
6.1.2. Solution NMR spectroscopy 196
6.1.3. Solid-state NMR spectroscopy 196
6.1.4. X-ray crystallography 196
6.1.5. Wide-angle X-ray scattering 197
6.1.6. Elemental analysis 197
6.1.7. Infrared spectroscopy 197

6.1.8. Scanning electron microscopy 198
6.1.9. Gel permeation chromatography 198
6.1.10. Differential scanning calorimetry 198
6.1.11. Thermogravimetry 199
6.1.12. Mechanical analysis 199
6.1.13. Optical measurements 200
6.1.14. Microcompounding 200
6.1.15. Dynamic mechanical thermal analysis 200
6.2. Commercially supplied materials 201
6.3. Literature preparations 202
6.4. Experimental details for Chapter Two 203
6.4.1. Synthesis of PHENI* ligands 203
6.4.1.1. $^{Me2}SB(^{tBu,Me}ArOAllyl,I^*)H$ (1e) 204
6.4.1.2. $^{Me2}SB(^{tBu2}ArOAllyl,I^*)H$ (2e) 205
6.4.1.3. $^{Me2}SB(^{Cumyl2}ArOAllyl,I^*)H$ (11e) 205
6.4.1.4. $^{Me2}SB(^{H2}ArOAllyl,I^*)H$ (19e) 206
6.4.1.5. $^{Me2}SB(^{tBu2}ArO,I^*)Li_2$ (2f) 207
6.4.1.6. $^{Me2}SB(^{Cumyl2}ArO,I^*)Li_2$ (11f) 207
6.4.1.7. rac-$^{Me,nPr}SB(^{tBu2}ArO,I^*)Li_2$ (12f) 207
6.4.1.8. rac-$^{Me,Ph}SB(^{tBu2}ArO,I^*)Li_2$ (13f) 208
6.4.2. Synthesis of group four PHENI* dichloride complexes 208
6.4.2.1. $^{Me2}SB(^{tBu,Me}ArO,I^*)TiCl_2$ (1) 209
6.4.2.2. $^{Me2}SB(^{tBu2}ArO,I^*)TiCl_2$ (2) 209
6.4.2.3. $^{Me2}SB(^{Cumyl2}ArO,I^*)TiCl_2$ (11) 210
6.4.2.4. $^{Me2}SB(^{H2}ArO,I^*)TiCl_2$ (19) 211
6.4.2.5. rac-$^{Me,nPr}SB(^{tBu2}ArO,I^*)TiCl_2$ (12) 211
6.4.2.6. rac-$^{Me,Ph}SB(^{tBu2}ArO,I^*)TiCl_2$ (13) 212
6.4.2.7. $^{Me2}SB(^{tBu2}ArO,I^*)ZrCl_2$ (15) 213
6.4.2.8. $^{Me2}SB(^{tBu2}ArO,I^*)HfCl_2$ (16) 214
6.4.3. Synthesis of $^{Me2}SB(^{tBu,Me}ArO,I^*)TiX_2$ 214
6.4.3.1. $^{Me2}SB(^{tBu,Me}ArO,I^*)TiMe_2$ (17) 215
6.4.3.2. $^{Me2}SB(^{tBu,Me}ArO,I^*)Ti(CH_2SiMe_3)_2$ (18) 215
6.4.4. Synthesis of $^{Me2}SB(^{tBu2}ArO,I^*)TiX_2$ 216

6.4.4.1. $^{Me2}SB(^{tBu2}ArO,I^*)TiBr_2$ (3) 216
6.4.4.2. $^{Me2}SB(^{tBu2}ArO,I^*)TiI_2$ (4) 217
6.4.4.3. $^{Me2}SB(^{tBu2}ArO,I^*)TiMe_2$ (5) 217
6.4.4.4. $^{Me2}SB(^{tBu2}ArO,I^*)Ti(CH_2SiMe_3)_2$ (6) 218
6.4.4.5. $^{Me2}SB(^{tBu2}ArO,I^*)Ti(NMe_2)_2$ (8) 219
6.4.4.6. $^{Me2}SB(^{tBu2}ArO,I^*)Ti(OEt)_2$ (9) 220
6.4.4.7. $^{Me2}SB(^{tBu2}ArO,I^*)Ti(ODipp)_2$ (10) 221
6.4.4.8. $^{Me2}SB(^{tBu2}ArO,I^*)Ti(CH_2Ph)_2$ (7) 222
6.4.5. Synthesis of cationic intermediates 223
6.4.6. Synthesis of solid catalysts 223
6.5. Experimental details for Chapter Three 227
6.5.1. Solution-phase ethylene polymerisation studies 227
6.5.2. Slurry-phase ethylene polymerisation studies 227
6.5.3. High-throughput screening (Xplore, University of Naples Federico II) 228
6.5.4. Large-scale polymerisation (SCG Chemicals PLC; Rayong, Thailand) 229
6.6. Experimental details for Chapter Four 229
6.6.1. Propylene polymerisation studies using supported catalysts 229
6.6.2. Solution-phase propylene polymerisation studies 230
6.6.3. Large-scale polymerisation (SCG Chemicals PLC; Rayong, Thailand) 230
6.7. Experimental details for Chapter Five 230
6.7.1. Copolymerisation of ethylene and propylene 230
6.7.2. Terpolymerisation of ethylene, propylene, and ethylidenenorbornene 231
6.7.3. Vulcanisation of EPDM 232
6.7.4. Copolymerisation of propylene with 1-hexene 233
6.7.5. Copolymerisation of ethylene with linear α-olefins 234
6.7.6. Multivariate regression analysis 235
6.8. References 235
Conclusions and outlook 237

Appendix A – Supplementary data A1
Appendix B – Analysis of variance (ANOVA) B1
Appendix C – Crystallographic information file ..... .cif
Appendix D D1

Chapter 1 – Introduction

1.1. Polyolefins

Polyolefins (POs) dominate the global thermoplastic polymer market, with an annual output greater than 180 million tons valued around US$ 300 billion. The most widespread POs are polyethylene (PE) and polypropylene (PP) which account for 31 and 23% of the overall polymer market respectively.[1,2] Within this, the commodity grades of PE are categorised as one of high density (HDPE), low density (LDPE), and linear low density (LLDPE), with the latter experiencing the highest annual growth rates.[3] The olefinic monomers – ethylene and propylene – are typically produced by petrochemical cracking of higher order fractions of crude oil and are highly economic feedstocks for conversion to polymers.[4] Due to the environmental impact of the linear economy based on virgin petrochemical polymers, the production of bio-ethylene and bio-propylene from bioethanol has been the focus of some commercial development.[5,6] In combination with pyrolytic chemical recycling, post-combustion photosynthetic carbon recycling in the biosphere, or carbon capture technologies, a circularised closed-loop PO economy is an attractive possibility.[2,7-9] The continued development of societally indispensable polyolefin-based materials, and efficient catalysts for their synthesis, is therefore an important pursuit both for academia and industry.

1.1.1. Polyethylene

First discovered in 1898 resulting from the thermal decomposition of diazomethane, polyethylene is the simplest PO having the structure –$(CH_2)_n$–.[10] The properties and applications of polyethylene are determined principally by the short- and long-chain

branching, molecular wight, and molecular weight distribution (MWD). High density PEs are generally perfectly linear polyethylenes, with negligible degrees of branching (Figure 1.1). This gives HDPE a high crystallinity, density, melting point, and mechanical strength, suited to applications including containers, ropes, pipes, and consumer products. The polymerisation of ethylene to HDPE is generally achieved through transition metal catalysed step-growth polymerisation. By contrast, low density PE is a highly branched polymer, including secondary branches, and finds applications such as plastic bags and packaging. LDPE is synthesised by the free radical polymerisation of ethylene.

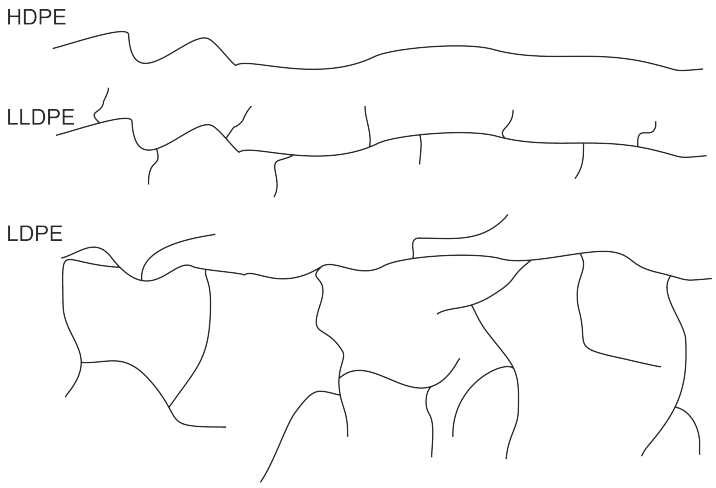

Figure 1.1 Schematic branching structure of HDPE, LLDPE, and LDPE.

1.1.1.1. Molecular weight distribution

The molecular weight and molecular weight distribution of polyethylene have a critical role in the mechanical, rheological, and morphological properties.[11] Generally, high molecular weight HDPE possesses increased toughness and strength which is desirable in many applications.[12] The dispersion and shape of the molecular weight distribution are parameters which also influence the properties of polyolefin materials.[13] MWD can be tuned through polymer blending,[14] bifunctional catalysts,[12,15,16] sequential reactivity,[17] and catalyst support composition.[18]

1.1.1.2. Ultra-high molecular weight polyethylene

Ultra-high molecular weight polyethylene (UHMWPE), defined by a molecular weight in the millions of Daltons, is a speciality grade of PE considered an important engineering plastic due to its desirable properties. UHMWPE has a tensile strength and impact resistance unmatched among polymers and more comparable to steel. It is chemically and abrasion resistant while also having a very low coefficient of friction, comparable to PTFE and described as self-lubricating.[19-24] Numerous applications exist for UHMWPE in the biomedical,[25] maritime, aerospace,[26] and ballistics sectors.[27,28] Outstanding performance is offered for total joint arthroplasty (Figure 1.2),[25,29-31] and UHMWPE is widely used as a bulletproof material.[27,32] Furthermore, UHMWPE may be melt- or gel-spun into fibres and woven into ropes and fabrics with extremely high toughness, higher strengths than para-amid fibres such as Kevlar®, and comparable properties to carbon fibre.[26,33-35] Single-polymer composite materials, such as UHMWPE-reinforced HDPE are of growing interest with useful intrinsic properties and applications such as aircraft and space structures.[36-38]



Figure 1.2 UHMWPE components for joint arthroplasty, reproduced from Musib *et al.* under a Creative Commons CC-BY 4.0 license.[39]

A feature of the extended chain length of UHMWPE macromolecules is their tendency to form interpenetrated networks of entanglements. Generally, UHMWPE is synthesised

in processes where the rate of chain growth is greater than that of chain crystallisation, resulting in a large entanglement density in the amorphous region.[40,41] The entanglements act as physical crosslinks and profoundly influence the physical and mechanical properties of the semicrystalline polymer such as deformation behaviour.[42] Entanglements and slow chain diffusion contribute to the extremely high melt viscosity of UHMWPE and renders it challenging to process, with common thermoplastic techniques like injection moulding impractical.[22] To circumvent this, the synthesis of substantially disentangled UHMWPE, which can be processed in the solid-state below the melting point,[43] and the production of polymer blends incorporating UHMWPE into a processable matrix have both been developed.[15,44] The production of nascently disentangled UHMWPE has been pursued through engineering heterogeneous catalysts with spatially diluted active sites,[45-47] selective reduction of active sites,[48] and nitrogen microbubbles,[49,50] as well as the development of specific single-site molecular catalysts.[28,51-56] The formation of interfacial entanglements has been exploited to enhance polymer welding and UHMWPE recycling.[57]

1.1.2. Polypropylene

Discovered in 1951, polypropylene (PP) comprises an important class of commodity and engineering materials, with diverse and desirable properties and the general form $–(CH_2CH(CH_3))_n–$.[58] Propylene is a prochiral monomer and can polymerise in a range of microstructures of dramatically distinct physical properties.[59] PP is predominantly synthesised using heterogeneous Ziegler-Natta catalysts where the inherent chirality of the titanium centres on the $TiCl_3$ crystal surface results in highly crystalline isotactic polypropylene (*i*PP).[60] It is clear from detailed computational modelling of these mechanistically elusive systems that steric considerations play a key role in enforcing

stereoselectivity, with the methyl group of the propylene interacting with chlorides adjacent to the metal centre.[61] Tacticity and molecular weights are highly coupled in these systems,[62] with low M_w partially crystalline atactic PP (*a*PP) obtained as a by-product.[63]

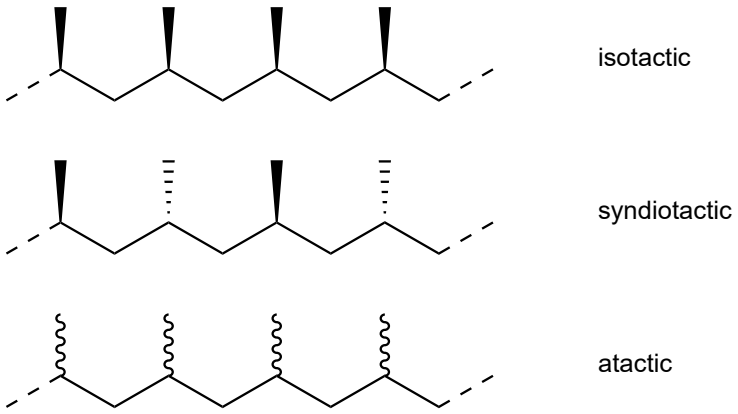

Figure 1.3 Schematic structures of isotactic, syndiotactic, and atactic polypropylene.

Single-site molecular catalysts are typically used where independent control over polymer tacticity and molecular weight are desired.[64] The relationship between the symmetry of single-site catalysts and resulting polypropylene tacticity is well understood,[64,65] with complexes in the C_{2v} and C_2 point groups typically producing atactic and isotactic PP respectively, while asymmetric C_1 complexes are reported to produce polymers with microstructures ranging from highly isotactic to atactic (Figure 1.4).[65] Stereoselectivity in prochiral monomer insertion results principally from enantiomorphic site control with steric constraints enforcing a preference for either the *re* or *si* configuration of the monomer. C_2 *ansa*-metallocenes are particularly effective, with the bridge requiring conformational rigidity of the ligand.[66,67]

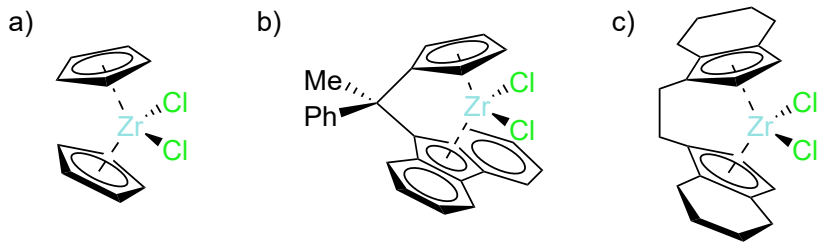

Figure 1.4 a) achiral zirconocene dichloride, and chiral *ansa*-metallocenes b) pseudo-C_s-symmetric ^{Me,Ph}C(cyclopentadienyl)(9-fluorenyl)$ZrCl_2$,[68] and c) C_2-symmetric *rac*-ethylene-bis(4,5,6,7-tetrahydro-1-indenyl)$ZrCl_2$.[69]

1.1.2.1. Ultra-high molecular weight polypropylene

Ultra-high molecular weight isotactic polypropylene has been well studied, with improvements reported in rheological and mechanical properties compared to low molecular weight *i*PP.[67,70-74] Ultra-high molecular weight syndiotactic polypropylene has also been investigated, as the chain-folding configuration is considered to be better suited to polymer processability, as well as having a beneficial combination of crystallinity and elasticity.[75,76]

Amorphous high molecular weight *a*PP is a material of growing industrial interest; beneficial elastic and optical properties lead to broad applications as adhesives, compatibilisers and as additives in a range of polymeric materials.[63,77] There has been limited development of catalysts that are selective for the synthesis of such materials, with complexes of titanium and zirconium receiving the most attention.[78,79] The synthesis of ultra-high molecular weight *a*PP (UHMWaPP, $M_w > 1$ MDa) has been reported, though typically only in relatively low-yielding processes.[79,80]

Ultra-high molecular weight homopolypropylene elastomers, synthesised by Rieger *et al.* as stereodefective *i*PP, were shown to have beneficial mechanical properties, including improved elastic recovery compared to lower M_w elastomeric PP.[81]

1.1.3. Higher polyolefins

Higher order polyolefins, such as poly(1-hexene), have received limited attention mostly focussed on reaction kinetics and mechanistic elucidation.[82] Catalysts have been developed to access a broad range of molecular weights,[83] and applications have been proposed including elastomers and impact modifiers.[84,85]

Ultra-high molecular weight homopolymers of higher olefins from 1-butene to 1-octadecene have also been reported, typically in moderate yields or under forcing low-temperature conditions, with relatively limited specific catalyst development, limited exploration of polymer properties, and few proposed applications.[82,86-89]

1.2. Olefinic copolymers

The incorporation of linear α-olefins (LAOs) into ethylene polymers allows for control over short-chain branching, enabling tuneability of the chemical and physical properties of the resulting linear low density polyethylene (LLDPE) polymers.[90-93] Propylene, 1-butene, 1-pentene, 1-hexene, 1-octene, and higher olefins up to at least 1-hexacosene have been studied as comonomers for ethylene copolymerisation.[87,94-101] While less studied, copolymers of propylene with 1-butene, 1-hexene, 1-octene, and higher olefins up to 1-octadecene have been synthesised using a range of catalysts.[102-105]

Heterogeneous Ziegler-Natta catalysts have been used in the copolymerisation of ethylene with LAOs with high activities, but relatively limited comonomer incorporation.[106,107] Single-site metallocene catalysts have shown good homogeneous catalytic activity towards E/LAO copolymerisation with a more uniform comonomer distribution than is possible with heterogeneous systems.[108-110]

1.2.1.1. Ethylene linear α-olefin copolymers

The structure and properties of linear low density polyethylenes has been the subject of intense study, with the degree and distribution of short-chain branching having a strong influence on morphological, thermal, and mechanical properties.[111,112] Commercial LLDPEs are typically random copolymers, with the distribution of monomers determined statistically, and can be produced with unimodal or bimodal interchain comonomer composition distributions.[113] The length of the side chains has proven significant in determining the physical properties of LLDPEs, with impact strength, ductility, and impact fatigue life increasing with increasing branch length.[114] LLDPE accounts for around a quarter of total polyethylene demand, and principally finds applications in films, packaging, sealants, plasticisers, modifiers, and compatibilisers.[115-121]

Wagener *et al*. employed an acyclic olefin metathesis reaction followed by exhaustive hydrogenation to produce precision-branched defect-free linear polyethylenes. It was found that polymer melting temperature decreased linearly as a function of branching density, and that lamellae thickness corresponded to the stretched all-*trans* configuration of the segments between branches, implying that the branches (except small methyl and ethyl branches) lie in the amorphous region (Figure 1.5).[122-128]

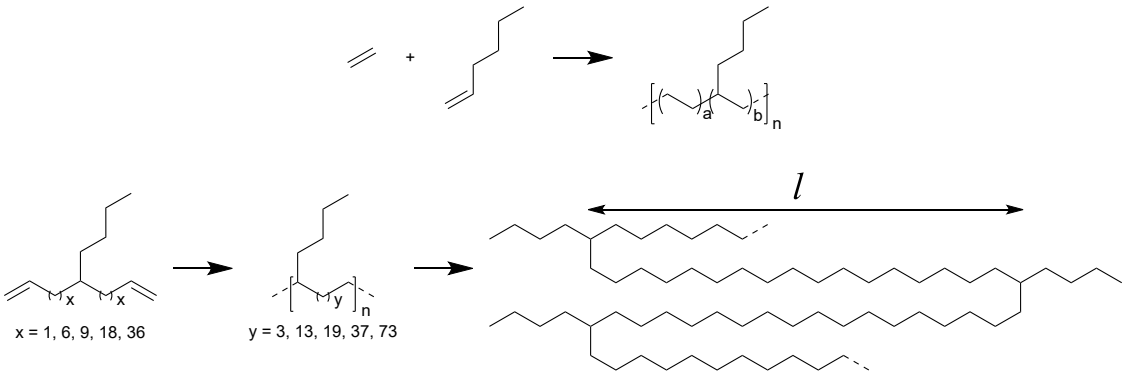

Figure 1.5 Random ethylene-LAO insertion copolymerisation (top), and diene metathesis polymerisation of precision-branched polyethylene (bottom), showing the lamellae thickness, *l*, corresponding to the all-*trans* conformation of inter-branch segments.

1.2.1.2. Thermoplastic polyolefin elastomers

Conventional rubbers are highly crosslinked polymers which are challenging to process and have poor recyclability.[129] Thermoplastic elastomers (TPEs) are an emerging class of materials that bridge the gap between classical thermoset rubbers and thermoplastics, having the elastic properties of the former and the processing flexibility and recyclability of the latter.[130,131] This requires a biphasic structure with crystalline and amorphous regions. Composite materials such as blends of polyolefins with natural, styrene-butadiene, silicone, and polyurethane rubbers have been explored, with compatibilisers required to improve miscibility. Copolymers of ethylene have also been investigated, with varying mechanical properties depending on crystallinity, composition, and structure.[130,132] Block copolymers have proved promising with hard and soft segments facilitating TPE behaviour.[133-135] Single-feed reactions have also been demonstrated, with the chain walking mechanism of late transition metal catalysts enabling the direct formation of highly branched elastomeric polyethylenes.[131]

1.2.1.3. Ethylene propylene diene terpolymers

Ethylene propylene diene terpolymers (EPDM) are a class of synthetic polyolefin rubber produced by the copolymerisation of ethylene and propylene in the presence of a diene for example butadiene, isoprene, 1,4-hexadiene, 5-ethylidene-2-norbornene, or 4-vinylcyclohexene.[136] Excellent physical and mechanical properties, including resistance to ozone, heat, chlorine, oxygen, and weathering, make EPDM the most suitable rubbers for outdoor applications, tubing, insulating materials, and automotive applications.[137] EPDM has a remarkable capacity to accept high loadings of fillers such as carbon black, silica, organoclays, and aluminosilicates.[138-141] The incorporation of dienes (typically up to 10%) can provide unsaturation for post-synthesis vulcanisation such as using UV light, sulphur, or organic peroxides,[142-145] with dynamic crosslinking of polymer blends enabling a high degree of stability.[146-149]

1.3. Catalysts for the polymerisation of olefins

The polymerisation of ethylene to LDPE is a free radical mediated process which occurs under high pressures and temperatures.[150,151] The production of linear HDPE, though highly exergonic, requires transition metal catalysis.

1.3.1. Heterogeneous catalysts

The majority of commercially produced PE and *i*PP are synthesised using classic heterogeneous Ziegler-Natta (ZN) catalysts. This four-component catalytic system comprises titanium (IV) chloride, magnesium (II) chloride, an alkyl aluminium (typically $AlEt_3$), and a suitable Lewis base, in which $MgCl_2$ acts as an inert support material.[61] Alternatively, Phillips catalysts are based on hexavalent chromium oxide supported on a high surface area material, usually silica but also alumina and titania.[152,153] These solid-state catalysts were developed with high activities towards olefin polymerisation,

eliminating the need for catalyst removal from the resin owing to the very low loading of residual catalyst in the final product. Additionally, they demonstrate a morphological templating effect, which allows polymers to be produced as spherical particles with controlled diameter and particle size distribution, aiding processability.[154] Despite being industrially ubiquitous, these are systems of extreme chemical complexity with poorly-defined active sites and mechanisms.[155] This limits the level of control that is possible over the molecular weight, dispersity, branching, stereochemistry, and comonomer incorporation of the resulting polymers.[154,156,157]

1.3.2. Homogeneous Kaminsky metallocenes

Traditional polymerisation catalysts are now commonly replaced by Kaminsky metallocenes for applications where fine control over the polymer's molecular weight and distribution, co-monomer content, and tacticity are required.[158,159] Metallocenes are hydrocarbon-soluble allowing for homogeneous single-site catalysis. Until the accidental discovery of methylaluminoxane (MAO) by Kaminsky *et al.* in 1975, metallocenes were not active enough to be exploited industrially, and were principally of academic interest.[94] MAO, synthesised by the controlled partial hydrolysis of trimethylaluminium (TMA), was found to increase the activity of metallocenes towards ethylene polymerisation by a factor of up to 10 000 compared to unhydrolysed alkyl aluminiums.[158,160] Kaminsky demonstrated the dual functionality of MAO, capable of both abstracting anionic ligands, and acting as an alkylating agent to create a cationic, electrophilic, and substitutionally labile active species (Scheme 1.1).[161]

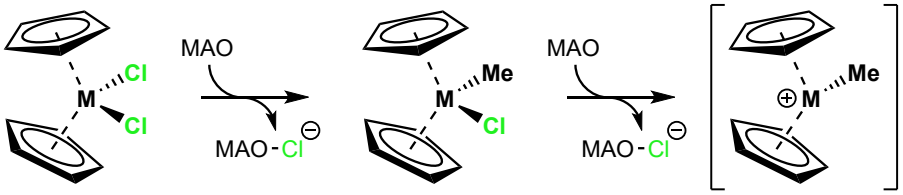

Scheme 1.1 Mechanism of activation of metallocenes by MAO proposed by Kaminsky.[161] M = Ti, Zr, Hf.

The ligand environment of metallocene catalysts can be tuned sterically, electronically, and stereo-geometrically to enhance catalytic activity and give fine control over both bulk and micro properties of the polymer.[162]

1.3.3. Supported single-site catalysts

The control and tuneability afforded by single-site catalysts is brought into the realms of industrial-scale applicability through heterogenisation. The immobilisation of single-site catalysts on suitable carriers facilitates their use in slurry-phase or fluidised bed reactors previously used for ZN reactions with minimal modifications, as well as ensuring the formation of polymer particles with dispersed morphologies and desirable bulk densities.[163,164] Many inert inorganic supports such as silica,[165] alumina,[166] zirconia,[167] and layered double hydroxides[168] have been developed, but these need pre-treating to enable metallocene immobilisation.[169] Solid polymethylaluminoxane (sMAO) is an insoluble form of MAO, and has been introduced as an activating catalyst support, which requires neither pre-treatment nor co-catalytic initiators. The structure of sMAO and of supported metallocenes is poorly understood, but many catalysts of this type yield polymer with narrow molecular weight distributions and apparent single-site behaviour, suggesting that a similar polymerisation mechanism is occurring both using solution-phase metallocenes and slurry-phase supported metallocenes.[169,170] Aside from immobilisation on inorganic supports, "self-supported" catalysts have also been developed,[171] with examples based on emulsions,[172] coordination polymers,[173]

bottle-brush polymers,[174] metal organic frameworks (MOFs),[175] or *in situ* incorporation into the growing polymer chain.[176,177] Organic and polymeric supports have additionally been proposed.[178-180]

1.3.3.1. Silica

Silica-based zeolites and mesoporous silicas are common catalyst supports in industry, as they possess high specific surface areas, and pore structures that reduce the energetic barriers associated with diffusion of reactants to the catalyst site and removal of products.[181] Amorphous silica is the preferred support for metallocene immobilisations – as well as excellent morphological control, the high concentration of surface hydroxyl groups readily facilitates functionalisation.[182,183] The silica particles are first reacted – *via* the surface hydroxyls – with the MAO cocatalyst which then enables electrostatic binding of the activated metallocene complex.[184,185]

As polymerisation progresses, efficient particle fragmentation ensures that catalyst activity is maintained as previously occluded active sites become diffusionally accessible. Fragmentation is also the mechanism by which morphological control is achieved.[186] Experimental and theoretical studies have proposed this to occur through a combination of the "shrinking core" and "bi-sectioning" models: describing the shedding of surface layers, and the propagation of cracks across the core of the particle respectively (Figure 1.6).[187] The X-ray nano-tomography methodology developed by Bossers *et al.* has recently given a direct 3-dimensional visualisation of early-stage particle fragmentation, and shown that continuous bisection is the dominating fragmentation regime.[188,189]

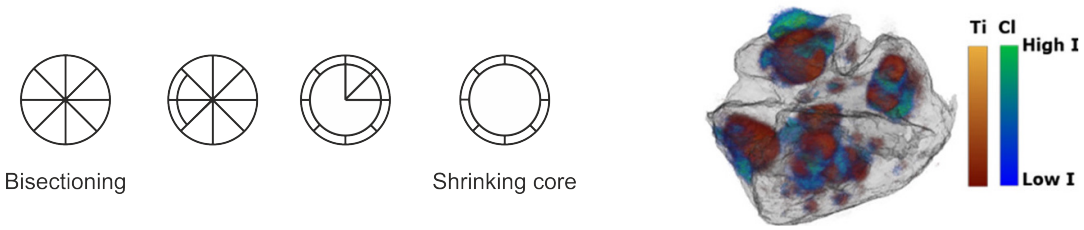

Figure 1.6 Schematic representation of proposed particle fragmentation pathways, adapted from Bossers *et al.*,[189] and elemental distribution, showing fragmented catalyst particles within a polymer particle, measured by 3D X-ray ptychography and fluorescence, reproduced from Bossers *et al.* under a Creative Commons CC-BY-NC-ND license.[188]

1.3.3.2. Layered double hydroxides

Layered double hydroxides (LDHs) are a class of layered nanoclays, consisting of positively-charged brucite-like layers intercalated with charge balancing anions and neutral solvent molecules. They have the general formula $[M^{II}_{1-x}M^{III}_{x}(OH)_2]^{y+}[A^{n-}]_{y/n}\cdot mH_2O$, where the range of di- and tri-valent metal cations can include Mg, Ca, Ni, Fe, and Al, and A^{n-} can be a variety of ions such as carbonate and nitrate.[190] Numerous LDHs have been synthesised and studied with applications including photo- and electro-catalysis,[191-194] organic catalysis,[195] carbon capture and utilisation,[196,197] and composite materials.[198]

More recently, LDHs have been treated with aqueous-miscible (AMO) and aqueous-immiscible (AIM) organic solvents resulting in increased surface areas, hydrophobicity, and improved dispersibility in non-polar solvents. The surface hydroxyl groups on the brucite sheets act analogously to those on silica and can react with MAO. When treated with MAO, these AMO/AIM-LDHs have proven to be effective and highly tuneable supports for single-site polymerisation catalysts (Figure 1.7),[199,200] with the metal composition of the support recently shown to control polymer molecular weight distribution.[18] Synergistic hybrid core@shell materials comprising silica@LDH have

been developed with the goal of combining the morphological templating benefits of the silica core the with catalytic tuneability of LDH.[201,202]

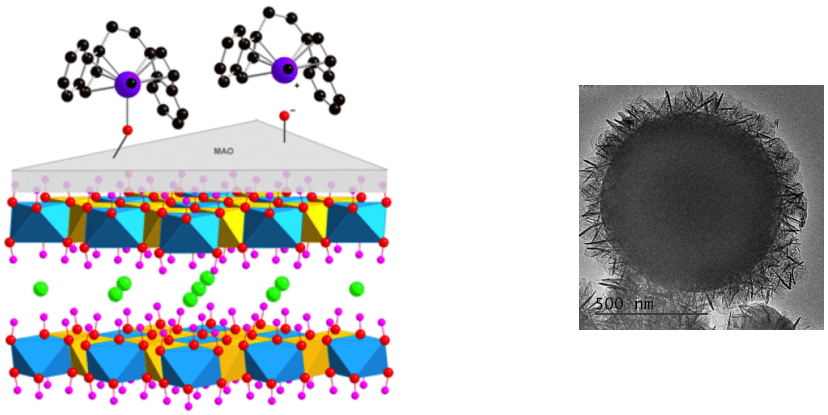

Figure 1.7 Suggested structure of AMO–MgAl–SO_4/MAO/(EBI)$ZrCl_2$ based upon EXAFS measurements, reproduced from Buffet *et al.* with permission © 2015 American Chemical Society.[199] TEM image of SiO_2@AMO-$MgAl_3$-CO_3 reproduced from Buffet *et al.* with permission © 2016 The Royal Society of Chemistry.[202]

1.3.3.3. Solid polymethylaluminoxane

Solid polymethylaluminoxane (sMAO) is a modified form of MAO and is synthesised from TMA by carbonyl-containing compounds in a non-hydrolytic method. The product of this reaction is a mixture of monomeric and oligomeric aluminoxanes, of the form "$Me_2Al–O–AlMe_2$", that is able to activate metallocene precatalysts.[203] Above 60 °C, insoluble higher aluminoxane oligomers were observed to precipitate *via* a condensation reaction and they have proven to be effective dual function activating supports for metallocene and post-metallocene catalysts.[169,204] Solid-state NMR spectroscopy has enabled insights into the poorly-defined structure of sMAO, implying the presence of long-chain aluminoxane oligomers, with incorporated "free" TMA and benzoate groups.[169]

sMAO has been demonstrated as an effective support with a range of tungsten-,[205] zirconium-,[170,206-209] and titanium-based complexes,[210,211] offering excellent morphological control over the polymer particles,[212] and higher activities than silica-based catalysts. sMAO has been modified with C_6F_5OH or $B(C_6F_5)_3$, to result in substantially increased polymerisation activities.[213,214] It has been suggested that upon immobilisation, the labile ligands of the precatalyst remain bound to the sMAO surface, possibly playing a non-innocent role in the catalytic cycle (Figure 1.8).[205,215]

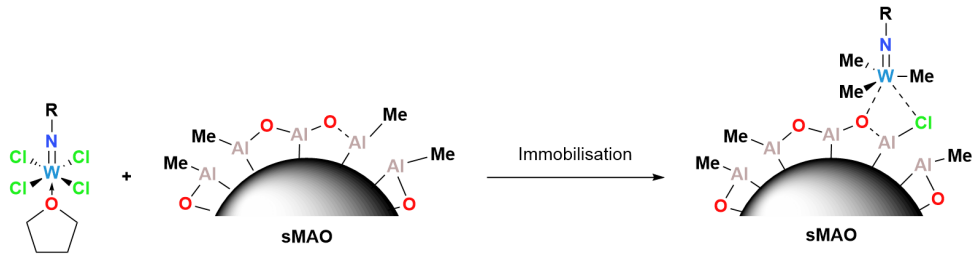

Figure 1.8 Schematic representation of the immobilisation of a tungsten imido complex on sMAO, adapted from Wright *et al.* with permission © 2016 The Royal Society of Chemistry,[216] showing the interaction of the bound surface chloride with the metal centre.

1.3.4. Polymerisation mechanism

Catalytic α-olefin polymerisation is proposed to proceed *via* the Cossée-Arlman 1,2-coordination-insertion mechanism. The catalyst reacts with MAO initiator to form the electrophilic coordinatively unsaturated active species which can then coordinate the alkene in a manner described by the Dewar-Chatt-Duncanson model.[217] This is followed by repetitive 1,2-insertion into the bond between the metal and the growing polymer chain *via* an α-agostic-stabilised transition state (Scheme 1.2).[218-220] Recently, direct experimental evidence for the molecular coordination-insertion polymerisation pathway has been obtained from *in situ* STM on a single crystal iron catalyst.[221] There are a number of possible termination pathways including chain transfer to aluminium, various β-hydrogen transfers, and hydrogenolysis when in the presence of molecular dihydrogen.

Calculations suggest that alkene π coordination is a barrierless process, whereas the migration and insertion steps pass through transition states. The relative activation energies of the propagation and termination steps correlate with the molecular weight of the resulting polymer. A low activation barrier in propagation and high barrier in termination steps favour higher molecular weight polymers. By comparing group 4 metallocenes *in silico*, Martínez-Araya *et al.* have shown that this condition is met for titanium, which is expected to produce higher molecular weight polymers than equivalent zirconium or hafnium systems.[222]

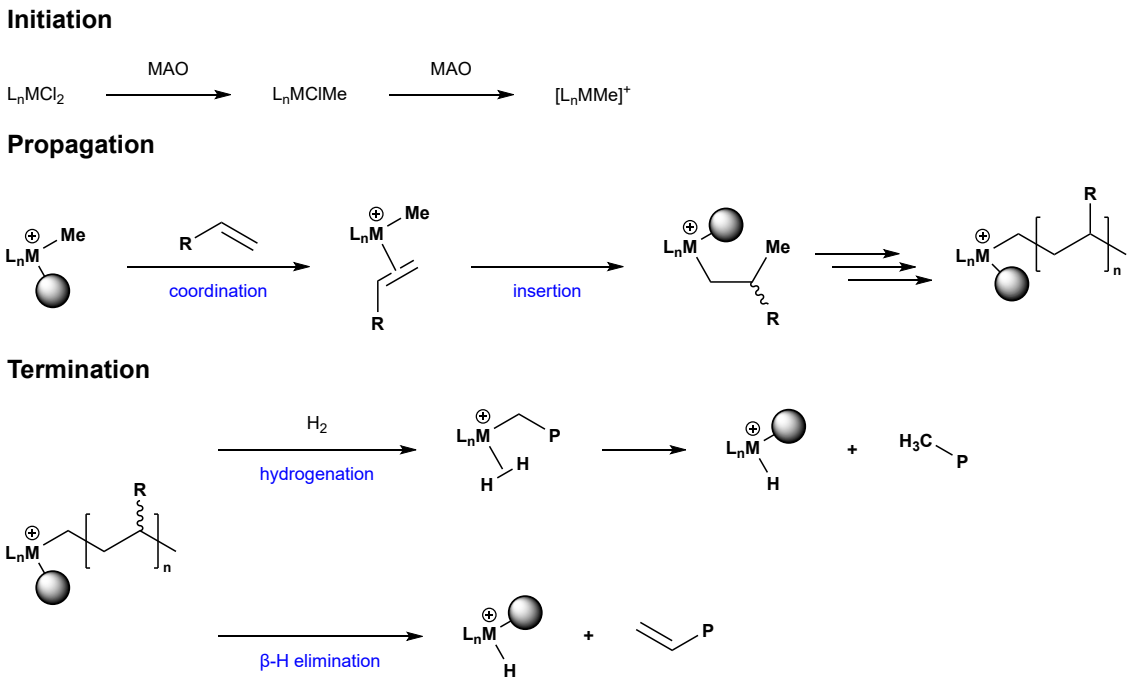

Scheme 1.2 Cossée-Arlman mechanism of coordination-insertion α-olefin polymerisation, with the hydrogenolysis and β-hydride elimination termination processes exemplified. P = polymeryl.

According to Ewen's symmetry rules, the enantiofacial discrimination of a prochiral alkene has been directly related to the chirality of the catalytic sites, with the R group of the α-olefin preferentially oriented in the least sterically demanding position.[66,223] Brintzinger *et al.* used α-deuterated olefins in stereokinetic studies with chiral *ansa* zirconocenes and scandocenes to show that an α-agostic interaction is responsible for the stereoinduction by controlling the stability of the alternative 1,2-insertion transition

states. The preference for the *re* or *si* orientation of the incoming olefin comes from the required placement of the β carbon atom of the growing polymer chain in the least incumbered of the two positions at a rigid three-member Zr-H(α)-C(α) ring (Scheme 1.3).

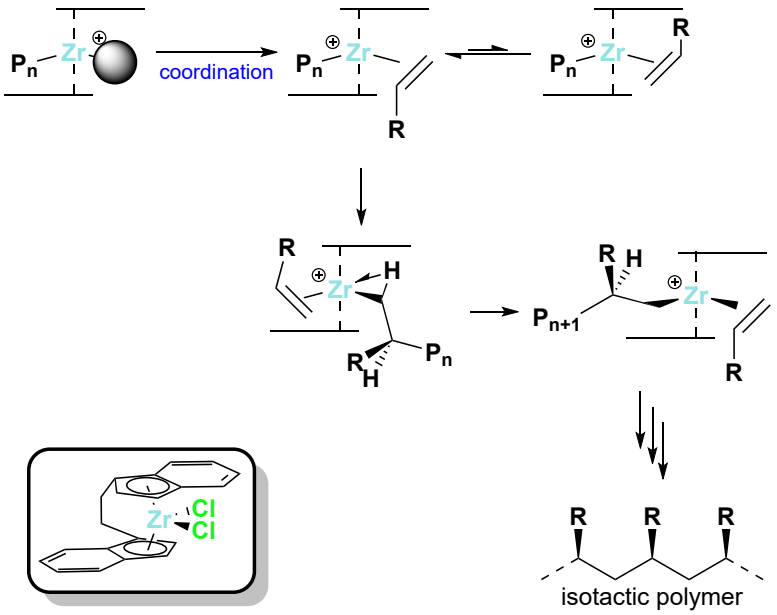

Scheme 1.3 Illustration of the steric origin of poly(α-olefin) stereospecificity in C_2-symmetric *ansa* metallocenes such as *rac*-(EBI)$ZrCl_2$. P_n = polymer chain of length *n*.

1.3.5. Polymerisation conditions

It is well known that catalytic activities are markedly affected by reaction conditions such as scale, mixing efficiency and stirring, solvent, cocatalysts and scavengers, temperature, pressure, and reaction time.[224-226] This is a large part of the reason for the poor inter-laboratory reproducibility of reported catalyst activities.[227-229]

1.3.5.1. Cocatalysts

MAO is typically preferred as the cocatalyst for single-site catalysts, being able to alkylate and abstract ligands to form the cationic active species. MAO comprises a mixture of different structures; the predominant topology at ambient temperatures consists of cages of the form $(AlOMe)_n \mid 6 \leq n \leq 20$ containing "free" TMA.[230-232] Very little is known about the true structure of MAO which is expected to vary both between

samples and over time.[233] In addition to the function of MAO in alkylating and abstracting ligands from metallocenes to form a cationic active species, a tight-contact ion pair is formed upon dissociation of the weakly-coordinating anion $[X–MAO]^-$.[234-236] It is now generally accepted than an outer-sphere ion pair is the polymerisation-active catalyst, while bridged and bimetallic adducts are dormant species.[233,237] The identity of the abstracted group plays a decisive role in the activation and polymerisation processes: the $[L_2ZrMe]^+[Cl–MAO]^-$ pair is much more tightly bound than with $[Me–MAO]^-$, and strong pairing with $[Me_2N–MAO]^-$ resulted in poor polymerisation activities.[238,239] Typically, highly superstoichiometric amounts of MAO are required, $[Al]/[M] \approx 10^2–10^4$, which can lead to the formation of side products that are not active towards polymerisation. These include the reduction of the transition metal centre, and the formation of M–Al bimetallic adducts.[240,241] The presence of "free" TMA may also result in the formation of dormant species of the form $[L_2Zr(\mu\text{-}Me)_2AlMe_2]^+$,[238] and chain transfer to aluminium is an important chain termination pathway which influences the polymer molecular weight.[233] In these ways, the MAO to metallocene ratio is a critical parameter for determining catalyst reactivity.

Well-defined molecular analogues of MAO have been developed, such as the $[AlHAl]^+[BAr^F{}_4]^-$ of Zaccaria *et al.* (AlHAl = iBu$_2$(PhMe$_2$N)Al]$_2$(μ-H)),[242] and other Lewis acids with non-coordinating counter-ions have been employed as stoichiometric activators such as trityl or anilinium borate salts.[161,243-246] By eliminating aluminium and thus supressing chain transfer processes, the use of borate activators can result in high molecular weight polyolefins.[247] The coordinating ability of the counteranion has been shown to influence activity, with more strongly bound ion pairs generally having lower activities.[248-250] Substitution of SF_5 sulphanyl groups at the *meta* positions of the aryl

borates by Langford *et al.* resulted in a two-fold increase in activity compared to the [BAr^F_4] analogue.[251] Activators covalently bound to silica have been used as a strategy for catalyst immobilisation.[252]

1.3.5.2. Scavengers

In addition to MAO or a stoichiometric catalyst activator, scavengers are employed to remove trace impurities, such was water and oxygen, from the reaction mixture. Trialkyl aluminium scavengers (R_3Al, where R includes methyl, ethyl, *iso*-butyl and *n*-octyl) are generally used as they result in increased activities relative to alkyl aluminium halides.[253-256] Catalyst activity and polymer molecular weight have both been increased with the use of larger alkyl groups.[255,257] The bulkier trialkylaluminium reagents can trap the "free" TMA in the MAO activator through ligand scrambling, with larger alkyl group resulting in more active systems.[258] There is a strong concentration dependence on the kinetic profile and high concentrations can both deactivate the metallocene,[259-261] and result in the leaching of an immobilised catalyst into solution.[262,263]

1.4. Permethylindenyl chemistry

1.4.1. Cyclopentadienyl ligands

Since the discovery of the prototypical metallocene complex, ferrocene, was reported in 1951, η^5-cyclopentadienyl has been the ligand at the forefront of organometallic chemistry.[264] The cyclopentadienide anion ($C_5H_5^-$, Cp) exists in complexes exhibiting a range of hapticities.[265] Pentahapto coordination leads to a rich variety of sandwich and half-sandwich compounds with elements from all parts of the periodic table.[266-271]

In the D_{5h} point group, Cp has an electronic configuration of $\sigma^2\pi^4\delta^0$, able to act as a σ donor through the filled a_2'' orbital, as a π donor through the filled doubly degenerate e_1''

pair of orbitals and as a δ acceptor through the vacant e_2'' pair (Figure 1.9).[272] As well as good orbital overlap between the molecular orbitals of Cp and those of the metal, the Coulombic attraction between the formally anionic ligand and a formally positive metal centre leads to strong bonding interactions and stable complexes. Bonding in sandwich compounds, like ferrocene, occurs principally through π- and δ-type interactions; σ bonding is weak due to the relatively poor orbital overlap with the metal d_{z2} which has a nodal cone in its spatial distribution function.[273]

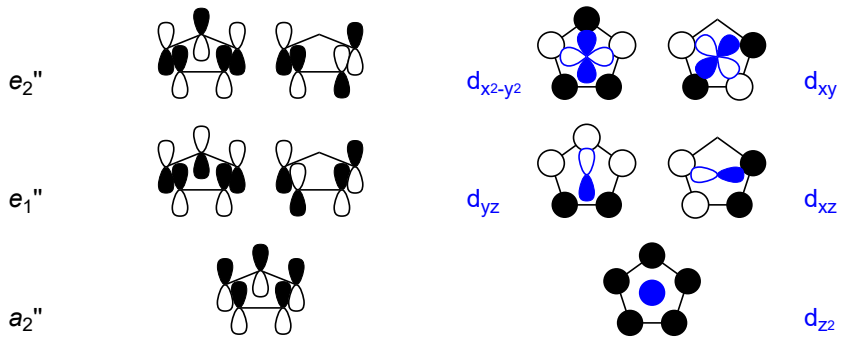

Figure 1.9 Molecular orbital diagram of the cyclopentadienyl ligand, showing interactions with transition metallic d orbitals. Figure adapted from *Inorganic Chemistry*, 7th ed. (OUP) under a Creative Commons CC BY-NC-SA 2.0 UK license.[272]

As a ligand, the properties of Cp can be tuned both sterically and electronically through substitution with electron donating or withdrawing groups, or bulky substituents.[274] In particular, the increased steric bulk caused by permethylation increases the kinetic stability of these complexes.[275]

1.4.2. The indenyl effect

Indenyl ligands ($C_9H_7^-$, Ind, I) are also common η^5 cyclic polyenes, bonding through the C_5 ring, although η^6-, η^3-, η^2- and η^1-indenyl complexes have also been reported.[276,277] Nesmeyanov *et al.* reported the synthesis of a tungsten complex with both η^3- and η^5-bound indenyl ligands at the same metal centre (Figure 1.10). [278]

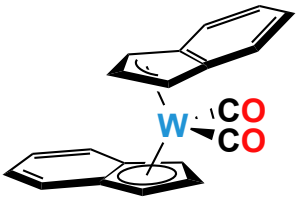

Figure 1.10 Structure of $(\eta^5\text{-}C_9H_7)(\eta^3\text{-}C_9H_7)W(CO)_2$ reported by Nesmeyanov *et al.*.[278]

Compared to Cp, there is a decreased kinetic barrier and increased thermodynamic driving force for indenyl complexes to undergo η^3,η^5-haptotropic ring slip (Figure 1.11). This results in re-aromatisation of the C_6 ring in indene and coordination to the metal through an η^3 allyl mode.[279] This is an example of ligand bifunctionality, and the coordinative flexibility that this affords leads to much more facile catalysis. This η^5-η^3 ring slip is formally a two-electron oxidation of the metal which becomes electrophilic and coordinatively unsaturated, allowing concomitant associative substitution processes not common for 18 electron complexes,[280] leading to a several-thousand-fold increase in the rate of ligand substitution.[281]

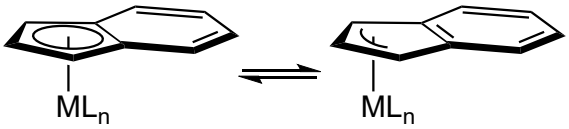

Figure 1.11 η^5-η^3 ring slip in metalloindenyl complexes, driven by rearomatisation of the C_6 ring.

Similarly to Cp, permethylation confers kinetic stability to permethylindenyl ($C_9Me_7^-$, Ind*, I*, Figure 1.12c) complexes through increased steric bulk. This reduces the propensity for reactive collision, and the positive inductive effect of the methyl groups through $\sigma_{CH} \rightarrow \pi^*_{CC}$ hyperconjugation increases the thermodynamic stability.[282]

Permethylindenyl metallocenes have been reported for Ti, Cr, Fe, Co, Zr, Rh, La, Nd, Er, Hf, and Th (Figure 1.13).[283-289] In all cases, the metalation reactions are straightforwardly achieved through the reaction of a metal source (such as $Co(acac)_2$ or $FeCl_2{\cdot}x$THF) with lithium, sodium, or potassium heptamethylindenide.

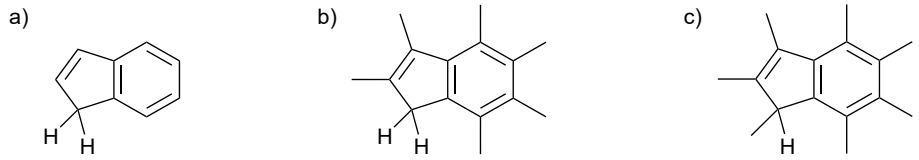

Figure 1.12 Selected indene derivatives: a) indene (IndH), b) 2,3,4,5,6,7-hexamethylindene (Ind#H), and c) permethylindene (Ind*H).

The synthesis of Ind*H from tiglic acid has been well developed.[282] The electronic properties of the I* ligand in FeI*$_2$ were studied by O'Hare *et al.* – a combined electrochemical and photoelectron spectroscopic approach quantitatively showed the electron donating nature of the I* ligand by a reduction in the first ionisation energies and redox potentials compared to FeCp*$_2$.[283]

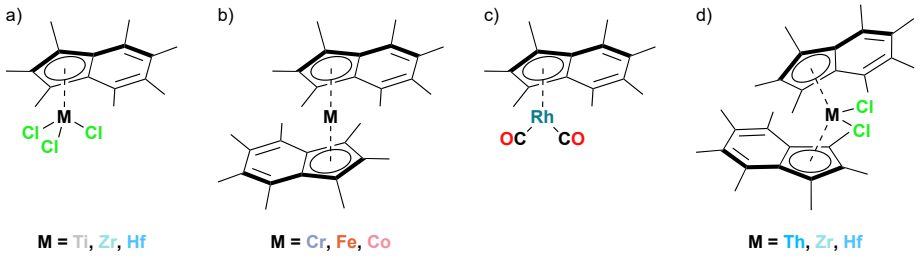

Figure 1.13 Examples of permethylindenyl complexes of d- and f-block elements. a) I*MCl$_3$ (M = Ti, Zr, Hf),[286] b) I*$_2$M (M = Cr, Fe, Co),[283,284] c) I*Rh(CO)$_2$,[285] d) I*$_2$MCl$_2$ (M = Th, Zr, Hf).[287,289]

1.4.3. The *ansa* effect

Metallocene sandwich complexes in which the two components of the ligand are joined by a bridging group are termed *ansa* complexes; the first, reported by Lüttringhaus *et al.*, were derived from ferrocene with alkyl bridging groups of the form (CH$_2$)$_n$ | n = 3, 4, 5.[290] Many bridges have since been reported (Figure 1.14), including methylene and ethylene, and a variety based on heteroatoms such as boron, silicon, tin, phosphorous and germanium; a bridge drastically increases the stereorigidity of these complexes and leads to stereoselective catalysis.[291] A variation of the permethylindenyl ligand is the

2,3,4,5,6,7-hexamethyl indenyl ligand ($C_9Me_6H^-$, Ind$^{\#}$, Figure 1.12b) first reported by Alías *et al.*, which allows for the inclusion of an *ansa* bridge (Figure 1.14e).[292]

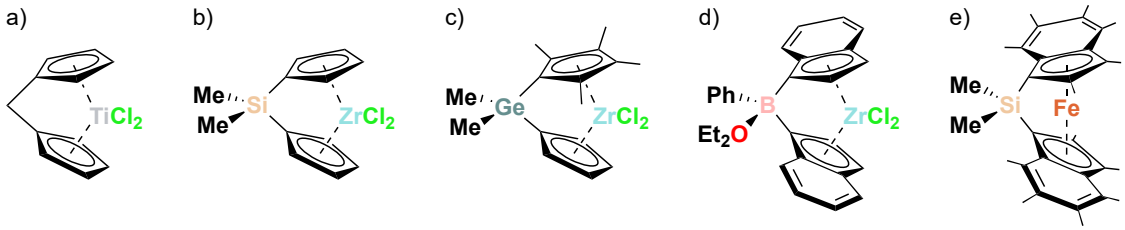

Figure 1.14 Examples of selected *ansa* metallocenes: a) $CH_2(Cp)_2TiCl_2$,[293] b) $^{Me}_2Si(Cp)_2ZrCl_2$,[294] c) $^{Me}_2Ge(Cp)(Cp^*)ZrCl_2$,[295] d) *rac*-(^{Ph,Et_2O}BBI)$ZrCl_2$,[296] and e) *rac*-($^{Me}_2$SBI*)Fe.[292]

Ansa metallocenes have been shown to be highly active in catalysis: *rac*-(SBI)$ZrCl_2$ and *rac*-(SBI*)$ZrCl_2$ have been shown to be active for ethylene polymerisation (18 450 and 22 622 $kg_{PE}\ mol_{Zr}^{-1}\ h^{-1}\ bar^{-1}$ respectively),[297] the Ind* complex more active than the Ind, and both substantially more so than an unbridged analogue *rac*-(Ind$^{\#}$)$_2ZrCl_2$ (433 $kg_{PE}\ mol_{Zr}^{-1}\ h^{-1}\ bar^{-1}$).[297]

1.5. Beyond metallocene catalysts

Recent advances in single-site molecular polymerisation catalysts have focussed on "post-metallocenes", where at least one of the cyclopentadienyl fragments has been replaced by an X-type heteroatomic donor ligand. This allows for a greater scope of steric and electronic parameters.

1.5.1. Constrained Geometry Catalysts

Constrained Geometry Complex (CGC) is a term originally describing *ansa*-bridged cyclopentadienyl amido complexes, but now encompasses a wide variety of related isoelectronic or isolobal systems based on transition and lanthanide metals (Figure 1.15),[270,298,299] many of which show exceptional activity towards polyolefin synthesis.[227,300-303] The improved performance of group four CGCs compared to more

classical Kaminsky metallocenes is believed to be a result of the less crowded coordination sphere, the smaller Cp–M–N bite angle, and a suppression of chain transfer processes.[298] This leads to increased activities and generally higher molecular weight polymers, but also the ability to incorporate comonomers with high efficiency,[304] and they are among the few catalysts able to copolymerise ethylene with styrene.[305] The incorporation of a wide variety of monomers has led to the production of polymers with unique material properties. Monomers successfully polymerised by CGCs include: branched olefins; conjugated and non-conjugated linear dienes; olefin functionalised silsesquioxanes, fullerenes, and thiophenes; cyclic monomers; and polar monomers including α,ω-eneols, methyl methacrylate, and acrylonitrile.[298]

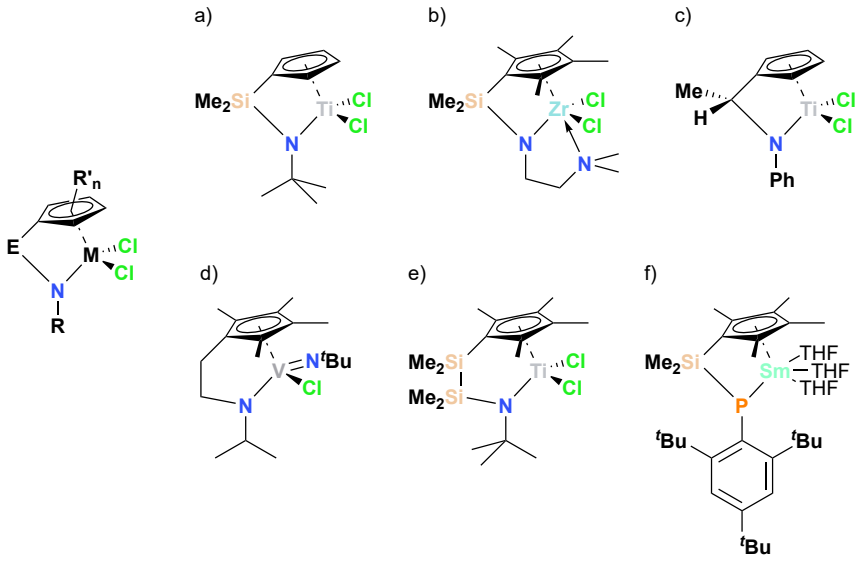

Figure 1.15 Molecular structured of selected Constrained Geometry Catalysts. a) ^{Me2}SB(^{tBu}N,Cp)TiCl$_2$, b) ^{Me2}SB(^{Me2}NCH$_2$CH$_2$N,Cp*)ZrCl$_2$, c) ^{Me,H}C(^{Ph}N,Cp)TiCl$_2$, d) EB(^{iPr}N,Cp*)V(=N^{t}Bu)Cl, e) ^{Me2}Si^{Me2}Si(^{tBu}N,Cp*)TiCl$_2$, d) ^{Me2}SB(^{tBu3}ArP,Cp*)Sm(THF)$_3$.[298]

In particular, the permethylcyclopentadienyl CGC – ^{Me2}SB(^{tBu}N,Cp*)TiCl$_2$ – was commercialised by Dow, Inc. as INSITE® as it offers excellent catalytic efficiency at high temperatures and can incorporate large amounts of olefinic comonomers including LAOs,

dienes, and aromatic olefins.[301,306] A further advantageous characteristic of these catalysts is the ability to reinsert the α-olefin macromonomers resulting from β-hydride elimination, which results in long-chain branching and increases the processability of the polymers.

The tuneability of the CGC ligand has been explored extensively, with variations in the η^5 ligand, the *ansa* bridge and the amido group.[224] Ligands with apical fragments including fluorenyl, indenyl, η^5-cyclohexadienyl, and heterocycles containing boron and phosphorous have been studied with both the steric and electronics having an effect on the catalytic activity and the polymer molecular weight. For example, the phospholyl-amido complex reported by Brown *et al.* had a similar activity to that of the Cp* CGC, but produced a lower molecular weight PE.[307] *Ansa* bridges based on carbon, silicon, and phosphorous are known, with the conformational strain induced by the bridge believed to be responsible for the enhanced catalytic performance.[308] More acute Cp–M–N angles have been shown to increase catalytic efficiency,[298] however, Kunz *et al*. have since cast doubt on the importance of a sterically constrained bridging group on the basis of experimentation and computational results.[309] Unbridged Cp* κ^1-amidinate complexes have proved highly effective for the copolymerisation of ethylene and propylene.[310-312]

While silicon-based *ansa* bridges are the most common, those utilising boron,[313] sp^2 and sp^3 carbon,[314,315] and phosphorous have all be reported.[316] Chiral silicon bridges were developed, giving rise to diastereomeric complexes and bimodal polymer molecular weight distributions.[317] Substitution at the *ansa* bridge also enabled the synthesis of tethered dinuclear catalysts for bifunctional catalysis.[318] The amido substituent can be tuned with a wide range of substitutions. The availability of enantiopure amines led to

the development of chiral CGCs for asymmetric catalysis.[319,320] An amido group with a bulky aromatic substituent was reported by Kleinschmidt *et al*. to produce substantially isotactic polypropylene.[321] Substituents bearing additional neutral or anionic donors forming tridentate ligands were found to result in decreased polymerisation activities.[322,323] From their inception, it has been appreciated that the catalytic efficiency of CGCs is correlated with increased electron density at the metal centre.[324] The steric bulk of the amido group was found to be correlated to polymer molecular weight, though the direction of the trend varies with the Cp fragment.[325]

1.5.2. Phenoxy imine catalysts

The phenoxy-imine (FI after the Japanese transliteration "Fenokisi-Imin Haiishi") catalysts were introduced in 2001 by Matsui *et al.* (Mitsui Chemicals, Inc.) as the result of a rational design incorporating multidentate and non-symmetric ligands with moderate electron donating properties (Figure 1.16).[326,327] Many group four FI complexes display exceptional activity towards olefin polymerisation.

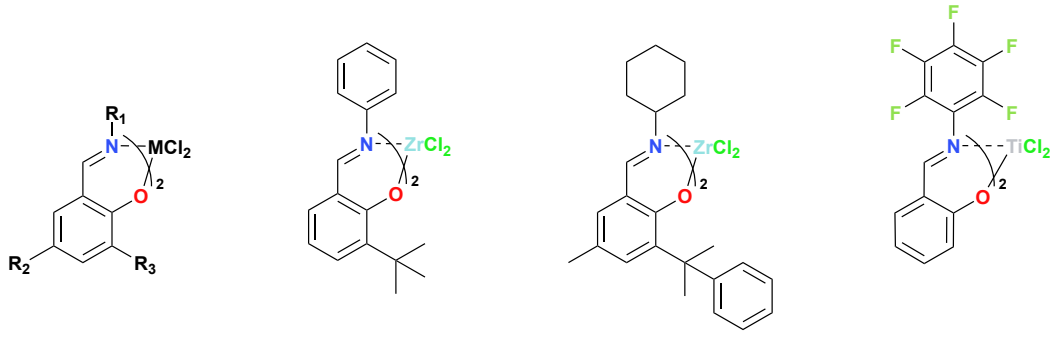

Figure 1.16 Molecular structure of selected phenoxy-imine (FI) complexes.

The zirconium FI catalyst with R_1 = Cy, R_2 = Me, and R_3 = Cumyl had a recorded activity for ethylene polymerisation of 4 315 000 kg_{PE} mol_{Zr}^{-1} h^{-1} bar^{-1} under conditions of ambient pressure and temperature. The turnover frequency (TOF) of this system is 1.5×10^8 h^{-1} atm^{-1}, which is the largest value reported for any catalytic chemical

reaction, not only polymerisations. Increasing the steric bulk of the R_3 position was proposed by the authors to increase activity both by protecting the phenolic oxygen from cocatalyst coordination and increasing cation-anion separation within the active species.

FI complexes of elements other than group four have been produced including aluminium, scandium, vanadium, chromium, cobalt, nickel, copper, yttrium, tin, and palladium, demonstrating the steric and electronic versatility of the ligand.[328] Facile, modular ligand synthesis by Schiff base condensation has enabled the rapid development of enormous structural diversity through substitution at the $R_{1–3}$ positions; numerous halide, alkyl, cycloalkyl, aryl, fluoroaryl, furanyl, anisole, pyrrolyl, imidazole, and ferrocenyl derivatives are known.[328] Related bidentate β-ketoimine,[329] phenoxy-oxazoline,[330] phenoxy-pyridine,[331] and phenoxy-imidazole ligands,[332] tridendate bis(imino)pyridine,[333] and tetradentate Salen ligands, composed of two FI fragments joined through the imine nitrogen atoms,[334] have broadened the scope of this chemistry considerably. As well as unprecedented activity, ultra-high molecular weight polyethylene with M_v up to 5 MDa was produced by using a stoichiometric borate activator and the zirconium FI catalyst with R_1 = Ph, R_2 = H, and R_3 = ^{t}Bu. Group four FI catalysts bearing fluorinated ligands have been developed as catalysts for the living polymerisation of ethylene, with monodispersed MWDs, trivial control of molecular weight, and the possibility of creating novel olefinic block copolymers.[335-337]

Group four complexes bearing bulky biphenoxide and binaphthoxide ligands have been shown to polymerise ethylene with activities of up to 1580 $kg_{PE}\ mol_{Zr}^{-1}\ h^{-1}\ bar^{-1}$ and broad molecular weight distributions (Đ up to 12). In 1-hexene homopolymerisation, steric modifications of the ligands were able to control not only the molecular weight (from oligomers to high molecular weight polyhexene), but also tacticity including the

production of isotactic polymer.[338] Chloroalkyl aluminium cocatalyst have been used in combination with titanium biphenoxide complexes to produce low molecular weight polyethylene waxes.[339,340]

1.5.3. Phenoxy-Induced Complexes of Sumitomo

The Phenoxy-Induced Complexes of Sumitomo (PHENICS) are post-metallocene half-sandwich complexes utilising *ansa*-bridged ligands comprising a cyclopentadienyl and a phenoxy fragment, being somewhat intermediate between the CGC and FI technologies (Figure 1.17).[341-348]

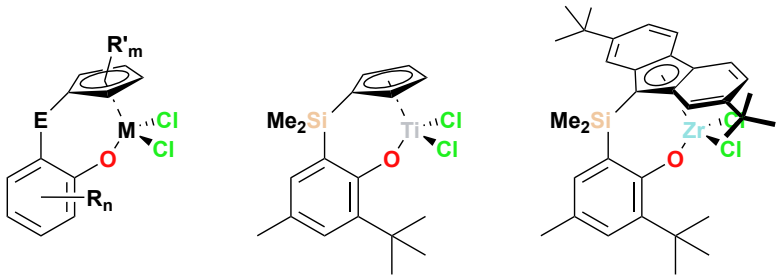

Figure 1.17 Structure of selected PHENICS complexes.

Introduced by Sumitomo Chemical Co., Ltd., group four and five PHENICS complexes bearing cyclopentadienyl, indenyl, and fluorenyl apical motifs have been produced along with a range of substitution patterns at the *ansa* bridge and phenoxide. This breadth is facilitated by a simple modular synthesis where substituted phenols and silanes can be readily interchanged.

Catalytic activities for olefin copolymerisation were comparable to that of CGC complexes,[342] but the production of very high molecular weight copolymers (up to 1.4 MDa) with greater levels of 1-hexene incorporation (up to 34 SCB/1000TC) was notable.[345,346] A significant feature of the PHENICS complexes was thermal stability,

with highly active controlled single-site copolymerisations reported at temperatures as high as 210 °C.[346] It was found by Nabika *et al.* that bulkier substituents at the *ortho*-phenoxy position resulted in increased activities and copolymer molecular weights,[345] a similar trend to that of the FI catalysts (*vide supra*). Conversely, a less bulky Cp fragment led to copolymers with the greatest 1-hexene incorporation, attributed to a less hindered active site.[342] Through manipulations of the PHENICS ligand afforded by the synthetic structural tunability, control over the delicate balance of steric and electronic factors was achieved, facilitating the synthesis of high molecular weight copolymers with high comonomer incorporation and in high activities, along with rational catalyst design.[346]

1.5.4. Permethylindenyl post-metallocenes

In addition to the permethylindenyl metallocenes that have been reported (Chapter 1.4), I* analogues of CGCs have been reported by Williams *et al.* (Figure 1.18).[210,349,350]

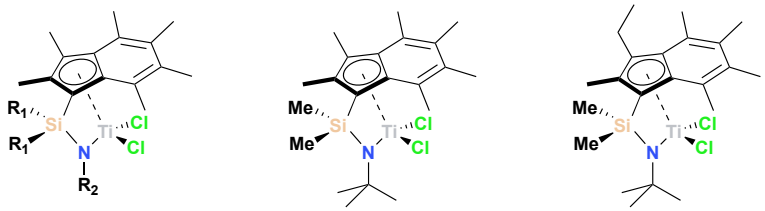

Figure 1.18 Structures of selected CGCI* complexes.

The reaction between lithium amides, $R^2N(H)Li$, and the permethylindenyl synthon $I^*Si(Cl)R^1{}_2$ resulted in proligands which could then be transformed under the action of ^{n}BuLi to ligand salts. Salt metathesis procedures utilising $TiCl_4{\cdot}2THF$ gave the desired CGCI* complexes in yields of up to 25%.

Ethylene polymerisation activities up to three times that of the Cp* analogue were reported when immobilised on sMAO, with activities of 8400 $kg_{PE}\ mol_{Ti}^{-1}\ h^{-1}\ bar^{-1}$

reported, alongside ultra-high molecular weight polyethylene, up to 3 MDa. Similar comonomer incorporation to that of Cp*-based CGCs was found. More electron donating substituents at the amido fragment were shown to result in increased catalytic activities.[210] Furthermore, a strong hydrogen response was demonstrated, where activity was maintained with a dramatic reduction in molecular weight (from 2.7 MDa to 41 kDa) in the presence of 1.6% hydrogen,[350] allowing access to a wide range of ethylene-based polymeric materials.

1.6. Scope of thesis

The aims of the research set out in this thesis are to introduce a new class of permethylindenyl-phenoxy (PHENI*) ligands, with a particular focus on group four complexes (Figure 1.19). These catalysts will be developed with regard to the homopolymerisation and copolymerisation of olefinic monomers, predominantly ethylene and propylene, for the synthesis of plastics with industrially relevant and tuneable physical properties.

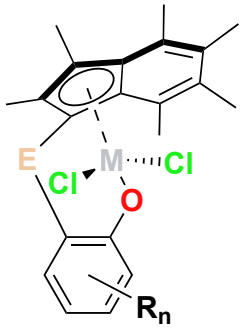

Figure 1.19 Structure of proposed group four PHENI* complexes. M = Ti, Zr, Hf; E = dialkylsilyl; R = alkyl.

1.7. References

1 I. A. Makaryan and I. V. Sedov, *Russ. J. Gen. Chem.*, 2020, **90**, 1141-1162.
2 A. H. Westlie, E. Y. X. Chen, C. M. Holland, S. S. Stahl, M. Doyle, S. R. Trenor, K. M. Knauer, *Macromol. Rapid Commun.*, 2022, 2200492.
3 W. Kaminsky, *Macromol. Chem. Phys.*, 2008, **209**, 459-466.
4 M. Kutz, *Applied Plastics Engineering Handbook*, Elsevier Inc., 2011.
5 M. H. Rahman and P. R. Bhoi, *J. Clean. Prod.*, 2021, **294**, 126218.
6 T. K. Phung, T. L. M. Pham, K. B. Vu, G. Busca, *J. Environ. Chem. Eng.*, 2021, **9**, 105673.
7 D. S. Achilias, C. Roupakias, P. Megalokonomos, A. A. Lappas, E. V. Antonakou, *J. Hazard. Mater.*, 2007, **149**, 536-542.
8 A. Somoza-Tornos, A. Gonzalez-Garay, C. Pozo, M. Graells, A. Espuña, G. Guillén-Gosálbez, *ACS Sustain. Chem. Eng.*, 2020, **8**, 3561-3572.
9 A. Reznichenko and A. Harlin, *SN Appl. Sci.*, 2022, **4**, 108.
10 E. Bamberger and F. Tschirner, *Ber. Dtsch. Chem. Ges.*, 1900, **33**, 955-959.
11 D. T. Gentekos, R. J. Sifri, B. P. Fors, *Nat. Rev. Mater.*, 2019, **4**, 761-774.
12 Y. Zhao, L. Wang, H. Yu, G. Jing, C. Li, Y. Chen, M. Saleem, *J. Polym. Res.*, 2014, **21**, 470.
13 C. Zou, S. Dai, C. Chen, *Macromolecules*, 2018, **51**, 49-56.
14 T. Kida, R. Tanaka, Y. Hiejima, K. H. Nitta, T. Shiono, *Polymer*, 2021, **218**, 123526.
15 M. Stürzel, T. Hees, M. Enders, Y. Thomann, H. Blattmann, R. Mülhaupt, *Macromolecules*, 2016, **49**, 8048-8060.
16 M. Stürzel, S. Mihan, R. Mülhaupt, *Chem. Rev.*, 2016, **116**, 1398-1433.
17 C. Long, Z. Dong, X. Liu, F. Yu, Y. Shang, K. Wang, S. Feng, X. Hou, C. He, Z. R. Chen, *Polymer*, 2022, **258**, 125287.
18 P. Kenyon, D. W. J. Leung, Z. R. Turner, J. C. Buffet, D. O'Hare, *Macromolecules*, 2022, **55**, 3408-3414.
19 T. A. Tervoort, J. Visjager, P. Smith, *Macromolecules*, 2002, **35**, 8467-8471.
20 F. Živić, M. Babić, S. Mitrović, D. Adamović, S. Pelemis, *Tribol. Ind.*, 2014, **36**, 281.
21 P. Bracco, A. Bellare, A. Bistolfi, S. Affatato, *Materials*, 2017, **10**, 791.
22 J. Fu, B. W. Ghali, A. J. Lozynsky, E. Oral, O. K. Muratoglu, *Polymer*, 2010, **51**, 2721-2731.
23 S. Rastogi, Y. Yao, S. Ronca, J. Bos, J. van der Eem, *Macromolecules*, 2011, **44**, 5558-5568.
24 K. Patel, S. H. Chikkali, S. Sivaram, *Prog. Polym. Sci.*, 2020, **109**, 101290.
25 M. Hussain, R. A. Naqvi, N. Abbas, S. M. Khan, S. Nawaz, A. Hussain, N. Zahra, M. W. Khalid, *Polymers*, 2020, **12**, 323.
26 Y. Wang and R. Hou, *J. Phys. Conf. Ser.*, 2022, **2263**, 012016.
27 S. Liu, J. Wang, Y. Wang, Y. Wang, *Mater. Des.*, 2010, **31**, 1711-1715.
28 D. Romano, S. Ronca, S. Rastogi, *Macromol. Rapid Commun.*, 2015, **36**, 327-331.
29 E. M. Brach del Prever, A. Bistolfi, P. Bracco, L. Costa, *J. Orthop. Traumatol.*, 2009, **10**, 1-8.
30 S. Santavirta, Y. T. Konttinen, R. Lappalainen, A. Anttila, S. B. Goodman, M. Lind, L. Smith, M. Takagi, E. Gómez-Barrena, L. Nordsletten, J. W. Xu, *Curr. Orthop.*, 1998, **12**, 51-57.
31 F. P. Zaribaf, *Mater. Sci. Technol.*, 2018, **34**, 1940-1953.
32 M. Cao, L. Chen, R. Xu, Q. Fang, *Compos. Struct.*, 2021, **277**, 114638.
33 H. Wang, D. Weerasinghe, D. Mohotti, P. J. Hazell, V. P. W. Shim, K. Shankar, E. V. Morozov, *Int. J. Mech. Sci.*, 2021, **204**, 106574.
34 C. J. Kuo and W. L. Lan, in *Advances in Filament Yarn Spinning of Textiles and Polymers*, ed. D. Zhang, Woodhead Publishing, 2014, p. 100-112.
35 S. Chhetri and H. Bougherara, *Compos. Part A Appl. Sci. Manuf.*, 2021, **140**, 106146.
36 X. Zhuang and X. Yan, *Compos. Sci. Technol.*, 2006, **66**, 444-449.
37 X. Zhang, Y. Wang, C. Lu, S. Cheng, *Polym. Bull.*, 2011, **67**, 527-540.
38 M. Mihailov and L. Minkova, *Colloid. Polym. Sci.*, 1987, **265**, 681-685.
39 M. K. Musib, *Int. J. Biol. Eng.*, 2011, **1**, 6-10.
40 A. Pandey, Y. Champouret, S. Rastogi, *Macromolecules*, 2011, **44**, 4952-4960.
41 X. Tang, J. H. Xing, X. Yan, C. L. Ye, L. T. Zhang, Y. Zhang, B. Q. Shu, J. S. Mu, W. Li, J. D. Wang, Y. R. Yang, *Adv. Polym. Tech.*, 2022, **2022**.
42 Z. Bartczak, *J. Polym. Sci., Part B: Polym. Phys.*, 2010, **48**, 276-285.
43 D. Romano, N. Tops, E. Andablo-Reyes, S. Ronca, S. Rastogi, *Macromolecules*, 2014, **47**, 4750-4760.
44 B. Wu, Y. Cai, X. Zhao, L. Ye, *Polym. Test.*, 2021, **93**.
45 Z. Yue, N. Wang, Y. Cao, W. Li, C. D. Dong, *Ind. Eng. Chem. Res.*, 2020, **59**, 3351-3358.

46 M. Chen, Y. Chen, W. Li, P. Liang, C. Ren, B. Jiang, J. Wang, Y. Yang, *Ind. Eng. Chem. Res.*, 2021, **60**, 3354-3362.
47 P. Chammingkwan, Y. Bando, L. T. T. Mai, T. Wada, A. Thakur, M. Terano, L. Sinthusai, T. Taniike, *Ind. Eng. Chem. Res.*, 2021, **60**, 2818-2827.
48 R. P. Gote, D. Mandal, K. Patel, K. Chaudhuri, C. P. Vinod, A. K. Lele, S. H. Chikkali, *Macromolecules*, 2018, **51**, 4541-4552.
49 J. Dai, C. Yu, S. Ye, W. Li, X. Kang, Y. Yang, P. Liang, Y. Ma, Z. Huang, B. Jiang, J. Wang, Y. Yang, *Macromolecules*, 2021, **54**, 9418-9426.
50 S. Ye, J. Dai, W. Li, Y. Yang, Z. Huang, J. Wang, Y. Yang, *Ind. Eng. Chem. Res.*, 2021, **60**, 15951-15959.
51 A. A. Antonov and K. P. Bryliakov, *Eur. Polym. J.*, 2021, **142**, 110162.
52 D. Romano, E. Andablo-Reyes, S. Ronca, S. Rastogi, *Polymer*, 2015, **74**, 76-85.
53 G. Forte and S. Ronca, *Int. J. Polym. Sci.*, 2017, **2017**, 1-8.
54 M. Spronck, A. Klein, B. Blom, D. Romano, *Z. Anorg. Allg. Chem.*, 2018, **644**, 993-998.
55 I. V. Oleynik, I. K. Shundrina, I. I. Oleyinik, *Polym. Adv. Technol.*, 2020, **31**, 1921-1934.
56 Z. Zhang, X. Kang, Y. Jiang, Z. Cai, S. Li, D. Cui, *Angew. Chem. Int. Ed.*, 2023, **62**, e202215582.
57 F. Christakopoulos, E. Troisi, N. Friederichs, J. Vermant, T. A. Tervoort, *Macromolecules*, 2021, **54**, 9452-9460.
58 H. A. Maddah, *Am. J. Polym. Sci.*, 2016, **6**, 1-11.
59 G. Natta, *J. Polym. Sci.*, 1959, **34**, 531-549.
60 P. Corradini, V. Barone, R. Fusco, G. Guerra, *Eur. Polym. J.*, 1979, **15**, 1133-1141.
61 N. Bahri-Laleh, A. Hanifpour, S. A. Mirmohammadi, A. Poater, M. Nekoomanesh-Haghighi, G. Talarico, L. Cavallo, *Prog. Polym. Sci.*, 2018, **84**, 89-114.
62 A. Shamiri, M. H. Chakrabarti, S. Jahan, M. A. Hussain, W. Kaminsky, P. V. Aravind, W. A. Yehye, *Materials*, 2014, **7**, 5069-5108.
63 Z. Zhang, R. Zhang, Y. Huang, J. Lei, Y. H. Chen, J. H. Tang, Z. M. Li, *Ind. Eng. Chem. Res.*, 2014, **53**, 10144-10154.
64 L. Resconi, L. Cavallo, A. Fait, F. Piemontesi, *Chem. Rev.*, 2000, **100**, 1253-1346.
65 G. W. Coates, *Chem. Rev.*, 2000, **100**, 1223-1252.
66 J. A. Ewen, *J. Am. Chem. Soc.*, 1984, **106**, 6355-6364.
67 W. Spaleck, M. Antberg, J. Rohrmann, A. Winter, B. Bachmann, P. Kiprof, J. Behm, W. A. Herrmann, *Angew. Chem. Int. Ed. Engl.*, 1992, **31**, 1347-1350.
68 L. Oliva, L. Caporaso, C. Pellecchia, A. Zambelli, *Macromolecules*, 1995, **28**, 4665-4667.
69 V. Busico, R. Cipullo, L. Caporaso, G. Angelini, A. L. Segre, *J. Mol. Catal. A Chem.*, 1998, **128**, 53-64.
70 T. Kida, T. Kimura, A. Eno, K. Janchai, M. Yamaguchi, Y. Otsuki, T. Kimura, T. Mizukawa, T. Murakami, K. Hato, T. Okawa, *Polymers*, 2021, **13**, 4222.
71 X. Jiang, Y. Bin, N. Kikyotani, M. Matsuo, *Polym. J.*, 2006, **38**, 419-431.
72 M. Matsuo, C. Sawatari, T. Nakano, *Polym. J.*, 1986, **18**, 759-774.
73 J. Chen, X. Si, S. Hu, Y. Wang, Y. Wang, *J. Macromol. Sci. B*, 2007, **47**, 192-200.
74 S. Deisenhofer, T. Feifel, J. Kukral, M. Klinga, M. Leskelä, B. Rieger, *Organometallics*, 2003, **22**, 3495-3501.
75 L. Stieglitz, D. Henschel, T. Pehl, B. Rieger, *Organometallics*, 2021, **40**, 4055-4065.
76 C. De Rosa, F. Auriemma, O. Ruiz de Ballesteros, L. Resconi, A. Fait, E. Ciaccia, I. Camurati, *J. Am. Chem. Soc.*, 2003, **125**, 10913-10920.
77 L. Resconi, R. L. Jones, A. L. Rheingold, G. P. A. Yap, *Organometallics*, 1996, **15**, 998-1005.
78 Q. Wu, Q. Su, L. Ye, G. Li, Y. Mu, *Dalton Trans.*, 2010, **39**, 2525-2535.
79 J. Saito, M. Onda, S. Matsui, M. Mitani, R. Furuyama, H. Tanaka, T. Fujita, *Macromol. Rapid Commun.*, 2002, **23**, 1118-1123.
80 T. Miyatake, K. Mizunuma, Y. Seki, M. Kakugo, *Makromol. Chem., Rapid Commun.*, 1989, **10**, 349-352.
81 B. Rieger, C. Troll, J. Preuschen, *Macromolecules*, 2002, **35**, 5742-5743.
82 K. C. Jayaratne and L. R. Sita, *J. Am. Chem. Soc.*, 2000, **122**, 958-959.
83 M. Khoshsefat, S. Ahmadjo, S. M. M. Mortazavi, G. H. Zohuri, J. B. P. Soares, *New J. Chem.*, 2018, **42**, 8334-8337.
84 S. F. Kurath, E. Passaglia, R. Pariser, *J. Appl. Phys.*, 1957, **28**, 499-502.
85 D. Nazari, N. Bahri-Laleh, M. Nekoomanesh-Haghighi, S. M. Jalilian, R. Rezaie, S. A. Mirmohammadi, *Polym. Adv. Technol.*, 2018, **29**, 1603-1612.
86 S. Segal, I. Goldberg, M. Kol, *Organometallics*, 2005, **24**, 200-202.
87 K. Nomura, S. Pengoubol, W. Apisuk, *Molecules*, 2019, **24**, 1634.

88 M. Fujita, Y. Seki, T. Miyatake, *J. Polym. Sci., Part A: Polym. Chem.*, 2004, **42**, 1107-1111.
89 K. Nomura, S. Pengoubol, W. Apisuk, *RSC Adv.*, 2016, **6**, 16203-16207.
90 K. Shirayama, S. I. Kita, H. Watabe, *Makromol. Chem.*, 1972, **151**, 97-120.
91 P. Starck and B. Löfgren, *Eur. Polym. J.*, 2002, **38**, 97-107.
92 F. J. Stadler and H. Münstedt, *J. Rheol.*, 2008, **52**, 697-712.
93 Y. S. Kim, C. I. Chung, S. Y. Lai, K. S. Hyun, *J. Appl. Polym. Sci.*, 1996, **59**, 125-137.
94 W. Kaminsky, *Macromol. Chem. Phys.*, 1996, **197**, 3907-3945.
95 W. Kaminsky and M. Schlobohm, *Makromol. Chem. Macromol. Symp.*, 1986, **4**, 103-118.
96 A. Rossi, J. Zhang, G. Odian, *Macromolecules*, 1996, **29**, 2331-2338.
97 S. Ohta, Y. Kasai, T. Toda, K. Nishii, M. Okazaki, *Polym. J.*, 2019, **51**, 345-349.
98 S. Kitphaitun, Q. Yan, K. Nomura, *ChemistryOpen*, 2021, **10**, 867-876.
99 S. Kitphaitun, H. Takeshita, K. Nomura, *ACS Omega*, 2022, **7**, 6900-6910.
100 J. Li, H. Li, Y. Zhang, Y. Mu, *J. Appl. Polym. Sci.*, 2011, **120**, 1514-1519.
101 W. Kaminsky, C. Piel, K. Scharlach, *Macromol. Symp.*, 2005, **226**, 25-34.
102 B. Poon, M. Rogunova, A. Hiltner, E. Baer, S. P. Chum, A. Galeski, E. Piorkowska, *Macromolecules*, 2005, **38**, 1232-1243.
103 M. Arnold, O. Henschke, J. Knorr, *Macromol. Chem. Phys.*, 1996, **197**, 563-573.
104 S. Rulhoff and W. Kaminsky, *Macromol. Chem. Phys.*, 2006, **207**, 1450-1460.
105 R. Quijada, J. L. Guevara, G. B. Galland, F. M. Rabagliati, J. M. Lopez-Majada, *Polymer*, 2005, **46**, 1567-1574.
106 T. E. Nowlin, Y. V. Kissin, K. P. Wagner, *J. Polym. Sci., Part A: Polym. Chem.*, 1988, **26**, 755-764.
107 Y. V. Kissin, R. I. Mink, T. E. Nowlin, A. J. Brandolini, *Top. Catal.*, 1999, **7**, 69-88.
108 H. S. Cho, J. S. Chung, J. H. Han, Y. G. Ko, W. Y. Lee, *J. Appl. Polym. Sci.*, 1998, **70**, 1707-1715.
109 B. Paredes, R. v. Grieken, A. Carrero, I. Suarez, J. B. P. Soares, *Macromol. Chem. Phys.*, 2011, **212**, 1590-1599.
110 R. Quijada, J. Dupont, M. S. L. Miranda, R. B. Scipioni, G. B. Galland, *Macromol. Chem. Phys.*, 1995, **196**, 3991-4000.
111 F. M. Mirabella Jr. and E. A. Ford, *J. Polym. Sci., Part B: Polym. Phys.*, 1987, **25**, 777-790.
112 S. Hosoda, *Polym. J.*, 1988, **20**, 383-397.
113 M. Ren, X. Chen, Y. Sang, R. G. Alamo, *Ind. Eng. Chem. Res.*, 2020, **59**, 19260-19271.
114 T. M. Liu and W. E. Baker, *Polym. Eng. Sci.*, 1992, **32**, 944-955.
115 P. Micic and S. N. Bhattacharya, *Polym. Int.*, 2000, **49**, 1580-1589.
116 R. K. Krishnaswamy and M. J. Lamborn, *Polym. Eng. Sci.*, 2000, **40**, 2385-2396.
117 F. Tornuk, M. Hancer, O. Sagdic, H. Yetim, *LWT*, 2015, **64**, 540-546.
118 C. S. Yuan, A. Hassan, M. I. H. Ghazali, A. F. Ismail, *J. Appl. Polym. Sci.*, 2007, **104**, 3736-3745.
119 S. M. Bhasney, P. Bhagabati, A. Kumar, V. Katiyar, *Compos. Sci. Technol.*, 2019, **171**, 54-61.
120 K. Shlosman, R. Y. Suckeveriene, J. Rosen-Kligvasser, R. Tchoudakov, E. Zelikman, R. Semiat, M. Narkis, *Polym. Adv. Technol.*, 2014, **25**, 1484-1491.
121 V. Das, V. Kumar, A. Singh, S. S. Gautam, A. Pandey, *Polym. Plast. Technol. Eng.*, 2012, **51**, 446-454.
122 J. E. O'Gara, K. B. Wagener, S. F. Hahn, *Makromol. Chem., Rapid Commun.*, 1993, **14**, 657-662.
123 J. C. Sworen, J. A. Smith, K. B. Wagener, L. S. Baugh, S. P. Rucker, *J. Am. Chem. Soc.*, 2003, **125**, 2228-2240.
124 G. Rojas, B. Inci, Y. Wei, K. B. Wagener, *J. Am. Chem. Soc.*, 2009, **131**, 17376-17386.
125 G. Rojas and K. B. Wagener, *Macromolecules*, 2009, **42**, 1934-1947.
126 F. Zuluaga, B. İnci, Y. Nozue, S. Hosoda, K. B. Wagener, *Macromolecules*, 2009, **42**, 4953-4955.
127 S. Hosoda, Y. Nozue, Y. Kawashima, K. Suita, S. Seno, T. Nagamatsu, K. B. Wagener, B. Inci, F. Zuluaga, G. Rojas, J. K. Leonard, *Macromolecules*, 2011, **44**, 313-319.
128 B. Inci and K. B. Wagener, *J. Am. Chem. Soc.*, 2011, **133**, 11872-11875.
129 A. A. Yehia, *Polym. Plast. Technol. Eng.*, 2004, **43**, 1735-1754.
130 A. S. Mohite, Y. D. Rajpurkar, A. P. More, *Polym. Bull.*, 2022, **79**, 1309-1343.
131 K. Lian, Y. Zhu, W. Li, S. Dai, C. Chen, *Macromolecules*, 2017, **50**, 6074-6080.
132 G. Zanchin and G. Leone, *Prog. Polym. Sci.*, 2021, **113**, 101342.
133 K. S. O'Connor, A. Watts, T. Vaidya, A. M. LaPointe, M. A. Hillmyer, G. W. Coates, *Macromolecules*, 2016, **49**, 6743-6751.
134 C. M. Koo, M. A. Hillmyer, F. S. Bates, *Macromolecules*, 2006, **39**, 667-677.
135 Y. Zhao, Y. Ma, Y. Xiong, T. Qin, Y. Zhu, H. Deng, J. Qin, X. Shi, G. Zhang, *Polymer*, 2022, **254**, 125075.
136 A. Ali, M. K. Tufail, M. I. Jamil, W. Yaseen, N. Iqbal, M. Hussain, A. Ali, T. Aziz, Z. Fan, L. Guo, *Molecules*, 2021, **26**, 2037.

137 I. Surya, M. Muniyadi, H. Ismail, *Polym. Compos.*, 2021, **42**, 1698-1711.
138 S. Hamza, *Polym. Test.*, 1998, **17**, 131-137.
139 A. Das, D. De, N. Naskar, S. Chandra Debnath, *J. Appl. Polym. Sci.*, 2006, **99**, 1132-1139.
140 S. J. Ahmadi, Y. Huang, W. Li, *Compos. Sci. Technol.*, 2005, **65**, 1069-1076.
141 H. Ismail, P. Pasbakhsh, M. N. A. Fauzi, A. Abu Bakar, *Polym. Test.*, 2008, **27**, 841-850.
142 W. Wang and B. Qu, *Polym. Degrad. Stab.*, 2003, **81**, 531-537.
143 G. Milani and F. Milani, *J. Appl. Polym. Sci.*, 2012, **124**, 311-324.
144 E. A. Snijders, A. Boersma, B. Van Baarle, P. Gijsman, *Polym. Degrad. Stab.*, 2005, **89**, 484-491.
145 M. Van Duin, R. Orza, R. Peters, V. Chechik, *Macromol. Symp.*, 2010, **291**, 66-74.
146 A. Moffett and M. Dekkerrs, *Polym. Eng. Sci.*, 1992, **32**, 1-5.
147 S. Mishra, B. Baweja, R. Chandra, *J. Appl. Polym. Sci.*, 1999, **74**, 2756-2763.
148 N. K. Gupta, A. K. Jain, R. Singhal, A. K. Nagpal, *J. Appl. Polym. Sci.*, 2000, **78**, 2104-2121.
149 H. Peng, M. Lu, H. Wang, Z. Zhang, F. Lv, M. Niu, W. Wang, *Polym. Eng. Sci.*, 2020, **60**, 1054-1065.
150 S. L. Aggarwal and O. J. Sweeting, *Chem. Rev.*, 1957, **57**, 665-742.
151 P. S. Chum and K. W. Swogger, *Prog. Polym. Sci.*, 2008, **33**, 797-819.
152 M. P. McDaniel, in *Advances in Catalysis*, eds. B. C. Gates and H. Knözinger, Academic Press, 2010, vol. 53, p. 123-606.
153 M. McDaniel, *Appl. Catal., A*, 2017, **542**, 392-410.
154 K. Soga and T. Shiono, *Prog. Polym. Sci.*, 1997, **22**, 1503-1546.
155 L. Cavallo, G. Guerra, P. Corradini, *J. Am. Chem. Soc.*, 1998, **120**, 2428-2436.
156 K. H. Theopold, *Proc. Natl. Acad. Sci. U.S.A.*, 2014, **111**, 11578-11579.
157 G. G. Hlatky, *Chem. Rev.*, 2000, **100**, 1347-1376.
158 W. Kaminsky, *J. Chem. Soc., Dalton Trans.*, 1998, 1413-1418.
159 C. Coperet, A. Comas-Vives, M. P. Conley, D. P. Estes, A. Fedorov, V. Mougel, H. Nagae, F. Nunez-Zarur, P. A. Zhizhko, *Chem. Rev.*, 2016, **116**, 323-421.
160 H. Sinn, *Macromol. Symp.*, 1995, **97**, 27-52.
161 E. Y. Chen and T. J. Marks, *Chem. Rev.*, 2000, **100**, 1391-1434.
162 W. Kaminsky, A. Funck, H. Hahnsen, *Dalton Trans.*, 2009, 8803-8810.
163 Y. Choi and J. B. Soares, *Can. J. Chem. Eng.*, 2012, **90**, 646-671.
164 J. R. Severn, J. C. Chadwick, R. Duchateau, N. Friederichs, *Chem. Rev.*, 2005, **105**, 4073-4147.
165 P. Wongwaiwattanakul and B. Jongsomjit, *Catal. Commun.*, 2008, **10**, 118-122.
166 K. Soga and M. Kaminaka, *Makromol. Chem.*, 1993, **194**, 1745-1755.
167 T. Pothirat, B. Jongsomjit, P. Praserthdam, *Catal. Commun.*, 2008, **9**, 1426-1431.
168 J. C. Buffet, N. Wanna, T. A. Q. Arnold, E. K. Gibson, P. P. Wells, Q. Wang, J. Tantirungrotechai, D. O'Hare, *Chem. Mater.*, 2015, **27**, 1495-1501.
169 A. F. R. Kilpatrick, J. C. Buffet, P. Nørby, N. H. Rees, N. P. Funnell, S. Sripothongnak, D. O'Hare, *Chem. Mater.*, 2016, **28**, 7444-7450.
170 T. A. Q. Arnold, Z. R. Turner, J. C. Buffet, D. O'Hare, *J. Organomet. Chem.*, 2016, **822**, 85-90.
171 Z. Wang, G. Chen, K. Ding, *Chem. Rev.*, 2009, **109**, 322-359.
172 M. Bartke, M. Oksman, M. Mustonen, P. Denifl, *Macromol. Mater. Eng.*, 2005, **290**, 250-255.
173 M. Mohammadikish and S. Yarahmadi, *J. Phys. Chem. Solids*, 2020, **141**, 109434.
174 Z. Dong, W. Huang, X. Liu, F. Yu, C. Long, S. Feng, L. Luo, Z. R. Chen, *Macromolecules*, 2021, **54**, 9385-9392.
175 T. A. Goetjen, J. Liu, Y. Wu, J. Sui, X. Zhang, J. T. Hupp, O. K. Farha, *Chem. Commun.*, 2020, **56**, 10409-10418.
176 H. G. Alt, *J. Chem. Soc., Dalton Trans.*, 1999, 1703-1710.
177 H. G. Alt and C. Görl, in *Tailor-Made Polymers*, 2008, p. 305-326.
178 B. Heurtefeu, C. Bouilhac, É. Cloutet, D. Taton, A. Deffieux, H. Cramail, *Prog. Polym. Sci.*, 2011, **36**, 89-126.
179 Y. Zhang and S. N. Riduan, *Chem. Soc. Rev.*, 2012, **41**, 2083-2094.
180 X. Wang, Z. Li, X. Han, Z. Han, Y. Bai, *Appl. Surf. Sci.*, 2017, **420**, 496-503.
181 M. Che, K. Mori, H. Yamashita, *Proc. Math. Phys. Eng. Sci.*, 2012, **468**, 2113-2128.
182 G. B. Galland, M. Seferin, R. Guimarães, J. A. Rohrmann, F. C. Stedile, J. H. Z. dos Santos, *J. Mol. Catal. A Chem.*, 2002, **189**, 233-240.
183 R. Duchateau, *Chem. Rev.*, 2002, **102**, 3525-3542.
184 X. Zheng, M. Smit, J. C. Chadwick, J. Loos, *Macromolecules*, 2005, **38**, 4673-4678.
185 S. L. Scott, T. L. Church, D. H. Nguyen, E. A. Mader, J. Moran, *Top. Catal.*, 2005, **34**, 109-120.
186 S. Zanoni, N. Nikolopoulos, A. Welle, A. Vantomme, B. M. Weckhuysen, *Catal. Sci. Technol.*, 2021, **11**, 5335-5348.

187 B. Horáčková, Z. Grof, J. Kosek, *Chem. Eng. Sci.*, 2007, **62**, 5264-5270.
188 K. W. Bossers, R. Valadian, S. Zanoni, R. Smeets, N. Friederichs, J. Garrevoet, F. Meirer, B. M. Weckhuysen, *J. Am. Chem. Soc.*, 2020, **142**, 3691-3695.
189 K. W. Bossers, R. Valadian, J. Garrevoet, S. van Malderen, R. Chan, N. Friederichs, J. Severn, A. Wilbers, S. Zanoni, M. K. Jongkind, B. M. Weckhuysen, F. Meirer, *JACS Au*, 2021, **1**, 852-864.
190 X. Guo, F. Zhang, D. G. Evans, X. Duan, *Chem. Commun.*, 2010, **46**, 5197-5210.
191 G. Gao, Z. Zhu, J. Zheng, Z. Liu, Q. Wang, Y. Yan, *J. Colloid Interface Sci.*, 2019, **555**, 1-10.
192 A. Razzaq, S. Ali, M. Asif, S. I. In, *Catalysts*, 2020, **10**, 1185.
193 H. S. Jadhav, A. Roy, B. Z. Desalegan, J. G. Seo, *Sustain. Energy Fuels*, 2020, **4**, 312-323.
194 Y. Wang, D. Yan, S. El Hankari, Y. Zou, S. Wang, *Adv. Sci.*, 2018, **5**, 1800064.
195 C. Chen, M. Greenwood, J. C. Buffet, D. O'Hare, *Green Chem.*, 2020, **22**, 3117-3121.
196 D. W. J. Leung, C. Chen, J. C. Buffet, D. O'Hare, *Dalton Trans.*, 2020, **49**, 9306-9311.
197 M. M. J. Li, C. Chen, T. Ayvalı, H. Suo, J. Zheng, I. F. Teixeira, L. Ye, H. Zou, D. O'Hare, S. C. E. Tsang, *ACS Catal.*, 2018, **8**, 4390-4401.
198 J. Yu, K. Ruengkajorn, D. G. Crivoi, C. Chen, J. C. Buffet, D. O'Hare, *Nat. Commun.*, 2019, **10**, 2398.
199 J. C. Buffet, N. Wanna, T. A. Q. Arnold, E. K. Gibson, P. P. Wells, Q. Wang, J. Tantirungrotechai, D. O'Hare, *Chem. Mater.*, 2015, **27**, 1495-1501.
200 G. E. Hickman, C. M. R. Wright, A. F. R. Kilpatrick, Z. R. Turner, J. C. Buffet, D. O'Hare, *Mol. Catal.*, 2019, **468**, 139-147.
201 C. Chen, R. Felton, J. C. Buffet, D. O'Hare, *Chem. Commun.*, 2015, **51**, 3462-3465.
202 J. C. Buffet, C. F. H. Byles, R. Felton, C. Chen, D. O'Hare, *Chem. Commun.*, 2016, **52**, 4076-4079.
203 T. Dalet, H. Cramail, A. Deffieux, *Macromol. Chem. Phys.*, 2004, **205**, 1394-1401.
204 E. Kaji and E. Yoshioka, US8404880B2, **2013**.
205 C. M. Wright, T. J. Williams, Z. R. Turner, J. C. Buffet, D. O'Hare, *Inorg. Chem. Front.*, 2017, **4**, 1048-1060.
206 J. V. Lamb, J. C. Buffet, Z. R. Turner, D. O'Hare, *Polym. Chem.*, 2019, **10**, 1386-1398.
207 J. V. Lamb, J. C. Buffet, Z. R. Turner, T. Khamnaen, D. O'Hare, *Macromolecules*, 2020, **53**, 5847-5856.
208 P. Angpanitcharoen, J. V. Lamb, J. C. Buffet, Z. R. Turner, D. O'Hare, *RSC Adv.*, 2021, **11**, 11529-11535.
209 A. F. Kilpatrick, N. H. Rees, Z. R. Turner, J. C. Buffet, D. O'Hare, *Mater. Chem. Front.*, 2020, **4**, 3226-3233.
210 T. J. Williams, J. C. Buffet, Z. R. Turner, D. O'Hare, *Catal. Sci. Technol.*, 2018, **8**, 5454-5461.
211 D. A. Fraser, Z. R. Turner, J. C. Buffet, D. O'Hare, *Organometallics*, 2016, **35**, 2664-2674.
212 J. C. Buffet, Z. R. Turner, D. O'Hare, *Chem. Commun.*, 2018, **54**, 10970-10973.
213 A. F. R. Kilpatrick, N. H. Rees, S. Sripothongnak, J. C. Buffet, D. O'Hare, *Organometallics*, 2018, **37**, 156-164.
214 J. V. Lamb, J. C. Buffet, Z. R. Turner, D. O'Hare, *Macromolecules*, 2020, **53**, 929-935.
215 J. V. Lamb, *Unsymmetrical Group 4 Permethylindenyl Ansa-Metallocenes as Polymerisation Catalysts*, D.Phil. Thesis, *University of Oxford*, 2019.
216 C. M. R. Wright, Z. R. Turner, J. C. Buffet, D. O'Hare, *Chem. Commun.*, 2016, **52**, 2850-2853.
217 J. Chatt and L. A. Duncanson, *J. Chem. Soc.*, 1953, 2939-2947.
218 P. Cossee, *J. Catal.*, 1964, **3**, 80-88.
219 E. Arlman, *J. Catal.*, 1964, **3**, 99-104.
220 M. Brookhart, A. F. Volpe, D. M. Lincoln, I. T. Horvath, J. M. Millar, *J. Am. Chem. Soc.*, 1990, **112**, 5634-5636.
221 W. Guo, J. Yin, Z. Xu, W. Li, Z. Peng, C. J. Weststrate, X. Yu, Y. He, Z. Cao, X. Wen, Y. Yang, K. Wu, Y. Li, J. W. Niemantsverdriet, X. Zhou, *Science*, 2022, **375**, 1188-1191.
222 J. I. Martínez-Araya, R. Quijada, A. Toro-Labbé, *J. Phys. Chem. C*, 2012, **116**, 21318-21325.
223 J. A. Ewen, *J. Mol. Catal. A Chem.*, 1998, **128**, 103-109.
224 V. C. Gibson and S. K. Spitzmesser, *Chem. Rev.*, 2003, **103**, 283-316.
225 K. J. Chu, J. B. Soares, A. Penlidis, *J. Polym. Sci., Part A: Polym. Chem.*, 2000, **38**, 1803-1810.
226 P. Roos, G. B. Meier, J. J. C. Samson, G. Weickert, K. R. Westerterp, *Macromol. Rapid Commun.*, 1997, **18**, 319-324.
227 G. J. P. Britovsek, V. C. Gibson, D. F. Wass, *Angew. Chem. Int. Ed. Engl.*, 1999, **38**, 428-447.
228 M. Baker, *Nature*, 2016, **533**, 452-454.
229 D. Fanelli, *Proc. Natl. Acad. Sci.*, 2018, **115**, 2628-2631.
230 M. Linnolahti, J. R. Severn, T. A. Pakkanen, *Angew. Chem. Int. Ed.*, 2008, **47**, 9279-9283.
231 M. Linnolahti, J. R. Severn, T. A. Pakkanen, *Angew. Chem. Int. Ed.*, 2006, **45**, 3331-3334.

232 Z. Falls, N. Tymińska, E. Zurek, *Macromolecules*, 2014, **47**, 8556-8569.
233 H. S. Zijlstra and S. Harder, *Eur. J. Inorg. Chem.*, 2015, **2015**, 19-43.
234 I. Tritto, S. X. Li, M. C. Sacchi, P. Locatelli, G. Zannoni, *Macromolecules*, 1995, **28**, 5358-5362.
235 I. Tritto, R. Donetti, M. C. Sacchi, P. Locatelli, G. Zannoni, *Macromolecules*, 1997, **30**, 1247-1252.
236 I. Tritto, R. Donetti, M. C. Sacchi, P. Locatelli, G. Zannoni, *Macromolecules*, 1999, **32**, 264-269.
237 D. E. Babushkin, N. V. Semikolenova, V. A. Zakharov, E. P. Talsi, *Macromol. Chem. Phys.*, 2000, **201**, 558-567.
238 J. N. Pédeutour, H. Cramail, A. Deffieux, *J. Mol. Catal. A Chem.*, 2001, **174**, 81-87.
239 J. N. Pédeutour, H. Cramail, A. Deffieux, *J. Mol. Catal. A Chem.*, 2001, **176**, 87-94.
240 W. Kaminsky, *Macromol. Symp.*, 1995, **97**, 79-89.
241 Y. Huang, Q. Yu, S. Zhu, G. Rempel, L. Li, *J. Polym. Sci., Part A: Polym. Chem.*, 1999, **37**, 1465-1472.
242 F. Zaccaria, C. Zuccaccia, R. Cipullo, P. H. Budzelaar, A. Vittoria, A. Macchioni, V. Busico, C. Ehm, *ACS Catal.*, 2021, **11**, 4464-4475.
243 L. Jia, X. M. Yang, A. Ishihara, T. J. Marks, *Organometallics*, 1995, **14**, 3135-3137.
244 S. Mehdiabadi, J. B. P. Soares, D. Bilbao, J. L. Brinen, *Macromol. React. Eng.*, 2011, **5**, 418-430.
245 M. Bochmann, *Organometallics*, 2010, **29**, 4711-4740.
246 J. N. Pédeutour, K. Radhakrishnan, H. Cramail, A. Deffieux, *Macromol. Rapid Commun.*, 2001, **22**, 1095-1123.
247 A. R. Siedle, W. M. Lamanna, R. A. Newmark, J. Stevens, D. E. Richardson, M. Ryan, *Makromol. Chem. Macromol. Symp.*, 1993, **66**, 215-224.
248 A. Yano, S. Hasegawa, S. Yamada, A. Akimoto, *J. Mol. Catal. A Chem.*, 1999, **148**, 77-86.
249 V. C. Williams, G. J. Irvine, W. E. Piers, Z. Li, S. Collins, W. Clegg, M. R. J. Elsegood, T. B. Marder, *Organometallics*, 2000, **19**, 1619-1621.
250 J. Zhou, S. J. Lancaster, D. A. Walker, S. Beck, M. Thornton-Pett, M. Bochmann, *J. Am. Chem. Soc.*, 2001, **123**, 223-237.
251 D. Langford, I. Göttker-Schnetmann, F. P. Wimmer, L. A. Casper, P. Kenyon, R. F. Winter, S. Mecking, *Organometallics*, 2019, **38**, 2710-2713.
252 K. Musikabhumma, T. P. Spaniol, J. Okuda, *J. Mol. Catal. A Chem.*, 2004, **208**, 73-81.
253 N. Senso, S. Khaubunsongserm, B. Jongsomjit, P. Praserthdam, *Molecules*, 2010, **15**, 9323-9339.
254 D. G. Boucher, I. W. Parsons, R. N. Haward, *Makromol Chem. Macromol. Chem. Phys.*, 1974, **175**, 3461-3473.
255 M. A. Bashir, V. Monteil, C. Boisson, T. F. L. McKenna, *J. Appl. Polym. Sci.*, 2018, **135**, 45670.
256 A. Muñoz-Escalona, H. García, A. Albornoz, *J. Appl. Polym. Sci.*, 1987, **34**, 977-988.
257 D. T. Lynch, M. O. Jejelowo, S. E. Wanke, *Can. J. Chem. Eng.*, 1991, **69**, 657-664.
258 R. Kleinschmidt, Y. van der Leek, M. Reffke, G. Fink, *J. Mol. Catal. A Chem.*, 1999, **148**, 29-41.
259 H. Hammawa, T. Mannan, D. Lynch, S. Wanke, *J. Appl. Polym. Sci.*, 2004, **92**, 3549-3560.
260 V. Busico, P. Corradini, A. Ferraro, A. Proto, *Makromol Chem. Macromol. Chem. Phys.*, 1986, **187**, 1125-1130.
261 F. Bonini, V. Fraaije, G. Fink, *J. Polym. Sci., Part A: Polym. Chem.*, 1995, **33**, 2393-2402.
262 V. Panchenko, L. Echevkaya, V. Zakharov, M. Matsko, *Appl. Catal., A*, 2011, **404**, 47-53.
263 J. P. Turunen and T. T. Pakkanen, *J. Appl. Polym. Sci.*, 2006, **100**, 4632-4635.
264 T. J. Kealy and P. L. Pauson, *Nature*, 1951, **168**, 1039-1040.
265 J. M. O'Connor and C. P. Casey, *Chem. Rev.*, 1987, **87**, 307-318.
266 S. Harder, *Coord. Chem. Rev.*, 1998, **176**, 17-66.
267 M. A. Beswick, J. S. Palmer, D. S. Wright, *Chem. Soc. Rev.*, 1998, **27**, 225-225.
268 T. P. Hanusa, *Organometallics*, 2002, **21**, 2559-2571.
269 R. Poli, *Chem. Rev.*, 1991, **91**, 509-551.
270 S. Arndt and J. Okuda, *Chem. Rev.*, 2002, **102**, 1953-1976.
271 B. E. Bursten and R. J. Strittmatter, *Angew. Chem. Int. Ed.*, 1991, **30**, 1069-1085.
272 M. Weller, T. Overton, F. Armstrong, J. Rourke, *Inorganic Chemistry*, Oxford University Press, 2018.
273 P. L. Pauson, *Q. Rev. Chem. Soc.*, 1955, **9**, 391-414.
274 T. Piou, F. Romanov-Michailidis, M. Romanova-Michaelides, K. E. Jackson, N. Semakul, T. D. Taggart, B. S. Newell, C. D. Rithner, R. S. Paton, T. Rovis, *J. Am. Chem. Soc.*, 2017, **139**, 1296-1310.
275 D. C. Calabro, J. L. Hubbard, C. H. Blevins, A. C. Campbell, D. L. Lichtenberger, *J. Am. Chem. Soc.*, 1981, **103**, 6839-6846.
276 I. A. Lobanova and V. I. Zdanovich, *Russ. Chem. Rev.*, 1988, **57**, 967-980.
277 M. Stradiotto and M. J. McGlinchey, *Coord. Chem. Rev.*, 2001, **219-221**, 311-378.
278 A. N. Nesmeyanov, N. A. Ustynyuk, L. G. Makarova, V. G. Andrianov, Y. T. Struchkov, S. Andrae, Y. A. Ustynyuk, S. G. Malyugina, *J. Organomet. Chem.*, 1978, **159**, 189-199.

279 M. E. Rerek, L. N. Ji, F. Basolo, *J. Chem. Soc., Chem. Commun.*, 1983, 1208-1209.
280 A. J. Hart-Davis and R. J. Mawby, *J. Chem. Soc. A*, 1969, **0**, 2403-2407.
281 A. J. Hart-Davis, C. White, R. J. Mawby, *Inorg. Chim. Acta*, 1970, **4**, 441-446.
282 T. K. Miyamoto, M. Tsutsui, L. B. Chen, *Chem. Lett.*, 1981, **10**, 729-730.
283 D. Ohare, J. C. Green, T. Marder, S. Collins, G. Stringer, A. K. Kakkar, N. Kaltsoyannis, A. Kuhn, R. Lewis, C. Mehnert, P. Scott, M. Kurmoo, S. Pugh, *Organometallics*, 1992, **11**, 48-55.
284 D. Ohare, V. J. Murphy, N. Kaltsoyannis, *J. Chem. Soc. Dalton Trans.*, 1993, 383-392.
285 T. M. Frankcom, J. C. Green, A. Nagy, A. K. Kakkar, T. B. Marder, *Organometallics*, 1993, **12**, 3688-3697.
286 D. Ohare, V. Murphy, G. M. Diamond, P. Arnold, P. Mountford, *Organometallics*, 1994, **13**, 4689-4694.
287 T. M. Trnka, J. B. Bonanno, B. M. Bridgewater, G. Parkin, *Organometallics*, 2001, **20**, 3255-3264.
288 M. Tsutsui, L. B. Chen, D. E. Bergbreiter, T. K. Miyamoto, *J. Am. Chem. Soc.*, 1982, **104**, 855-856.
289 D. O'Hare, V. Murphy, G. M. Diamond, P. Arnold, P. Mountford, *Organometallics*, 1994, **13**, 4689-4694.
290 A. Lüttringhaus and H. Schuster, *Angew. Chem.*, 1958, **70**, 438-438.
291 B. Q. Wang, *Coord. Chem. Rev.*, 2006, **250**, 242-258.
292 F. M. Alías, S. Barlow, J. S. Tudor, D. O'Hare, R. T. Perry, J. M. Nelson, I. Manners, *J. Organomet. Chem.*, 1997, **528**, 47-58.
293 J. A. Smith, J. Vonseyerl, G. Huttner, H. H. Brintzinger, *J. Organomet. Chem.*, 1979, **173**, 175-185.
294 C. S. Bajgur, W. Tikkanen, J. L. Petersen, *Inorg. Chem.*, 1985, **24**, 2539-2546.
295 G. Tian, B. Wang, X. Dai, S. Xu, X. Zhou, J. Sun, *J. Organomet. Chem.*, 2001, **634**, 145-152.
296 M. T. Reetz, M. Willuhn, C. Psiorz, R. Goddard, *Chem. Commun.*, 1999, 1105-1106.
297 J. C. Buffet, T. A. Q. Arnold, Z. R. Turner, P. Angpanitcharoen, D. O'Hare, *RSC Adv.*, 2015, **5**, 87456-87464.
298 H. Braunschweig and F. M. Breitling, *Coord. Chem. Rev.*, 2006, **250**, 2691-2720.
299 J. Okuda, *Dalton Trans.*, 2003, 2367-2378.
300 J. Klosin, P. P. Fontaine, R. Figueroa, *Acc. Chem. Res.*, 2015, **48**, 2004-2016.
301 J. C. Stevens, F. J. Timmers, D. R. Wilson, G. F. Schmidt, P. N. Nickias, R. K. Rosen, G. W. Knight, S. Y. Lai, EP0416815A2, **1991**.
302 J. A. M. Canich, US6265338B1, **2001**.
303 A. M. Stephen and J. L. Irwin US2006025299A1, **2006**.
304 J. Suhm, M. J. Schneider, R. Mülhaupt, *J. Mol. Catal. A Chem.*, 1998, **128**, 215-227.
305 A. L. McKnight and R. M. Waymouth, *Chem. Rev.*, 1998, **98**, 2587-2598.
306 P. S. Chum, W. J. Kruper, M. J. Guest, *Adv. Mater.*, 2000, **12**, 1759-1767.
307 S. J. Brown, X. Gao, D. G. Harrison, L. Koch, R. E. v. H. Spence, G. P. A. Yap, *Organometallics*, 1998, **17**, 5445-5447.
308 P. J. Shapiro, *Coord. Chem. Rev.*, 2002, **231**, 67-81.
309 G. Erker, K. Kunz, S. Doring, R. Frohlich, G. Kehr, *Abstr. Pap. Am. Chem. Soc.*, 2001, **222**, U411-U411.
310 G. van Doremaele, M. van Duin, M. Valla, A. Berthoud, *J. Polym. Sci., Part A: Polym. Chem.*, 2017, **55**, 2877-2891.
311 R. A. Collins, A. F. Russell, R. T. W. Scott, R. Bernardo, G. H. J. van Doremaele, A. Berthoud, P. Mountford, *Organometallics*, 2017, **36**, 2167-2181.
312 E. G. Ijpeij, B. Coussens, M. A. Zuideveld, G. H. J. van Doremaele, P. Mountford, M. Lutz, A. L. Spek, *Chem. Commun.*, 2010, **46**, 3339-3341.
313 H. Braunschweig, F. M. Breitling, K. Radacki, F. Seeler, *J. Organomet. Chem.*, 2005, **690**, 5000-5005.
314 A. Bertuleit, M. Könemann, L. Duda, G. Erker, R. Fröhlich, *Top. Catal.*, 1999, **7**, 37-44.
315 K. Kunz, G. Erker, S. Döring, S. Bredeau, G. Kehr, R. Fröhlich, *Organometallics*, 2002, **21**, 1031-1041.
316 V. V. Kotov, E. V. Avtomonov, J. Sundermeyer, K. Harms, D. A. Lemenovskii, *Eur. J. Inorg. Chem.*, 2002, **2002**, 678-691.
317 A. Reb and H. G. Alt, *J. Mol. Catal. A Chem.*, 2001, **174**, 35-49.
318 H. G. Alt, R. Ernst, I. K. Böhmer, *J. Organomet. Chem.*, 2002, **658**, 259-265.
319 J. Okuda, S. Verch, T. P. Spaniol, R. Stürmer, *Chem. Ber.*, 1996, **129**, 1429-1431.
320 J. Okuda, S. Verch, R. Stürmer, T. P. Spaniol, *J. Organomet. Chem.*, 2000, **605**, 55-67.
321 R. Kleinschmidt, Y. Griebenow, G. Fink, *J. Mol. Catal. A Chem.*, 2000, **157**, 83-90.
322 J. Okuda, T. Eberle, T. P. Spaniol, V. Piquet-Fauré, *J. Organomet. Chem.*, 1999, **591**, 127-137.
323 F. Amor, A. Butt, K. E. du Plooy, T. P. Spaniol, J. Okuda, *Organometallics*, 1998, **17**, 5836-5849.

324 J. C. Stevens, in *Studies in Surface Science and Catalysis*, eds. K. Soga and M. Terano, Elsevier, 1994, vol. 89, p. 277-284.
325 P. J. Sinnema, B. Hessen, J. H. Teuben, *Macromol. Rapid Commun.*, 2000, **21**, 562-566.
326 S. Matsui, Y. Inoue, T. Fujita, *J. Syn. Org. Chem. Jpn.*, 2001, **59**, 232-240.
327 S. Matsui and T. Fujita, *Catal. Today*, 2001, **66**, 63-73.
328 H. Makio, H. Terao, A. Iwashita, T. Fujita, *Chem. Rev.*, 2011, **111**, 2363-2449.
329 A. Amodio, G. Zanchin, F. De Stefano, A. Piovano, B. Palucci, V. Guiotto, R. Di Girolamo, G. Leone, E. Groppo, *Catalysts*, 2022, **12**, 119.
330 P. G. Cozzi, E. Gallo, C. Floriani, A. Chiesi-Villa, C. Rizzoli, *Organometallics*, 1995, **14**, 4994-4996.
331 Y. Inoue, T. Nakano, H. Tanaka, N. Kashiwa, T. Fujita, *Chem. Lett.*, 2001, **30**, 1060-1061.
332 M. P. Batten, A. J. Canty, K. J. Cavell, T. Rüther, B. W. Skelton, A. H. White, *Inorg. Chim. Acta*, 2006, **359**, 1710-1724.
333 T. M. Smit, A. K. Tomov, G. J. P. Britovsek, V. C. Gibson, A. J. P. White, D. J. Williams, *Catal. Sci. Technol.*, 2012, **2**, 643-655.
334 M. Mandal and D. Chakraborty, *Polym. Sci. Ser. B*, 2020, **62**, 597-601.
335 J. Saito, M. Mitani, J. i. Mohri, Y. Yoshida, S. Matsui, S. i. Ishii, S. i. Kojoh, N. Kashiwa, T. Fujita, *Angew. Chem. Int. Ed.*, 2001, **40**, 2918-2920.
336 M. Mitani, J. I. Mohri, Y. Yoshida, J. Saito, S. Ishii, K. Tsuru, S. Matsui, R. Furuyama, T. Nakano, H. Tanaka, S. I. Kojoh, T. Matsugi, N. Kashiwa, T. Fujita, *J. Am. Chem. Soc.*, 2002, **124**, 3327-3336.
337 R. Furuyama, J. Saito, S. Ishii, H. Makio, M. Mitani, H. Tanaka, T. Fujita, *J. Organomet. Chem.*, 2005, **690**, 4398-4413.
338 A. van der Linden, C. J. Schaverien, N. Meijboom, C. Ganter, A. G. Orpen, *J. Am. Chem. Soc.*, 1995, **117**, 3008-3021.
339 P. S. Umare, K. Rao, G. L. Tembe, D. A. Dhoble, B. Trivedi, *J. Appl. Polym. Sci.*, 2007, **104**, 1531-1539.
340 A. Mehta, G. Tembe, P. Umare, M. Białek, P. Parikh, G. Mehta, *J. Polym. Res.*, 2012, **19**, 17.
341 H. Katayama, M. Nabika, A. Imai, A. Miyashita, T. Watanabe, H. Johohji, Y. Oda, H. Hanaoka, *Intl. Pat.*, WO9703992A1, **1997**.
342 H. Hanaoka, T. Hino, H. Souda, K. Yanagi, Y. Oda, A. Imai, *J. Organomet. Chem.*, 2007, **692**, 4059-4066.
343 H. Hanaoka, T. Hino, M. Nabika, T. Kohno, K. Yanagi, Y. Oda, A. Imai, K. Mashima, *J. Organomet. Chem.*, 2007, **692**, 4717-4724.
344 T. Senda, H. Hanaoka, T. Hino, Y. Oda, H. Tsurugi, K. Mashima, *Macromolecules*, 2009, **42**, 8006-8009.
345 M. Nabika, H. Katayama, T. Watanabe, H. Kawamura-Kuribayashi, K. Yanagi, A. Imai, *Organometallics*, 2009, **28**, 3785-3792.
346 T. Senda, H. Hanaoka, S. Nakahara, Y. Oda, H. Tsurugi, K. Mashima, *Macromolecules*, 2010, **43**, 2299-2306.
347 T. Senda, H. Hanaoka, T. Hino, Y. Oda, H. Tsurugi, K. Mashima, *Macromolecules*, 2010, **43**, 5162-5162.
348 T. Senda, H. Hanaoka, Y. Oda, H. Tsurugi, K. Mashima, *Organometallics*, 2010, **29**, 2080-2084.
349 T. J. Williams, *Olefin polymerisation using group 4 permethylindenyl complexes*, D.Phil. Thesis, *University of Oxford*, 2020.
350 T. J. Williams, J. V. Lamb, J. C. Buffet, T. Khamnaen, D. O'Hare, *RSC Adv.*, 2021, **11**, 5644-5650.

Chapter 2 – Group four permethylindenyl-phenoxy (PHENI*) complexes

2.1. Introduction

Many approaches have been explored for the synthesis of group four post-metallocenes such as the Constrained Geometry Complexes (CGCs). These include salt metathesis, protonolysis, and template-directed synthesis.[1,2] *Ansa*-bridged complexes have been synthesised using a bridged ligand precursor in the "flytrap" method,[3] or by reaction in the ligand sphere of a complex.[4] The synthesis of titanium complexes is often hindered by the reduction of Ti(IV) to Ti(III). It has been shown that efficient reactions can be achieved using a Ti(III) precursor and subsequent oxidation with $PbCl_2$,[5] or by metalation in the presence of MeLi, directly forming the dimethylated CGC.[6] Subsequent derivatisation of the dihalide complexes can readily be achieved through reaction with lithium alkyls, potassium alkyls, or Grignard reagents.[7,8]

2.1.1. Synthesis of PHENICS complexes

The Phenoxy-Induced Complexes of Sumitomo (PHENICS) are a class of *ansa*-bridged post-metallocenes bearing an apical Cp derivative and a basal aryloxide motif (Figure 2.1). Complexes have been reported with titanium, zirconium, hafnium, and tantalum metal centres; Me_2Si, Et_2Si, MePhSi, MeEtSi, MeCySi, silolyl (C_4H_8Si), and Me_2C *ansa* bridges; Cp, $^{t\text{Bu}}$Cp, Cp*, Ind, Flu, and $^{t\text{Bu}_2}$Flu apical ligands; and phenoxy substituents including Me, ^{i}Pr, ^{t}Bu, and Adm.[9-15] PHENICS complexes were shown to be useful catalysts for the copolymerisation of ethylene and 1-hexene at elevated

temperature, producing high molecular weight copolymers with high comonomer incorporation.[14]

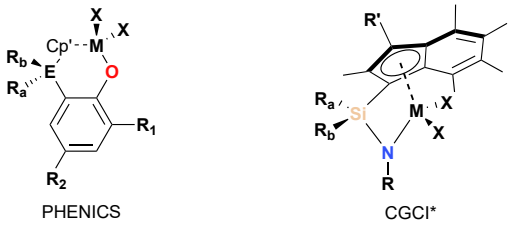

Figure 2.1 Generalised structures of PHENICS and CGCI* complexes.[9-18]

The synthesis of PHENICS ligands has been reasonably well developed: substituted phenols are first *ortho*-brominated using either Br_2 or NBS, and the hydroxyl protected as a methoxy group,[13] though it was subsequently shown that an allyloxy protecting group led to improved yields.[10] The resulting aryl bromide is exchanged for lithium, and the *ansa* bridge incorporated by reaction with either 6,6-dimethylfulvene or the desired $R_aR_bSiCl_2$. Reactions with the lithium or sodium salt of the desired Cp derivative led to the proligands in yields of 75–86%. Attempts to deallylate using TMSI or catalytic palladium complexes were unsuccessful,[10] and as such group four complexes were made by *in situ* deprotection with ^{n}BuLi followed by the addition of $TiCl_4$, $TiCl_2(NMe_2)_2$, $ZrCl_4$, $ZrCl_2(NMe_2)_2$, or $HfCl_2(NMe_2)_2$ in yields of 2–50%.[10,13,14] The amido metal sources were found to react more selectively towards the deprotected dilithium salt, and subsequent chlorination could be accomplished with TMSCl.[14] The addition of Et_3N to the deprotonation and deprotection step was found to significantly increase yields of the isolated complexes.[13] In the case of tantalum, better yields were obtained by following a stepwise procedure where the dilithium salt of the ligand is isolated and washed with hexane prior to slurrying with $TaCl_5$.[19]

2.1.2. Permethylindenyl post-metallocenes

Following the synthesis of permethylindenyl-based metallocenes,[20-25] Williams *et al.* have reported the synthesis of permethylindenyl (I*) analogues of CGCs of the type ^{Me2}SB(^{R}N,I*)TiCl$_2$ ({(η^5-C$_9$Me$_6$)Me$_2$Si(^{R}N)}TiCl$_2$, Figure 2.1).[16-18] The proligand synthesis involved reaction of LiN(H)R with the I*SiMe$_2$Cl synthon. The dilithium ligand salts were prepared and either isolated or used in a one pot procedure, where salt metathesis with TiCl$_4$·2THF yielded the desired complexes in 5–20% yield.[17]

2.1.3. Chapter synopsis

This chapter describes the synthesis and characterisation of a family of permethylindenyl-phenoxy (PHENI*) *ansa* post-metallocene complexes. A variety of substitution patterns on the aryloxide ring and silyl bridge is reported, along with a range of ancillary ligands as leaving groups. Complexes of all of the group four elements are reported. The attempted syntheses of other ligands, and of two dinuclear complexes are discussed. Catalytically relevant cationic species are studied through reactions with common catalyst activators: polymethylaluminoxane (MAO), trityl tetrakis(perfluorophenyl)borate (TB), and *N*,*N*-dimethylanilinium tetrakis(perfluorophenyl)borate (AB). The synthesis and characterisation of heterogenised supported catalysts is reported, with complexes immobilised on solid polymethylaluminoxane (sMAO), MAO-modified silica (SSMAO), and MAO-modified layered double hydroxide (LDHMAO).

2.1.4. Definition of geometric parameters

Throughout this chapter, I*$_{cent}$ refers to the centroid of the C$_5$ fragment of the permethylindenyl ring. The ring slip parameter, Δ_{M-C}, corresponds to the difference between the metal–I*$_{cent}$ distance and that of the projection of the metal onto the least

squares plane defined by I^*_{C5}, such that $\Delta_{M-C} = \sqrt{(M-I^*_{cent})^2 - (M-I^*_{C_5})^2}$, and is a measure of how far the complex is distorted towards η^3 coordination compared to η^5. The torsion angle, TA', is a measure of the twist between the apical I* and basal aryloxy motifs. It is based upon the parameter first used by Calhorda *et al.*,[26] which for homoleptic metallocenes was defined as C(2)–Cp_{cent}–Cp_{cent}'–Cp(2'). It has been adapted for PHENI* complexes, and is defined henceforth as TA' = C(10)–C(2)–O(1)–C(18). I*–ArO refers to the dihedral angle between the least squares plane defined by I^*_{C5} and that defined by the aryloxy C_6 ring.

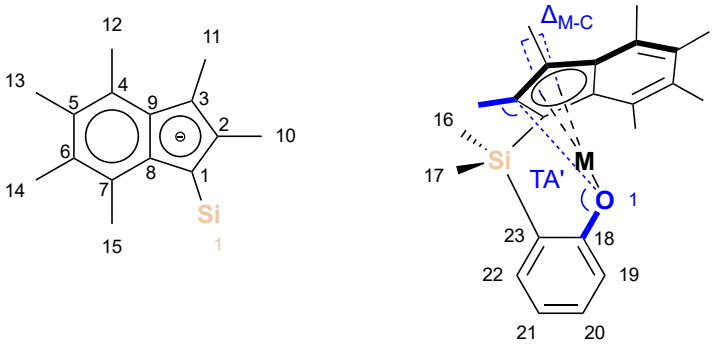

Figure 2.2 Permethylindenyl numbering scheme, and definitions of the ring slip parameter, Δ_{M-C}, and the characteristic torsion angle, TA'.

2.2. Synthesis of PHENI* complexes

2.2.1. Synthesis of proligands, ^{Me_2}SB(^{R_1,R_2}ArOAllyl,I*)H

PHENI* proligands, ^{Me_2}SB(^{R_1,R_2}ArOAllyl,I*)H (I* = C_9Me_6; R_1, R_2 = Me, ^{t}Bu, Cumyl; Cumyl = CMe_2Ph), were synthesised from substituted phenols (Scheme 2.1).

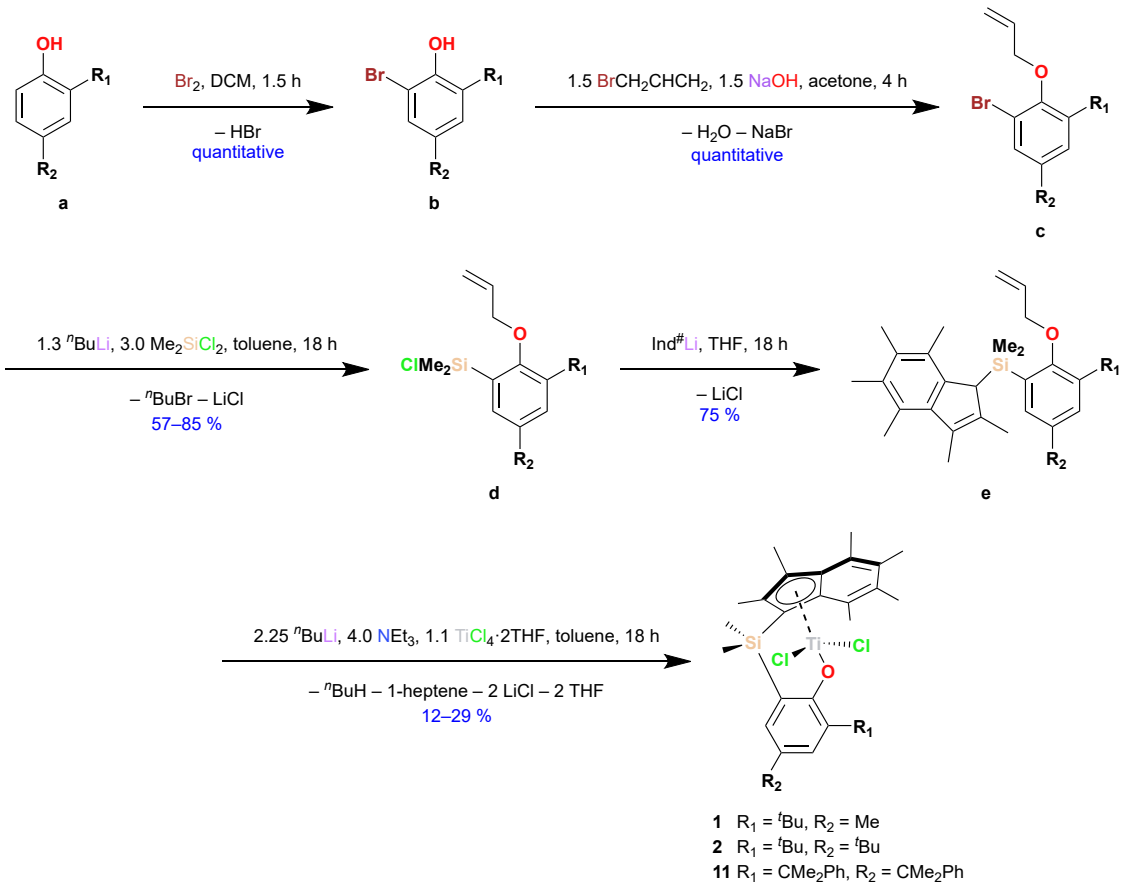

Scheme 2.1 Synthesis of PHENI* complexes from alkylphenols. R_1, R_2 = H, Me, ^{t}Bu, Cumyl.

The 2,4-dialkyl phenols (^{R1,R2}ArOH, **a**) were first *ortho*-brominated with elemental bromine in dichloromethane (^{Br,R1,R2}ArOH, **b**), then reacted with allyl bromide under basic conditions in acetone to effect protection of the phenolic hydroxyl (^{Br,R1,R2}ArOAllyl, **c**; Scheme 2.1). An attempt was made to use MeI under basic conditions to synthesise the methoxy-protected phenol, however this resulted in a mixture of products and the route was not pursued further. Protection was followed by lithium-halogen exchange from the dropwise addition of ^{n}BuLi at –78 °C. Subsequent *in situ* reaction with dichlorodimethylsilane in toluene affords the chlorosilyl products (^{Me2SiCl,R1,R2}ArOAllyl, **d**) as pale yellow to colourless oils in reasonable yields (57–85%). Stirring these intermediates with 2,3,4,5,6,7-hexamethyl-1*H*-inden-1-yl lithium (Ind$^{\#}$Li,

Ind$^{\#}$ = C_9Me_6H) in tetrahydrofuran (THF) overnight afforded the allyl-protected PHENI* proligands (^{Me_2}SB(^{R_1,R_2}ArOAllyl,I*)H, **e**) in 75% yields on multigram scales. Proligands **1e** and **2e** formed as thick orange waxy oils and were used without further purification, while **11e** was an off-white solid and could be washed with cold pentane.

The ^{1}H NMR spectrum of ^{Me_2}SB($^{t\mathrm{Bu}_2}$ArOAllyl,I*)H (**2e**) is characteristic of PHENI* proligands (Figure 2.3). The dimethylsilyl bridge appears as two singlets at δ 0.28 and 0.17 ppm, and six singlets between δ 2.53 and 1.86 ppm correspond to the I*C**H**$_3$ methyl protons. Additionally, the singlet at δ 3.98 ppm is assigned to the I***H** proton which, being at a chiral centre, makes the two allyl protons α to the oxygen diastereotopic and thus differentiable in the NMR spectrum. These protons are seen as resonances at δ 4.26 and 4.47 ppm, which split into doublets of doublets of triplets as a result of coupling to the geminal, vicinal and both terminal protons (Figure 2.4). The terminal protons at δ 5.16 and 5.56 ppm are chemically inequivalent with $^3J_{H–H}$ constants of 10.8 and 17.2 Hz respectively from the *cis* and *trans* vicinal couplings. The $^4J_{H–H}$ and $^2J_{H–H}$ geminal coupling are coincident so the resonances appear in the spectrum as apparent doublets of quartets. The proton β to the oxygen resonates at δ 5.87 ppm splitting into a doublet of doublets of triplets. Finally, the two ArO *meta* protons couple to each other as doublets at δ 7.59 and 7.37 ppm with a $^4J_{H–H}$ constant of 2.5 Hz. The two *tert*-butyl groups are observed as singlets at δ 1.53 and 1.30 ppm.

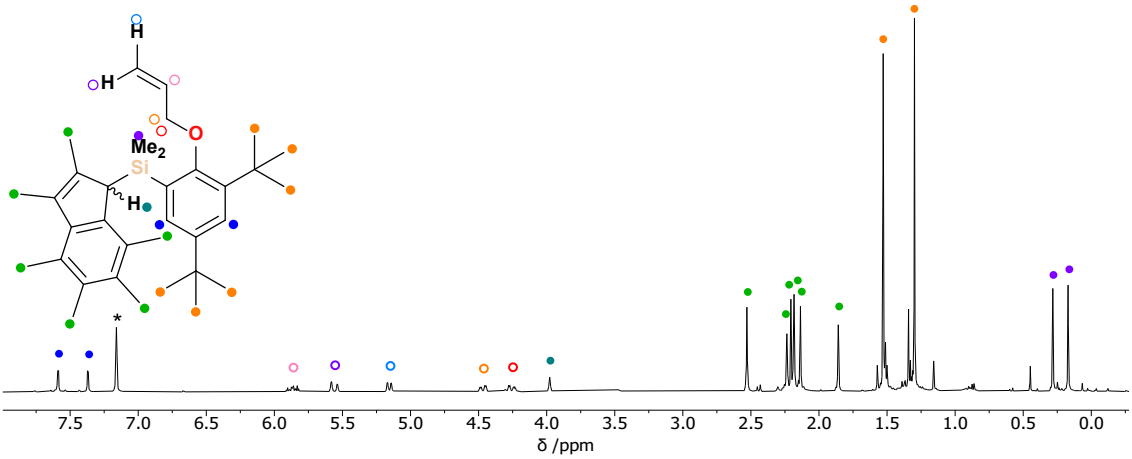

Figure 2.3 ^{1}H NMR spectrum (400 MHz, benzene-d_6, 298 K) of ^{Me_2}SB($^{t\mathrm{Bu}_2}$ArOAllyl,I*)H (**2e**). The asterisk (*) denotes residual *protio*-benzene.

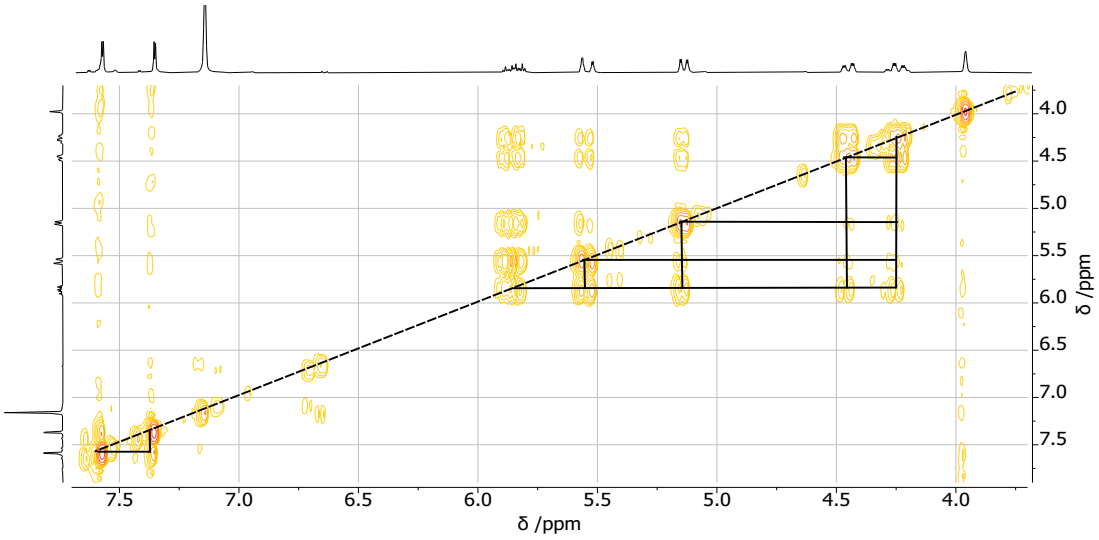

Figure 2.4 ^{1}H–^{1}H COSY NMR spectrum (400 MHz, benzene-d_6, 298 K) of ^{Me_2}SB($^{t\mathrm{Bu}_2}$ArOAllyl,I*)H (**2e**) plotted between δ 3.70–7.70 ppm to display the allylic and aromatic regions. The asterisk (*) denotes residual *protio*-benzene.

The 4-methyl-2-*tert*-butyl proligand (**1e**) displays many of the same characteristic resonances, though the aryl substituents resonate at δ 1.49 and 2.17 ppm for the *tert*-butyl and methyl group respectively, the latter overlapping with the I*C**H**$_3$ resonances. Likewise, the 2,4-biscumyl proligand (**11e**) contains the same diagnostic I* resonances, with the four cumyl methyl resonances distinct from the I*C**H**$_3$ and a downfield complex multiplet structure from the cumyl aromatic protons.

2.2.2. Synthesis of ^{Me2}SB(^{R1,R2}ArO,I*)TiCl$_2$

Initially, attempts were made to isolate dianionic ligand salts, as precursors for salt metathesis reactions to synthesise transition metal complexes, using a range of strong bases to effect deallylation of the phenol and deprotonation of the I* ring. Both potassium hydride and potassium hexamethyldisilazide (KHMDS) were reacted with the proligands in benzene-d_6 or THF-d_8 and the reactions monitored by ^{1}H NMR spectroscopy. The reaction with KH was very slow, with just 18% conversion to the dipotassium salt after 8 hours at 80 °C for the *tert*-butyl-methyl proligand **1e**. KHMDS reacted more quickly, with the I***H** allylic proton resonance no longer observed after 8 hours at 80 °C. However, attempts to isolate the dipotassium salt were unsuccessful, and decomposition products were observed by NMR spectroscopy. Treating the proligand with ^{n}BuLi in THF did not yield the expected dilithium salt, and decomposition products were observed by NMR spectroscopy. Protonolysis was found to be an ineffective route to titanium complexes, with no reaction observed between the proligands and Ti(O^{i}Pr)$_4$ in benzene-d_6 even after 68 hours at 80 °C.

Titanium dichloride complexes, ^{Me2}SB(^{R1,R2}ArO,I*)TiCl$_2$ ({(η^5-C$_9$Me$_6$)Me$_2$Si(2-R$_1$-4-R$_2$-C$_6$H$_2$O)}TiCl$_2$; R$_1$, R$_2$ = Me, ^{t}Bu, or Cumyl), were successfully synthesised without isolation of the dilithium salt, by using *in situ* deprotection, deprotonation, and complexation: reaction of the proligands with ^{n}BuLi/NEt$_3$, followed by TiCl$_4$·2THF in toluene gave brick-red microcrystalline solids after workup in yields of 12–29%.

The role of the tertiary amine is somewhat unclear, with Hanaoka *et al.* reporting significantly increased yields of PHENICS complexes in the presence of NEt$_3$ which they attribute to an "enhancement in reactivity" of the lithium reagent,[10] presumably by a

disaggregation process analogous to more common reagents such as TMEDA.[27] They also note that a high molar ratio of ^{n}BuLi contributed to an increase in yield. It is presumed that ^{n}BuLi attacks the allyloxy protecting group, eliminating 1-heptene (which was observed spectroscopically by Hanaoka *et al.*) as well as deprotonating the I* C_5 fragment, eliminating butane. The transient dilithium salt then engages in *in situ* salt metathesis with $TiCl_4$·2THF to form the dichloro titanium complexes.

2.2.2.1. Synthesis of ^{Me2}SB(^{R1,R2}ArO,I)Li$_2$*

Subsequent optimisations were performed to the synthesis: it was found that isolation and work-up of each intermediate was not necessary and that the transformation of **c** to **f** could be achieved in a one pot process. The proligands were reacted with ^{n}BuLi/NEt_3 in toluene, and dilithiated ligand salts $^{Me2}SB(^{R1,R2}ArO,I^*)Li_2$ ((C$_9$Me$_6$Li)-Me$_2$Si(2-R$_1$-4-R$_2$-C$_6$H$_2$O)Li, **f**) were obtained in quantitative yields and reasonable purities following removal of the volatile components under vacuum. The presence of 1-heptene and NEt_3 were indentified in the distillate by ^{1}H NMR spectroscopy, confirming the proposed deprotection mechanism and the catalytic role of the tertiary amine. The as-obtained dilithium complexes could then be directly combined with $TiCl_4$·2THF in toluene to afford PHENI* titanium dichloride complexes in recrystallised yields of 20–30%.

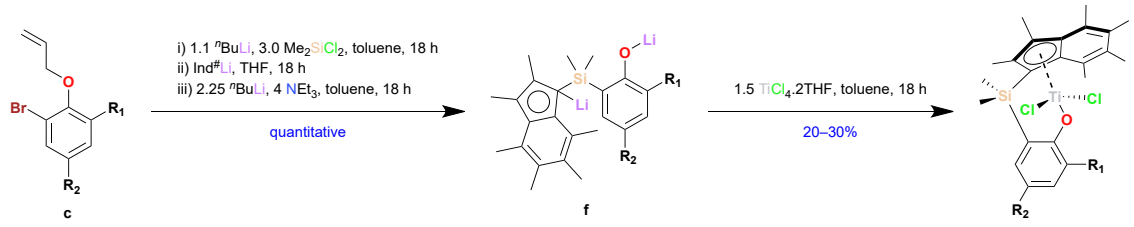

Scheme 2.2 Optimised synthesis of PHENI* complexes from allyloxybromobenzenes. R_1, R_2 = ^{t}Bu, Cumyl.

The dilithiated ligands **2f** and **11f** were isolated and could be characterised by multinuclear NMR spectroscopy. ^{1}H NMR spectra show complete removal of the allyloxy protecting group and the I*H allylic proton.

2.2.2.2. Characterisation of ^{Me2}SB(^{R1,R2}ArO,I)TiCl$_2$*

The ^{1}H NMR spectra of ^{Me2}SB($^{t\text{Bu,Me}}$ArO,I*)TiCl$_2$ (**1**), ^{Me2}SB($^{t\text{Bu2}}$ArO,I*)TiCl$_2$ (**2**), and ^{Me2}SB($^{\text{Cumyl2}}$ArO,I*)TiCl$_2$ (**11**, Figure 2.5) show a number of similarities, with the same diagnostic resonances. The spectra each contain six I*C**H**$_3$ singlets between δ 2.66 and 1.96 ppm, C(C**H**$_3$)$_3$ singlets between δ 1.50 and 1.38 ppm, SiC**H**$_3$ singlets between δ 0.72 and 0.66 ppm and an aromatic pair of doublets between δ 7.58 and 7.19 ppm for the *meta*-aryl protons with a $^{4}J_{\text{H–H}}$ constant of 2 Hz. The I* and SiMe$_2$ resonances are in the same region as for permethylindenyl CGC complexes.[17] The spectrum of **11** displays the four cumyl methyl resonances, C(C**H**$_3$)$_2$Ph, as singlets upfield from the I*C**H**$_3$, and a complex multiplet structure from the cumyl aromatic protons. The two C(C**H**$_3$)$_2$Ph resonances at δ 1.73 ppm are approaching coalescence due to rotation around the OAr–CMe$_2$Ph bond which is less restricted at the *para* position than the *ortho*. In variable temperature ^{1}H NMR (Figure A.52), the *para*-cumyl C**H**$_3$ resonances coalesce fully above 313 K, and appear as distinct singlets below 213 K, however the *ortho*-cumyl remain distinct even at 363 K, though this observation may be attributed to temperature-dependent chemical shifts as significant peak broadening is not seen in the VT NMR.

All three PHENI* complexes show good thermal stability and robust, well-defined structures across a temperature range of –80 to +90 °C as observed by VT ^{1}H NMR studies (Figures A.21, A.24, and A.52).

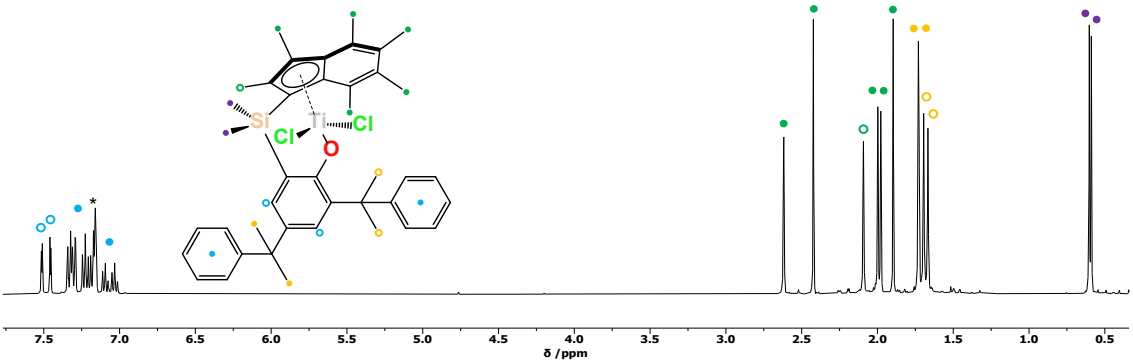

Figure 2.5 ^{1}H NMR spectrum (400 MHz, benzene-d_6, 298 K) of ^{Me2}SB(^{Cumyl2}ArO,I*)TiCl$_2$. The asterisk (*) denotes residual *protio*-benzene.

Crystals of **1** and **11** suitable for single crystal X-ray diffraction studies were grown from slow evaporation of a diethyl ether solution at –30 °C, and of **2** from a saturated pentane solution at –30 °C (Figure 2.6, Table 2.1). While **1** crystallised in the orthorhombic space group *P*bca, both **2** and **11** crystallised in the triclinic space group $P\bar{1}$.

Compared to the indenyl-PHENICS complex reported by Hanaoka *et al.*, ^{Me2}SB(^{tBu,Me}ArO,Ind)TiCl$_2$ (**14**),[10] the PHENI* complexes are significantly more twisted, as defined by the larger torsion angle C(1)–Si(1)–C(23)–C(18) = 45.3(2)°, 35.89(1)°, and 27.1(4)° (*c.f.* 11.75° for the indenyl complex) and a smaller I*–ArO interplanar dihedral angle (54.38°, 45.08°, and 46.31° *c.f.* 60.85° for the indenyl complex). The I* system is oriented away from the active centre, counterintuitively leaving the titanium atom much more accessible than in the less bulky indenyl complex. The ring slip parameters of 0.1–0.2 Å demonstrate the tendency for indenyl complexes to undergo η^5–η^3 ring slip, with a slightly larger parameter for **14** in the solid state than the PHENI* complexes. In the solid-state structure of **11**, the *ortho*-cumyl phenyl ring is held at a distance of Ti–Ph$_{cent}$ = 4.657 Å from the metal centre in a conformation which may enable a degree of long range π–d stabilisation despite the steric incentive to dispose the ring away from the metal centre (Figure 2.6c).

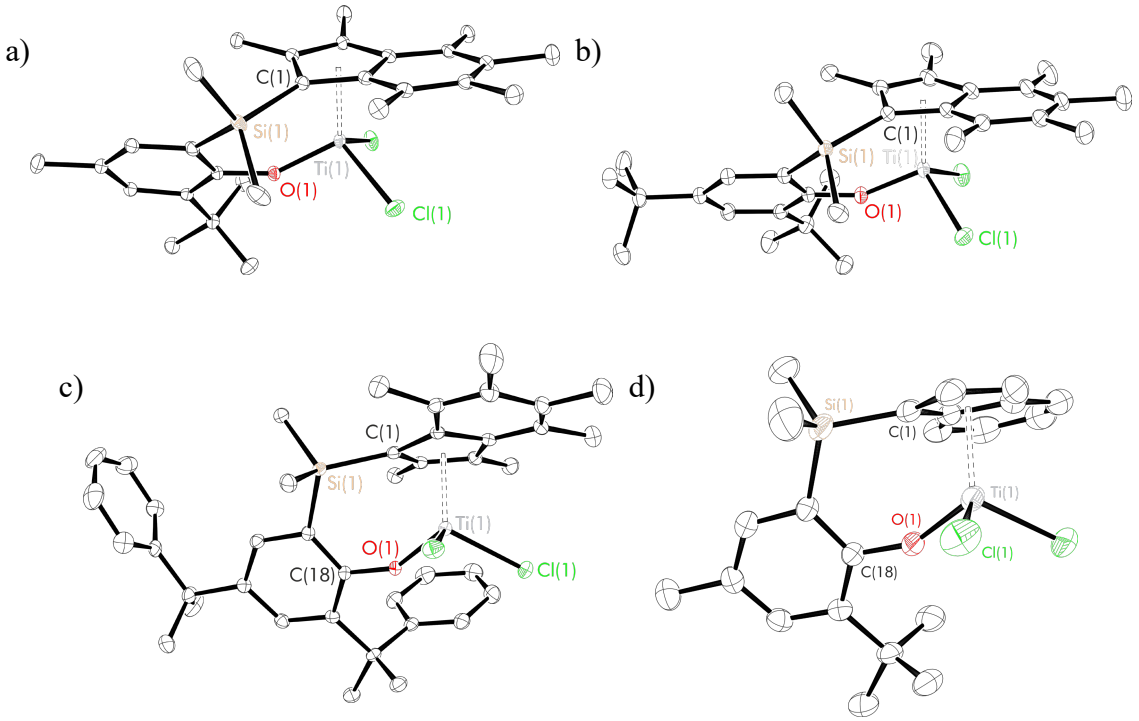

Figure 2.6 Solid-state ellipsoid plots of a) ^{Me_2}SB(^{tBu,Me}ArO,I*)TiCl$_2$ (**1**), b) ^{Me_2}SB(^{tBu_2}ArO,I*)TiCl$_2$ (**2**), c) ^{Me_2}SB(^{Cumyl_2}ArO,I*)TiCl$_2$ (**11**), and d) ^{Me_2}SB(^{tBu,Me}ArO,Ind)TiCl$_2$ (**14**)[10]. Hydrogen atoms omitted for clarity; thermal ellipsoids drawn at 30% probability.

Table 2.1 Selected geometric parameters (lengths in Å, angles in °) for titanium PHENI* complexes ^{Me_2}SB(^{tBu,Me}ArO,I*)TiCl$_2$ (**1**), ^{Me_2}SB(^{tBu_2}ArO,I*)TiCl$_2$ (**2**), and ^{Me_2}SB(^{Cumyl_2}ArO,I*)TiCl$_2$ (**11**), and the indenyl PHENICS complex, ^{Me_2}SB(^{tBu,Me}ArO,Ind)TiCl$_2$ (**14**)[10]. Estimated standard deviations (ESDs) given in parentheses. (a) Calculated using the equivalent Ind$_{cent}$. (b) H(1)–C(2)–O(1)–C(18).

Complex	**1**	**2**	**11**	**14**
Space group	*P*bca	$P\bar{1}$	$P\bar{1}$	$P2_1/c$
Ti(1)–O(1)	1.7949(12)	1.7838(1)	1.791(2)	1.7722(18)
Ti(1)–I*$_{cent}$	2.0242(9)	2.0156(1)	2.0243(17)	2.031 [a]
O(1)–Ti(1)–I*$_{cent}$	115.49(5)	114.16(1)	114.53(10)	115.86 [a]
C(1)–Si(1)–C(23)–C(18)	45.3(2)	35.89(1)	27.1(4)	11.8(3)
TA’	31.8(1)	33.0(2)	42.9(3)	71.6 [b]
I*–ArO	54.38	45.08	46.31	60.85 [a]
Δ_{M-C}	0.098	0.096	0.136	0.180

The geometry of PHENI* complexes can be categorised according to the proposed conformational regime in Figure 2.7. This interconversion can be considered to occur

through breaking of the Ti–I*$_{C5}$ bond, and rotation of the Si–C$_{I*}$ bond. This is quantified by the TA' parameter, adapted from Arnold *et al.*,[28] calculated as the torsion angle C(10)–C(2)–O(1)–C(18). The "A" geometry is defined as having TA' between 70–80°, while the "B" geometry has TA' between 30–40°. Under this parametrisation, it is interesting to note that, while the indenyl PHENICS complex (**14**) crystallises with the A geometry, all three PHENI* complexes (**1**, **2** and **11**) crystallise with the B conformation. This may have implications in catalysis, where the geometry around the metal centre influences the energy barrier for coordination.

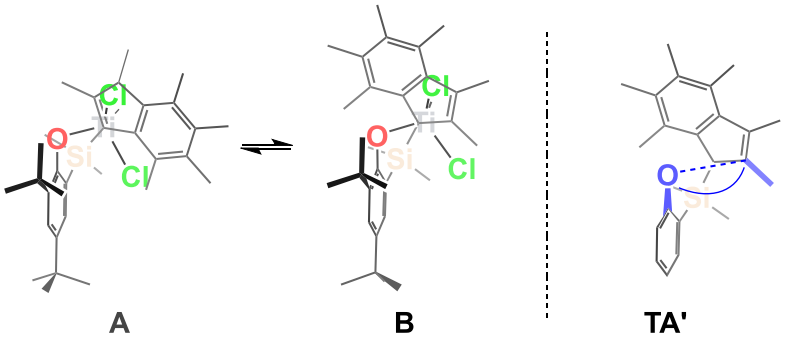

Figure 2.7 Permethylindenyl structural rearrangement equilibrium between the A and B geometries of PHENI* complexes, and the torsion angle TA' ([TiCl$_2$] fragment and ArO substituents omitted for clarity).

The solution-phase dynamics of a Cp* PHENICS complex was explored by Nabika *et al.* through NMR studies and *ab initio* DFT calculations. They proposed a phenoxide flipping mechanism with a calculated activation energy of 18.5 kcal mol^{-1}, substantially greater than k_BT at ambient temperature.[13] The flip takes the complex from a C_s state to a C_1 transition state and bears a remote conformational similarity to the I* flip proposed for the PHENI* complexes in this work.

The solid-state structures of PHENI* complexes show similar Ti–I*$_{cent}$ distances both to permethylindenyl post metallocene complexes,[17] and to the analogous Ti–Cp$_{cent}$ for

PHENICS complexes,[10,13,14] and titanium constrained geometry complexes.[29,30] The Ti–O bond length and I*$_{cent}$–Ti–O angle is in the same range as PHENICS complexes,[10,13,14] and the Ti–O bond is slightly shorter than in other phenoxy-titanium systems such as phenoxy-tetrazole,[31] phenoxy-imine,[32] phenoxy-amine,[33,34] bis-phenoxy,[35] and phenoxy-azo ligands.[36]

2.2.2.3. Attempted syntheses

The synthesis of ^{Me2}SB(^{Me2}ArO,I*)TiCl$_2$, ^{Me2}SB(^{H2}ArO,I*)TiCl$_2$, and ^{Me2}SB(^{F2}ArO,I*)TiCl$_2$ was attempted from the starting materials 2,4-dimethylphenol (^{Me2}ArOH), 2-bromophenol (^{Br,H2}ArOH), and 2-bromo-4,6-difluorophenol (^{Br,F2}ArOH) respectively.

Silylation of ^{Br,Me2}ArOAllyl led to the formation of a dimeric species, presumed to be Me$_2$Si(^{Me2}ArOAllyl)$_2$, rather than the desired chlorosilyl synthon. Synthesis of the {Me$_2$} proligands was also attempted *via* direct reaction of the protected bromophenol with chloro(I*)dimethylsilane (I*SiMe$_2$Cl), however no reaction was observed after 18 h at 23 °C, and heating to 60 °C for 60 h resulted in an intractable mixture of products (Scheme 2.3).

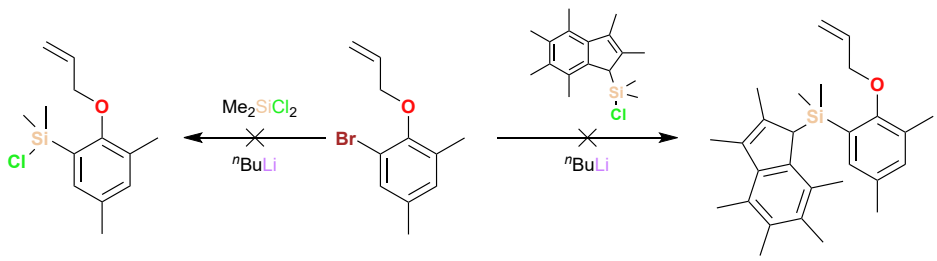

Scheme 2.3 Attempted syntheses of the dimethyl substituted PHENI* ligand.

The complex ^{Me_2}SB(^{H_2}ArO,I*)TiCl$_2$ (**19**) was observed spectroscopically as the major component of the products from the *in situ* reaction of the proligand ^{Me_2}SB(^{H_2}ArOAllyl,I*)H (**19e**) with ^{n}BuLi/NEt$_3$ followed by TiCl$_4$·2THF (Scheme 2.4). However repeated washing and recrystallisation from pentane or hot hexane did not result in the clean isolation of the complex, and attempted recrystallisation from hot toluene resulted in decomposition products. In the ^{1}H NMR spectrum, resonances corresponding to the desired product can be clearly identified, with SiC**H**$_3$ singlets at δ 0.57 and 0.60 ppm, six I*C**H**$_3$ singlets between 1.85–2.65 ppm, and multiplets corresponding to the four phenoxy protons at 6.69, 6.97, and 7.33 ppm (Figure A.69).

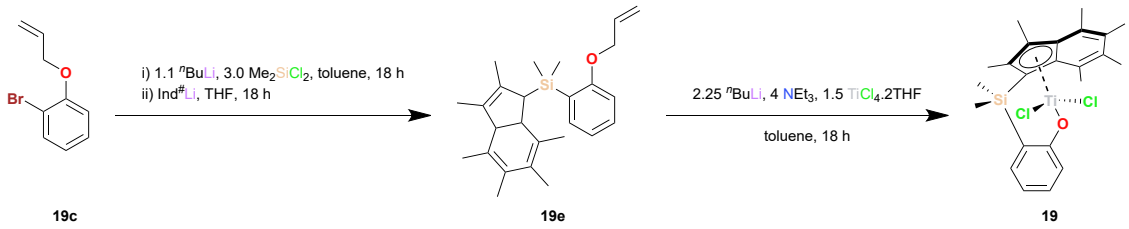

Scheme 2.4 Synthesis of the unsubstituted PHENI* complex ^{Me_2}SB(^{H_2}ArO,I*)TiCl$_2$ (**19**).

Silylation of ^{Br,F_2}ArOAllyl afforded a mixture of products as observed by ^{19}F NMR spectroscopy. Subsequent reaction with Ind$^{\#}$Li led to a mixture of products from which the desired {F$_2$} proligands could not be isolated. The reaction of ^{Br,F_2}ArOAllyl with magnesium turnings to afford a Grignard reagent and subsequent treatment with I*SiMe$_2$Cl resulted in an inseparable mixture of products. Despite the kinetic preference for metalation of the weaker Ar–Br bond rather than Ar–F, insufficient selectivity was achieved to enable the desired reactions (Scheme 2.5).

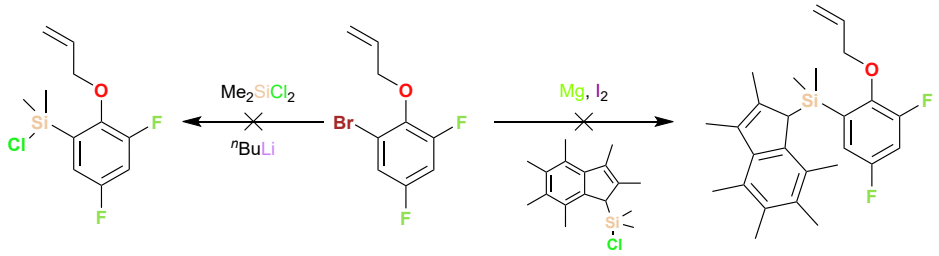

Scheme 2.5 Attempted synthesis of the difluoro substituted PHENI* ligand.

2.2.3. Synthesis of ^{Me2}SB(^{tBu,R2}ArO,I*)TiX$_2$ (X = halide, alkyl, alkoxide, aryloxide, amide)

The chloride ancillary ligands of ^{Me2}SB(^{tBu,R2}ArO,I*)TiCl$_2$ (**2**) could readily be replaced by halide, alkyl, alkoxide, aryloxide, and amide groups through stoichiometric reactions with suitable reagents (Equation 2.1). Attempts to synthesise titanium hydride complexes by treating **2** with KH or KBH$_4$ in THF-d_8 were unsuccessful, with mixtures of products observed by ^{1}H NMR spectroscopy.

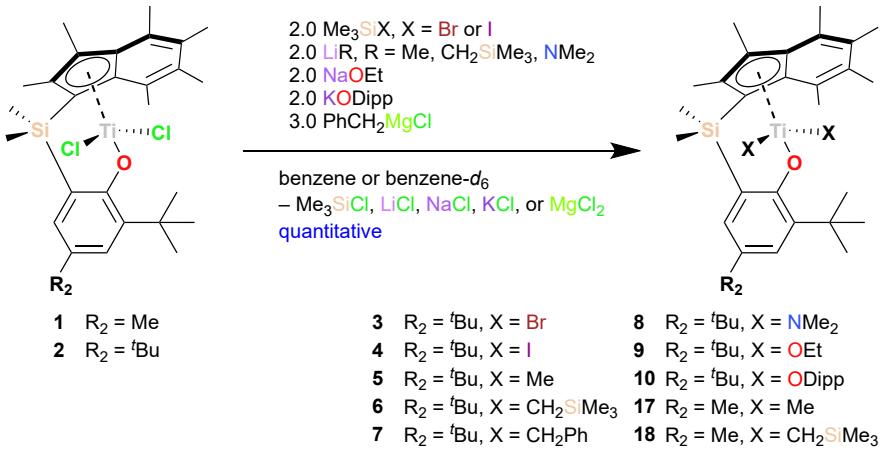

1 R_2 = Me
2 R_2 = ^{t}Bu

3 R_2 = ^{t}Bu, X = Br
4 R_2 = ^{t}Bu, X = I
5 R_2 = ^{t}Bu, X = Me
6 R_2 = ^{t}Bu, X = CH_2SiMe_3
7 R_2 = ^{t}Bu, X = CH_2Ph
8 R_2 = ^{t}Bu, X = NMe_2
9 R_2 = ^{t}Bu, X = OEt
10 R_2 = ^{t}Bu, X = ODipp
17 R_2 = Me, X = Me
18 R_2 = Me, X = CH_2SiMe_3

Equation 2.1 Synthesis of ^{Me2}SB(^{tBu,R2}ArO,I*)TiX$_2$ (R_2 = Me, ^{t}Bu; X = Br, I, Me, CH_2SiMe_3, CH_2Ph, OEt, ODipp, NMe_2) from ^{Me2}SB(^{tBu,R2}ArO,I*)TiCl$_2$. Dipp = 2,6-di*iso*propylphenyl.

2.2.3.1. X = halide

Chloride could be exchanged for bromide or iodide using TMSBr or TMSI respectively, with the elimination of TMSCl observed by ^{1}H NMR spectroscopy. The reaction of **2**

with TMSBr was complete after 6 h at 60 °C, and with TMSI after 1.75 h at 80 °C. Removal of the solvent, TMSCl, and excess reagent under vacuum resulted in the quantitative isolation of the desired product.

The ^{1}H NMR spectra of ^{Me2}SB(^{t}Bu$_2$ArO,I*)TiBr$_2$ (**3**), and ^{Me2}SB(^{t}Bu$_2$ArO,I*)TiI$_2$ (**4**) display the same characteristic resonances as **2**. It is notable, however, that while the *para* C(C**H**$_3$)$_3$ resonance is constant at δ 1.38 ppm, the *ortho* substituent shifts downfield from δ 1.50 ppm (**2**, Cl) to δ 1.58 ppm (**3**, Br) to δ 1.70 ppm (**4**, I) despite the halogens becoming less electronegative (Figure 2.8). Moreover, the two downfield I*C**H**$_3$ resonances also shift further downfield from δ 2.55 and 2.65 ppm (**2**, Cl), to δ 2.63 and 2.71 ppm (**3**, Br), to δ 2.76 and 2.80 ppm (**4**, I). It is proposed that this change in chemical shifts is a result of a conformational change in the ligand induced by the heavier halogens. This effect was not seen with the ^{Me2}SB(Cp^{Me},I*)ZrX$_2$ (X = Cl, Br) complexes synthesised by Lamb *et al.*,[24] or the *rac*-($^{3\text{-Ph}}$Ind$^{\#}$)$_2$ZrX$_2$ (X = Cl, Br) complexes synthesised by Angpanitcharoen *et al.*:[37] in both cases, the I*C**H**$_3$ resonances were largely unaffected by the substitution of bromide for chloride.

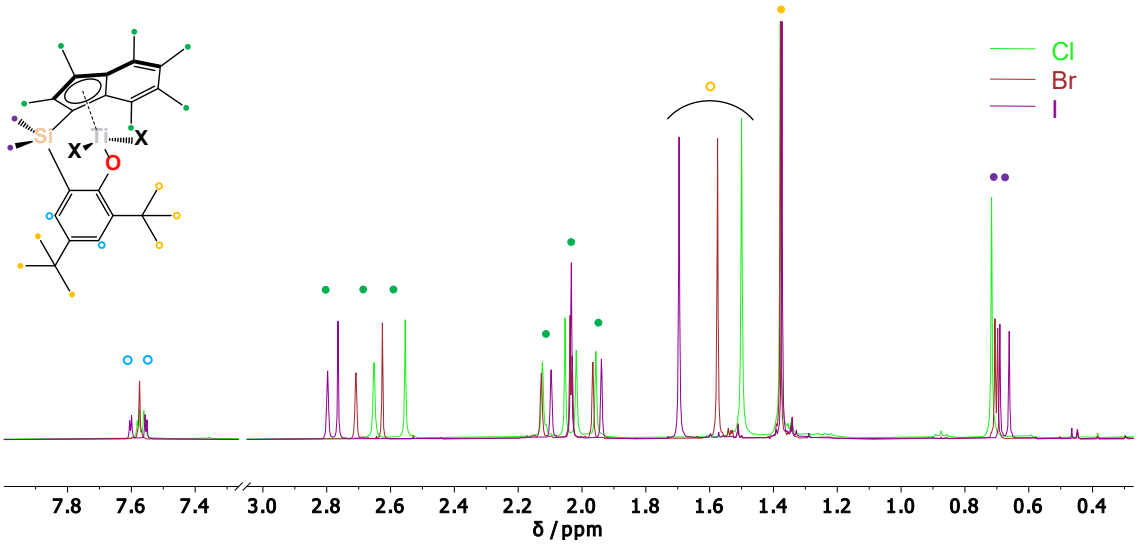

Figure 2.8 ^{1}H NMR spectra (400 MHz, benzene-d_6, 298 K) of ^{Me_2}SB($^{t Bu_2}$ArO,I*)TiCl$_2$ (**2**, green), ^{Me_2}SB($^{t Bu_2}$ArO,I*)TiBr$_2$ (**3**, maroon), and ^{Me_2}SB($^{t Bu_2}$ArO,I*)TiI$_2$ (**4**, purple).

Crystals of **3** suitable for an X-ray diffraction study were deposited from the benzene-d_6 solution in the NMR tube stored at room temperature, and of **4** were grown from slow evaporation of a diethyl ether solution at –30 °C (Figure 2.9, Table 2.2). Both complexes crystallise in the triclinic space group $P\bar{1}$, with the solid-state structure of **3** exhibiting the A geometry (TA' = 78.8(2)°). Uniquely, the solid-state structure of **4** contains crystallographically distinct molecules in the asymmetric unit (Z' = 3), which are in a 2:1 ratio of and A and B conformations (Figure A.70), having TA' angles of 36.7(5)° and 72.4(7)° respectively. This is excellent evidence for the existence of the proposed A–B conformational regime, with the observed symmetric ^{1}H NMR spectrum of **4** suggestive of a time-averaged structure, and conformational interconversion. It is clearly a finely balanced system, with small changes in sterics and electronics able to promote one conformation over the other.

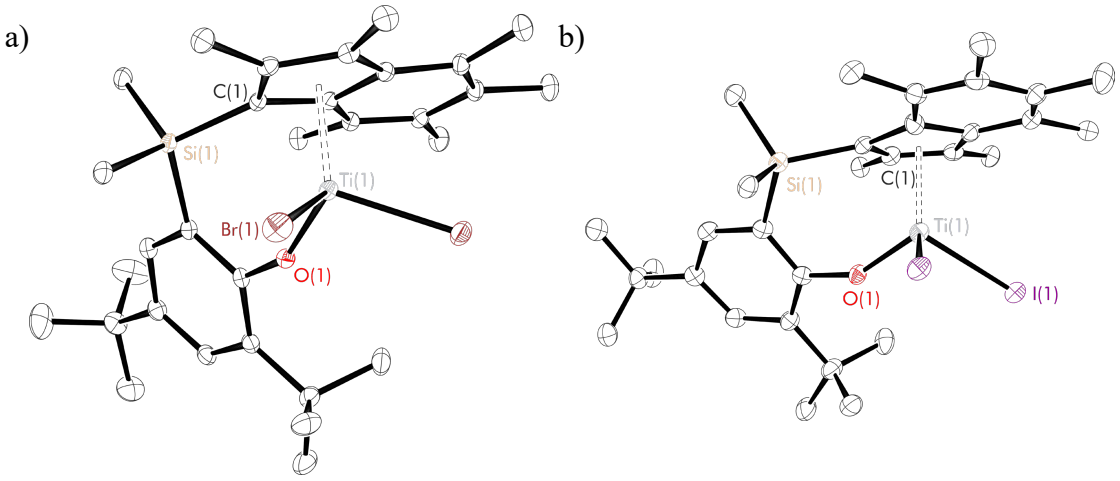

Figure 2.9 Solid-state ellipsoid plot of a) ^{Me_2}SB($^{t Bu_2}$ArO,I*)TiBr$_2$ (**3**), and b) ^{Me_2}SB($^{t Bu_2}$ArO,I*)TiI$_2$ (**4**; residue 1, **4**-B, shown). Hydrogen atoms omitted for clarity; thermal ellipsoids drawn at 30% probability.

Table 2.2 Selected geometric parameters (lengths in Å, angles in °) for PHENI* complexes ^{Me_2}SB($^{t Bu_2}$ArO,I*)TiCl$_2$ (**2**), ^{Me_2}SB($^{t Bu_2}$ArO,I*)TiBr$_2$ (**3**), and ^{Me_2}SB($^{t Bu_2}$ArO,I*)TiI$_2$ (**4**). Estimated standard deviations (ESDs) given in parentheses.

Complex	**2**	**3**	**4**-A	**4**-B
Space group	$P\bar{1}$	$P\bar{1}$	$P\bar{1}$	
Ti(1)–O(1)	1.7838(1)	1.7960(14)	1.794(5)	1.793(5)
Ti(1)–I*$_{cent}$	2.0156(1)	2.0342(10)	2.033(4)	2.031(3)
O(1)–Ti(1)–I*$_{cent}$	114.16(1)	118.29(6)	117.80(19)	114.92(18)
C(1)–Si(1)–C(23)–C(18)	35.89(1)	38.16(18)	17.1(8)	36.3(7)
TA'	33.0(2)	78.8(2)	72.4(7)	36.7(5)
I*–ArO	45.08	61.46	58.50	48.53
Δ_{M-C}	0.096	0.174	0.210	0.165

2.2.3.2. X = alkyl

Alkyl complexes with methyl and neosilyl (CH_2SiMe_3) ancillary ligands were formed from both **1** and **2** as the parent complex, using MeLi (as an Et_2O solution) or $LiCH_2SiMe_3$, both with the elimination of LiCl. Both reactions were practically instantaneous at room temperature. The insoluble by-products were removed by filtration, and the volatiles under vacuum. In both methyl complexes – ^{Me_2}SB($^{t Bu,Me}$ArO,I*)TiMe$_2$ (**17**), and ^{Me_2}SB($^{t Bu_2}$ArO,I*)TiMe$_2$ (**5**) – two TiC**H**$_3$ ^{1}H NMR

resonances are found at δ 0.16 and 0.87 ppm. The neosilyl complexes – ^{Me_2}SB($^{t Bu,Me}$ArO,I*)Ti(CH_2SiMe_3)$_2$ (**18**), and ^{Me_2}SB($^{t Bu_2}$ArO,I*)Ti(CH_2SiMe_3)$_2$ (**6**) – each display two $CH_2Si\mathbf{Me}_3$ resonances between δ 0.12–0.17 ppm. In addition, the $C\mathbf{H}_2SiMe_3$ resonances appear as two pairs of diastereotopic doublets at δ 1.91, 0.97, 0.94, and –0.89 ppm with $^2J_{H–H}$ geminal coupling constants of 11 Hz.

Crystals suitable for X-ray diffraction studies were grown of **5** and of **6** by slow evaporation of pentane solutions at –30 °C. Both crystallise in the triclinic space group $P\bar{1}$, and while **5** adopts the B conformation (TA' = 33.8(1)°), **6** displays a torsion angle towards A-type geometry (TA' = 65.4(2)°). This demonstrates that methylation has little structural effect compared to the parent dichloride complex, which is significant as methylation is involved in the initiation step of catalytic olefin polymerisation.

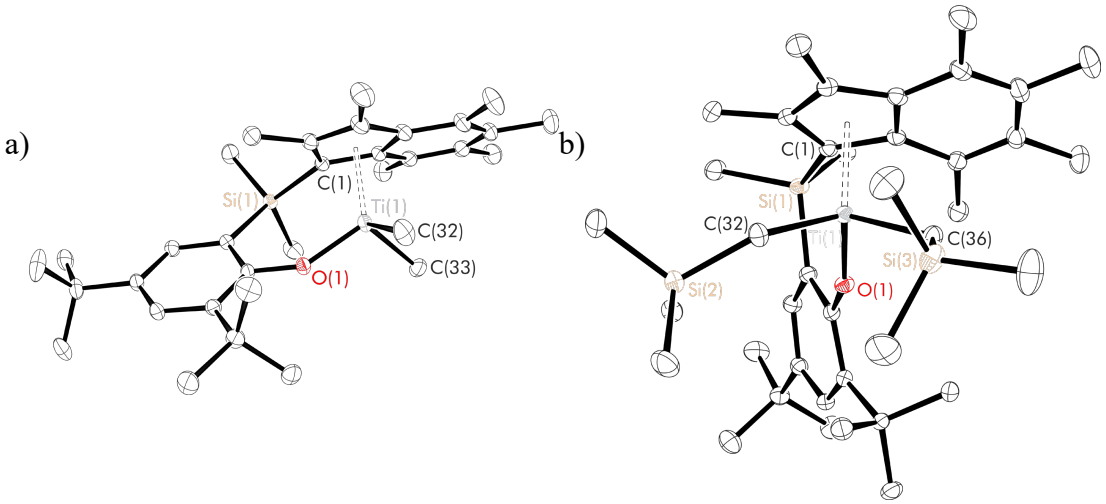

Figure 2.10 Solid-state ellipsoid plots of a) ^{Me_2}SB($^{t Bu_2}$ArO,I*)TiMe_2 (**5**), b) ^{Me_2}SB($^{t Bu_2}$ArO,I*)Ti(CH_2SiMe_3)$_2$ (**6**). Hydrogen atoms omitted for clarity; thermal ellipsoids drawn at 30% probability.

Table 2.3 Selected geometric parameters (lengths in Å, angles in °) for PHENI* complexes **5**, and **6**. Estimated standard deviations (ESDs) given in parentheses.

Complex	^{Me_2}SB($^{t Bu_2}$ArO,I*)TiMe$_2$	^{Me_2}SB($^{t Bu_2}$ArO,I*)Ti(CH$_2$SiMe$_3$)$_2$
Space group	$P\bar{1}$	$P\bar{1}$
Ti(1)–O(1)	1.8021(9)	1.8174(1)
Ti(1)–I*$_{cent}$	2.0357(8)	2.0842(1)
O(1)–Ti(1)–I*$_{cent}$	118.02(4)	119.10(1)
C(1)–Si(1)–C(23)–C(18)	40.25(15)	1.69(1)
TA’	33.8(1)	65.4(2)
I*–ArO	54.24	70.86
Δ_{M-C}	0.117	0.287

Attempts to synthesise benzyl (CH$_2$Ph, Bn) complexes derived from both **1** and **2** were unsuccessful using KBn. A clean reaction was obtained between **2** and the Grignard reagent PhCH$_2$MgCl in a mixed benzene/THF solvent system. The bright orange product, ^{Me_2}SB($^{t Bu_2}$ArO,I*)TiBn$_2$ (**7**), was then extracted in toluene, using 1,4-dioxane to aid precipitation of the by-product MgCl$_2$. In the ^{1}H NMR spectrum of **7**, the benzyl aromatic protons are seen as three multiplets at δ 6.86, 6.93, and 7.04 ppm, and the diastereotopic C**H**$_2$Ph protons are two pairs of doublets at δ 1.31, 2.12, 2.66, and 2.74 ppm, with a $^2J_{H-H}$ geminal coupling constant of 11 Hz, similar to the C**H**$_2$SiMe$_3$ resonances in **6**.

2.2.3.3. X = alkoxide, aryloxide, amide

Alkoxide, aryloxide, and amide complexes were formed from the reaction between **2** and two equivalents of either NaOEt, KODipp (Dipp = 2,6-di*iso*propylphenyl), or LiNMe$_2$, eliminating the corresponding alkali metal chloride salt. These reactions occurred more slowly than the halide and alkyl exchanges: complete substitution was observed with the amide after 42 h at 80 °C, the alkoxide after 137 h at 60–80 °C, and the aryloxide after 24 h at 60 °C. In all cases the presence of the monosubstituted intermediate ^{Me_2}SB($^{t Bu_2}$ArO,I*)Ti(Cl)X could be observed by ^{1}H NMR spectroscopy (Figure 2.11).

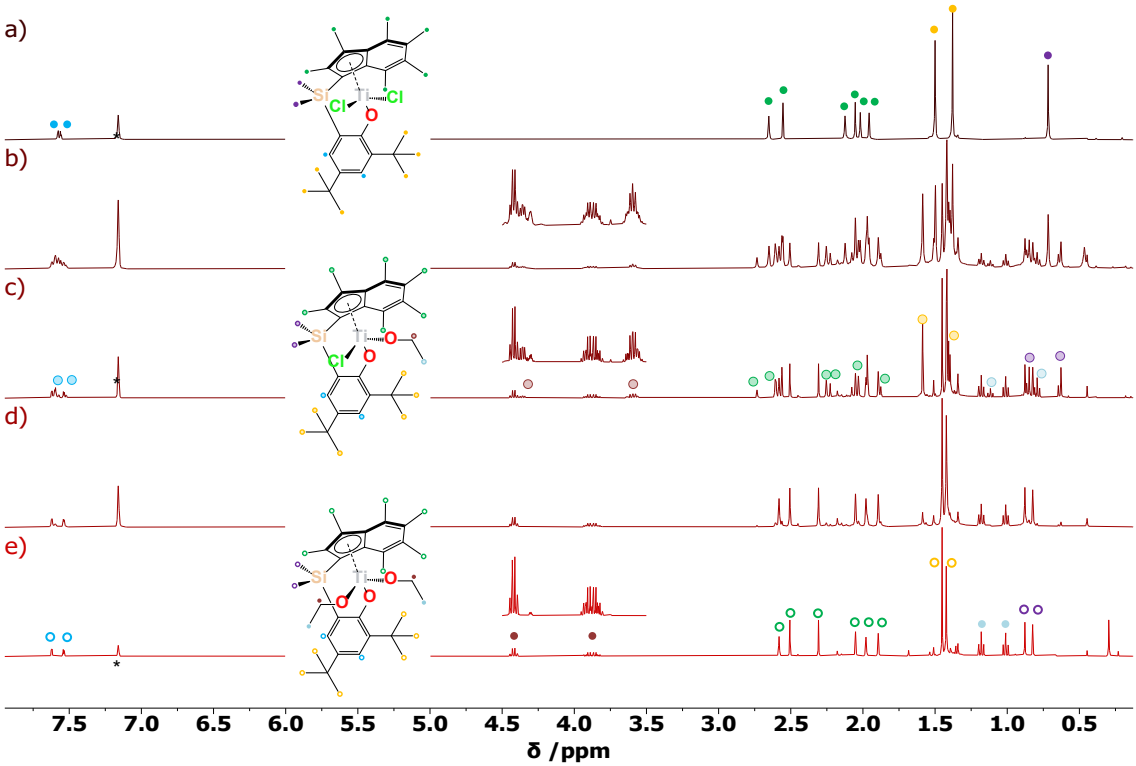

Figure 2.11 ^{1}H NMR spectra (400 MHz, benzene-d_6, 298 K) of the reaction between ^{Me2}SB(^{tBu2}ArO,I*)TiCl$_2$ (**2**) and NaOEt evolving as a function of time, forming first ^{Me2}SB(^{tBu2}ArO,I*)Ti(Cl)OEt, then ^{Me2}SB(^{tBu2}ArO,I*)Ti(OEt)$_2$ (**9**). Sample heated at b) 60 °C for 17 h, c) 80 °C for 1 h, d) 80 °C for 2.5 h, and e) 60 °C for 14.5 h between spectrum collections. Asterisk (*) denotes residual *protio*-benzene.

The monosubstituted complexes are chiral at the metal centre and form as a mixture of isomers. In the slow reaction of **2** with NaOEt, complete assignment of the monosubstituted intermediate ^{Me2}SB(^{tBu2}ArO,I*)Ti(Cl)OEt from the *in situ* ^{1}H NMR spectrum of the reaction mixture is possible. The diagnostic resonance corresponding to the OC**H**$_2$CH$_3$ protons can be seen at δ 3.59 ppm in the monosubstituted complex, with a minor component at δ 4.36 ppm presumably corresponding to the isomer in which the other chloride is substituted, showing both that there is a kinetic preference for one of the chlorides to substitute first and that exchange over the two coordination sites does not occur on the NMR timescale. The triplet resonance arising from the OCH$_2$C**H**$_3$ protons

is seen at δ 0.79 ppm, with a minor component, likely the other diastereomer, at δ 1.12 ppm, both with $^{3}J_{H–H}$ = 6.9 Hz.

For the fully substituted amide complex, ^{Me2}SB(^{tBu2}ArO,I*)Ti(NMe$_2$)$_2$ (**8**), the N**Me**$_2$ protons have resonances at δ 2.60 and 3.00 ppm in the ^{1}H NMR spectrum. For the alkoxide complex, ^{Me2}SB(^{tBu2}ArO,I*)Ti(OEt)$_2$ (**9**), the OCH$_2$C**H**$_3$ protons resonate as triplets at δ 1.01 and 1.18 ppm ($^{3}J_{H–H}$ = 6.9 Hz), and the OC**H**$_2$CH$_3$ protons are seen as a multiplet at δ 3.88 ppm and a quartet at δ 4.42 ppm, all shifted slightly downfield compared to the monosubstituted intermediate. In the ^{1}H NMR spectrum of the aryloxide complex, ^{Me2}SB(^{tBu2}ArO,I*)Ti(ODipp)$_2$ (**10**), the ArC**H**Me$_2$ resonances are binomial septets at δ 3.14 and 3.52 ppm ($^{3}J_{H–H}$ ≈ 6.8 ppm), the ArCH**Me**$_2$ protons exist as doublets at δ 0.89, 0.98, 1.16, and 1.20 ppm ($^{3}J_{H–H}$ ≈ 6.7 ppm). This suggests that, while the ODipp leaving groups are magnetically inequivalent to each other, rotation about the O–Dipp bond is fast on the NMR timescale leading to a time-averaged signal from the two *iso*-propyl groups on each Dipp. The Dipp aromatic protons are seen as multiplets between δ 6.81–7.12 ppm. In all cases, therefore, the two ancillary ligand leaving groups are inequivalent and do not exchange on the NMR timescale.

Crystals suitable for X-ray diffraction studies were grown of **8** from slow evaporation of a pentane solution at –30 °C, and of **10** from slow evaporation of a benzene solution at 23 °C, both in the triclinic space group $P\bar{1}$. Both **8** and **10** have solid-state structures in the A geometry (TA' = 78.5(1)° and 62.5(1)° respectively), though **10** is somewhat intermediate between the A- and B-type conformations.

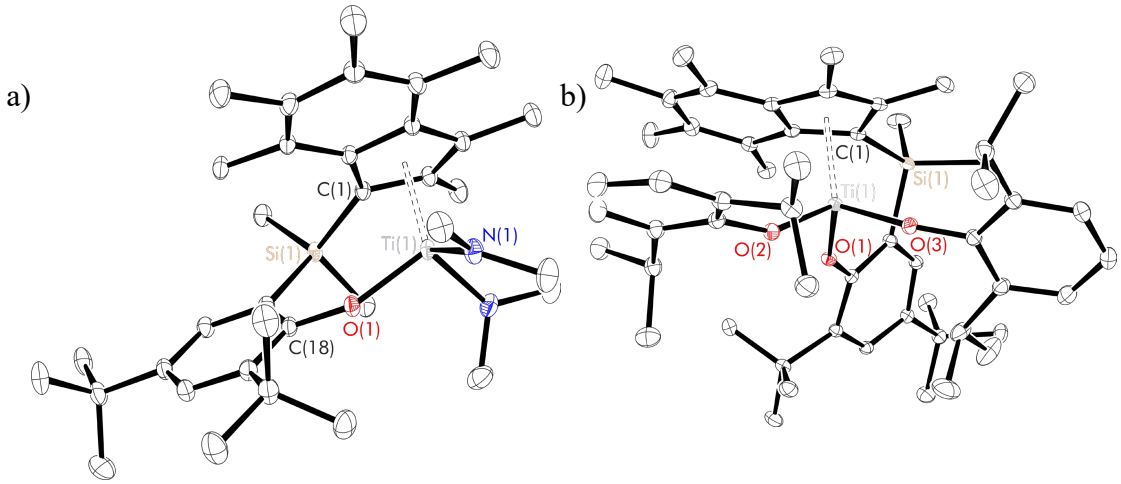

Figure 2.12 Solid-state ellipsoid plots of a) ^{Me_2}SB($^{t Bu_2}$ArO,I*)Ti(NMe$_2$)$_2$ (**8**), b) ^{Me_2}SB($^{t Bu_2}$ArO,I*)Ti(ODipp)$_2$ (**10**). Hydrogen atoms omitted for clarity; thermal ellipsoids drawn at 30% probability.

Table 2.4 Selected geometric parameters (lengths in Å, angles in °) for PHENI* complexes **8**, and **10**. Estimated standard deviations (ESDs) given in parentheses.

Complex	^{Me_2}SB($^{t Bu_2}$ArO,I*)Ti(NMe$_2$)$_2$	^{Me_2}SB($^{t Bu_2}$ArO,I*)Ti(ODipp)$_2$
Space group	$P\bar{1}$	$P\bar{1}$
Ti(1)–O(1)	1.8603(13)	1.8595(1)
Ti(1)–I*$_{cent}$	2.1003(9)	2.0971(1)
O(1)–Ti(1)–I*$_{cent}$	113.18(5)	112.17(1)
C(1)–Si(1)–C(23)–C(18)	34.46(17)	7.51(1)
TA’	78.5(1)	62.5(1)
I*–ArO	51.92	56.00
Δ_{M-C}	0.054	0.245

2.2.4. Synthesis of *rac*-^{Me,R_a}SB($^{t Bu_2}$ArO,I*)TiCl$_2$ (R$_a$ = ^{n}Pr, Ph)

Complexes bearing an unsymmetrical “mixed-bridge” ligand (^{Me,R_a}SB, R$_a$ ≠ Me) are of interest as they are chiral at the silicon and thus possess potentially enantioselective catalytic active sites. A series of mixed-bridge PHENICS complexes (^{Me,R_a}SB($^{t Bu,Me}$ArO,Cp*)TiCl$_2$; R$_a$ = Et, Cy, Ph) were synthesised by Senda *et al.*, and it

was found that the substituents at the silicon controlled regioselectivity in propylene polymerisation.[12]

Ligands with Me^{n}PrSi and MePhSi bridges were synthesised by analogy to the symmetric Me_2Si case (Scheme 2.6). The presence of diastereoisomerism in the proligands **12e** and **13e** resulted in complex ^{1}H NMR spectra, with multiple resonances corresponding to each proton environment. However, upon lithiation, the ligands **12f** and **13f** reverted to simple ^{1}H NMR spectra, comparable to **2f**, with six I*C**H**$_3$ peaks between δ 2.38–3.12 ppm, *tert*-butyl signals between δ 1.43–1.92 ppm, and aromatic doublets between δ 7.32–8.13 ppm (Figures A.12–A.18). A broad resonance is observed in the ^{7}Li NMR spectra of both **12f** and **13f** around δ 1.9–2.6 ppm. A single ^{29}Si resonance is observed for **13f** at δ –15 ppm, while **12f** has resonances at δ –2, –13 and –19 ppm. Titanium dichloride complexes were synthesised by an analogous method to compounds **1**, **2**, and **11**, affording *rac*-^{Me,nPr}SB(^{tBu2}ArO,I*)$TiCl_2$ (**12**), and *rac*-^{Me,Ph}SB(^{tBu2}ArO,I*)$TiCl_2$ (**13**) in yields of 6% and 3% respectively. The low yields are attributed to less favourable crystallisation compared to the symmetrically substituted congeners, and decreased differential solubility with respect to impurities, resulting in the need for additional solvent wash steps. Improved yields may be obtained by using $TiCl_2(NMe_2)_2$ as the metal source, or through derivatisation of the crude by *in situ* methylation to result in a more readily crystallisable product. The synthesis of *rac*-^{Me,tBu}SB(^{tBu2}ArO,I*)$TiCl_2$ was attempted analogously to **12** and **13**, however the reaction between Me^{t}BuSiCl_2 and ^{Br,tBu2}ArOAllyl was found to be unselective according to ^{1}H and ^{29}Si NMR spectroscopy.

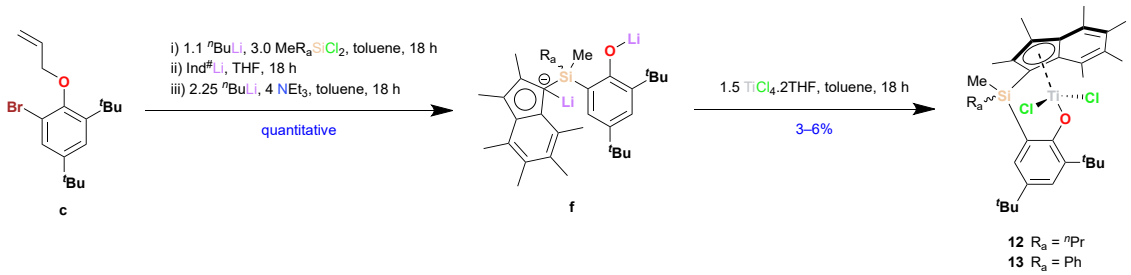

Scheme 2.6 Synthesis of mixed-bridge PHENI* complexes, *rac*-^{Me,R_a}SB($^{t Bu_2}$ArO,I*)TiCl$_2$. R_a = ^{n}Pr, Ph.

The ^{1}H NMR spectra of **12** and **13** share many of the features of the parent symmetrically-bridged PHENI* complex **2**. For **12**, the SiC**H**$_3$ resonance is a singlet at δ 0.73 ppm, and the SiCH$_2$CH$_2$C**H**$_3$ resonance is a triplet at δ 0.94 ppm ($^3J_{H–H}$ = 7.1 Hz). The SiC**H**$_2$C**H**$_2$CH$_3$ resonances are obscured by the *tert*-butyl signals but can be clearly identified in the ^{1}H–^{13}C HSQC spectrum at δ^2 (1.37, 20) and (1.43, 18) ppm, with the negative phase DEPT editing confirming the assignment as CH$_2$ groups (Figure 2.13). In the ^{1}H NMR spectrum of **13**, the SiC**H**$_3$ singlet is at δ 1.04 ppm, and the SiC$_6$**H**$_5$ resonances are multiplets at δ 7.23–7.32 and 7.78–7.82 ppm, distinct from the phenoxy aromatic protons which are doublets at δ 7.48 and 7.59 ppm ($^4J_{H–H}$ = 2.4 Hz). A single ^{29}Si resonance is observed for each complex, at δ –11 ppm for **12**, and δ –16 ppm for **13**.

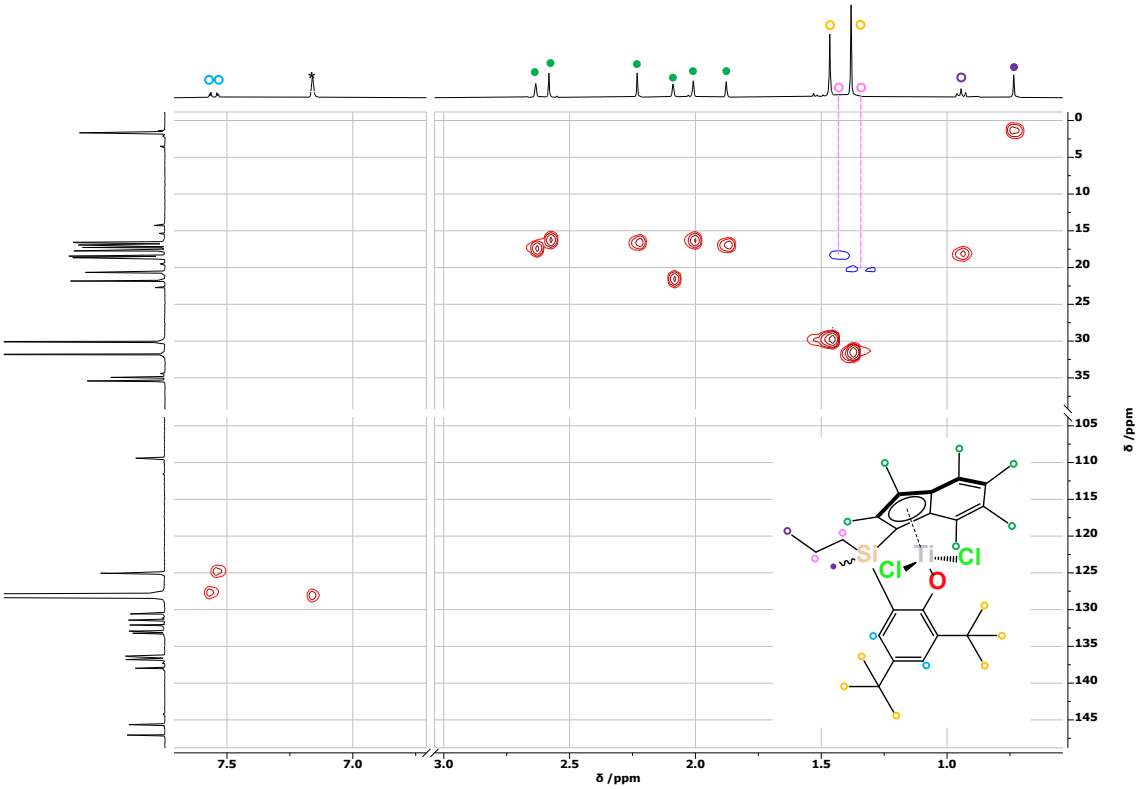

Figure 2.13 ^{1}H–^{13}C HSQC spectrum (400, 101 MHz, DEPT edited, benzene-d_6, 298 K) of *rac*-^{Me,nPr}SB(^{tBu2}ArO,I*)TiCl$_2$ (**12**). Asterisk (*) denotes residual *protio*-benzene.

Crystals of **12** suitable for a X-ray diffraction study were grown from slow evaporation of a diethyl ether solution at –30 °C in the orthorhombic space group *P*n2$_1$a, and of **13** from a saturated pentane solution at –30 °C in the monoclinic space group *P*2$_1$/c (Figure 2.14, Table 2.5). The solid-state geometry of **13** is consistent with B-type conformation, with a very similar TA' angle (35.8(7)°) to that of **2** (33.0(2)°), which shows that additional steric bulk at the bridge does not significantly impact the ligand conformation. Conversely, **12** has a solid-state structure with the A-type conformation, having a TA' angle of 56.4(5)°, demonstrating the delicate balance of steric, electronic, and packing factors in determining crystallographic conformation. In both cases, racemic mixtures are obtained with a 1:1 ratio of the (R) and (S) configurations at the silicon. Notably, though, the A–B conformation results in the possibility of diastereomers: in the

solid-state structure of **12** the I* C_6 ring is orientated *cis* to the Si^{n}Pr (*Z*), whereas **13** displays the (*E*) configuration with the I* C_6 disposed *trans* to the SiPh.

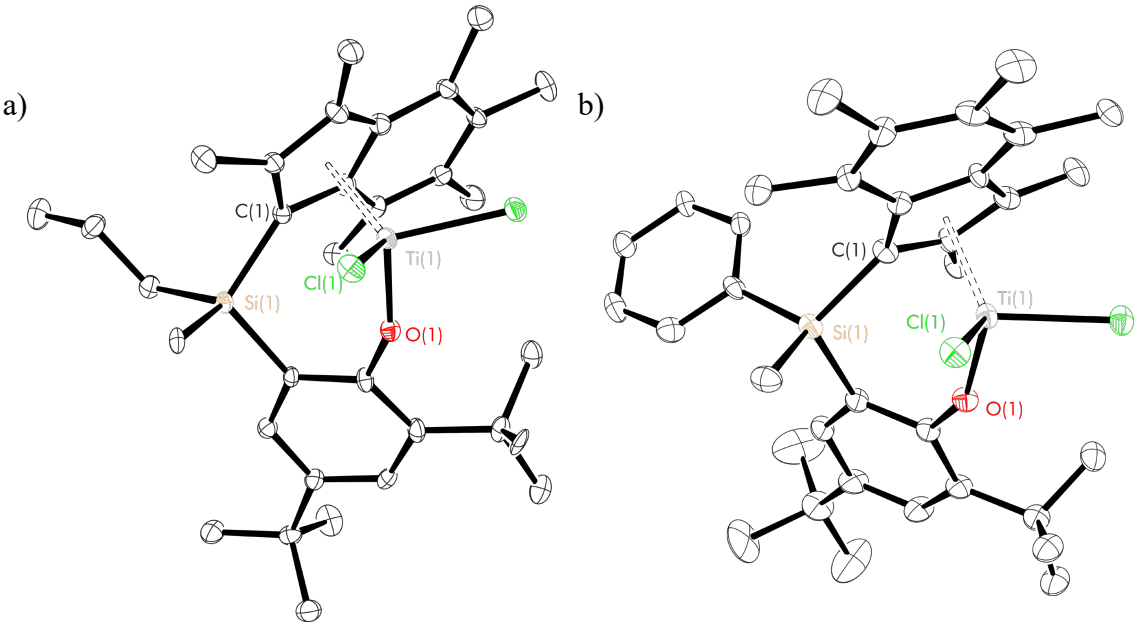

Figure 2.14 Solid-state ellipsoid plots of a) (R)-*Z*-^{Me,nPr}SB(^{tBu2}ArO,I*)TiCl$_2$ (**12**), and b) (R)-*E*-^{Me,Ph}SB(^{tBu2}ArO,I*)TiCl$_2$ (**13**). One stereoisomer shown; hydrogen atoms omitted for clarity; thermal ellipsoids drawn at 15% and 30% probability respectively. The solid-state structure of **12** contains crystallographically independent molecules (*Z*' = 2), which have similar structures – the present discussion relates to residue 1 (containing Ti(1)).

Table 2.5 Selected geometric parameters (lengths in Å, angles in °) for chiral mixed-bridge PHENI* complexes **12**, and **13**. Estimated standard deviations (ESDs) given in parentheses.

Complex	*Z*-^{Me,nPr}SB(^{tBu2}ArO,I*)TiCl$_2$	*E*-^{Me,Ph}SB(^{tBu2}ArO,I*)TiCl$_2$
Space group	*P*n2$_1$a	*P*2$_1$/c
Ti(1)–O(1)	1.783(4)	1.798(6)
Ti(1)–I*$_{cent}$	2.010(3)	2.0280(2)
O(1)–Ti(1)–I*$_{cent}$	115.13(14)	116.42(1)
C(1)–Si(1)–C(23)–C(18)	33.2(5)	44.75(1)
TA'	86.4(5)	35.8(7)
I*–ArO	49.25	51.86
Δ_{M-C}	0.078	0.084

2.2.5. Synthesis of ^{Me2}SB(^{tBu2}ArO,I*)MCl$_2$ (M = Zr, Hf)

Heavier group four congeners of **2** were synthesised from the ligand **2e** by reaction with either $ZrCl_4$ or $HfCl_4$ (Equation 2.2). The zirconium complex, ^{Me2}SB(^{tBu2}ArO,I*)$ZrCl_2$ (**15**), was synthesised by Dr. Nichabhat Blake (University of Oxford) as a dark brown solid in 32% yield with respect to **2e**. The hafnium analogue, ^{Me2}SB(^{tBu2}ArO,I*)$HfCl_2$ (**16**), was isolated by recrystallisation from pentane at –80 °C as a yellow solid in a low yield of 1% with respect to **2f**. The low yield of the hafnium complex is attributed to the poor solubility of $HfCl_4$ in toluene and poor reaction selectivity. It is possible that using a more soluble reagent such as $HfCl_4$·2THF, or a more selective reagent such as $HfCl_2(NMe_2)_2$ would result in an improved yield.

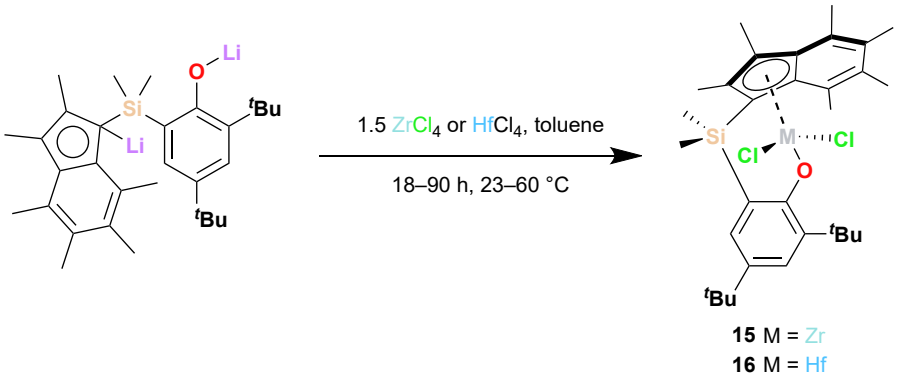

Equation 2.2 Synthesis of zirconium and hafnium PHENI* complexes. M = Zr, Hf.

The ^{1}H NMR spectra of **15** and **16** display many similarities to each other and to the titanium congener **2**. The SiC**H**$_3$ resonances are largely insensitive to the nature of the metal centre but are split into two resonances for the heavier Group 4 elements, whereas coalescence is observed for the titanium complex **2**. A slightly upfield shift of the *ortho tert*-butyl resonances was observed relative to **2**, and the six I* methyl resonances are particularly sensitive to chemical environment and are singlets between δ 1.90–2.65 ppm.

The phenoxy aromatic resonances are an almost identical pair of doublets for the titanium and zirconium complexes, by contrast the hafnium complex has a single broad resonance.

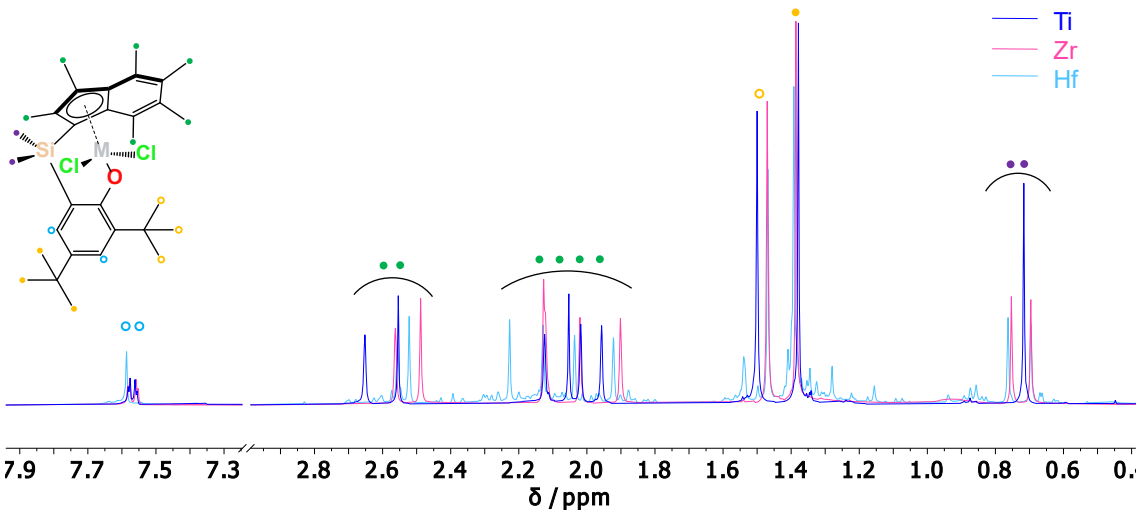

Figure 2.15 ^{1}H NMR spectra (400 MHz, benzene-d_6, 298 K) of ^{Me_2}SB($^{t Bu_2}$ArO,I*)TiCl$_2$ (**2**, blue), ^{Me_2}SB($^{t Bu_2}$ArO,I*)ZrCl$_2$ (**15**, pink), and ^{Me_2}SB($^{t Bu_2}$ArO,I*)HfCl$_2$ (**16**, turquoise).

Crystals suitable for X-ray diffraction studies were grown of **15** from slow evaporation of a benzene solution at room temperature and of **16** from slow evaporation of a diethyl ether solution at –30 °C, both in the triclinic space group $P\bar{1}$ (Figure 2.16, Table 2.6).

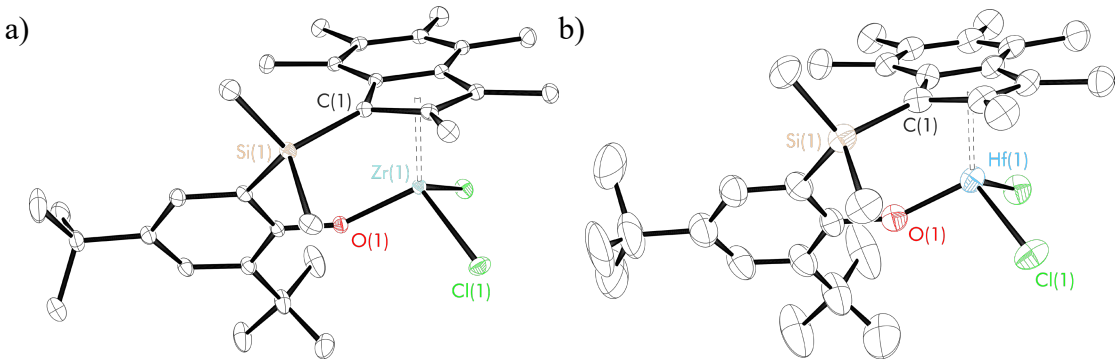

Figure 2.16 Solid-state ellipsoid plots of a) ^{Me_2}SB($^{t Bu_2}$ArO,I*)ZrCl$_2$ (**15**), b) ^{Me_2}SB($^{t Bu_2}$ArO,I*)HfCl$_2$ (**16**). Hydrogen atoms omitted for clarity; thermal ellipsoids drawn at 30% probability.

Table 2.6 Selected geometric parameters (lengths in Å, angles in °) for titanium, zirconium, and hafnium PHENI* complexes **2**, **15**, and **16**. Estimated standard deviations (ESDs) given in parentheses.

Complex	$^{Me}_2$SB(^{t}Bu$_2$ArO,I*)TiCl$_2$	$^{Me}_2$SB(^{t}Bu$_2$ArO,I*)ZrCl$_2$	$^{Me}_2$SB(^{t}Bu$_2$ArO,I*)HfCl$_2$
Space group	$P\bar{1}$	$P\bar{1}$	$P\bar{1}$
M(1)–O(1)	1.7838(1)	1.9236(16)	1.918(3)
M(1)–I*$_{cent}$	2.0156(1)	2.1703(11)	2.140(2)
O(1)–M(1)–I*$_{cent}$	114.16(1)	115.30(6)	115.32(12)
C(1)–Si(1)–C(23)–C(18)	35.89(1)	44.4(2)	41.2(5)
TA’	33.0(2)	80.2(2)	79.2(5)
I*–ArO	45.08	66.52	64.00
Δ_{M-C}	0.096	0.122	0.118

The zirconium (IV) and hafnium (IV) complexes are isostructural as expected from the similar ionic radii r_{Zr}^{4+} = 0.59 Å and r_{Hf}^{4+} = 0.58 Å by virtue of the lanthanide contraction present for hafnium.[38,39] Both display A-type conformation in the solid state, with comparable M–O and M–I*$_{cent}$ distances, and O–M–I*$_{cent}$ and TA’ angles. By contrast, the smaller radius of Ti^{4+} (0.42 Å) and higher charge density may account for shorter M–L bonds, a smaller bridge torsion angle, a smaller interplanar dihedral angle, and B-type conformation in complex **2** (Figure 2.17). The heavy group four congeners have a dihedral angle and TA’ torsion angle comparable to the indenyl complex **14**, perhaps indicating that the larger metals compensate for the steric bulk of the permethylated ligand.

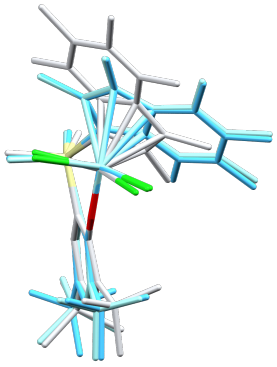

Figure 2.17 Overlayed solid-state structures of group four PHENI* complexes of titanium **2** (grey), zirconium **15** (turquoise), and hafnium **16** (blue).

2.2.6. Attempted syntheses of dinuclear complexes

Dinuclear catalysts have been proposed to facilitate dual-site catalysis, such as for the synthesis of multimodal polymer molecular weight distributions or cooperative copolymerisation.[40,41] Approaches have included polymethylene linkers between the η^5 fragments,[42] or between the silyl *ansa* bridges,[40] as well as rigid spacers.[43] Homo- and heteroleptic systems have been synthesised including heterobimetallic complexes.[40,44]

Two target complexes were identified, one utilising a Si-alkyl-Si tether analogous to the work of Lee *et al.*,[45,46] and the other incorporating a hydroquinone-derived fragment (Figure 2.18).[43,47,48] The tethered dibridge, $Cl_2Si(Me)\text{-}(CH_2)_6\text{-}(Me)SiCl_2$, was synthesised by the hydrosilylation of 1,5-hexadiene using $HSi(Me)Cl_2$ and Karstedt's Pt(0) catalyst.[45] This was then used in a synthetic procedure analogous to mononuclear PHENI* compounds. The presence of chiral centres at both silicon atoms as well as at the allylic position of the I* system in the proligand led to the production of several diastereomers and highly complex NMR spectra, which are not amenable to unambiguous assignment. The desired complex could not be isolated from the final reaction mixture. Mass spectrometry revealed a molecular ion with m/z = 765.004 (calculated target m/z = 1214.46), indicating that the targeted dinuclear species had not been formed.

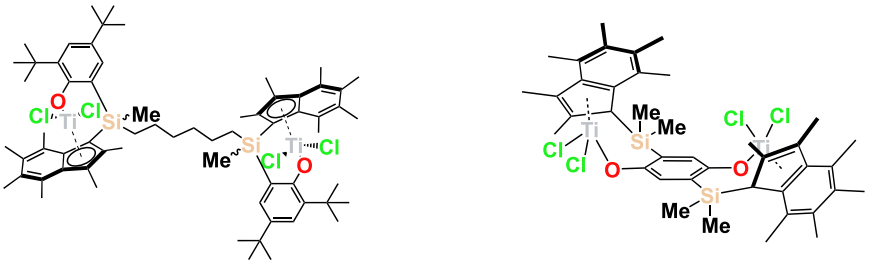

Figure 2.18 Target dinuclear PHENI* complexes.

Towards dinuclear hydroquinone-based complexes, the starting material 2,5-dibromohydroquinone was successfully converted to the allyl-protected intermediate. However, subsequent silylation of this using Me_2SiCl_2 in conditions analogous to the mononuclear PHENI* ligands proved unsuccessful, and competitive polymerisation was presumed to occur resulting in an insoluble waxy solid.

2.3. Formation of cationic reactive intermediates

The catalytically active species in group four metallocene polymerisation is proposed to be a cationic alkyl complex of the form $[[L]MMe]^+$, formed by the reaction of the precatalyst with a suitable activator. Activators such as $[Ph_3C][BAr^F_4]$ (TB; $Ar^F = C_6F_5$) or $[PhNHMe_2][BAr^F_4]$ (AB) are able to abstract an alkyl group from the metal centre, while MAO is additionally able to alkylate the precatalyst prior to abstraction (Scheme 2.7).[49,50]

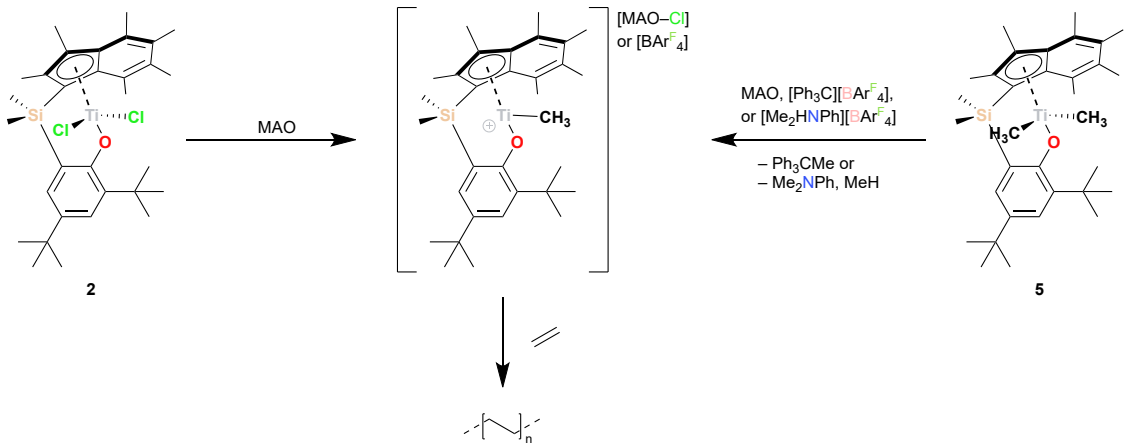

Scheme 2.7 Reaction between PHENI* complexes and catalyst activators.

To probe this reaction, and the identity and stability of the reactive intermediate, **2** and **5** were reacted separately with MAO and monitored by ^{1}H NMR spectroscopy in a range of solvents (benzene-d_6, bromobenzene-d_5, and dichloromethane-d_2). In all cases, the formation of a single PHENI* species is observed, with a resonance corresponding to the

TiC**H**$_3$ environment of the presumed complex cation. For **2**/MAO this ^{1}H resonance is seen at δ 0.17 ppm, correlating to a ^{13}C shift of δ 66 ppm in the HSQC spectrum (dichloromethane-d_2; Figure 2.19); for **5**/MAO the resonance is at δ 0.46 ppm, correlated to a ^{13}C shift of δ 55 ppm. Notably, the species formed from **2** and **5** gave resonances with different absolute chemical shifts, which suggests non-negligible interaction of the counterion with the cationic metal centre. This may have implications for catalysis, where ion-pairing of this sort is commonly found to affect activity.[51] Exposing the NMR tubes to an atmosphere of ethylene (1 bar) resulted in the instant formation of a polyethylene precipitate, demonstrating that both activated PHENI* complexes are effective catalysts for olefinic polymerisation.

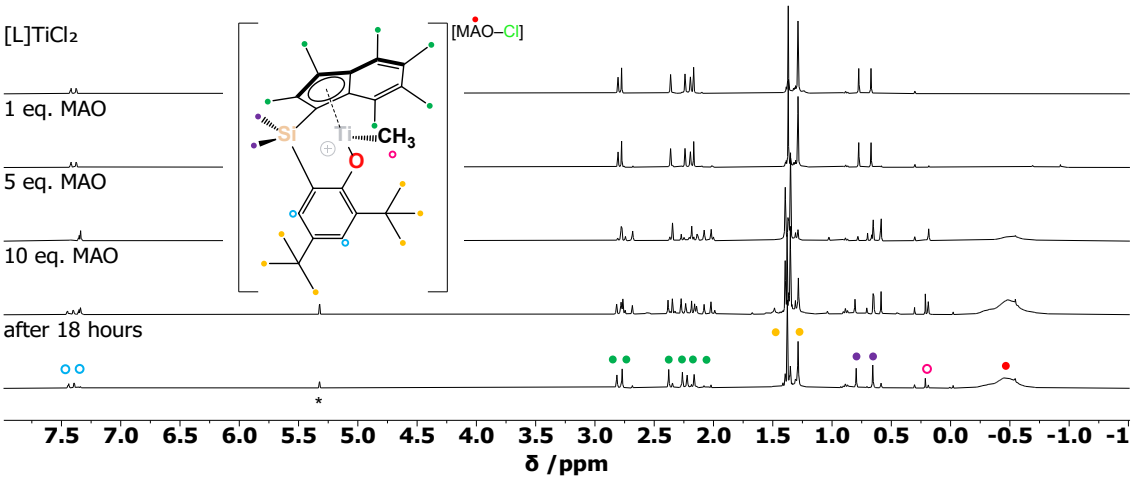

Figure 2.19 ^{1}H NMR spectra (400 MHz, dichloromethane-d_2, 298 K) of the reaction between $^{Me}{}_2$SB(^{t}Bu$_2$ArO,I*)TiCl$_2$ (**2**, [L]TiCl$_2$) and MAO. Asterisk (*) denoted residual *protio*-dichloromethane.

The PHENI* dimethyl complex **5** was also reacted with TB and AB and monitored by ^{1}H NMR spectroscopy in a range of solvents (benzene-d_6, bromobenzene-d_5, dichloromethane-d_2, pyridine-d_5, and acetonitrile-d_3).

Reactions between **5** and TB resulted in the instant formation of a dark red solution. The resulting salt was virtually insoluble in any of the non-coordinating solvents studied. The

formation of Ph_3CMe could be clearly identified by ^1H NMR spectroscopy, and the formation of a single BAr^F salt was confirmed by ^{11}B and ^{19}F NMR spectroscopy. The resonances corresponding to the PHENI* ligand were not assignable, possibly indicating a mixture of products or ligand decomposition. A peak at δ 0.21 ppm (dichloromethane-d_2) is consistent with the $[TiC\mathbf{H}_3]^+$ resonance observed from the reactions with MAO. Subsequent exposure of the NMR tubes to ethylene (1 bar) led to the instant formation of a polyethylene precipitate. It was postulated that a coordinating solvent may stabilise and solubilise the ionic salt product, however reactions between **5** and TB in pyridine-d_5 or acetonitrile-d_3 led to a mixture of products. A broad resonance at δ 0.62 ppm (acetonitrile-d_3) is tentatively assigned to the $[TiC\mathbf{H}_3]^+$ resonance, but catalyst decomposition is seen to occur in these coordinating solvents.

The reaction between **5** and AB was studied in benzene-d_6, bromobenzene-d_5, and dichloromethane-d_2. A mixture of products was obtained, indicating poor solution-phase stability of the cationic titanium complex, however the presence of $C\mathbf{H}_4$ in the NMR spectrum (δ 0.16 ppm (benzene-d_6), 0.15 ppm (bromobenzene-d_5), 0.21 ppm (dichloromethane-d_2)) is suggestive that AB is able to abstract a methyl group from **5**. The poorly coordinating BAr^F_4 anion is expected to reduce the ion pairing effect and increase catalytic activity. However, it also results in a destabilised cation relative to the more tightly bound pair in $[L_nTiMe][Cl–MAO]$.

2.3.1. Immobilisation of PHENI* complexes on sMAO

The synthesised complexes **1**–**16** were immobilised on third generation solid polymethylaluminoxane (sMAO) in a $[Al_{sMAO}]$:[M] (M = Ti, Zr, or Hf) ratio of 200:1. sMAO is a partially hydrolysed insoluble form of MAO that serves as a dual function activator and catalyst support.[52,53] The complex and sMAO were combined and swirled

in toluene at 60 °C for one hour or until the supernatant became nearly colourless. After being allowed to settle, the solution was decanted and the remaining pale orange to brown solids were dried under vacuum to yield the finished heterogenised catalysts in recovered yields of 60–96%. Only the synthesis of **10$_{sMAO}$** did not reach completion, with a significantly coloured supernatant even after an extended reaction time, presumably due to the larger size of the ODipp ligands.

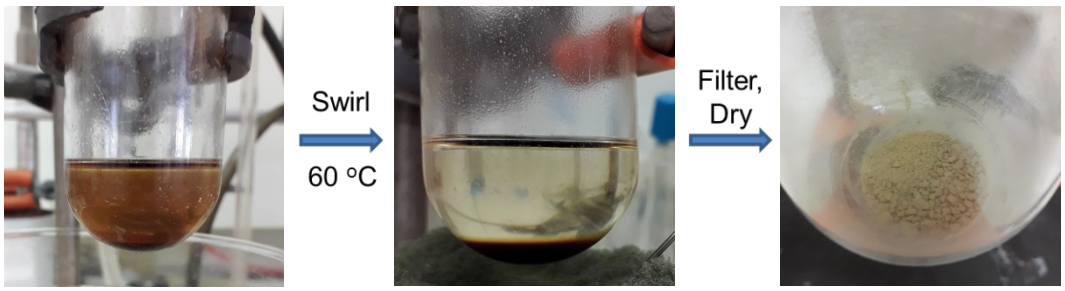

Figure 2.20 Immobilisation procedure of PHENI* complexes onto sMAO.

The supported catalysts **2$_{sMAO}$**, **5$_{sMAO}$**, and **11$_{sMAO}$** were analysed by ^{1}H, ^{13}C, ^{27}Al, and ^{29}Si solid-state NMR, and IR spectroscopy. In the ^{13}C CPMAS spectra, features corresponding to sMAO are observed as strong resonances at δ –8, and 128 ppm, respectively assigned to Al**Me** environments and those arising from the benzoic acid used to produce sMAO.[53] Resonances arising from the PHENI* ligand of the immobilised complexes are comparatively weak, but can be assigned by analogy to solution-phase spectra of the complexes.[17] The aromatic and aliphatic resonances associated with the PHENI* ligand can also be observed in the spectra of the supported complexes. ^{13}C resonances in the region δ 45–60 ppm are assigned to Ti**Me**$^{+}$, indicative of alkylation occurring upon immobilisation, and consistent with the ^{13}C shifts assigned to Ti**Me**$^{+}$ in the solution-phase reactions in Chapter 2.3 (*vide supra*). The analogous resonances for sMAO-^{Me2}SB(^{R}N,I*)TiCl$_2$ were reported at similar values around δ 50 ppm by Williams

et al..[17] In all cases a single species is observed in the ^{29}Si CPMAS ssNMR spectra at δ –13 ppm, suggesting that there is a single environment for the immobilised species. The presence of a single ^{29}Si environment was also reported for sMAO-supported zirconocnenes and titanium post-metallocenes.[17,23,24] The ^{27}Al ($I = 5/2$) ssNMR spectra show a broad envelope of resonances between 800 and –900 ppm consistent with previously reported observations and computational studies of sMAO.[53]

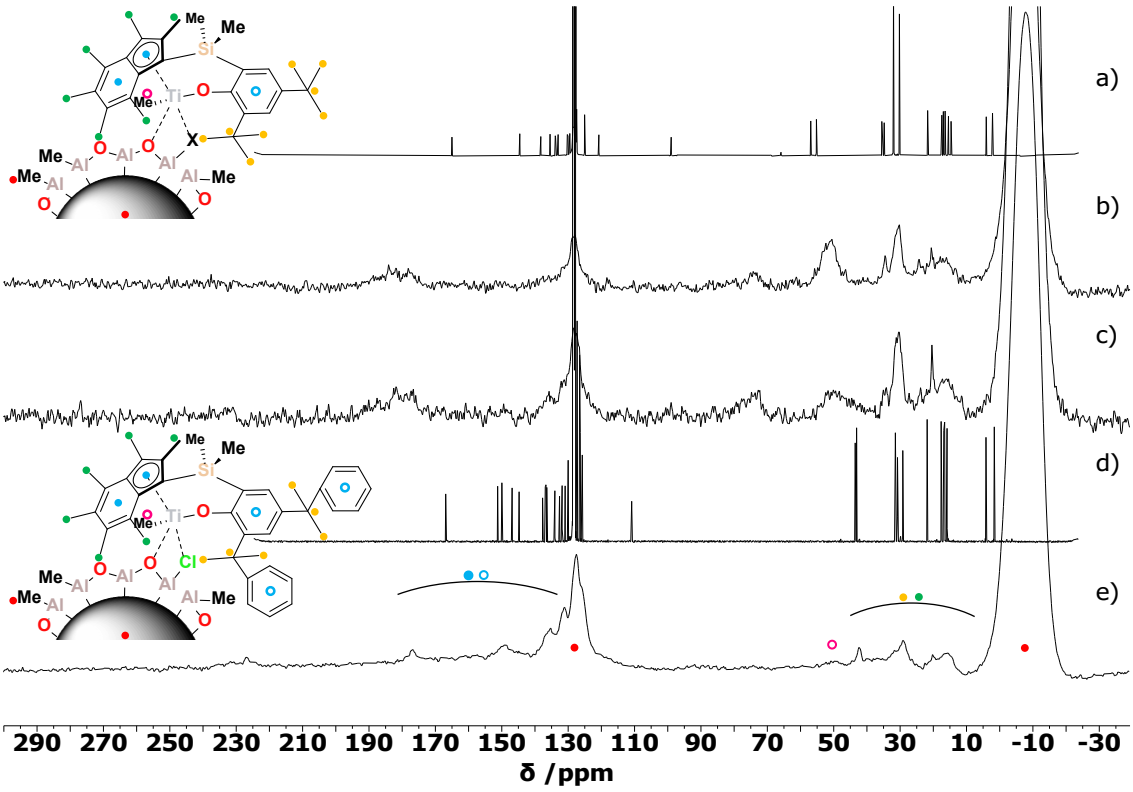

Figure 2.21 a) ^{13}C{^{1}H} NMR spectrum (126 MHz, benzene-d_6, 298 K) of **5**. b) ^{13}C CPMAS ssNMR spectrum (214 MHz, 60 kHz, 298 K) of $\mathbf{2}_{\mathbf{sMAO}}$. c) ^{13}C CPMAS ssNMR spectrum (214 MHz, 60 kHz, 298 K) of $\mathbf{5}_{\mathbf{sMAO}}$. d) ^{13}C{^{1}H} NMR spectrum (126 MHz, benzene-d_6, 298 K) of **11**. e) ^{13}C CPMAS ssNMR spectrum (101 MHz, 10 kHz, 298 K) of $\mathbf{11}_{\mathbf{sMAO}}$.

Heating $\mathbf{2}_{\mathbf{sMAO}}$ in toluene-d_8 at 60 °C for 1 hour showed no leaching of the catalyst into solution as monitored by ^{1}H NMR spectroscopy, indicative of a strongly bound and thermally stable immobilisation (Figure A.91).

2.3.2. Immobilisation of PHENI* complexes on SSMAO and LDHMAO

Silica and a layered double hydroxide (LDH) were also used as catalyst supports. Silica (PQ-ES70X) was supplied by PQ Corporation (USA) and was calcined at 600 °C for 6 h by Dr. Philip Kenyon (University of Oxford). The layered double hydroxide (LDH) was prepared by Ms. Katherine Laney (University of Oxford) and was a 1-hexanol washed $Mg_3Al–CO_3$ aqueous immiscible LDH (AIM-LDH),[54,55] and was calcined for 6 h at 150 °C prior to use. Calcination of the supports serves to remove surface and interlayer water. By varying the solvent used for AMO/AIM treatment, Hickman *et al.* found that 1-hexanol resulted in the greatest polymerisation activities with $(Cp^{Me4})_2ZrCl_2$, being ten times higher than the equivalent support treated with ethyl acetate.[54] Silica-supported MAO (SSMAO) and MAO-modified LDH (LDHMAO) were prepared by treating the silica or LDH with 40 wt% MAO in toluene at 80 °C for two hours. The PHENI* complex **2** was then immobilised analogously to sMAO, with a $[Al_{MAO}]$:[Ti] ratio of 200:1. The catalysts $\mathbf{2}_{\mathbf{SSMAO}}$ and $\mathbf{2}_{\mathbf{LDHMAO}}$ were characterised by ^{1}H, ^{13}C, ^{27}Al, and ^{29}Si solid-state NMR spectroscopy.

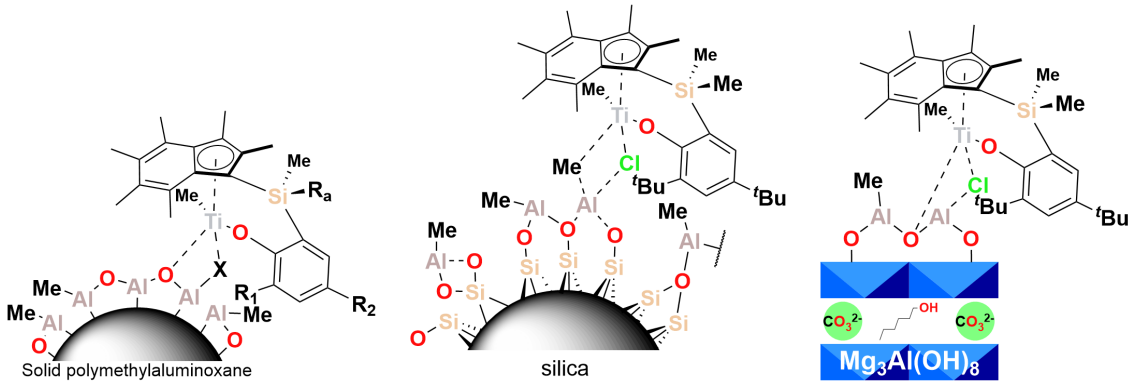

Figure 2.22 PHENI* complexes immobilised on sMAO, SSMAO, and LDHMAO.

The ^{29}Si CPMAS ssNMR spectrum of $\mathbf{2}_{\mathbf{SSMAO}}$ shows a broad resonance at δ –107 ppm from the silica support, and a resonance at δ –13 ppm corresponding to the single

environment of the *ansa* bridge of the PHENI* complex. By contrast the SSMAO-supported zirconocenes reported by Buffet *et al.* displayed several ^{29}Si environments.[23] The ^{13}C CPMAS ssNMR spectrum has a resonance at δ –10 ppm from the MAO, and weak resonances associated with the PHENI* ligand at δ 31 ppm for the aliphatic carbons and δ 128 ppm for the aromatic. A resonance at δ 50 ppm is assigned to the Ti**C**H$_3$ carbon.

There are two peaks in the ^{29}Si CPMAS ssNMR spectrum of $\mathbf{2_{LDHMAO}}$ at δ –14 and –25 ppm suggestive of there being two distinct environments of the immobilised complex. The LDHMAO-supported zirconocenes reported by Buffet *et al.* also showed several ^{29}Si environments,[23] and two ^{11}B environments were seen for LDHMAO-*rac*-(^{Ph}BBI*)ZrCl$_2$.[54] The ^{27}Al Hahn echo experiment shows a broad set of resonances corresponding to the MAO, and the ^{27}Al DPMAS experiment has two peaks at δ 67 and 8 ppm corresponding to the high-symmetry tetrahedral and octahedral environments respectively of aluminium in the LDH. In the ^{13}C CPMAS ssNMR spectrum, a peak at δ –9 ppm corresponds to MAO, and δ 164 ppm to the interlayer carbonate anions of LDH. Resonances between δ 13 and 62 ppm are attributable to the interlayer 1-hexanol, and largely obscure the aliphatic resonances of the PHENI* complex,[56] however a resonance at δ 128 ppm from the aromatic carbons of the ligand is indicative of the immobilised PHENI* complex.

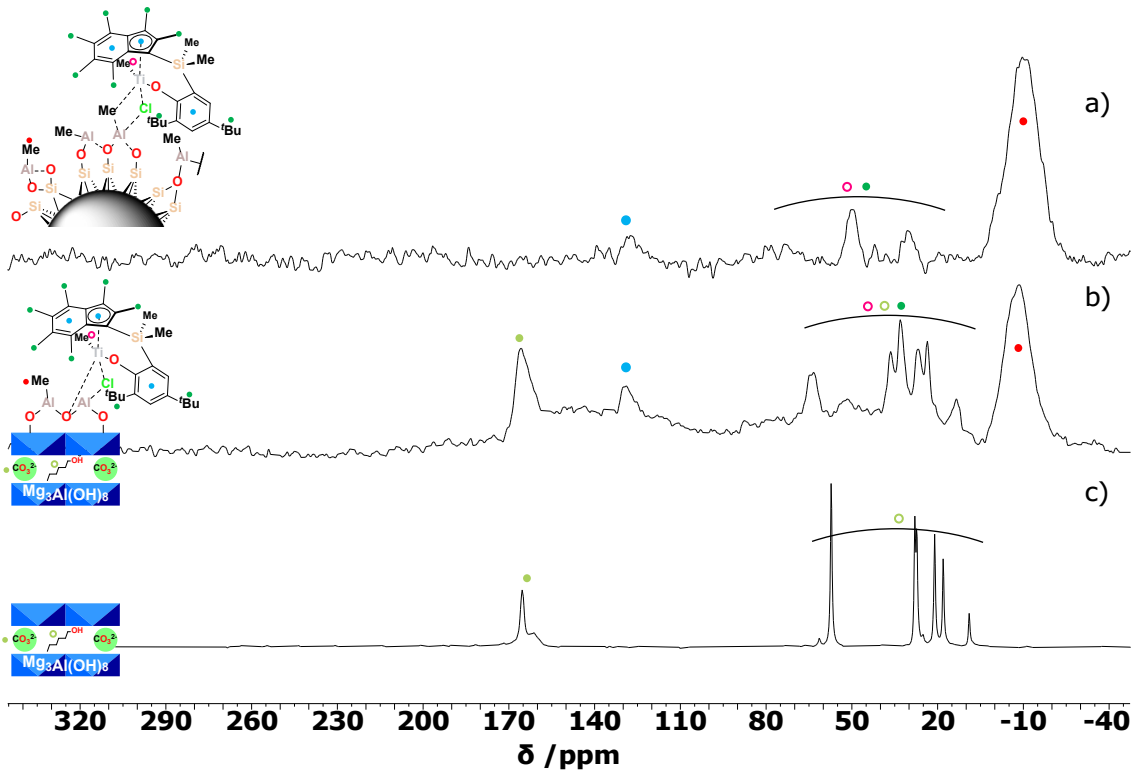

Figure 2.23 ^{13}C CPMAS ssNMR spectra (101 MHz, 10 kHz, 298 K) of a) **2**$_{SSMAO}$, b) **2**$_{LDHMAO}$, and c) Mg_3Al-CO_3-(1-hexanol) (reproduced from Hickman *et al.* with permission © 2019 Elsevier).[54]

2.4. Conclusions

Eighteen PHENI* complexes have been synthesised with a variety of phenoxide substituents, bridge substituents, ancillary ligands, and group four elements. They have been characterised by multinuclear NMR spectroscopy, elemental analysis, IR spectroscopy, and single-crystal X-ray diffraction. An efficient, scalable, and adaptable synthetic route has been developed from low-cost readily-available commodity chemicals. The influence of steric and electronic considerations on synthesis, structure, bonding, and reactivity has been discussed. For the titanium dichloride complexes, it appears that the permethylindenyl complexes adopt a distorted conformation (B-type) compared to the indenyl-PHENICS, which results in a potentially more open active site.

The complexes have been immobilised on sMAO, SSMAO, and LDHMAO to afford heterogenised catalysts which have been characterised by solid-state NMR spectroscopy and IR spectroscopy.

The reactions of PHENI* complexes with catalyst activators to form alkylated cationic complexes have been studied with MAO, TB, and AB. These active species have shown reactivity towards ethylene.

In addition to subsequent reports of PHENI* complexes of scandium, yttrium, lanthanum, lutetium, aluminium, bismuth, and tantalum,[57-60] this chapter establishes the PHENI* ligand as a versatile platform for post-metallocene organometallic chemistry, and of group four PHENI* complexes in particular as catalysts for olefin polymerisation. The remainder of this thesis concerns itself with the application of group four PHENI* complexes to the polymerisation and copolymerisation of industrially relevant olefins.

2.5. References

1 J. Okuda, *Chem. Ber.*, 1990, **123**, 1649-1651.
2 G. M. Diamond, S. Rodewald, R. F. Jordan, *Organometallics*, 1995, **14**, 5-7.
3 D. E. Herbert, U. F. J. Mayer, I. Manners, *Angew. Chem. Int. Ed.*, 2007, **46**, 5060-5081.
4 H. Braunschweig and F. M. Breitling, *Coord. Chem. Rev.*, 2006, **250**, 2691-2720.
5 F. Amor and J. Okuda, *J. Organomet. Chem.*, 1996, **520**, 245-248.
6 L. Resconi, I. Camurati, C. Grandini, M. Rinaldi, N. Mascellani, O. Traverso, *J. Organomet. Chem.*, 2002, **664**, 5-26.
7 R. E. v. H. Spence and W. E. Piers, *Organometallics*, 1995, **14**, 4617-4624.
8 F. Amor, A. Butt, K. E. du Plooy, T. P. Spaniol, J. Okuda, *Organometallics*, 1998, **17**, 5836-5849.
9 H. Katayama, M. Nabika, A. Imai, A. Miyashita, T. Watanabe, H. Johohji, Y. Oda, H. Hanaoka, *Intl. Pat.*, WO9703992A1, **1997**.
10 H. Hanaoka, T. Hino, H. Souda, K. Yanagi, Y. Oda, A. Imai, *J. Organomet. Chem.*, 2007, **692**, 4059-4066.
11 H. Hanaoka, T. Hino, M. Nabika, T. Kohno, K. Yanagi, Y. Oda, A. Imai, K. Mashima, *J. Organomet. Chem.*, 2007, **692**, 4717-4724.
12 T. Senda, H. Hanaoka, T. Hino, Y. Oda, H. Tsurugi, K. Mashima, *Macromolecules*, 2009, **42**, 8006-8009.
13 M. Nabika, H. Katayama, T. Watanabe, H. Kawamura-Kuribayashi, K. Yanagi, A. Imai, *Organometallics*, 2009, **28**, 3785-3792.
14 T. Senda, H. Hanaoka, S. Nakahara, Y. Oda, H. Tsurugi, K. Mashima, *Macromolecules*, 2010, **43**, 2299-2306.
15 T. Senda, H. Hanaoka, T. Hino, Y. Oda, H. Tsurugi, K. Mashima, *Macromolecules*, 2010, **43**, 5162-5162.

16 T. J. Williams, *Olefin polymerisation using group 4 permethylindenyl complexes*, D.Phil. Thesis, *University of Oxford*, 2020.
17 T. J. Williams, J. C. Buffet, Z. R. Turner, D. O'Hare, *Catal. Sci. Technol.*, 2018, **8**, 5454-5461.
18 T. J. Williams, J. V. Lamb, J. C. Buffet, T. Khamnaen, D. O'Hare, *RSC Adv.*, 2021, **11**, 5644-5650.
19 T. Senda, H. Hanaoka, Y. Oda, H. Tsurugi, K. Mashima, *Organometallics*, 2010, **29**, 2080-2084.
20 J. Tudor, S. Barlow, B. R. Payne, D. O'Hare, P. Nguyen, C. E. B. Evans, I. Manners, *Organometallics*, 1999, **18**, 2281-2284.
21 P. Ransom, A. Ashley, A. Thompson, D. O'Hare, *J. Organomet. Chem.*, 2009, **694**, 1059-1068.
22 J. C. Buffet, T. A. Q. Arnold, Z. R. Turner, P. Angpanitcharoen, D. O'Hare, *RSC Adv.*, 2015, **5**, 87456-87464.
23 J. C. Buffet, Z. R. Turner, D. O'Hare, *Chem. Commun.*, 2018, **54**, 10970-10973.
24 J. V. Lamb, J. C. Buffet, Z. R. Turner, D. O'Hare, *Polym. Chem.*, 2019, **10**, 1386-1398.
25 J. V. Lamb, *Unsymmetrical Group 4 Permethylindenyl Ansa-Metallocenes as Polymerisation Catalysts*, D.Phil. Thesis, *University of Oxford*, 2019.
26 M. J. Calhorda, V. Félix, L. F. Veiros, *Coord. Chem. Rev.*, 2002, **230**, 49-64.
27 D. B. Collum, *Acc. Chem. Res.*, 1992, **25**, 448-454.
28 T. A. Q. Arnold, *Group 4 indenyl complexes for ethylene polymerisation*, D.Phil. Thesis, *University of Oxford*, 2015.
29 J. Klosin, W. J. Kruper, P. N. Nickias, G. R. Roof, P. De Waele, K. A. Abboud, *Organometallics*, 2001, **20**, 2663-2665.
30 S. Feng, J. Klosin, W. J. Kruper, M. H. McAdon, D. R. Neithamer, P. N. Nickias, J. T. Patton, D. R. Wilson, K. A. Abboud, C. L. Stern, *Organometallics*, 1999, **18**, 1159-1167.
31 Y. J. Park, J. Y. Ryu, S. Hwang, K. H. Park, J. M. Lee, S. Cho, S. Lee, M. L. Saha, P. J. Stang, J. Lee, *Inorg. Chem.*, 2017, **56**, 14060-14068.
32 M. Mitani, J. I. Mohri, Y. Yoshida, J. Saito, S. Ishii, K. Tsuru, S. Matsui, R. Furuyama, T. Nakano, H. Tanaka, S. I. Kojoh, T. Matsugi, N. Kashiwa, T. Fujita, *J. Am. Chem. Soc.*, 2002, **124**, 3327-3336.
33 D. C. H. Oakes, V. C. Gibson, A. J. P. White, D. J. Williams, *Inorg. Chem.*, 2006, **45**, 3476-3477.
34 R. K. J. Bott, D. L. Hughes, M. Schormann, M. Bochmann, S. J. Lancaster, *J. Organomet. Chem.*, 2003, **665**, 135-149.
35 J. Okuda, S. Fokken, H. C. Kang, W. Massa, *Chem. Ber.*, 1995, **128**, 221-227.
36 R. Tanaka, P. Viehmann, S. Hecht, *Organometallics*, 2012, **31**, 4216-4220.
37 P. Angpanitcharoen, J. V. Lamb, J. C. Buffet, Z. R. Turner, D. O'Hare, *RSC Adv.*, 2021, **11**, 11529-11535.
38 R. Shannon, *Acta Crystallogr. A*, 1976, **32**, 751-767.
39 R. D. Shannon and C. T. Prewitt, *Acta Crystallographica Section B*, 1969, **25**, 925-946.
40 H. G. Alt, R. Ernst, I. K. Böhmer, *J. Organomet. Chem.*, 2002, **658**, 259-265.
41 S. K. Noh, J. Lee, D. H. Lee, *J. Organomet. Chem.*, 2003, **667**, 53-60.
42 S. K. Noh, W. L. Jiang, D. H. Lee, *Macromolecular Research*, 2004, **12**, 100-106.
43 S. Arévalo, M. R. Bonillo, E. de Jesús, F. J. de la Mata, J. C. Flores, R. Gómez, P. Gómez-Sal, P. Ortega, *J. Organomet. Chem.*, 2003, **681**, 228-236.
44 J. Wang, H. Li, N. Guo, L. Li, C. L. Stern, T. J. Marks, *Organometallics*, 2004, **23**, 5112-5114.
45 S. M. Bae, S. M. Jeong, J. W. Baek, H. J. Lee, H. Kim, Y. Yoon, S. C. Chung, B. Y. Lee, *Eur. Polym. J.*, 2021, **144**, 110243.
46 S. M. Jeong, J. Y. Park, Y. B. Hyun, J. W. Baek, H. Kim, Y. Yoon, S. Chung, J. Lee, B. Y. Lee, *Catalysts*, 2022, **12**, 283.
47 A. Künzel, M. Sokolow, F. Q. Liu, H. W. Roesky, M. Noltemeyer, H. G. Schmidt, I. Usón, *J. Chem. Soc., Dalton Trans.*, 1996, 913-919.
48 M. Horáček, R. Gyepes, I. Císařová, J. Kubišta, J. Pinkas, K. Mach, *J. Organomet. Chem.*, 2010, **695**, 2338-2344.
49 W. Kaminsky, *Macromol. Chem. Phys.*, 1996, **197**, 3907-3945.
50 A. Yano, S. Hasegawa, S. Yamada, A. Akimoto, *J. Mol. Catal. A Chem.*, 1999, **148**, 77-86.
51 M. C. Chen, J. A. S. Roberts, T. J. Marks, *J. Am. Chem. Soc.*, 2004, **126**, 4605-4625.
52 T. A. Q. Arnold, Z. R. Turner, J. C. Buffet, D. O'Hare, *J. Organomet. Chem.*, 2016, **822**, 85-90.
53 A. F. R. Kilpatrick, J. C. Buffet, P. Nørby, N. H. Rees, N. P. Funnell, S. Sripothongnak, D. O'Hare, *Chem. Mater.*, 2016, **28**, 7444-7450.
54 G. E. Hickman, C. M. R. Wright, A. F. R. Kilpatrick, Z. R. Turner, J. C. Buffet, D. O'Hare, *Mol. Catal.*, 2019, **468**, 139-147.
55 C. P. Chen, M. S. Yang, Q. Wang, J. C. Buffet, D. O'Hare, *J. Mater. Chem. A*, 2014, **2**, 15102-15110.

56 G. E. Hickman, *Boron-bridged Zirconocene Complexes Supported on Layered Double Hydroxides*, M.Chem. Part II Thesis, *University of Oxford*, 2018.
57 I. D. R. Stephens, *Organo-Scandium Complexes for Biodegradable Polylactide Synthesis*, M.Chem. Part II Thesis, *University of Oxford*, 2021.
58 J. Bland, *Trivalent metal indenyl complexes for lactide polymerisation*, M.Chem. Part II Thesis, *University of Oxford*, 2022.
59 A. Hawkins, *Synthesis of next-generation functional polymers: exploration of PHENI* transition metal complexes*, M.Chem. Part II Thesis, *University of Oxford*, 2022.
60 J. A. Hayden and D. O'Hare, *Unpublished work*.

Chapter 3 – Polymerisation of ethylene to *dis*UHMWPE

3.1. Introduction

Polyethylene is the most-produced polymer globally, with production overwhelmingly based on traditional Ziegler-Natta technologies.[1] Molecular metallocene and post-metallocene catalysts are employed where fine control is desired over polymer molecular weight and distribution, and the incorporation of comonomers.[2] Constrained geometry complexes (CGC) and Phenoxy-Induced Complexes of Sumitomo (PHENICS) have proved to be efficient polymerisation catalysts while enabling tunability through the steric and electronic properties of the ligands.[3-9]

Ultra-high molecular weight polyethylene (UHMWPE) is a high-value grade of polyethylene with tensile strength and impact resistance unmatched among polymers and more comparable to steel. It is chemically and abrasion resistant while also having a coefficient of friction comparable to PTFE.[10-12] This makes UHMWPE a valuable material, with applications in the biomedical,[13] maritime, aerospace,[14] and ballistics sectors.[15,16] The extremely high melt viscosity of UHMWPE renders it challenging to process, and common thermoplastic techniques such as injection moulding are impractical.[17] Processability may be improved by blending UHMWPE with a low M_w polymer having desirable rheology,[18] or by the synthesis of substantially disentangled UHMWPE, which can be processed in the solid-state below the melting point.[19]

3.1.1. Chapter synopsis

Chapter three investigates the application of group four PHENI* catalysts to the polymerisation of ethylene, in both homogeneous and heterogenised systems. The relationship between catalyst structure and polymerisation activity is studied through modifications of both the PHENI* and ancillary ligands. Polymerisation was also studied as a function of reaction conditions by varying the cocatalytic scavenger, catalyst loading, reaction scale and time, and the hydrogen response. The synthesis of UHMWPE is reported, and the material has been characterised extensively by thermal and mechanical techniques, with a particular emphasis on demonstrating a reduced entanglement density. Finally, UHMWPE was blended with more conventional polyethylene grades with the aim of combining the processability of low molecular weight PE with the mechanical properties of UHMWPE.

3.2. Homogeneous ethylene polymerisation

The PHENI* complexes ^{Me2}SB(^{tBu2}ArO,I*)TiCl$_2$ (**2**), and ^{Me2}SB(^{Cumyl2}ArO,I*)TiCl$_2$ (**11**) were initially screened for polymerisation activity in homogeneous solution-phase reactions, activated by MAO ([Al$_{MAO}$]/[Ti] = 1000), across a temperature of polymerisation (T_p) range of $30 \leq T_p \leq 90$ °C (Figure 3.2). Polymerisation runs were performed in hexanes for 5 minutes or until reactor fouling resulted in the cessation of stirring. Solution-phase polymerisation runs with **11**/MAO were performed by Mr. Adam Hawkins (University of Oxford).[20] Both complexes show high activities towards ethylene polymerisation, with **2**/MAO up to 4 220 kg$_{PE}$ mol$_{Ti}^{-1}$ h^{-1} bar^{-1} (T_p = 70 °C), and **11**/MAO up to a remarkable 23 300 kg$_{PE}$ mol$_{Ti}^{-1}$ h^{-1} bar^{-1} (T_p = 40 °C). Nabika *et al.* claimed that bulkier *ortho* substituents on PHENICS complexes resulted in increased polymerisation activities,[7] and this also appears to be the case for PHENI* catalysts. As

is commonly seen for solution-phase polymerisations, the polymer formed with a highly aggregated morphology which caused reactor fouling.[21] Reactor fouling occurred within 2 minutes for **11**/MAO due to rapid polymer formation, and runs were stopped when the mechanical stirring became hindered. This contributes to the extremely high reported activities, and also results in reduced experimental reproducibility. The activity of **11**/MAO is greater than that reported for unbridged indenyl zirconocenes (($^{2,4,6\text{-Me}_3}$Ind)$_2$ZrCl$_2$: 3 890 kg$_{PE}$ mol$_{Zr}^{-1}$ h^{-1} bar^{-1} (T_p = 50 °C, 1 bar)),[22] constrained geometry complexes (^{Me_2}SB($^{t\text{Bu}}$N,Cp*)TiMe$_2$: 114 kg$_{PE}$ mol$_{Ti}^{-1}$ h^{-1} bar^{-1} (T_p = 25 °C, 1 bar)),[23] PHENICS complexes (^{Me_2}SB($^{t\text{Bu,Me}}$ArO,Cp*)TiCl$_2$: 10 267 kg$_{PE}$ mol$_{Ti}^{-1}$ h^{-1} bar^{-1} (T_p = 40 °C, 6 bar)),[24] CGCI* complexes (^{Me_2}SB($^{t\text{Bu}}$N,I*)TiCl$_2$: 4 421 kg$_{PE}$ mol$_{Ti}^{-1}$ h^{-1} bar^{-1} (T_p = 70 °C, 2 bar)),[25] and permethylindenyl heteroleptic metallocenes (^{Me_2}SB(I*,Cp)ZrCl$_2$: 6 284 kg$_{PE}$ mol$_{Ti}^{-1}$ h^{-1} bar^{-1} (T_p = 80 °C, 2 bar)).[26] Activity is comparable to that of *rac*-(SBI*)ZrCl$_2$ (22 622 kg$_{PE}$ mol$_{Zr}^{-1}$ h^{-1} bar^{-1} (T_p = 60 °C, 2 bar),[27] and less than that of *rac*-(EBI*)ZrCl$_2$ (61 800 kg$_{PE}$ mol$_{Zr}^{-1}$ h^{-1} bar^{-1} (T_p = 70 °C, 2 bar).[28]

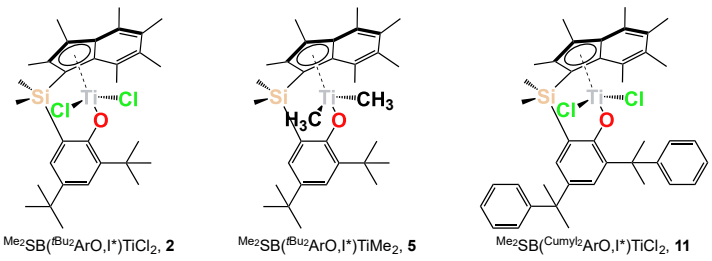

Figure 3.1 Structures of complexes used in this section.

3.2.1. Influence of cocatalyst on solution-phase polymerisation

Solution-phase polymerisations were also performed using complex **5** and the stoichiometric activator trityl borate (TB; [Ph$_3$C][BAr$^F_4$]; Ar^F = C$_6$F$_5$). Activators bearing

weakly coordinating anions such as $BAr^{F}{}_{4}^{-}$, $CN(BAr^{F}{}_{3})_{2}^{-}$, C_6F_4-1,2-$[BAr^{F}{}_{2}]_2(\mu\text{-}OAr^{F})^{-}$, or tetrakis[3,5-bis(pentafluorosulfanyl)phenyl]borate have been shown to result in extremely high polymerisation activities.[29-33] TIBA ([Al]/[Ti] = 200) was included to act as a scavenger for protic impurities. Runs with **5**/TB/TIBA ([Ti]:[TB]:[Al] = 1:1:200) were performed across a temperature range of $30 \leq T_p \leq 90$ °C. Polymerisation activities were much higher than with **2**/MAO, up to 27 000 $kg_{PE}\ mol_{Ti}^{-1}\ h^{-1}\ bar^{-1}$ (T_p = 50 °C). As with **11**/MAO, reactor fouling interfered with the mechanical stirring and runs were terminated after 26–190 s. The temperature profile of **5**/TB/TIBA is broadly similar to that of **11**/MAO, suggestive of a common rate-limiting process, likely resulting from mass-transport and morphological limitations.

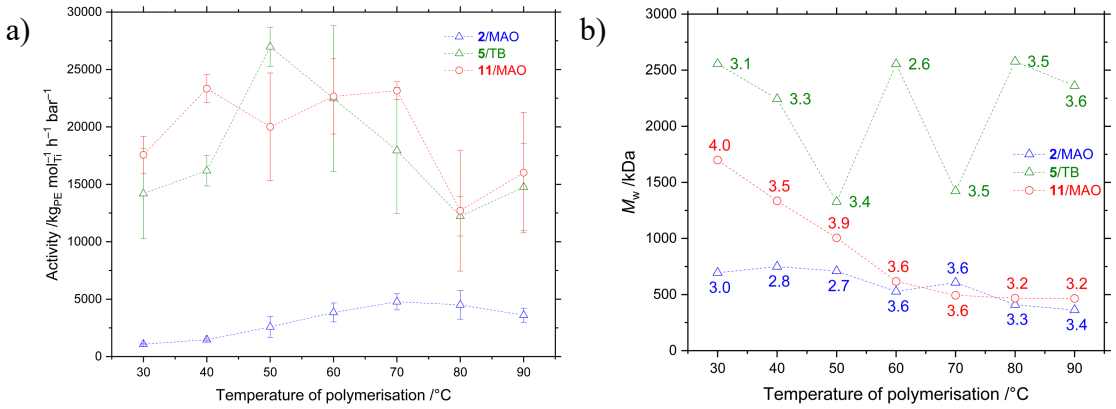

Figure 3.2 a) Solution-phase mean polymerisation activity, and b) polymer molecular weight (with PDIs annotated) as a function of temperature of polymerisation using the catalysts $^{Me_2}SB(^{tBu_2}ArO,I^*)TiCl_2$ (**2**), $^{Me_2}SB(^{tBu_2}ArO,I^*)TiMe_2$ (**5**), and $^{Me_2}SB(^{Cumyl_2}ArO,I^*)TiCl_2$ (**11**). Polymerisation conditions: 715 nmol complex, MAO ($[Al_{MAO}]/[Ti]$ = 1000) or TB/TIBA ([TB]:[TIBA]:[Ti] = 1:200:1), 2 bar ethylene, 50 mL hexanes, and 5 minutes or until stirring ceased. Error bars shown at one standard deviation.

3.2.2. Polymer characterisation

The polymers resulting from solution-phase polymerisations were analysed by differential scanning calorimetry (DSC) and gel-permeation chromatography (GPC). The polymers displayed melting transition temperatures at 141–143 °C and crystallinities of

56–66%, consistent with UHMWPE.[34] Polymer molecular weight was estimated by GPC: both **2**/MAO and **11**/MAO produced high or ultra-high molecular weight polyethylene, with **11**/MAO consistently greater than **2**/MAO: at 30 °C, **11**/MAO produced UHMWPE with a M_w of 1.7 MDa, while **2**/MAO produced PE with M_w of 690 kDa. This is greater than the M_w of polyethylene produced by homogeneous CGCI* catalysts (^{Me,Pr}SB($^{t Bu}$N,I*)TiCl$_2$: 240 kDa (T_p = 70 °C, 2 bar))[25] and reported PHENICS complexes (^{Me2}SB($^{t Bu,Me}$ArO,Cp*)TiCl$_2$: 635 kDa (T_p = 40 °C, 6 bar)), though in the latter case the presence of 1-hexene is expected to lower the molecular weight compared to a homopolymerisation.[24] Both complexes produced polymers with decreasing M_w at increasing temperatures, resulting from an increased rate of chain termination processes relative to propagation.[35] By contrast **5**/TB produced polymers with ultra-high molecular weights, up to 2.6 MDa, and largely independent of polymerisation temperature, though with a large variance resulting from irregular reaction times. Increased molecular weights with a borate activator are expected from a reduction in chain transfer to aluminium.

3.3. Slurry-phase polymerisation

Due to the morphological limitations of homogeneous solution-phase polymerisation, and resulting reactor fouling, polymerisations were attempted using heterogenised catalysts immobilised on insoluble inorganic supports: sMAO, SSMAO, and LDHMAO.

3.3.1. Variation of heterogeneous catalyst support

To investigate the effect of the support on polymerisation activity and polymer properties, the PHENI* complex ^{Me2}SB($^{t Bu2}$ArO,I*)TiCl$_2$ (**2**) was immobilised on silica-supported MAO (SSMAO), MAO-modified 1-hexanol-washed layered double hydroxide (LDHMAO) and solid polymethylaluminoxane (sMAO). Silica is commonly used as an

industrial catalyst support,[36] and LDHMAO and sMAO have been shown to be highly effective supports for olefin polymerisation.[37-39] Hickman *et al.* tested a range of AMO solvent treated LDH supports using $(Cp^{Me4})_2ZrCl_2$ and found 1-hexanol to result in higher polymerisation activities than acetone, ethanol, toluene, and ethyl acetate.[40] Polymerisation runs were performed using 10 mg of the supported catalyst, 50 mL hexanes, and 150 mg TIBA under 2 bar ethylene pressure for 30 minutes (Figure 3.3). The polymerisation activity of $\mathbf{2}_{\mathbf{sMAO}}$/TIBA is broadly similar to that of **2**/MAO (3719 $kg_{PE}\ mol_{Ti}^{-1}\ h^{-1}\ bar^{-1}$ at $T_p = 60$ °C) though much reduced compared to **5**/TB/TIBA. Williams found the polymerisation activities of CGCI* complexes to increase relative to solution-phase when supported on sMAO,[25] and the same trend was observed by Lamb for permethylindenyl metallocenes.[26] In comparison, both $\mathbf{2}_{\mathbf{LDHMAO}}$/TIBA and $\mathbf{2}_{\mathbf{SSMAO}}$/TIBA were substantially less active – 876 $kg_{PE}\ mol_{Ti}^{-1}\ h^{-1}\ bar^{-1}$ (60 °C) and 446 $kg_{PE}\ mol_{Ti}^{-1}\ h^{-1}\ bar^{-1}$ (70 °C) respectively. Both Williams and Lamb observed similar reductions in activity with systems immobilised on SSMAO and LDHMAO compared to sMAO, though in both cases activity was higher with SSMAO than LDHMAO.[25,26] All three heterogeneous PHENI* catalytic systems showed a peak in activity at 60–70 °C, though a sharper reduction in activity at higher temperatures was observed with sMAO. Buffet *et al.* reported activities of up to 1542 $kg_{PE}\ mol_{Zr}^{-1}\ h^{-1}\ bar^{-1}$ for $(EBI)ZrCl_2$ supported on the LDH support AMO-Mg_3Al-CO_3/MAO, higher than the PHENI* complex in this work, as well as demonstrating the efficacy of the LDH support with a wide scope of metallocene and non-metallocene complexes.[41]

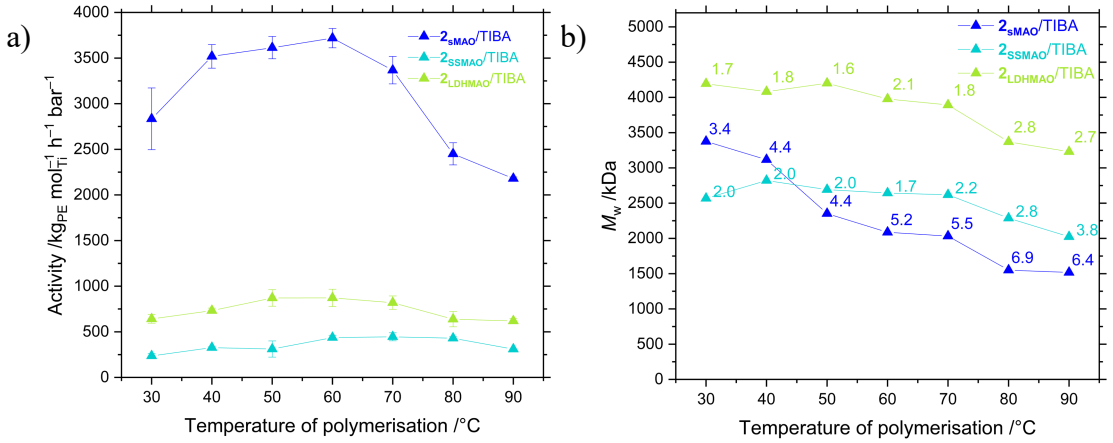

Figure 3.3 a) Slurry-phase mean polymerisation activities, and b) polymer molecular weight (M_w, PDIs annotated) as a function of temperature of polymerisation using ^{Me2}SB(^{tBu2}ArO,I*)TiCl$_2$ supported on sMAO (**2$_{sMAO}$**), SSMAO (**2$_{SSMAO}$**), and LDHMAO (**2$_{LDHMAO}$**). Polymerisation conditions: 10 mg solid catalyst, 150 mg TIBA, 50 mL hexanes, 2 bar ethylene, and 30 minutes. Error bars shown at one standard deviation.

3.3.1.1. Polymer characterisation

The morphology of polyethylene produced in slurry-phase polymerisations is well dispersed and uniform, in contrast to the substantially aggregated morphology of homogeneous polymerisations. The templating effect of the support can be seen in scanning electron microscopy (SEM) images of the polymers (Figure 3.4), with sMAO producing particles with "popcorn" morphology (diameter 30–50 μm),[42,43] silica producing spherical particles (diameter 40–260 μm), and LDHMAO producing particles with a more irregular geometry (diameter 30–210 μm). This effect arises as a result of the fragmentation of catalyst particles as polymerisation progresses.[44-46] sMAO results in a far more uniform particle size distribution (PSD; log-normal distribution;[47-50] $\mu = 3.86$, $\sigma = 0.255$; Figure 3.4e) than either SSMAO ($\mu = 4.53$, $\sigma = 0.501$) or LDHAMO ($\mu = 4.29$, $\sigma = 0.484$), which both produce some large particles. It is possible that the low polymerisation activity in these cases reduces the rate of particle fragmentation, and so decreases the observed PSD uniformity for a constant reaction time.

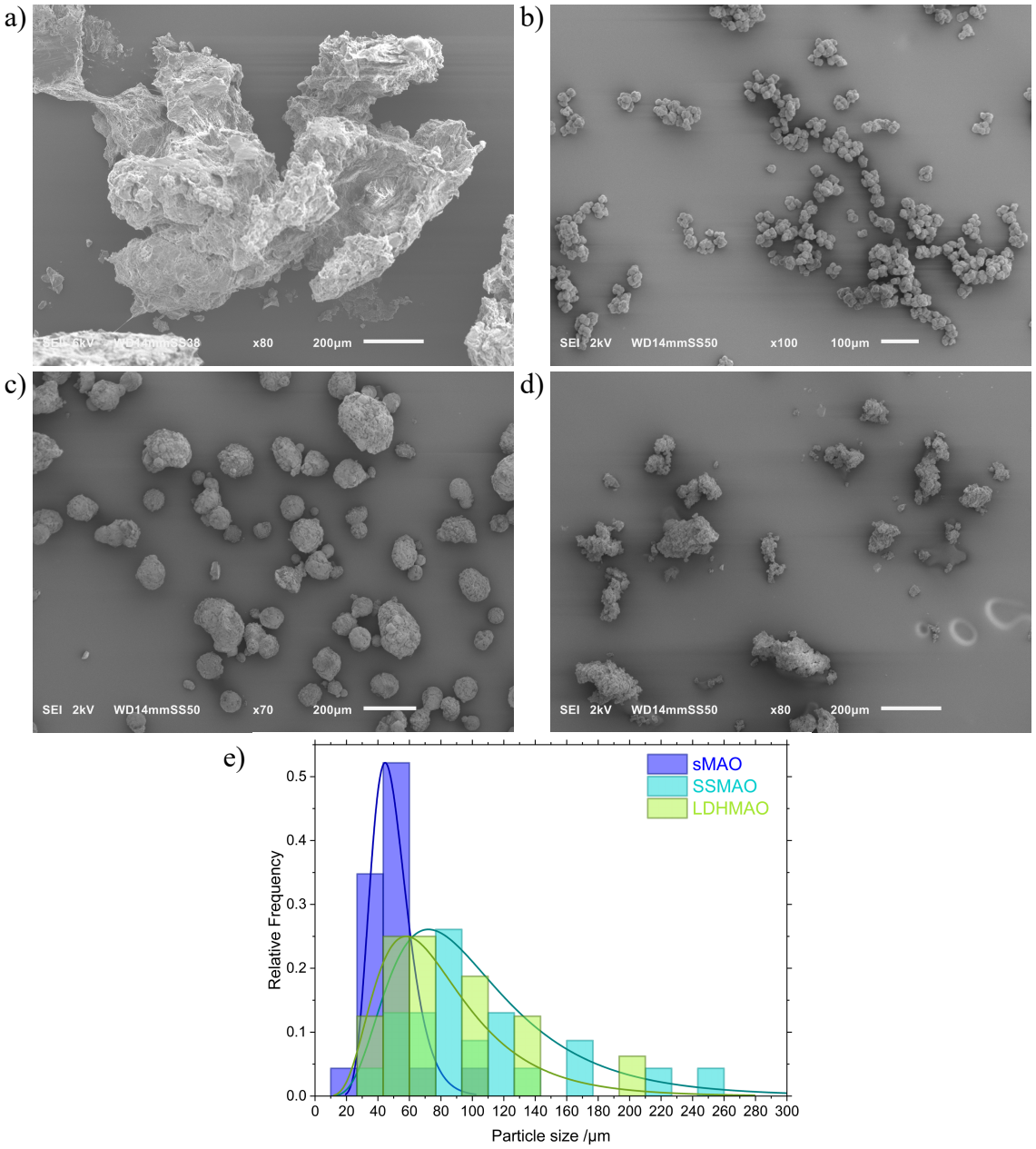

Figure 3.4 Scanning electron micrographs of polyethylene produced by a) **2**/MAO, b) $\mathbf{2}_{\mathbf{sMAO}}$/TIBA, c) $\mathbf{2}_{\mathbf{SSMAO}}$/TIBA, and d) $\mathbf{2}_{\mathbf{LDHMAO}}$/TIBA. e) Particle size distributions (PSDs) of polyethylene produced by heterogeneous supported catalysts, measured by SEM, and fitted with log-normal distributions.

Polyethylene was also studied by DSC and GPC. Polyethylene melting transitions were observed at 133–134 °C for the supported catalysts, slightly lower than for the solution-phase regime, and consistent with the formation of linear HDPE.[51] Polymer crystallinity was found to decrease in the order sMAO (78%) > SSMAO (64%) > LDHMAO (51%).

The weight-average molecular weight (M_w) of polyethylene resulting from slurry-phase polymerisations using sMAO- and SSMAO-supported complexes were roughly similar, and significantly greater than the solution-phase results using **2**/MAO, though broadly in line with the results for **5**/TB/TIBA. UHMWPE ($M_w \geq 1$ MDa) is synthesised at all temperatures studied, up to 3.4 MDa (**2**$_{\mathbf{sMAO}}$/TIBA) and 2.8 MDa (**2**$_{\mathbf{SSMAO}}$/TIBA). The catalyst supported on LDHMAO resulted in substantially greater molecular weights, up to 4.2 MDa. The presence of "free" TMA in sMAO has been shown to reduce M_w through chain transfer to aluminium.[38,52] The supports SSMAO and LDHMAO resulted in polymers with narrower dispersities than sMAO, close to the ideal Flory-Schulz value of 2.0. This is likely attributable to the lower activities in these cases. It has recently been shown that, for a series of LDH supports, polyethylene molecular weight distributions can be tuned through variations of the Lewis acidity of the support, highlighting the influence of the support on the polymerisation mechanism.[53]

3.3.2. Variation of the PHENI* ligands

To investigate the role of the post-metallocene ligand further, titanium dichloride complexes **1**, **2**, **11**–**14** (Figure 3.5) were immobilised on sMAO and investigated for slurry-phase ethylene polymerisation under conditions analogous to **2**$_{\mathbf{sMAO}}$/TIBA above (Figure 3.6).

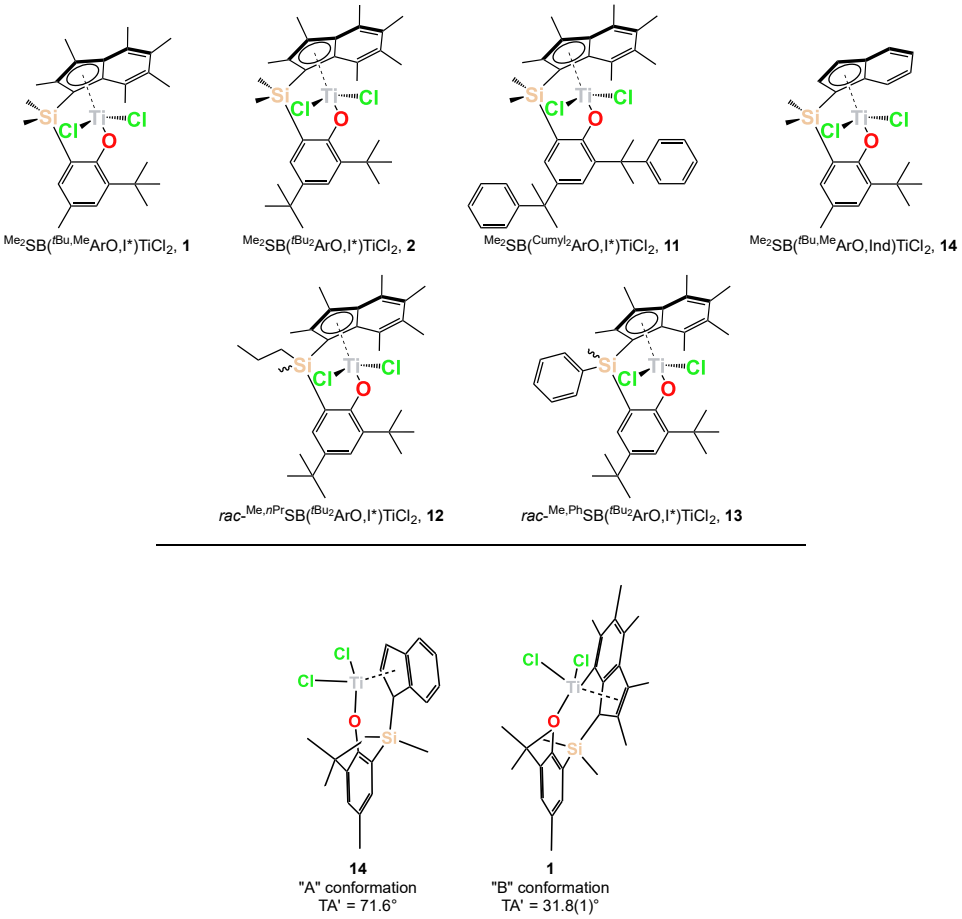

Figure 3.5 Structures of complexes used in this section, and the solid-state crystallographic conformations of complexes **14** and **1** (Chapter 2). TA' = C(10)–C(2)–O(1)–C(18).

Comparing the indenyl-PHENICS complex, $\mathbf{14}_{\mathbf{sMAO}}$/TIBA, with the permethylindenyl analogue, $\mathbf{1}_{\mathbf{sMAO}}$/TIBA, a dramatic 22-fold increase in activity is observed – at 60 °C, 3231 and 144 $kg_{PE}\ mol_{Ti}^{-1}\ h^{-1}\ bar^{-1}$ respectively. In addition to the typical kinetic and thermodynamic advantages of permethylation, increased stability, and hindered TIBA coordination, it is proposed that the dramatic increase in activity is related to the conformational geometry of the catalyst, as defined by the torsion angle, TA' (Figure 2.2, see Chapter 2 for detailed discussion) with **14** having a characteristic torsion angle, TA', of 71.6°, and **1**, **2** and **11** being in the range 32–43° (Chapter 2 *passim*). The reduced torsion angle in the B-conformation means that the I* system is oriented away from the coordination sites at the metal, thus increasing accessibility and reducing the energy

barrier for coordination-insertion. While methylation of **2** did not significantly change the TA' parameter compared to the dichloride precatalyst (Chapter 2.2.2.2), it remains unclear how the ligand geometry is affected by the formation of the cationic active species, or by immobilisation at the sMAO surface.

Contrary to the preliminary homogeneous solution-phase results, it was found that **2**$_{\mathbf{sMAO}}$/TIBA had a higher activity for ethylene polymerisation than **11**$_{\mathbf{sMAO}}$/TIBA – 3719 and 2110 $kg_{PE}\ mol_{Ti}^{-1}\ h^{-1}\ bar^{-1}$ respectively at T_p = 60 °C. It is postulated that the steric bulk of the cumyl groups interacts at the sMAO surface forcing a conformational rearrangement in the complex and hindering the coordination of monomers. This suggests a limitation of the PHENICS hypothesis that bulkier *ortho* substituents at the phenoxide resulted in increased activities.[7] For sMAO-supported CGCI* catalysts, it was shown that the electron donating ability of the amido substituents was the principal factor in controlling activity,[54] though in this case steric effects are expected to be minimised by the distal arrangement of the amido group from the metal centre. While the MePhSi mixed-bridge complex, **13**$_{\mathbf{sMAO}}$/TIBA, was found to have virtually identical activity to that of **2**$_{\mathbf{sMAO}}$/TIBA, the Me^{n}PrSi complex, **12**$_{\mathbf{sMAO}}$/TIBA, displayed slightly higher activities. This is despite **12** having an A-type solid-state conformation which has previously been correlated with decreased activity, highlighting the complex nature of structure-activity relationships in olefin polymerisation chemistry.

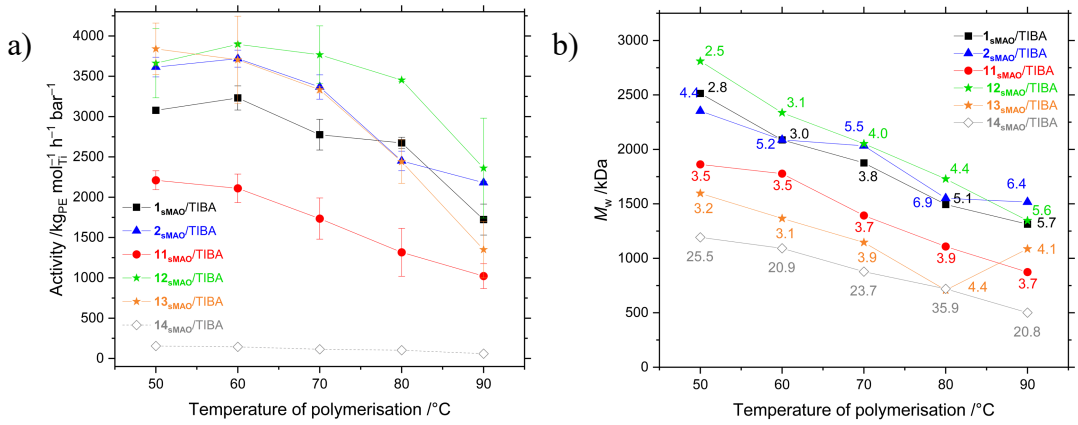

Figure 3.6 a) Slurry-phase mean polymerisation activity and b) polyethylene molecular weight (M_w, PDIs annotated) as a function of polymerisation temperature for sMAO-supported ^{Me}SB(^{tBu,Me}ArO,I*)TiCl$_2$ (**1**), ^{Me}SB(^{tBu}$_2$ArO,I*)TiCl$_2$ (**2**), ^{Me}SB(^{Cumyl}$_2$ArO,I*)TiCl$_2$ (**11**), *rac*-^{Me,nPr}SB(^{tBu}$_2$ArO,I*)TiCl$_2$ (**12**), *rac*-^{Me,Ph}SB(^{tBu}$_2$ArO,I*)TiCl$_2$ (**13**), and ^{Me}SB(^{tBu,Me}ArO,Ind)TiCl$_2$ (**14**). Polymerisation conditions: 10 mg solid catalyst, 150 mg TIBA, 2 bar ethylene, 50 mL hexanes, and 30 minutes. Error bars shown at one standard deviation.

3.3.2.1. Polymer characterisation

The resulting polyethylene was characterised by DSC and GPC. In all cases HDPE was produced with a melting point of 133–136 °C, and crystallinity of 65–78%. GPC data demonstrated that all five PHENI*-based catalysts produce UHMWPE. The molecular weight of PE produced by the PHENI* complex **1$_{sMAO}$**/TIBA was substantially greater than that by the indenyl-PHENICS analogue **14$_{sMAO}$**/TIBA as well having a much narrower dispersity. The bimodal distribution observed for **14$_{sMAO}$**/TIBA is indicative of a departure from single-site catalytic behaviour. A bimodal polymer distribution was not reported by Hanaoka *et al.* for **14**/AB/TIBA (Đ = 1.9) though only homogeneous ethylene/1-hexene copolymerisations have previously been reported.[24] The molecular weight of PE produced by **1$_{sMAO}$**/TIBA and **2$_{SMAO}$**/TIBA is similar, suggesting that substitution at the *para* position of the phenoxy group has little bearing on polymerisation kinetics. Cumyl substitution at the *ortho* position resulted in reduced molecular weights,

with the additional steric bulk seemingly unable to reduce chain transfer processes. Substitution at the silicon bridge was found to have a more significant effect on the polymer molecular weight, with the Me^{n}PrSi bridge (**12$_{sMAO}$**/TIBA; 2.3 MDa, T_p = 60 °C) producing slightly higher M_w polymer than the Me$_2$Si bridge (**2$_{sMAO}$**/TIBA; 2.1 MDa, T_p = 60 °C), and the MePhSi bridge (**13$_{sMAO}$**/TIBA; 1.4 MDa, T_p = 60 °C) significantly lower. This is evidence that the substituents at the silicon *ansa* bridge influence the kinetics of the polymerisation mechanism, altering the relative rates of termination and propagation.

3.3.3. Variation of the ancillary ligand leaving group

The influence of the ancillary ligand of the PHENI* complexes on polymerisation was studied by immobilising the complexes **2**–**10** on sMAO and testing for ethylene polymerisation activity (Figure 3.7). While all of these complexes are theorised to form the same [L]TiMe$^+$ active species, the activator counteranion has been shown to have a significant influence on polymerisation activity (Chapter 3.2.1), and the ancillary ligands have been shown to have a marked effect on complex geometry (Chapter 2).

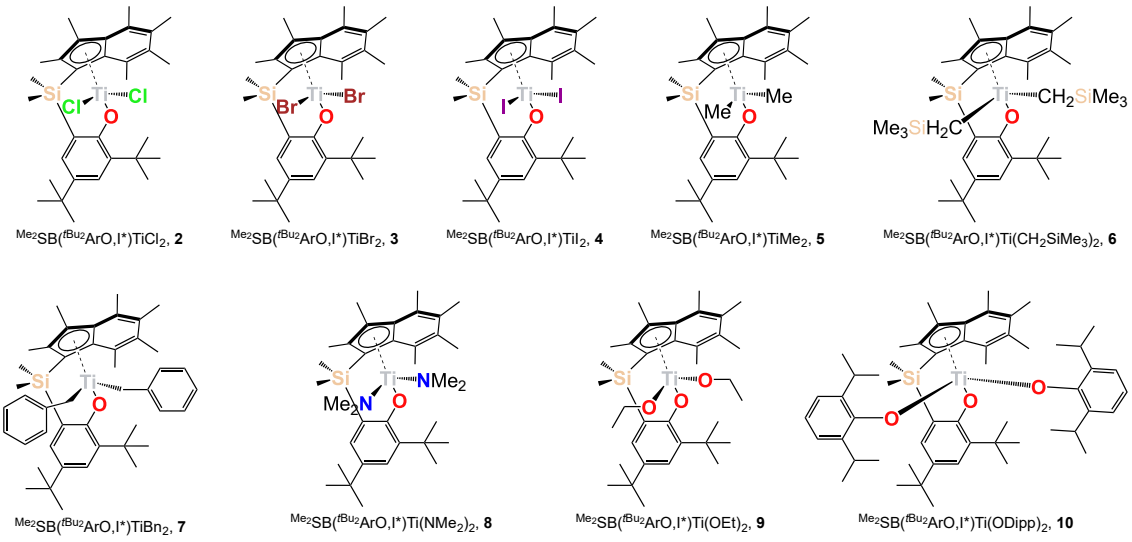

Figure 3.7 Structures of complexes used in this section.

The set of ^{Me2}SB(^{tBu2}ArO,I*)TiX$_2$ complexes tend towards mutually similar polymerisation activities at high temperatures (Figure 3.8). A particular exception to this is the ODipp complex **10**, though a confounding factor in this case was incomplete immobilisation shown by a significantly coloured supernatant even after heating at 80 °C for 3 hours with stirring. Otherwise, the chloride and bromide complexes show activities of 2180–2190 kg_{PE} mol_{Ti}^{-1} h^{-1} bar^{-1}, and the complexes $\mathbf{4_{sMAO}}$–$\mathbf{9_{sMAO}}$ show activities between 1187–1583 kg_{PE} mol_{Ti}^{-1} h^{-1} bar^{-1} at a polymerisation temperature of 90 °C. At lower polymerisation temperatures much more substantial deviations in polymerisation activities are observed, with the catalysts $\mathbf{2_{sMAO}}$–$\mathbf{9_{sMAO}}$ having activities of 1379–3614 kg_{PE} mol_{Ti}^{-1} h^{-1} bar^{-1}. It was anticipated that alkylated complexes would have increased activities relative to halide precatalysts, since halide abstraction is the first step of the initiation pathway, however the general trend halide ≳ alkyl ≳ amide ≳ alkoxide ≳ aryloxide emerges. A mixture of steric, electronic, and stability effects are likely at play: since charge separation is disfavoured in non-polar solvents, ion pairing between $[[L]TiMe]^+$ and $[sMAO–X]^-$ in a secondary coordination sphere is the most probable justification for the influence of the leaving group. Metallocenium ion pairing has been shown to be a significant factor in ethylene polymerisation, with Lewis acidity and free energy of ion pair separation correlating with catalytic activity.[55] Alkylated permethylindenyl metallocenes, supported on sMAO, have been shown to have higher ethylene polymerisation activities than the parent halide complexes.[43] However, in the current work, the methyl and neosilyl complexes demonstrated activities comparable to the iodide and less than both the bromide and chloride, with the benzyl having still lower activities. These results suggest that precatalyst activation is comparatively facile, with steric, electronic, and secondary coordination effects dominating the propagation kinetics. Ionic reassociation leads to the

formation of long-lived resting states.[56] Superimposed on the ion pair effect is the influence of the ancillary ligands on PHENI* conformation, which has been explored in detail in Chapter 2. In the slurry-phase it has been shown that the A–B conformation is a relevant controlling parameter when comparing Ind and I* titanium dichloride complexes (Chapter 3.3.2). The ancillary ligands alter the conformation of the solid-state structures, and this may be expected to have a profound effect on catalysis if the initial conformation is preserved upon immobilisation. A weak negative correlation between TA' and polymerisation activity at T_p = 60 °C suggests that this factor may be somewhat relevant, though the structure of the active, supported complexes remains elusive.

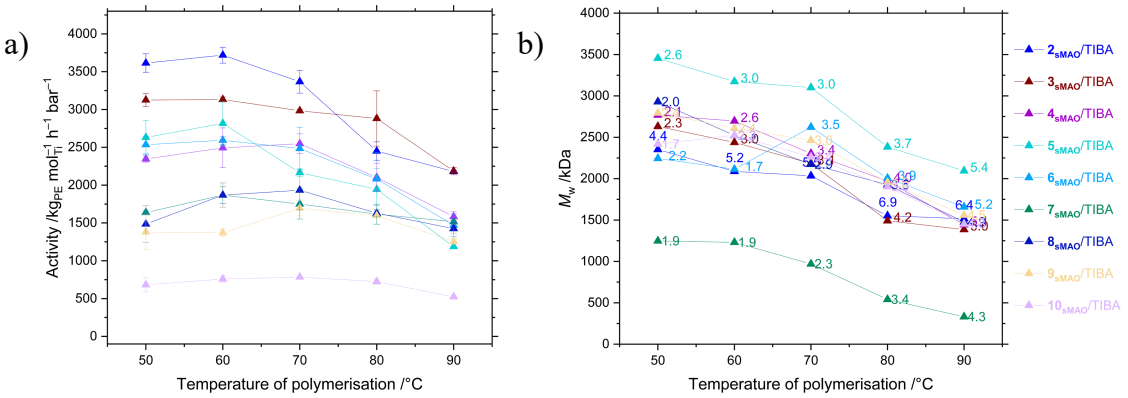

Figure 3.8 a) Slurry-phase mean ethylene polymerisation activity, and b) polymer molecular weight (M_w, PDI annotated) as a function of temperature for sMAO-supported ^{Me_2}SB($^{t Bu_2}$ArO,I*)TiCl$_2$ (**2**), ^{Me_2}SB($^{t Bu_2}$ArO,I*)TiBr$_2$ (**3**), ^{Me_2}SB($^{t Bu_2}$ArO,I*)TiI$_2$ (**4**), ^{Me_2}SB($^{t Bu_2}$ArO,I*)TiMe$_2$ (**5**), ^{Me_2}SB($^{t Bu_2}$ArO,I*)Ti(CH$_2$SiMe$_3$)$_2$ (**6**), ^{Me_2}SB($^{t Bu_2}$ArO,I*)TiBn$_2$ (**7**), ^{Me_2}SB($^{t Bu_2}$ArO,I*)Ti(NMe$_2$)$_2$ (**8**), ^{Me_2}SB($^{t Bu_2}$ArO,I*)Ti(OEt)$_2$ (**9**), ^{Me_2}SB($^{t Bu_2}$ArO,I*)Ti(ODipp)$_2$ (**10**). Polymerisation conditions: 10 mg solid catalyst, 150 mg TIBA, 2 bar ethylene, 50 mL hexanes, and 30 minutes. Error bars shown at one standard deviation.

3.3.3.1. Polymer characterisation

The polyethylene synthesised by catalysts **3$_{sMAO}$**–**10$_{sMAO}$** have been characterised by DSC and GPC. All samples showed melting transitions between 133–136 °C and

crystallinities of 58–83%, consistent with the formation of HDPE in all cases. With the exception of the dimethyl complex (**5**) and the dibenzyl complex (**7**), all of the catalysts produce PE within a narrow molecular weight envelope, spanning 2.2–2.9 MDa at T_p = 50 °C, and 1.4–1.7 MDa at T_p = 90 °C. This is to be expected from the formation of a common propagating cationic active species. Surprisingly, **5**$_{sMAO}$/TIBA produced PE with notably higher M_w (3.5 MDa at T_p = 50 °C), and **7**$_{\mathbf{sMAO}}$/TIBA with notably lower M_w (1.2 MDa at T_p = 50 °C). In all cases, PDIs are relatively narrow in the range 1.9–4.4 at T_p = 50 °C, indicative of consistent single-site catalysis. A trend towards broader MWDs at higher polymerisation temperatures is observed, with a PDI range at T_p = 90 °C of 4.3–6.4, possibly due to partial thermal degradation of the catalyst, or increased ligand flexibility.

3.3.4. Variation of the group 4 metal

The effect of the group 4 metal centre was explored by testing the titanium, zirconium, and hafnium PHENI* complexes for ethylene polymerisation (Figure 3.9). Complexes **2**, **15**, **16** were immobilised on sMAO and tested in the slurry-phase polymerisation of ethylene analogously to the other catalysts.

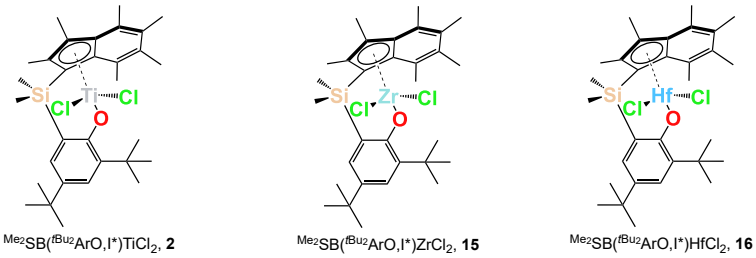

Figure 3.9 Structures of complexes used in this section.

The zirconium complex **15**$_{\mathbf{sMAO}}$/TIBA showed moderate polymerisation activity, up to 353 kg_{PE} mol_{Zr}^{-1} h^{-1} bar^{-1} at T_p = 50 °C. Polymerisation with the hafnium complex,

16$_{sMAO}$/TIBA, resulted in only trace quantities of polymer being isolated (< 20 mg) with activities of < 30 kg_{PE} mol_{Hf}^{-1} h^{-1} bar^{-1}. A similar trend was reported for PHENICS complexes by Hanaoka *et al.* with ^{Me2}SB(^{tBu,Me}ArO,Cp*)$TiCl_2$ and ^{Me2}SB(^{tBu,Me}ArO,Cp*)$ZrCl_2$ having activities of 10 267 and 533 kg mol_M^{-1} h^{-1} bar^{-1} respectively.[24] Likewise, Senda *et al.* report a series of fluorenyl PHENICS complexes with activities of 2 800, 1 033, and 200 kg mol_M^{-1} h^{-1} bar^{-1} respectively for ^{Me2}SB(^{tBu,Me}ArO,^{tBu2}Flu)$TiCl_2$, ^{Me2}SB(^{tBu,Me}ArO,^{tBu2}Flu)$ZrCl_2$, and ^{Me2}SB(^{tBu,Me}ArO,^{tBu2}Flu)$HfCl_2$.[9] In both cases, polymerisation data for PHENICS complexes were reported only for ethylene/1-hexene copolymerisation.

a)

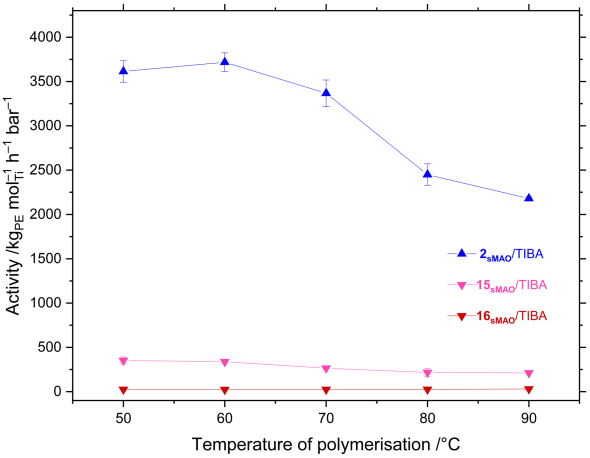

b)

T_p /°C	M_w /kDa		PDI		High M_w fraction
50	2110.8	16.2	1.9	6.0	13%
60	1303.2	12.0	3.4	3.8	20%
70	1367.3	16.3	2.7	4.6	19%
80	1193.4	14.1	3.4	3.4	21%
90	1664.4	25.4	2.0	7.9	14%

Figure 3.10 a) Mean polymerisation activity as a function of temperature of polymerisation of sMAO-supported ^{Me2}SB(^{tBu2}ArO,I*)$TiCl_2$ (**2$_{sMAO}$**/TIBA), ^{Me2}SB(^{tBu2}ArO,I*)$ZrCl_2$ (**15$_{sMAO}$**/TIBA), and ^{Me2}SB(^{tBu2}ArO,I*)$HfCl_2$ (**16$_{sMAO}$**/TIBA). b) GPC data for polyethylene produced by **15$_{sMAO}$**/TIBA. Polymerisation conditions: 10 mg solid catalyst, 150 mg TIBA, 2 bar ethylene, 50 mL hexanes, and 30 minutes. Error bars shown at one standard deviation.

Density functional theory studies *in silico* have found that the activation barrier for ethylene insertion is lower for Ti(IV) constrained geometry complexes, modelled as [^{H2}SB(^{H}N,Cp)MMe]$^+$, than either Zr(IV) or Hf(IV).[57] Similar results have also been found for metallocenic systems, $Cp_2MMe_2/B(C_6F_5)_3$, with titanocenes having lower

complexation and insertion barriers than zirconocenes or hafnocenes.[58] These trends are somewhat controversial, with claims published that both titanium-[59,60] and zirconium-based[61,62] complexes are more active for ethylene polymerisation, with counterclaims that there is little difference.[63,64] The divergence of experimental results from computed insertion energy barriers highlights the role of non-trivial reaction mechanisms and kinetics, with polymerisation activity determined by the subtle interplay of many steric, electronic, kinetic, and thermodynamic factors. In the current work, the less active catalysts, **15** and **16**, both have A-type solid-state conformations, while **2** is B-type, further providing evidence for the significance of this parameter.

3.3.4.1. Polymer characterisation

While the titanium catalyst produces UHMWPE with a narrow PDI, the zirconium catalyst **15**$_{\mathbf{sMAO}}$/TIBA produces polyethylene with a bimodal MWD with large total PDIs in the range 41.0–92.3. Peak deconvolution reveals that approximately 80% of the polymer mass is composed of low molecular weight PE ($M_w \leq 25$ kDa) with a moderately narrow PDI of 3.4–7.9. The remainder is composed of UHMWPE (M_w = 1.2–2.1 MDa) with narrow MWDs, having PDIs in the range 1.9–3.4. This is a clear departure from single-site catalysis, with at least two reaction modes active, and may in part be due the increased chain transfer to aluminium possible with the larger group four metals. No evidence was found for a bimodal copolymer M_w distribution for zirconium PHENICS complexes.[9,24] By modelling group four metallocenes *in silico*, Martínez-Araya *et al.* calculated, on the basis of energetic barriers, that titanocenes were expected to produce higher molecular weight polymer than either zirconocenes or hafnocenes.[65] For the reported PHENI* complexes it is clear that titanium gives not only dramatically higher polymerisation activity than its heavier congeners, but also better controlled single-site

reactivity. The melting temperature of 136 °C (α = 95%) is consistent with the formation of a single thermal phase of HDPE. The quantity of PE isolated from polymerisation using the hafnium catalyst **16$_{sMAO}$**/TIBA was insufficient for GPC characterisation, though the identity of the sample as HDPE was confirmed by DSC analysis, having a weak melting transition at 121 °C, slightly lower than expected possibly due to relatively high amounts of catalyst residue in the polymer resin.

3.3.5. Effect of reaction conditions

The influence of reaction conditions on polymerisation activity and polymer properties was investigated using the catalyst **2$_{sMAO}$**. In particular, the identity of the co-catalytic scavenger, the [Al]/[Ti] loading, reaction scale and time were investigated, and the hydrogen response of the catalyst was studied.

3.3.5.1. Variation of cocatalyst

Polymerisation runs were performed using **2$_{sMAO}$** and either TMA, TEA, TIBA, or MAO as cocatalytic scavenger, with the ratio [Al]/[Ti] = 1000 (Figure 3.11). Polymerisation activity was greatest with **2$_{sMAO}$**/TIBA, decreasing in the order TIBA > MAO > TMA > TEA. Activity was over 5 times greater with **2$_{sMAO}$**/TIBA than with **2$_{sMAO}$**/TEA. The formation of heterobimetallic species, [L]Ti(μ-polymeryl)(μ-R)AlR$_2$, is proposed which are both inactive for further polymerisation and more readily formed with less bulky alkyl aluminium species.[66-69] Both polymer molecular weight and dispersity were also influenced by the scavenger, with **2$_{sMAO}$**/MAO producing the highest molecular weight polymer (2.6 MDa), a greater than three-fold increase over that produced by **2$_{sMAO}$**/TEA (791 kDa). Bulkier alkyl groups suppress chain transfer to aluminium, resulting in higher molecular weights.[70,71]

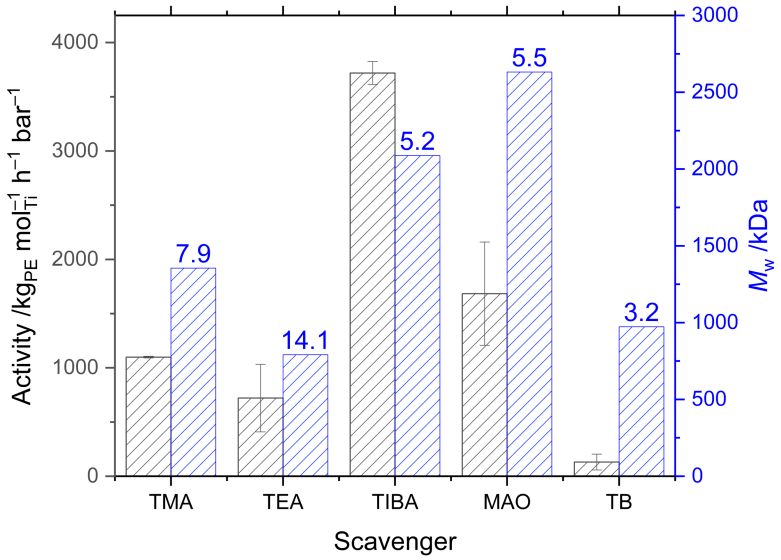

Figure 3.11 Slurry-phase mean polymerisation activity and polymer molecular weight (M_w, PDI annotated) as a function of cocatalytic scavenger using **2$_{sMAO}$**. Polymerisation conditions: 10 mg solid catalyst, TB AlR_3 or MAO ([Al]/[Ti] = 1000; R = Me, Et, ^{i}Bu; or [TB]/[Ti] = 1), 2 bar ethylene, 50 mL hexanes, 60 °C, and 30 minutes. Error bars shown at one standard deviation.

$[Ph_3C][BAr^F{}_4]$ (TB) was also used as a cocatalyst with **2$_{sMAO}$**, however low activities were observed (<400 kg$_{PE}$ mol$_{Ti}^{-1}$ h^{-1} bar^{-1}) and molecular weights of 1.0–2.3 MDa. While TB is an effective activator for solution-phase polymerisations, it functions poorly as a co-catalytic scavenger for the sMAO-supported regime.

3.3.5.2. Effect of the Al:Ti ratio

The cocatalyst loading was investigated by varying the [TIBA]/[Ti] ratio from 0–5000 (Figure 3.12). In the absence of a scavenger, moderate polymerisation activity is observed (242 kg$_{PE}$ mol$_{Ti}^{-1}$ h^{-1} bar^{-1}), highlighting the dual-function activating nature of the sMAO support. With low scavenger concentrations, trace protic impurities result in catalyst decomposition and decreased activities. Activity rapidly increases upon the addition of TIBA and is greatest at [Al$_{TIBA}$]/[Ti] = 500 (4325 kg$_{PE}$ mol$_{Ti}^{-1}$ h^{-1} bar^{-1}), reaching a plateau with the high activity maintained upon further increasing the cocatalyst loading. High activities at relatively low scavenger loadings is industrially desirable as TIBA is a

significant proportion of the cost of the catalytic system. The slight decrease at high TIBA concentrations may be attributed to the formation of an inactive titanium-aluminium heterobimetallic complex. After reaching a peak value of 2.8 MDa at [Al_{TIBA}]/[Ti] = 250, polymer molecular weight decreases with increasing cocatalyst loading as a result of increased chain transfer to aluminium.

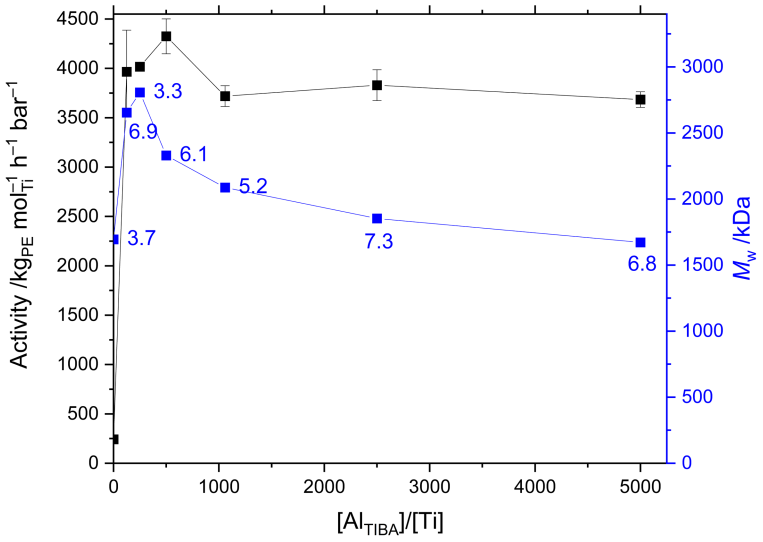

Figure 3.12 Slurry-phase mean polymerisation activity and polymer molecular weight (M_w, PDI annotated) as a function of [Al_{TIBA}]/[Ti] using **2**$_{sMAO}$. Polymerisation conditions: 10 mg solid catalyst, 2 bar ethylene, 50 mL hexanes, 60 °C, and 30 minutes. Error bars shown at one standard deviation.

3.3.5.3. Effect of reaction scale and time

Reaction scale was investigated by varying the quantity of catalyst to simulate the effects of varying reactor size (Figure 3.13). Runs were also performed in a 500 mL glass vessel containing 250 mL hexanes (Figure 3.14). In all cases the volume of TIBA scavenger added was such as to maintain a concentration of 15.1 mM (150 mg for 50 mL reactions and 750 mg for 250 mL reactions). Larger reaction scales have been shown to increase the activities of sMAO-supported zirconocenes ^{Me2}SB(I*,Cp^{R})ZrX$_2$ due to reductions in gas-liquid mass-transfer limitations.[43]

Ethylene polymerisation activity was not found to depend strongly on reaction scale (Figure 3.13), varying between 3719 $kg_{PE}\ mol_{Ti}^{-1}\ h^{-1}\ bar^{-1}$ with 10 mg (5 $mL_{solvent}\ mg_{cat.}^{-1}$) and 2779 $kg_{PE}\ mol_{Ti}^{-1}\ h^{-1}\ bar^{-1}$ with 20 mg (2.5 $mL_{solvent}\ mg_{cat.}^{-1}$). The slight decrease in activity at higher catalyst amounts (*i.e.* smaller reaction scales) may be attributed to a lower effective concentration of ethylene. With roughly constant activities, the polymer yield scaled with increasing quantities of catalyst, with up to 4 g of polymer isolated from a single run with 20 mg catalyst. The excellent morphological control afforded by the sMAO support allows for this quantity of well-dispersed polymer particles to form a free-flowing slurry without causing increased diffusional or mass-transport barriers, nor reactor fouling. Increased ethylene pressures were found to increase activity (*vide infra*, Chapter 3.3.6) showing that while the mass-transport kinetics of ethylene dissolution are not rate-limiting, the equilibrium concentration of monomer is.

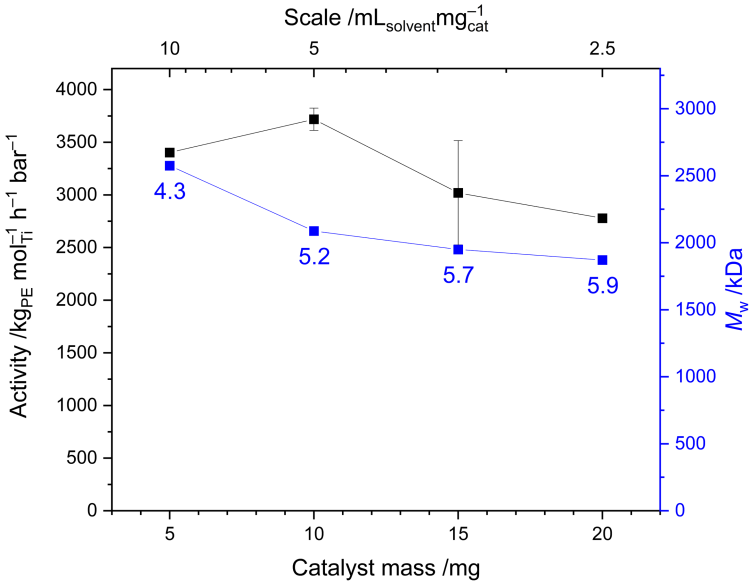

Figure 3.13 Slurry-phase mean polymerisation activity and polymer molecular weight (M_w, PDI annotated) as a function of catalyst loading (reaction scale) using **2$_{sMAO}$**. Polymerisation conditions: 150 mg TIBA, 2 bar ethylene, 50 mL hexanes, 60 °C and 30 minutes. Error bars shown at one standard deviation.

This was further investigated by performing runs for long reaction times of up to 2 hours; in this case 6.5 g polyethylene was isolated from a single run. Performing the reaction in a larger reaction vessel, on a 250 mL scale (25 $mL_{solvent}$ $mg_{cat.}^{-1}$) resulted in only a 12% increase in activity, further demonstrating the morphological efficiency of popcorn-shaped polymer particles afforded by sMAO-supported complexes.

Catalyst stability was determined through studying the polymerisations as a function of reaction time (Figure 3.14). A typical profile is seen, with very high activities observed at short reaction times – up to 6997 kg_{PE} mol_{Ti}^{-1} h^{-1} bar^{-1} at 5 minutes and the 50 mL reaction scale, and within 2% of the value recorded using the large-scale 250 mL regime. Following the initial decrease, good catalyst stability is maintained over time, decreasing 25% from 30 minutes to 1 hour (2782 kg_{PE} mol_{Ti}^{-1} h^{-1} bar^{-1}), and 21% from 1 hour to 2 hours (2188 kg_{PE} mol_{Ti}^{-1} h^{-1} bar^{-1}), attributed to catalyst deactivation.

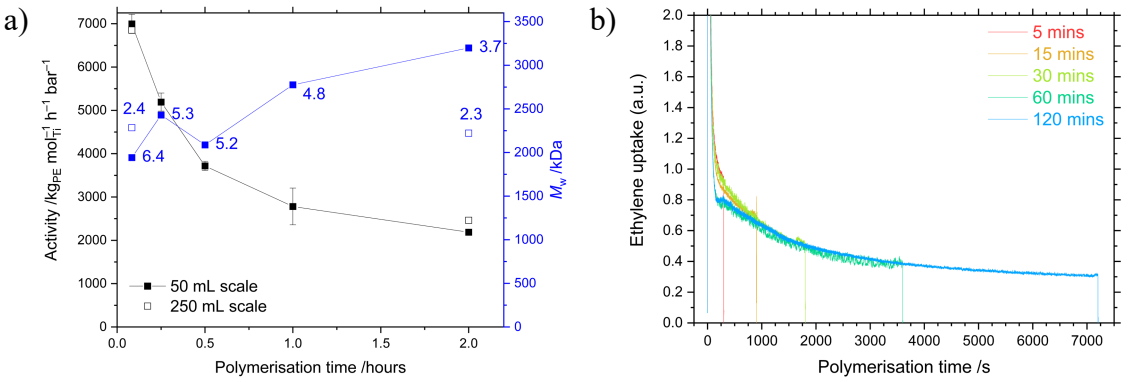

Figure 3.14 a) Slurry-phase mean polymerisation activity and polymer molecular weight (M_w, PDI annotated), and b) ethylene uptake as a function of reaction time using $\mathbf{2}_{\mathbf{sMAO}}$. Polymerisation conditions: 10 mg solid catalyst, 150 or 750 mg TIBA, 2 bar ethylene, 50 or 250 mL hexanes, and 60 °C. Error bars shown at one standard deviation.

This is mirrored in ethylene uptake plots, obtained from an inline mass-flow controller (Figure 3.14b). Following the initial pressurisation of the reaction vessel, ethylene uptake shows the same profile as polymerisation as a function of time, both reaching an

approximately steady-state plateau. This is important for industrial applications where long catalyst lifetimes are highly desirable.

Both polymer molecular weight and PDI were found to be largely independent of reaction scale, being in the range 1.9–2.6 MDa over the set of conditions studied. M_w increased slightly as a function of time, from 1.9 MDa at 5 minutes to 3.2 MDa after 2 hours. This is far from the linear relationship that would be found with a living polymerisation and is consistent with the proposed chain-growth mechanism. Living polymerisation must usually be performed using a borate activator since MAO acts as a chain transfer agent. That M_w increases with reaction time shows that $\mathbf{2}_{\mathbf{sMAO}}$/TIBA possesses some of the characteristics of living polymerisation.[72] This is in contradistinction to supported zirconocenes of the form sMAO-^{Me2}SB(I*,Cp)ZrX$_2$ where M_w was found to decrease over time.[43] The effect is likely due to the TIBA cocatalyst being consumed over time, which is also consistent with the reduction in dispersity.

3.3.5.4. Hydrogen response

The addition of molecular dihydrogen to the polymerisation system is expected to reduce the molecular weight of the polymer by acting as a chain transfer agent, promoting hydrogenation of the growing polymeryl chain and increasing the rate of chain termination relative to propagation. No reaction was observed by ^{1}H NMR spectroscopy when a benzene-d_6 solution of complex **2** was exposed to an atmosphere of hydrogen at 1 bar, even after heating at 80 °C (Figure A.25). This indicated that the ligand is not prone to hydrogenolysis, and that the catalyst is expected to be stable towards hydrogen.

Slurry-phase polymerisation was performed using $\mathbf{2}_{\mathbf{sMAO}}$/TIBA and a monomer feed consisting of ethylene/hydrogen in a ratio of 98:2 (Figure 3.15). Although the

polymerisation activity was 50–65% decreased in the presence of hydrogen, high catalytic activities are reported, up to 1765 $kg_{PE}\ mol_{Ti}^{-1}\ h^{-1}\ bar^{-1}$ at 60 °C. In addition to the slight reduction in partial pressure of ethylene, the addition of hydrogen likely leads to catalyst deactivation by the formation of a dormant hydride or bimetallic catalytic resting state.[73-78] Decreased activity in the presence of hydrogen is commonly seen for group four metallocene catalysts such as Cp_2ZrCl_2,[73,75] though calculations have suggested that ethylene insertion of the zirconocene hydride formed by hydrogenolysis ought to be kinetically facile.[79]

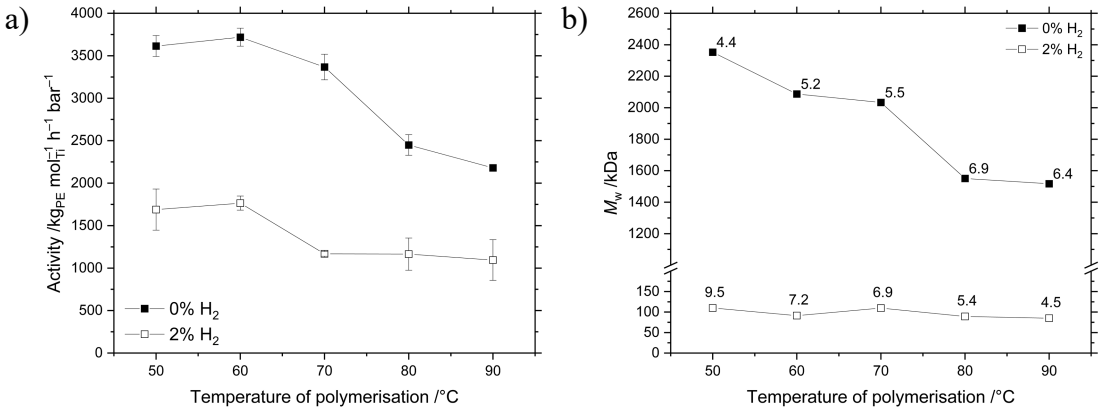

Figure 3.15 a) Slurry-phase mean ethylene polymersiation activity, and b) polymer molecular weight (M_w, PDI annotated) as a function of temperature for sMAO-^{Me_2}SB(^{tBu_2}ArO,I*)$TiCl_2$ (**2$_{sMAO}$**) in the presence of dihydrogen. Polymerisation conditions: 10 mg solid catalyst, 150 mg TIBA, 2 bar ethylene or ethylene/hydrogen (98:2), 50 mL hexanes, and 30 minutes. Error bars shown at one standard deviation.

As expected, polymer molecular weights were significantly suppressed in the presence of 2% hydrogen, decreasing by as much as 96% compared to polymerisation in the absence of hydrogen. Molecular weights in the region of 85–110 kDa are reported with dispersities in the range 4.5–9.5. The relatively lower calculated energy barrier for hydrogen insertion compared to that of ethylene is consistent with the observed large reduction in M_w at relatively low concentrations of H_2.[79] Industrially prevalent zirconocenes such as Cp_2ZrCl_2 and (EBI)$ZrCl_2$ are known to show similarly significant

hydrogen responses, though in these cases producing low molecular weight PE and PE waxes.[73,75] The CGCI* catalyst, ^{Me2}SB($^{t Bu}$N,I*)TiCl$_2$, supported on sMAO shows a stronger hydrogen response than PHENI*, with polymer molecular weights decreasing from 2.7 MDa to 41 kDa at 1.6% H_2 concentration with a 27% decrease in activity.[80]

3.3.6. High pressure high-throughput screening

Parallelised high-throughput studies were performed at Xplore s.r.l. under 120 psi (8.3 bar) ethylene in 23 mL cells containing 5 mL heptane, 10 μmol TIBA, and 0.05–0.80 mg of the precatalysts **1**$_{\mathbf{sMAO}}$, **2**$_{\mathbf{sMAO}}$, **6**$_{\mathbf{sMAO}}$, **11**$_{\mathbf{sMAO}}$, **14**$_{\mathbf{sMAO}}$, and **15**$_{\mathbf{sMAO}}$ across a temperature range of $40 \leq T_p \leq 80$ °C.[81] Contrary to the observed behaviour at 2 bar (Chapter 3.3.2), polymerisation activity was greater at 80 °C than 60 °C. This suggests that the dominating factor in the previously-observed high temperature activity decease is the reduced solubility of ethylene, rather than catalyst thermal degradation. The ligand effects are fairly consistent across the two polymerisation regimes, with **2**$_{\mathbf{sMAO}}$/TIBA displaying the highest activities at 8.3 bar, up to 6001 $kg_{PE}\ mol_{Ti}^{-1}\ h^{-1}\ bar^{-1}$ at 80 °C, more than double that reported at 2 bar pressure. The activity of **1**$_{\mathbf{sMAO}}$/TIBA at 80 °C was 3750 $kg_{PE}\ mol_{Ti}^{-1}\ h^{-1}\ bar^{-1}$, 34 times greater than for the analogous indenyl-PHENICS complex **14**$_{\mathbf{sMAO}}$/TIBA under the same conditions. Kinetic profiles are comparatively stable up to a reaction time of 1 hour (Figure 3.16c). A further catalyst, **2**$_{\mathbf{sMAO\text{-}400}}$, synthesised using a reduced complex loading of [Al$_{sMAO}$]/[Ti] = 400, was studied, and demonstrated still greater catalytic activity, up to 11 005 $kg_{PE}\ mol_{Ti}^{-1}\ h^{-1}\ bar^{-1}$ at $T_p = 80$ °C. That the per-mole activity increases with a more dilute solid catalyst suggests that there remains ample scope for further optimisations of the PHENI*/sMAO system.

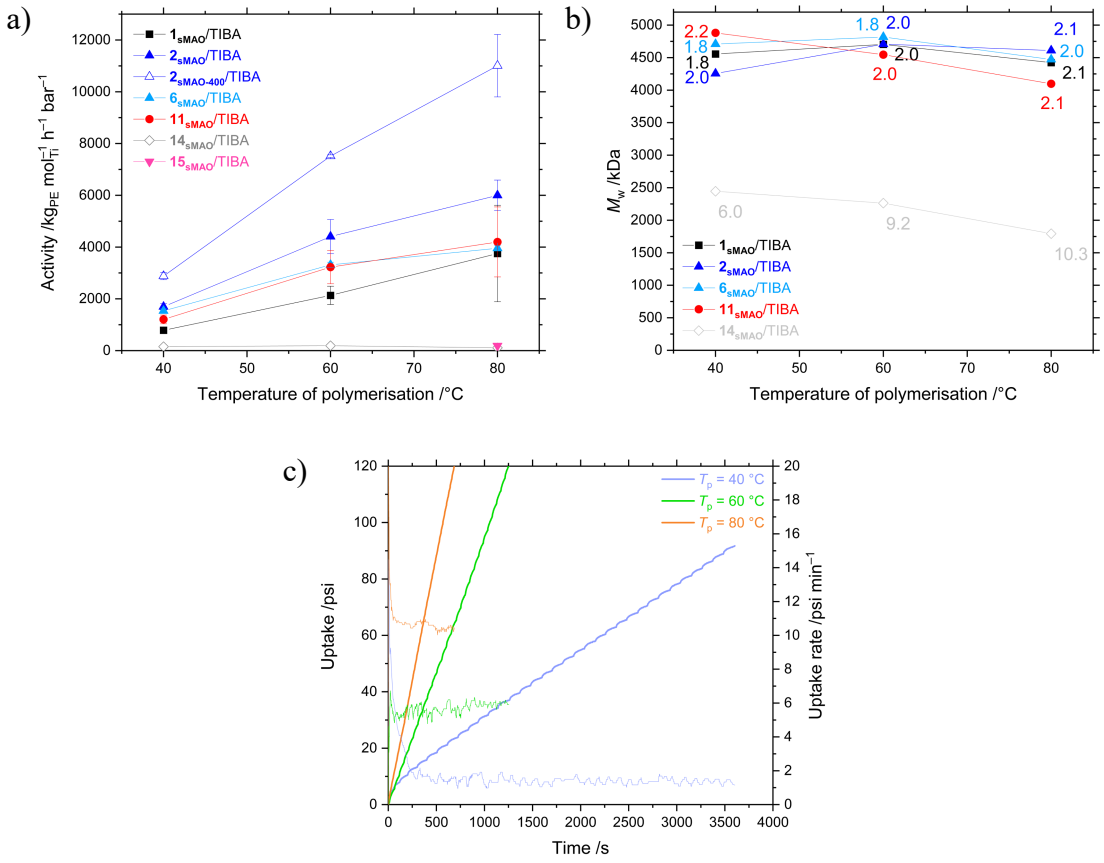

Figure 3.16 a) Slurry-phase mean polymerisation activity and b) polymer molecular weight (M_w, PDI annotated) as a function of polymerisation temperature for sMAO-supported ^{Me2}SB(^{tBu,Me}ArO,I*)TiCl$_2$ (**1**), ^{Me2}SB(^{tBu2}ArO,I*)TiCl$_2$ (**2**), ^{Me2}SB(^{tBu2}ArO,I*)Ti(CH$_2$SiMe$_3$)$_2$ (**6**), ^{Me2}SB(^{Cumyl2}ArO,I*)TiCl$_2$ (**11**), ^{Me2}SB(^{tBu,Me}ArO,Ind)TiCl$_2$ (**14**), and ^{Me2}SB(^{tBu2}ArO,I*)ZrCl$_2$ (**15**). c) Ethylene uptake profiles for **2$_{sMAO}$**/TIBA as a function of reaction time. Polymerisation conditions: 0.05–0.80 mg solid catalyst, 10 µmol TIBA, 8.3 bar ethylene, 5 mL heptane, and either 60 minutes or until 120 psi ethylene uptake. Error bars shown at one standard deviation.

In all cases, the polyethylene produced had significantly greater molecular weights, as measured by GPC, than when synthesised under 2 bar (Figure 3.16b). At a polymerisation temperature of 60 °C, the indenyl-PHENICS catalyst **14$_{sMAO}$**/TIBA produced PE with a M_w of 2.3 MDa, double that recorded at 2 bar, and with a narrower, though still poorly controlled, dispersity of 9.2. The PHENI* catalysts all produce UHMWPE in a narrow range between 4.1–4.9 MDa, approximately double that recorded at 2 bar. Remarkable temperature invariance was displayed, while also being excellently

controlled single-site catalysts, with PDIs in the range 1.8–2.2. Furthermore, very little ligand dependence is observed, with all four PHENI* catalysts producing similar PEs which indicates a common limiting factor. It is anticipated that increased ethylene pressure leads to increased rates of chain propagation and therefore high polymer molecular weights for cases where the controlling process is not chain transfer to monomer.[82-84]

The complexes were also screened for ethylene/1-hexene copolymerisation activity with 75–250 μL 1-hexene per reactor. A positive comonomer effect is observed, with activities increasing with the addition of 1-hexene, and comonomer incorporations up to 5.2 mol% are reported. Catalyst behaviour was heavily affected by physical effects – copolymers either encapsulated the catalyst granules or formed gels, and the observed kinetics were limited by mass transfer phenomena, resulting in relatively poor control. The activity of PHENI* catalysts towards the polymerisation and copolymerisation of linear α-olefins is explored further in Chapters 4 (propylene) and 5 (linear α-olefin copolymerisation).

3.4. Characterisation of UHMWPE

A large quantity of UHMWPE was synthesised using the 250 mL scale reactor and the $\mathbf{2}_{\mathbf{sMAO}}$/TIBA catalyst system at T_p = 60 °C with a reaction time of 2 hours. Several runs were combined into a single 61 g batch and used for bulk characterisation. The molecular weight was determined by high-temperature GPC to be 3.5 MDa, with a dispersity of 3.6, and an intrinsic viscosity, [η], of 20.0 dL g^{-1}.

3.4.1. Thermomechanical characterisation

Due to the high viscosity of high molecular weight polymer solutions, the estimation of M_w by GPC becomes less reliable as M_w increases.[85] Melt-phase rheology was performed

to confirm the ultra-high molecular weight, and additionally assess entanglement density (Chapter 3.4.2). The polymer was pressed into a disc, and heated to 160 °C in the rheometer, well above the T_m. A frequency sweep was performed from 10^{-3} to 10^{2} rad s^{-1}, with the viscoelastic response measured. Upon application of a shear force, the energy is partially stored elastically in the melt (storage modulus, *G*'), with the remainder lost as heat through viscous flow (loss modulus, *G*''). Taken together, this technique allows for the full characterisation of the flow behaviour of a melt, crucial for determining industrial processability, and is somewhat analogous to dynamic mechanical thermal analysis (DMTA) for a solid sample (Chapter 3.5).

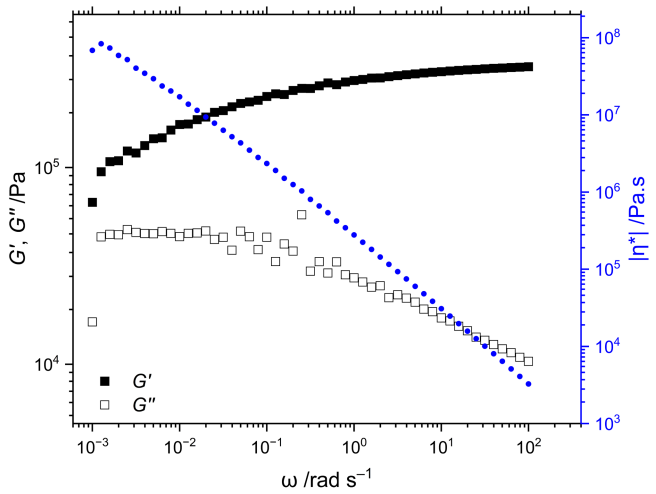

Figure 3.17 Frequency sweep rheometric curves measured at 160 °C for UHMWPE synthesised by **2**$_{sMAO}$/TIBA. Storage modulus, *G*'; loss modulus, *G*''; complex viscosity, |η*|; radial frequency, ω.

The UHMWPE melt shows an extremely high melt viscosity, |η*|, approaching 10^{8} Pa.s at low ω, but demonstrates a degree of shear-thinning, reducing below 10^{4} Pa.s at high ω. This is substantially greater than a commercial HDPE (SCG Chemicals PLC; M_w = 225 kDa; Đ = 25) which was found to have |η*| in the range 10^{4} Pa.s (10^{-2} rad s^{-1}) to 10^{3} Pa.s (10^{2} rad s^{-1}; *vide infra*), and an intrinsic viscosity [η], measured by GPC, of 2.30 dL g^{-1}. The frequency-domain crossover point of storage and loss moduli is related

to the molecular weight, with a lower crossover frequency corresponding to higher molecular weight. Using UHMWPEs with narrow dispersity, Talebi *et al.* used a "modulus model" to show that a crossover point of 10^{-3} rad s^{-1} corresponded to a polymer having a molecular weight around 3 MDa.[86] They were able to use static stress-relaxation time-domain experiments, transformed into the frequency-domain, to extend the range of measurement as low as 10^{-7} rad s^{-1} in order to determine the crossover point of UHMWPEs – a value around 10^{-5} rad s^{-1} corresponded to a polymer sample having a molecular weight around 10 MDa, despite being measured by GPC at 5.7 MDa. This highlights the limitations of GPC for the determination of extremely high molecular weights, and the advantages of rheological techniques combined with detailed physical modelling. Gote *et al.* found that a crossover point of 10^{-2} and 10^{-3} rad s^{-1} related to a polymers having M_w of 1 and 2 MDa respectively, consistent with the work of Talebi *et al.*.[87] In the current work, the rheological crossover point appears to be below 10^{-3} rad s^{-1}, and so a M_w of 3–5 MDa is plausible, within the region estimated by high-temperature GPC.

A quantity of the sample was pressed into a plate at 180 °C, from which was cut ISO type 5A test specimens. BHT was added to inhibit thermooxidative degradation.[88] Density was determined at Norner AS (Norway) according to ISO1183-1 and was found to be 930 kg m^{-3}. Tensile testing was performed according to ISO527-1/-2 (Figure 3.18). The Young's modulus was measured as 0.627 GPa, with an ultimate tensile strength of 50.9 MPa at a strain of 198%. A yield point is seen between 19.5–22.0 MPa. These values are all in the range of commercially available UHMWPEs (average values: ρ = 951 kg m^{-3}, E = 0.715 GPa, σ_B = 36.5 MPa, ε_B = 244%, σ_y = 19.3 MPa).[89]

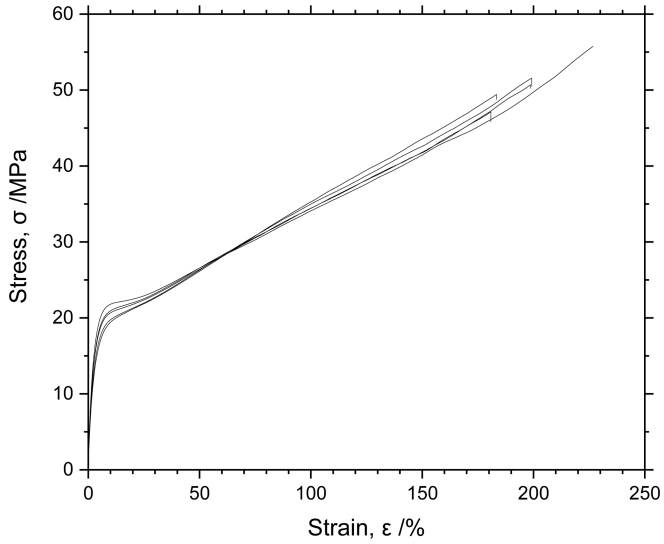

Figure 3.18 Engineering stress-strain tensile curves of UHMWPE synthesised by $\mathbf{2}_{\mathbf{sMAO}}$/TIBA.

3.4.2. Assessment of entanglement density

A key characteristic of UHMWPE is the entanglement density. "Disentangled" UHMWPE (*dis*UHMWPE), has an entanglement density sufficiently low to allow processing in the solid state below T_m, thus overcoming many of the processability challenges that result from the extremely high intrinsic viscosity.[19,90-94] *dis*UHMWPE can be produced from the controlled crystallisation of dilute polymer solutions,[95] directly from some single-site catalysts,[16,96,97] or by heterogeneous catalysts at low polymerisation temperatures.[92,98-100] The entangled state is the entropically driven thermodynamically favoured state, and thus *dis*UHMWPE, heated well above its T_m, reverts to an entangled state.[101] Observing the formation of the entangled state is therefore direct evidence for nascent disentanglement in the sample.

Time-domain rheometry was used to probe the entanglement density. Under a shear force, more energy can be stored in an entangled polymer than disentangled by virtue of the entanglements acting as physical crosslinks with elastic properties. Since the equilibrium entangled state therefore has a higher storage modulus, G', than the nascent

disentangled state, the build-up of storage modulus over time has been shown to correlate with the degree of entanglement.[102,103] The sample of UHMWPE synthesised by **2$_{sMAO}$**/TIBA shows *G*' increasing over a long timescale, having not reached a completely flat plateau even after 10^5 s (27 hours; Figure 3.19). This compares against the commercial ZN UHMWPE (entangled; M_w = 4.5 MDa, Đ = 31) studied by Liu *et al.* which reaches a plateau of 1.45 MPa after approximately 5 minutes, having had an initial *G*' value of 1.40 MPa, in contradistinction to their *dis*UHMWPE (M_w = 4.8 MDa, Đ = 3.1) which increased from an initial value of 0.65 MPa to reach a plateau at 1.9 MPa after 18 hours.[101] In the current work, the particularly low initial *G*' of 0.14 MPa, and the increase observed over very long timescales is strong evidence for a significant degree of disentanglement in the nascent polymer produced by the PHENI* catalyst.

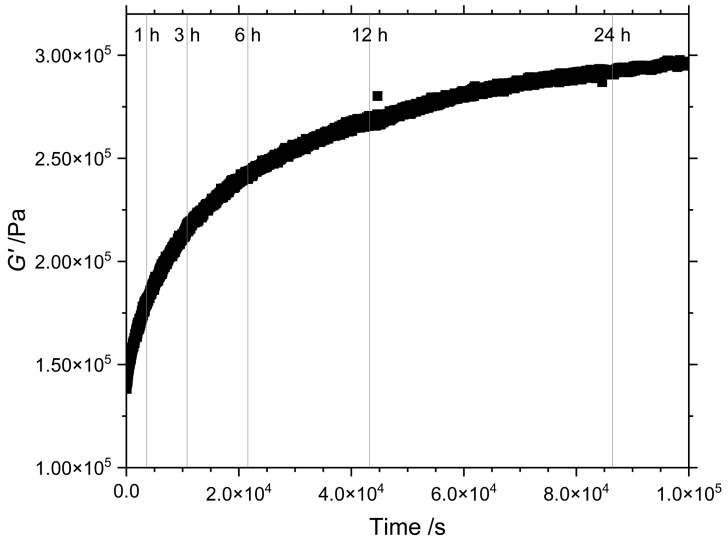

Figure 3.19 Time sweep rheometric curve, measured at 160 °C, of UHMWPE synthesised by **2$_{sMAO}$**/TIBA. The build-up of storage modulus over time is evidence for nascent disentanglement.

A DSC annealing protocol was also employed to demonstrate the formation of entanglements in a sample of *dis*UHMWPE, in a method established by Romano *et al.*.[16,19,104] In this method, polymer samples are annealed below the melting temperature

which causes melting by sequential chain detachment from the surface of the crystalline lamellae.[105] Upon cooling, these chains form entangled melt-crystallised regions, with a T_m ~ 135 °C, while the remaining nascent crystals have a T_m ~ 141 °C, these can be distinguished in a subsequent DSC heating cycle (Figure 3.20). Disentangled UHMWPE is characterised by a low T_m peak (~ 135 °C) growing as a function of annealing time at the expense of the high T_m peak (~141 °C).

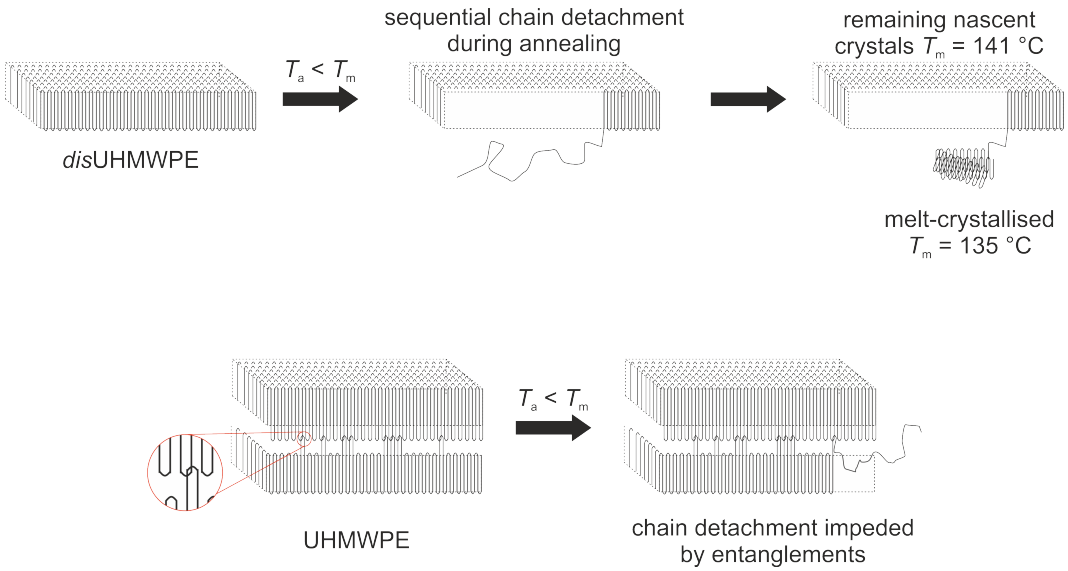

Figure 3.20 Schematic diagram depicting sequential chain detachment during annealing at $T_a < T_m$.

Entanglement density is ultimately controlled by the rate of polymer crystallisation in relation to formation and is expected to vary with polymerisation temperature.[106] UHMWPE samples synthesised by **2**$_{\mathbf{sMAO}}$/TIBA, **2**$_{\mathbf{SSMAO}}$/TIBA, and **2**$_{\mathbf{LDHMAO}}$/TIBA at a range of temperatures were analysed by DSC annealing (T_a = 135 °C). For samples of a given molecular weight, the faster the increase in normalised area as a function of annealing time, the more disentangled the polymer.[19] Notwithstanding the anticipated M_w dependence, it is clear the UHMWPE synthesised by sMAO-supported catalysts is substantially disentangled, with 82% and 96% melting after annealing for just 30 minutes (T_p = 30 and 60 °C respectively). Despite having only slightly higher M_w, the samples

synthesised by SSMAO- and LDHMAO-supported complexes show drastically impeded melting kinetics, reaching 53–87% melting after 24 hours of annealing.

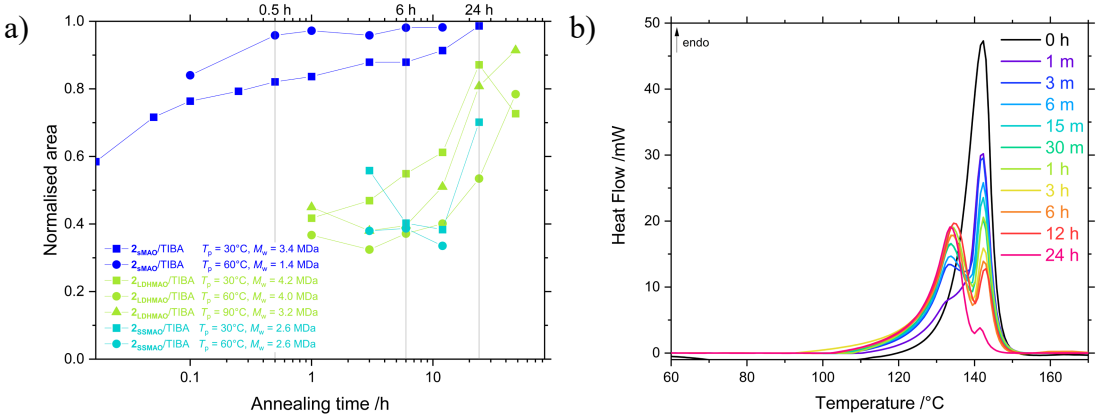

Figure 3.21 a) Evolution of the area ratio $T_{m,135}/T_{m,141}$, and b) differential scanning thermograms of *dis*UHMWPE synthesised by **2$_{sMAO}$**/TIBA at T_p = 30 °C as a function of annealing time.

The rationale for the dependence of entanglement density on support is somewhat unclear, since less active catalysts – having a higher rate of crystallisation relative to polymerisation – might be expected to produce less entangled polymer. The observed phenomenon may relate to the fragmentation or pore structure of the supports and therefore distribution of active sites within the catalyst particles, with spatial separation of the growing polymer chains reducing the tendency to form entanglements.[107]

3.5. Polyethylene–polyethylene blends

The extremely high melt viscosity of UHMWPE (Chapter 3.4.1) limits its processability and restricts applications such as injection moulding. In addition to the study of entanglements, this motivates the exploration of polymer blends, using a lower molecular weight PE – to improve the melt flow index (MFI) – blended with UHMWPE to confer high-performance properties such as tensile strength and impact resistance. One important aspect of this is polyethylene-polyethylene miscibility, which has been the

subject of extensive study, with somewhat contradictory conclusions. Chen *et al.* found inconsistencies between thermal and rheological measurements, and concluded that UHMWPE was miscible with LDPE but with neither HDPE nor LLDPE.[108,109] By contrast, Kyu *et al.* concluded that UHMWPE is miscible with HDPE, LDPE, and LLDPE in the melt but that only HDPE and LLDPE were able to co-crystallise with UHMWPE in the solid state.[110] It has been found that the branching content of polyethylenes is a major factor in determining miscibility.[111,112] Moreover, Tao *et al.* have recently showed that entanglement density greatly influenced the microstructure and mechanical properties of UHMWPE/HDPE blends, with the improved chain diffusion of weakly entangled UHMWPE conferring preferable reinforcing properties.[113] To explore this further, UHMWPE synthesised by a PHENI* catalyst was microcompounded with either a commercial LDPE (Sigma Aldrich; M_w = 89 kDa; Đ = 8.5; MFI = 25 g/10 min (190 °C, 2.16 kg)), or HDPE (SCG Chemicals PLC; M_w = 225 kDa; Đ = 25; MFI = 15.7 g/10 min (190 °C, 2.16 kg)) and extruded into ribbons (Table 3.1). In both cases, up to 30 wt% UHMWPE could be achieved. Samples were prepared at 10, 15, 20, and 30 wt% loadings of UHMWPE in either LDPE or HDPE.

Table 3.1 Polyethylene-polyethylene blends prepared by microcompounding UHMWPE with either LDPE or HDPE.

	LDPE		HDPE	
UHMWPE	Thickness /μm	Image	Thickness /μm	Image
0 wt%	50–150	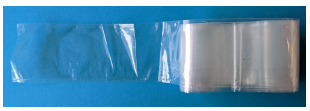	60–180	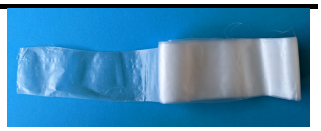
10 wt%	150–300		250–500	
15 wt%	100–400		80–250	
20 wt%	250–500		150–400	
30 wt%	300–550	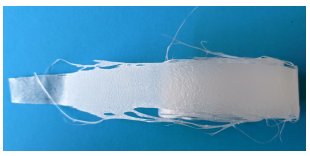	150–190	

3.5.1. LDPE/UHMWPE polymer blends

It was immediately obvious from visual inspection of the LDPE/UHMWPE blends that significant macroscopic phase separation had occurred – particles of UHMWPE were visible embedded within the LDPE matrix resulting in a grainy texture.

The presence of two distinct thermal phases was observed clearly by DSC (Figure 3.22a). The pure LDPE had a melting transition at 110 °C, and the LDPE/UHMWPE blends showed two transitions, one corresponding to LDPE and the other to UHMWPE at 131 °C. The high melting point peak grew relative to the low melting peak as the proportion of UHMWPE increased in the blends.

Rheological characterisation of the melts (Figure 3.22c), shows that the complex viscosity, |η*|, of LDPE/UHMWPE blends is at least two orders of magnitude less than the pure UHMWPE. The viscosity curves are intermediate between that of the pure materials, in accordance with the law of mixtures. This demonstrates that the processability advantages of the high MFI LDPE are maintained to an extent in the LDPE/UHMWPE blends.

The solid-state viscoelastic properties of the LDPE/UHMWPE blends were studied by DMTA across a temperature range of –100 to +120 °C (Figure 3.22d). Two distinct β relaxation processes are observed with maxima in tan(δ) around –13 and 62 °C relating to the chain mobility of distinct thermal phases. The transition at –13 °C corresponds to chain mobility of the LDPE phase, while the transition at 62 °C, which is not present in LDPE0 (0 wt% UHMWPE), corresponds to the UHMWPE phase. The low-temperature subglass transition is coincident with the limit of the rubbery plateau, with flow-like behaviour emerging at increased temperatures, as the LDPE chains become mobile.

The mechanical properties of the LDPE/UHMWPE blends were investigated in the solid state by tensile analysis (Figure 3.22b). Pure LDPE had a Young's modulus of 140 MPa, which decreased upon the addition of UHMWPE to 87.8 MPa for LDPE15 (15 wt% UHMWPE). In addition to the reduction in stiffness, the blends became more brittle than either of the pure polymers, with the fracture strain decreasing from 139% (LDPE0) to 53.7% (LDPE15). Moreover, the tensile strength of the blends also decreased from 16.8 MPa (LDPE0) to 12.5 MPa (LDPE30). The reduction in stiffness, ductility, and strength with increasing UHMWPE content is a result of the poor PE-PE miscibility and consequent phase separation.

Despite good melt-flow properties and processability, the poor LDPE-UHMWPE miscibility means that the advantageous mechanical properties of UHMWPE are not conferred upon LDPE blends.

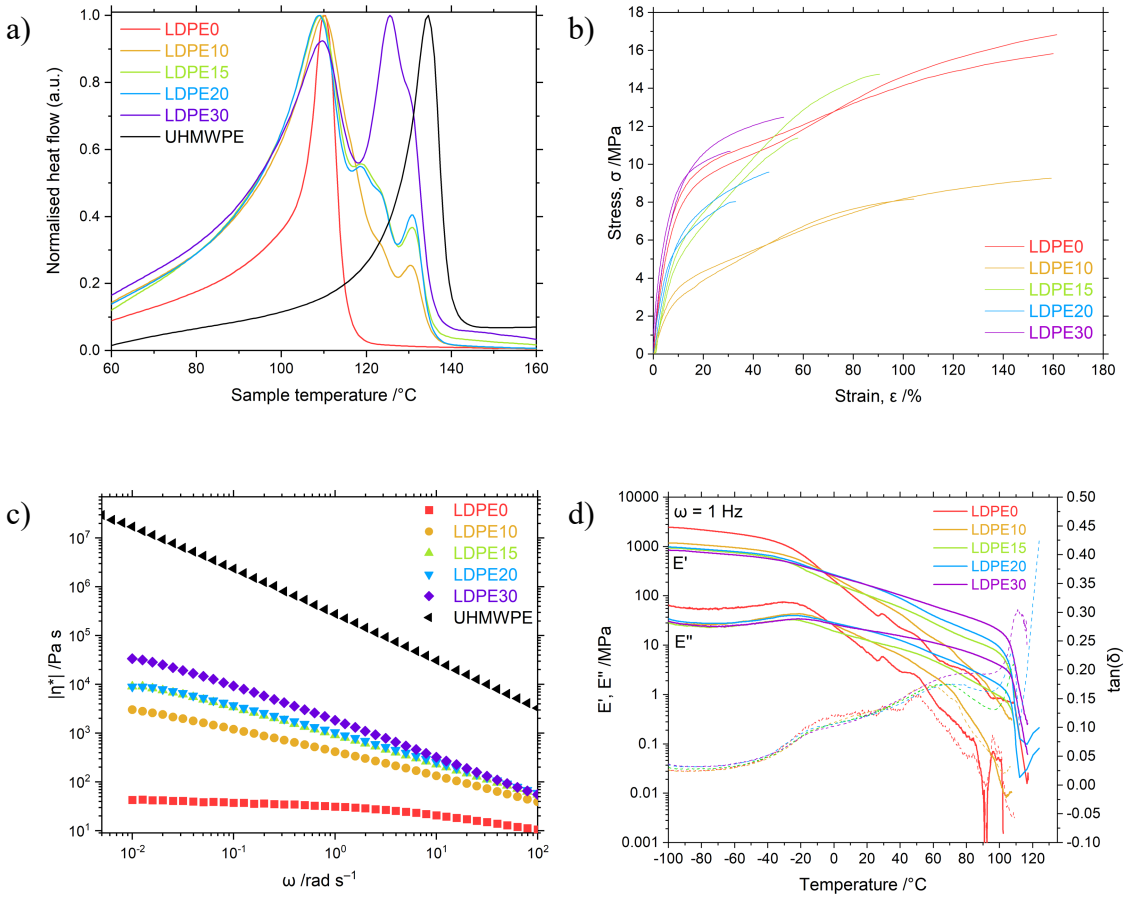

Figure 3.22 a) DSC thermograms, b) engineering stress-strain curves, c) rheological frequency sweep, and d) DMTA of LDPE/HMWPE blends across a composition range of 0–30 wt% UHMWPE.

3.5.2. HDPE/UHMWPE polymer blend

In contrast to the LDPE/UHMWPE blends, those based on an HDPE matrix appeared, at least superficially, homogeneous. A single thermal phase is observed by DSC, with the HDPE/UHMWPE blends having melting transition temperatures intermediate between that of the pure polymers, fulfilling the rule of mixtures (Figure 3.23a). This is evidence for good PE-PE miscibility between the two molecular weight grades.

The melt flow properties were studied by rheometry (Figure 3.23c). A less drastic reduction in complex viscosity was observed with HDPE than LDPE, as a result of the higher molecular weight and lower MFI. At high shear rates, the complex viscosities of all of the HDPE/UHMWPE samples converged. However, at lower shear rates, the viscosity of HDPE30 is up to three orders of magnitude lower compared to UHMWPE.

The solid-state viscoelastic properties of the HDPE/UHMWPE blends were studied by DMTA across a temperature range of –100 to +120 °C (Figure 3.23d). The formation of a fully miscible single thermal phase is confirmed by the presence of a single β transition. The HDPE0 transition is observed at 80 °C, while the β transition of the HDPE/UHMWPE blends appears instead at 100 °C. A slight maxima in tan(δ) at –60 °C for HDPE30 may indicate a deviation from ideal mixing at higher UHMWPE loadings. The rubbery plateau is maintained until 10 °C after which a smooth transition to flow-like behaviour is observed.

The mechanical properties of HDPE/UHMWPE blends are improved relative to HDPE0 (Figure 3.23b), with the Young's modulus increasing 71% from 425 to 726 MPa (HDPE0 and HDPE30 respectively), and the tensile strength increasing 103% from 25.6 to 51.9 MPa (HDPE0 and HDPE30 respectively). The increase in strength and stiffness came at the expense of ductility however, with the strain at break decreasing from 171% to 12%.

The significantly improved melt processability of HDPE/UHMWPE compared to pure UHMWPE, and the synergistic increase of strength, stiffness, and brittleness as a function of UHMWPE content shows that the desirable properties of both polymer components are maintained in the blend.

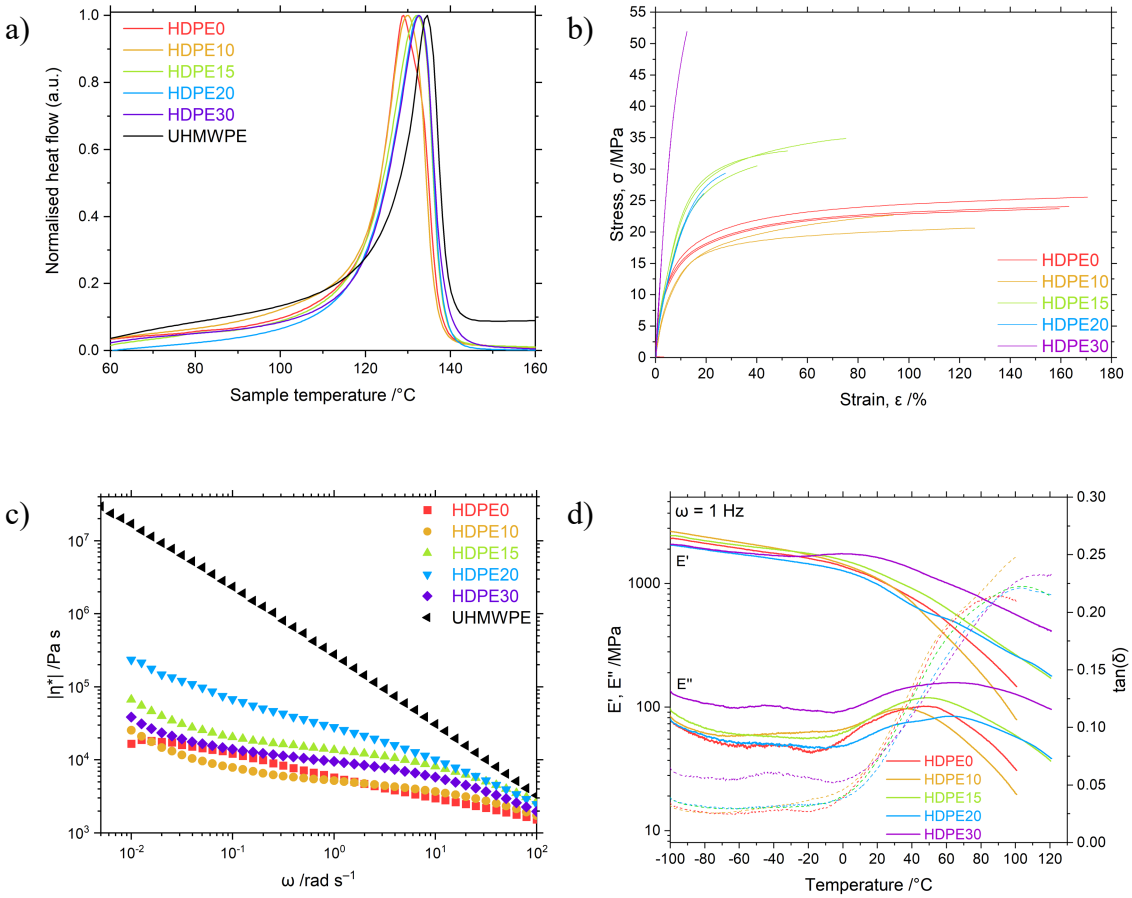

Figure 3.23 a) DSC thermograms, b) engineering stress-strain curves, c) rheological frequency sweep, and d) DMTA of HDPE/HMWPE blends across a composition range of 0–30 wt% UHMWPE.

3.6. Conclusions

Chapter 3 has demonstrated the efficacy of catalysts based on group four PHENI* complexes, described in Chapter 2, towards the polymerisation of ethylene. In addition to exceptional homogeneous catalytic activities, up to 27 000 $kg_{PE}\ mol_{Ti}^{-1}\ h^{-1}\ bar^{-1}$, the complexes have been immobilised on a range of solid supports which offer excellent morphological control. Ultra-high molecular weight polyethylene is produced, with M_w up to 4.2 MDa. In addition, complexes immobilised on sMAO were shown to produce substantially disentangled UHMWPE.

The influence of catalyst structure on polymerisation has been studied through variations to the PHENI* ligand, the metal centre, and the ancillary ligands, and steric, conformational, electronic, and coordinative influences have been discussed. Furthermore, polymerisations have been optimised with respect to a range of industrially relevant reaction conditions, including by high-throughput high pressure screening. At 8.3 bar, slurry-phase activities over 11 000 $kg_{PE}\ mol_{Ti}^{-1}\ h^{-1}\ bar^{-1}$ are reported, with polymer molecular weights up to 4.9 MDa. An excellent hydrogen response is observed, with M_w decreasing by up to 96%, while maintaining high activities.

The bulk physical properties of *dis*UHMWPE have been investigated by a range of thermomechanical techniques, both in the melt and solid states. Polyethylene-polyethylene blends using commercial grades of commodity molecular weight LDPE and HDPE along with UHMWPE have been produced and studied in the melt and solid states with a particular emphasis on combining the processability advantages of conventional grades of PE with the high-performance characteristics of UHMWPE. While LDPE/UHMWPE shows poor miscibility and physical properties, HDPE/UHMWPE blends have substantially lower melt viscosities than UHMWPE while showing a two-fold increase in tensile strength and stiffness compared to HDPE.

The application of PHENI* catalysts towards propylene polymerisation will form the focus of Chapter 4, and the initial ethylene/1-hexene copolymerisation screening experiments reported in this chapter will be developed extensively in Chapter 5.

3.7. References

1 W. Kaminsky, *Macromol. Chem. Phys.*, 1996, **197**, 3907-3945.
2 W. Kaminsky, *J. Chem. Soc., Dalton Trans.*, 1998, 1413-1418.
3 H. Braunschweig and F. M. Breitling, *Coord. Chem. Rev.*, 2006, **250**, 2691-2720.
4 J. Klosin, P. P. Fontaine, R. Figueroa, *Acc. Chem. Res.*, 2015, **48**, 2004-2016.

5 H. Katayama, M. Nabika, A. Imai, A. Miyashita, T. Watanabe, H. Johohji, Y. Oda, H. Hanaoka, *Intl. Pat.*, WO9703992A1, **1997**.
6 H. Hanaoka, T. Hino, M. Nabika, T. Kohno, K. Yanagi, Y. Oda, A. Imai, K. Mashima, *J. Organomet. Chem.*, 2007, **692**, 4717-4724.
7 M. Nabika, H. Katayama, T. Watanabe, H. Kawamura-Kuribayashi, K. Yanagi, A. Imai, *Organometallics*, 2009, **28**, 3785-3792.
8 T. Senda, H. Hanaoka, T. Hino, Y. Oda, H. Tsurugi, K. Mashima, *Macromolecules*, 2009, **42**, 8006-8009.
9 T. Senda, H. Hanaoka, S. Nakahara, Y. Oda, H. Tsurugi, K. Mashima, *Macromolecules*, 2010, **43**, 2299-2306.
10 T. A. Tervoort, J. Visjager, P. Smith, *Macromolecules*, 2002, **35**, 8467-8471.
11 F. Živić, M. Babić, S. Mitrović, D. Adamović, S. Pelemis, *Tribol. Ind.*, 2014, **36**, 281.
12 P. Bracco, A. Bellare, A. Bistolfi, S. Affatato, *Materials*, 2017, **10**, 791.
13 M. Hussain, R. A. Naqvi, N. Abbas, S. M. Khan, S. Nawaz, A. Hussain, N. Zahra, M. W. Khalid, *Polymers*, 2020, **12**, 323.
14 Y. Wang and R. Hou, *J. Phys. Conf. Ser.*, 2022, **2263**, 012016.
15 S. Liu, J. Wang, Y. Wang, Y. Wang, *Mater. Des.*, 2010, **31**, 1711-1715.
16 D. Romano, S. Ronca, S. Rastogi, *Macromol. Rapid Commun.*, 2015, **36**, 327-331.
17 J. Fu, B. W. Ghali, A. J. Lozynsky, E. Oral, O. K. Muratoglu, *Polymer*, 2010, **51**, 2721-2731.
18 B. Wu, Y. Cai, X. Zhao, L. Ye, *Polym. Test.*, 2021, **93**.
19 D. Romano, N. Tops, E. Andablo-Reyes, S. Ronca, S. Rastogi, *Macromolecules*, 2014, **47**, 4750-4760.
20 A. Hawkins, *Synthesis of next-generation functional polymers: exploration of PHENI* transition metal complexes*, M.Chem. Part II Thesis, *University of Oxford*, 2022.
21 F. Ciardelli, A. Altomare, M. Michelotti, *Catal. Today*, 1998, **41**, 149-157.
22 W. Wang, Z. q. Fan, L. x. Feng, *Eur. Polym. J.*, 2005, **41**, 2380-2387.
23 Y. X. Chen and T. J. Marks, *Organometallics*, 1997, **16**, 3649-3657.
24 H. Hanaoka, T. Hino, H. Souda, K. Yanagi, Y. Oda, A. Imai, *J. Organomet. Chem.*, 2007, **692**, 4059-4066.
25 T. J. Williams, *Olefin polymerisation using group 4 permethylindenyl complexes*, D.Phil. Thesis, *University of Oxford*, 2020.
26 J. V. Lamb, *Unsymmetrical Group 4 Permethylindenyl Ansa-Metallocenes as Polymerisation Catalysts*, D.Phil. Thesis, *University of Oxford*, 2019.
27 J. C. Buffet, T. A. Q. Arnold, Z. R. Turner, P. Angpanitcharoen, D. O'Hare, *RSC Adv.*, 2015, **5**, 87456-87464.
28 P. Ransom, A. E. Ashley, N. D. Brown, A. L. Thompson, D. O'Hare, *Organometallics*, 2011, **30**, 800-814.
29 A. R. Siedle, W. M. Lamanna, R. A. Newmark, J. Stevens, D. E. Richardson, M. Ryan, *Makromol. Chem. Macromol. Symp.*, 1993, **66**, 215-224.
30 K. Musikabhumma, T. P. Spaniol, J. Okuda, *J. Mol. Catal. A Chem.*, 2004, **208**, 73-81.
31 J. Zhou, S. J. Lancaster, D. A. Walker, S. Beck, M. Thornton-Pett, M. Bochmann, *J. Am. Chem. Soc.*, 2001, **123**, 223-237.
32 V. C. Williams, G. J. Irvine, W. E. Piers, Z. Li, S. Collins, W. Clegg, M. R. J. Elsegood, T. B. Marder, *Organometallics*, 2000, **19**, 1619-1621.
33 D. Langford, I. Göttker-Schnetmann, F. P. Wimmer, L. A. Casper, P. Kenyon, R. F. Winter, S. Mecking, *Organometallics*, 2019, **38**, 2710-2713.
34 E. Rudnik and Z. Dobkowski, *J. Therm. Anal.*, 1997, **49**, 471-475.
35 M. Eskelinen and J. V. Seppälä, *Eur. Polym. J.*, 1996, **32**, 331-335.
36 P. Wongwaiwattanakul and B. Jongsomjit, *Catal. Commun.*, 2008, **10**, 118-122.
37 J. C. Buffet, N. Wanna, T. A. Q. Arnold, E. K. Gibson, P. P. Wells, Q. Wang, J. Tantirungrotechai, D. O'Hare, *Chem. Mater.*, 2015, **27**, 1495-1501.
38 A. F. R. Kilpatrick, J. C. Buffet, P. Nørby, N. H. Rees, N. P. Funnell, S. Sripothongnak, D. O'Hare, *Chem. Mater.*, 2016, **28**, 7444-7450.
39 T. A. Q. Arnold, Z. R. Turner, J. C. Buffet, D. O'Hare, *J. Organomet. Chem.*, 2016, **822**, 85-90.
40 G. E. Hickman, *Boron-bridged Zirconocene Complexes Supported on Layered Double Hydroxides*, M.Chem. Part II Thesis, *University of Oxford*, 2018.
41 J. C. Buffet, Z. R. Turner, R. T. Cooper, D. O'Hare, *Polym. Chem.*, 2015, **6**, 2493-2503.
42 J. C. Buffet, Z. R. Turner, D. O'Hare, *Chem. Commun.*, 2018, **54**, 10970-10973.
43 J. V. Lamb, J. C. Buffet, Z. R. Turner, D. O'Hare, *Polym. Chem.*, 2019, **10**, 1386-1398.

44 K. W. Bossers, R. Valadian, S. Zanoni, R. Smeets, N. Friederichs, J. Garrevoet, F. Meirer, B. M. Weckhuysen, *J. Am. Chem. Soc.*, 2020, **142**, 3691-3695.
45 K. W. Bossers, R. Valadian, J. Garrevoet, S. van Malderen, R. Chan, N. Friederichs, J. Severn, A. Wilbers, S. Zanoni, M. K. Jongkind, B. M. Weckhuysen, F. Meirer, *JACS Au*, 2021, **1**, 852-864.
46 M. J. Werny, D. Muller, C. Hendriksen, R. Chan, N. H. Friederichs, C. Fella, F. Meirer, B. M. Weckhuysen, *ChemCatChem*, 2022, **14**.
47 J. J. Maurer, *J. Polym. Sci. A*, 1963, **1**, 577-590.
48 J. C. Thomas, *J. Colloid Interface Sci.*, 1987, **117**, 187-192.
49 J. C. Ferrari, F. Castilhos, P. H. H. Araújo, C. Sayer, *Braz. J. Chem. Eng.*, 2016, **33**, 469-478.
50 E. Limpert, W. A. Stahel, M. Abbt, *BioScience*, 2001, **51**, 341-352.
51 J. E. O'Gara, K. B. Wagener, S. F. Hahn, *Makromol. Chem., Rapid Commun.*, 1993, **14**, 657-662.
52 A. Tynys, J. L. Eilertsen, E. Rytter, *Macromol. Chem. Phys.*, 2006, **207**, 295-303.
53 P. Kenyon, D. W. J. Leung, Z. R. Turner, J. C. Buffet, D. O'Hare, *Macromolecules*, 2022, **55**, 3408-3414.
54 T. J. Williams, J. C. Buffet, Z. R. Turner, D. O'Hare, *Catal. Sci. Technol.*, 2018, **8**, 5454-5461.
55 L. Luo and T. J. Marks, *Top. Catal.*, 1999, **7**, 97-106.
56 M. Bochmann, *J. Organomet. Chem.*, 2004, **689**, 3982-3998.
57 L. Fan, D. Harrison, T. K. Woo, T. Ziegler, *Organometallics*, 1995, **14**, 2018-2026.
58 I. Silanes, J. M. Mercero, J. M. Ugalde, *Organometallics*, 2006, **25**, 4483-4490.
59 W. Kaminsky, *Catal. Today*, 1994, **20**, 257-271.
60 S. J. Kim, Y. J. Lee, E. Kang, S. H. Kim, J. Ko, B. Lee, M. Cheong, I. H. Suh, S. O. Kang, *Organometallics*, 2003, **22**, 3958-3966.
61 P. C. Möhring and N. J. Coville, *J. Organomet. Chem.*, 1994, **479**, 1-29.
62 C. Alonso-Moreno, A. Antiñolo, I. López-Solera, A. Otero, S. Prashar, A. M. Rodríguez, E. Villaseñor, *J. Organomet. Chem.*, 2002, **656**, 129-138.
63 R. K. J. Bott, D. L. Hughes, M. Schormann, M. Bochmann, S. J. Lancaster, *J. Organomet. Chem.*, 2003, **665**, 135-149.
64 M. P. Gil and O. L. Casagrande, *J. Organomet. Chem.*, 2004, **689**, 286-292.
65 J. I. Martínez-Araya, R. Quijada, A. Toro-Labbé, *J. Phys. Chem. C*, 2012, **116**, 21318-21325.
66 R. A. Collins, A. F. Russell, P. Mountford, *Appl. Petrochem. Res.*, 2015, **5**, 153-171.
67 J. T. Hirvi, M. Bochmann, J. R. Severn, M. Linnolahti, *ChemPhysChem*, 2014, **15**, 2732-2742.
68 M. Bochmann and S. J. Lancaster, *Angew. Chem. Int. Ed. Engl.*, 1994, **33**, 1634-1637.
69 R. Kleinschmidt, Y. van der Leek, M. Reffke, G. Fink, *J. Mol. Catal. A Chem.*, 1999, **148**, 29-41.
70 V. F. Tisse, C. Boisson, T. F. L. McKenna, *Macromol. Chem. Phys.*, 2014, **215**, 1358-1369.
71 F. Ghiotto, C. Pateraki, J. R. Severn, N. Friederichs, M. Bochmann, *Dalton Trans.*, 2013, **42**, 9040-9048.
72 M. Mitani, J. I. Mohri, Y. Yoshida, J. Saito, S. Ishii, K. Tsuru, S. Matsui, R. Furuyama, T. Nakano, H. Tanaka, S. I. Kojoh, T. Matsugi, N. Kashiwa, T. Fujita, *J. Am. Chem. Soc.*, 2002, **124**, 3327-3336.
73 W. Kaminsky and H. Lüker, *Makromol. Chem., Rapid Commun.*, 1984, **5**, 225-228.
74 Y. V. Kissin, R. I. Mink, T. E. Nowlin, A. J. Brandolini, *J. Polym. Sci., Part A: Polym. Chem.*, 1999, **37**, 4281-4294.
75 K. J. Chu, J. B. P. Soares, A. Penlidis, *Macromol. Chem. Phys.*, 2000, **201**, 552-557.
76 A. K. Rappé, W. M. Skiff, C. J. Casewit, *Chem. Rev.*, 2000, **100**, 1435-1456.
77 F. Song, R. D. Cannon, S. J. Lancaster, M. Bochmann, *J. Mol. Catal. A Chem.*, 2004, **218**, 21-28.
78 M. Bochmann, *Organometallics*, 2010, **29**, 4711-4740.
79 J. Ramos, V. Cruz, A. Muñoz-Escalona, J. Martínez-Salazar, *Polymer*, 2000, **41**, 6161-6169.
80 T. J. Williams, J. V. Lamb, J. C. Buffet, T. Khamnaen, D. O'Hare, *RSC Adv.*, 2021, **11**, 5644-5650.
81 V. Busico, R. Pellecchia, F. Cutillo, R. Cipullo, *Macromol. Rapid Commun.*, 2009, **30**, 1697-1708.
82 S. Mehdiabadi, O. Lhost, A. Vantomme, J. B. P. Soares, *Ind. Eng. Chem. Res.*, 2021, **60**, 9739-9754.
83 D. P. Gates, S. A. Svejda, E. Oñate, C. M. Killian, L. K. Johnson, P. S. White, M. Brookhart, *Macromolecules*, 2000, **33**, 2320-2334.
84 J. B. P. Soares, J. D. Kim, G. L. Rempel, *Ind. Eng. Chem. Res.*, 1997, **36**, 1144-1150.
85 E. P. C. Mes, H. de Jonge, T. Klein, R. R. Welz, D. T. Gillespie, *J. Chromatogr. A*, 2007, **1154**, 319-330.
86 S. Talebi, R. Duchateau, S. Rastogi, J. Kaschta, G. W. M. Peters, P. J. Lemstra, *Macromolecules*, 2010, **43**, 2780-2788.
87 R. P. Gote, D. Mandal, K. Patel, K. Chaudhuri, C. P. Vinod, A. K. Lele, S. H. Chikkali, *Macromolecules*, 2018, **51**, 4541-4552.
88 P. P. Klemchuk and P. L. Horng, *Polym. Degrad. Stab.*, 1984, **7**, 131-151.

89 MatWeb.com, *Overview of materials for High Density Polyethylene (HDPE), Ultra High Molecular Weight*, https://www.matweb.com/search/DataSheet.aspx?MatGUID=f9470672aa5549cb9c7b157677d02062, Accessed 5 December, 2022.
90 S. Rastogi, D. Lippits, S. Talebi, B. Wang, *Abstr. Pap. Am. Chem. Soc.*, 2007, **234**.
91 G. Forte and S. Ronca, *Int. J. Polym. Sci.*, 2017, **2017**, 1-8.
92 A. Heidari, H. Zarghami, S. Talebi, M. Rezaei, *Iran. Polym. J.*, 2018, **27**, 701-708.
93 K. Patel, S. H. Chikkali, S. Sivaram, *Prog. Polym. Sci.*, 2020, **109**, 101290.
94 F. Christakopoulos, E. M. Troisi, A. S. Sologubenko, N. Friederichs, L. Stricker, T. A. Tervoort, *Polymer*, 2021, **222**, 123633.
95 P. Smith, P. J. Lemstra, H. C. Booij, *J. Polym. Sci. Polym. Phys.*, 1981, **19**, 877-888.
96 D. Romano, E. Andablo-Reyes, S. Ronca, S. Rastogi, *Polymer*, 2015, **74**, 76-85.
97 I. V. Oleynik, I. K. Shundrina, I. I. Oleyinik, *Polym. Adv. Technol.*, 2020, **31**, 1921-1934.
98 D. R. Lippits, *Controlling the melting kinetics of polymers: a route to a new melt state*, Ph.D. Thesis, *Technische Universiteit Eindhoven*, 2007.
99 D. R. Lippits, S. Rastogi, G. W. H. Höhne, B. Mezari, P. C. M. M. Magusin, *Macromolecules*, 2007, **40**, 1004-1010.
100 B. P. Rotzinger, H. D. Chanzy, P. Smith, *Polymer*, 1989, **30**, 1814-1819.
101 K. Liu, E. L. de Boer, Y. Yao, D. Romano, S. Ronca, S. Rastogi, *Macromolecules*, 2016, **49**, 7497-7509.
102 N. Li, Q. Zhang, Q. Yang, Y. Huang, X. Liao, W. Zhao, *J. Polym. Res.*, 2015, **22**, 55.
103 J. D. Ferry, *Viscoelastic properties of polymers*, John Wiley & Sons, 1980.
104 M. Spronck, A. Klein, B. Blom, D. Romano, *Z. Anorg. Allg. Chem.*, 2018, **644**, 993-998.
105 S. Rastogi, D. R. Lippits, G. W. H. Höhne, B. Mezari, P. C. M. M. Magusin, *J. Phys.: Condens. Matter*, 2007, **19**, 205122.
106 A. Pandey, Y. Champouret, S. Rastogi, *Macromolecules*, 2011, **44**, 4952-4960.
107 P. Chammingkwan, Y. Bando, L. T. T. Mai, T. Wada, A. Thakur, M. Terano, L. Sinthusai, T. Taniike, *Ind. Eng. Chem. Res.*, 2021, **60**, 2818-2827.
108 Y. Chen, H. Zou, Y. Cao, M. Liang, *Polym. Sci. Ser. A*, 2014, **56**, 630-639.
109 Y. Chen, H. Zou, M. Liang, P. Liu, *J. Appl. Polym. Sci.*, 2013, **129**, 945-953.
110 T. Kyu and P. Vadhar, *J. Appl. Polym. Sci.*, 1986, **32**, 5575-5584.
111 L. Zhao and P. Choi, *Mater. Manuf. Processes*, 2006, **21**, 135-142.
112 B. Crist and M. J. Hill, *J. Polym. Sci., Part B: Polym. Phys.*, 1997, **35**, 2329-2353.
113 G. Tao, Y. Chen, J. Mu, L. Zhang, C. Ye, W. Li, *J. Appl. Polym. Sci.*, 2021, **138**, 50741.

Chapter 4 – Polymerisation of propylene to UHMWaPP

4.1. Introduction

Commercially, polypropylene (PP) is predominantly synthesised using conventional Ziegler-Natta (ZN) catalyst technologies.[1] The inherent chirality of the titanium centres on the $TiCl_3$ crystal surface results in highly crystalline isotactic polymers.[2] It is clear from detailed computational modelling of these mechanistically elusive systems, that steric considerations play a key role in enforcing stereoselectivity, with the $–CH_3$ group of the propylene interacting with chlorides adjacent to the metal centre.[3] Tacticity and molecular weights (M_w) are highly coupled in these systems,[4] with low M_w partially crystalline atactic PP (*a*PP) obtained as a by-product.[5] The *i*PP produced in this manner has a non-uniform distribution of stereodefects, resembling a stereoblock microstructure in contrast to the uniform polymers produced by single-site metallocene catalysts; it has been claimed that this is responsible for the difference in physical properties of *i*PP produced by ZN and metallocene catalysts.[6]

Group four metallocene and post-metallocene catalysts are typically used where independent control over polymer tacticity and molecular weight are desired, and have been shown to be particularly effective in the synthesis of elastomeric high molecular weight *a*PP which is inaccessible using Ziegler-Natta technology.[7,8] The relationship between the symmetry of single-site catalysts and resulting polypropylene tacticity is well understood,[9,10] with complexes in the C_{2v} and C_2 point groups typically producing atactic and isotactic PP respectively, while asymmetric C_1 complexes are reported to produce polymers with microstructures ranging from highly isotactic to atactic.[9] Stereoselectivity

in prochiral monomer insertion results principally from enantiomorphic site control with steric constraints enforcing a preference for either the *re* or *si* configuration of the monomer. C_2-symmetric *ansa*-metallocenes are particularly effective, with the bridge enforcing conformational rigidity of the ligand.[11,12]

Amorphous high molecular weight *a*PP (HMWaPP, $M_w > 200$ kDa) is a material of growing industrial interest; beneficial elastic and optical properties lead to broad applications as adhesives, compatibilisers, and as additives in a range of polymeric materials.[5,7] There has been limited development of catalysts that are selective for the synthesis of such materials, with metallocene and post-metallocene complexes of titanium and zirconium receiving the most attention.[8,13] The synthesis of ultra-high molecular weight *a*PP (UHMWaPP, $M_w > 1$ MDa) has been reported, though typically only in relatively low-yielding processes.[13,14] Ultra-high molecular weight homopolymers of higher olefins from 1-butene to 1-octadecene have also been reported, typically in moderate yields or under forcing low-temperature conditions, with relatively limited specific catalyst development, exploration of polymer properties, and few proposed applications.[15-19]

Ultra-high molecular weight homopolypropylene elastomers, synthesised by Rieger *et al.* as stereodefective isotactic PP, were shown to have beneficial mechanical properties, including improved elastic recovery compared to lower M_w elastomeric PP.[20] Homopolymer olefinic thermoplastic elastomers would offer beneficial processability and recyclability when compared with more conventional cross-linked rubbers.[21,22] One such class of thermoplastic elastomer, copolymeric ethylene propylene rubber (EPM), is commercially synthesised using highly active titanium cyclopentadienyl-amidinate complexes.[23]

4.1.1. Chapter synopsis

Post-metallocene *ansa*-bridged complexes based on nitrogen and oxygen donors – such as the Constrained Geometry Complexes (CGCs),[24,25] and Phenoxy-Induced Complexes of Sumitomo (PHENICS)[26-28] have been shown to be highly active catalysts for ethylene and propylene polymerisation. Following the application of PHENI* complexes to ethylene polymerisation with excellent activities and ultra-high molecular weight polymer, in this chapter we report their application in the homopolymerisation of propylene, both in solution-phase and sMAO-supported regimes. This catalytic system demonstrates extremely high activities, excellent control, and the selective production of high and ultra-high molecular weight amorphous atactic polypropylene. The polypropylenes are shown to have excellent tensile and elastic properties, comparable to commercial engineering thermoplastic elastomers.

4.2. Polymerisation of propylene

Initial polymerisation studies using sMAO-supported solid catalysts were performed in 150 mL Rotaflo® ampoules using 10 mg ^{Me2}SB(^{tBu,Me}ArO,I*)TiCl$_2$ (**1**), ^{Me2}SB(^{tBu2}ArO,I*)TiCl$_2$ (**2**), ^{Me2}SB(^{tBu2}ArO,I*)Ti(CH$_2$SiMe$_3$)$_2$ (**6**), ^{Me2}SB(^{Cumyl2}ArO,I*)TiCl$_2$ (**11**), or ^{Me2}SB(^{tBu,Me2}ArO,Ind)TiCl$_2$ (**14**) with 2 bar propylene in 50 mL hexanes for 30 minutes with MAO ([Al$_{MAO}$]/[Ti] = 1000) acting as co-catalytic initiator and scavenger across a temperature of polymerisation (T_p) range of $60 \leq T_p \leq 80$ °C (Figure 4.1).

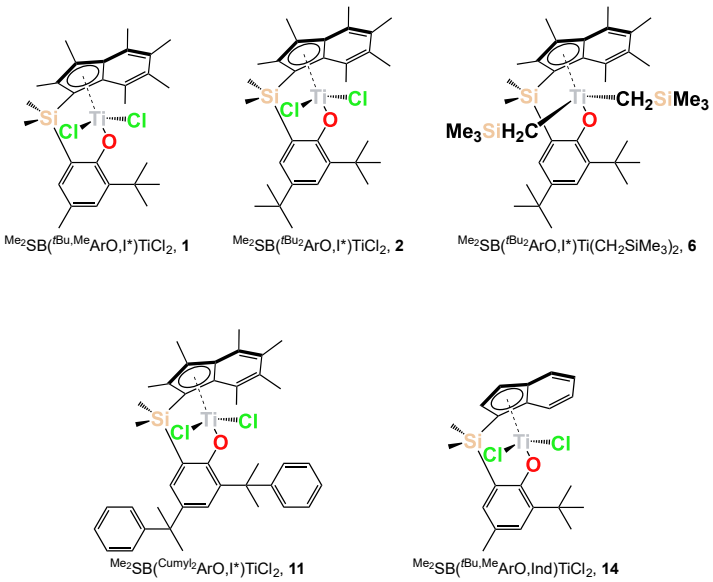

Figure 4.1 Complexes used in this section.

As was found previously for ethylene polymerisation using supported catalysts (Chapter 3.3), $\mathbf{2}_{\mathbf{sMAO}}$/MAO displayed the highest activity, 3200 kg_{PP} mol_{Ti}^{-1} h^{-1} bar^{-1} at 60 °C, with the trend $\mathbf{2}_{\mathbf{sMAO}}$/MAO > $\mathbf{1}_{\mathbf{sMAO}}$/MAO > $\mathbf{11}_{\mathbf{sMAO}}$/MAO (Table 4.1). The neosilyl catalyst $\mathbf{6}_{\mathbf{sMAO}}$ had substantially reduced activities than the chloride, 310 kg_{PP} mol_{Ti}^{-1} h^{-1} bar^{-1} at 60 °C. Comparing the indenyl and permethylindenyl analogues ($\mathbf{14}_{\mathbf{sMAO}}$/MAO and $\mathbf{1}_{\mathbf{sMAO}}$/MAO) – a larger increase in activity was seen even than for ethylene polymerisation, being 26-fold greater for the I* complex at T_p = 60 °C. The weight-average molecular weight (M_w) of the resulting polypropylenes was determined by gel permeation chromatography (GPC) (Table 4.1, Figure 4.2, Figure 4.4). The PHENI* sMAO supported catalyst $\mathbf{1}_{\mathbf{sMAO}}$/MAO produced *a*PP with a 5-fold higher M_w than the analogous PHENICS sMAO supported catalyst, $\mathbf{14}_{\mathbf{sMAO}}$/MAO, as well as having reduced dispersity (PDI, Đ). sMAO supported catalyst $\mathbf{2}_{\mathbf{sMAO}}$/MAO produced the highest molecular weight polymers of the four PHENI* supported catalysts studied, up to 630 kDa at T_p = 60 °C.

Table 4.1 Propylene polymerisation results with sMAO-supported catalysts **1**$_{\mathbf{sMAO}}$/MAO, **2**$_{\mathbf{sMAO}}$/MAO, **6**$_{\mathbf{sMAO}}$/MAO, **11**$_{\mathbf{sMAO}}$/MAO, and **14**$_{\mathbf{sMAO}}$/MAO. Polymerisation conditions: 10 mg catalyst, 2 bar propylene, 50 mL hexanes, 30 minutes, and MAO ([Al$_{MAO}$]/[Ti] = 1000). a) Determined by GPC, PDI = Đ = M_w/M_n.

Catalyst	T_p /°C	Activity / kg_{pp} mol_{Ti}^{-1} h^{-1} bar^{-1}	M_w[a] /kDa	PDI[a]
1$_{\mathbf{sMAO}}$/MAO	60	2610	470	2.2
	70	1440	370	2.3
	80	1120	230	2.3
2$_{\mathbf{sMAO}}$/MAO	60	3210	630	2.2
	70	2180	430	2.2
	80	1610	350	2.1
6$_{\mathbf{sMAO}}$/MAO	60	311	250	2.1
	70	581	330	2.1
	80	448	230	2.2
11$_{\mathbf{sMAO}}$/MAO	60	1730	370	2.3
	70	623	290	2.3
	80	637	200	2.2
14$_{\mathbf{sMAO}}$/MAO	60	105	96	4.5
	70	37	63	3.2
	80	19	75	3.5

During the course of the polymerisation, the formation of hexanes-soluble *a*PP led to an increasingly viscous reaction mixture. Runs were attempted as before with **2**$_{\mathbf{sMAO}}$/MAO at $T_p < 60$ °C but the increased viscosity resulting from a greater polymer yield inhibited stirring. Thus, the reaction time was reduced to 10 minutes to allow complete thermal profiling of **2**$_{\mathbf{sMAO}}$/MAO over a range of $4 \leq T_p \leq 90$ °C (Figure 4.2). As there was no advantage to be gained from a morphological templating effect of supported polymerisation, the homogeneous propylene polymerisation activity of complex **2**/MAO was also investigated. Polymerisation conditions were as for runs using sMAO-supported solid catalysts, using 0.714 μmol **2** (414 μg, [Ti] = 14 μM, equal to the quantity supported on 10 mg **2**$_{\mathbf{sMAO}}$), and MAO as co-catalyst. As anticipated, the activities of **2**$_{\mathbf{sMAO}}$/MAO and **2**/MAO are broadly consistent, with the moderate increase in sMAO-supported activities largely attributed to the 20% increase in [Al] (from [Al$_{MAO}$]/[Ti] = 1000 in

solution-phase, to $[Al_{(sMAO + MAO)}]/[Ti] = 1200$ with $\mathbf{2_{sMAO}}$/MAO) which is shown *vide infra* to effect an increase in activity. While the per-mole$_{Ti}$ activities were consistent it should be noted that the per-mass$_{cat}$ productivities of the solution-phase system are far in excess of the supported catalysts.

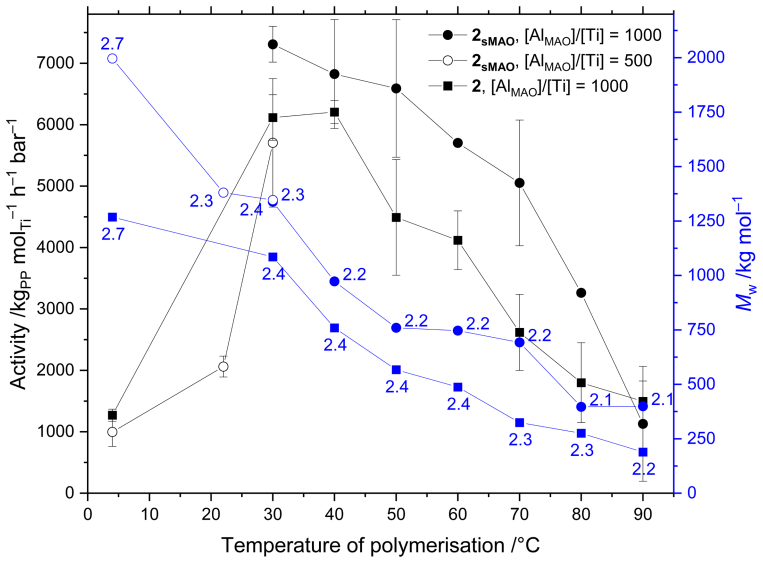

Figure 4.2 Mean propylene polymerisation activity and polypropylene molecular weight (dispersity values (PDI, Đ = M_w/M_n) annotated) as a function of the temperature of polymerisation using homogeneous and sMAO-supported ^{Me2}SB(^{tBu2}ArO,I*)TiCl$_2$ (**2**, and $\mathbf{2_{sMAO}}$ respectively). Polymerisation conditions: 0.714 μmol Ti (10 mg solid catalyst, or 414 μg complex), 2 bar propylene, 50 mL hexanes, 10 minutes, and MAO ($[Al_{MAO}]/[Ti]$ = 500 or 1000). Error bars shown at one standard deviation.

A typical molecular weight temperature profile was observed using both $\mathbf{2_{sMAO}}$/MAO and **2**/MAO (Figure 4.2), with M_w decreasing as polymerisation temperature increases, due to the increase in the rate of chain termination processes, including β-elimination and chain transfer, relative to propagation at higher temperatures.[29,30] With $\mathbf{2_{sMAO}}$/MAO, M_w was found to be largely unaffected by the reduction in reaction time from 30 to 10 minutes, and continued to increase to 1.3 MDa as polymerisation temperature decreased to 30 °C. In solution-phase polymerisations with **2**/MAO, polymer molecular weights were found to be consistently lower than for sMAO-supported catalysts, though still affording

UHMWaPP, up to 1.1 MDa at 30 °C, and 1.3 MDa at 4 °C. Dispersities are low across this temperature range, with $M_w/M_n \leq 2.7$, indicative of well-controlled single-site catalysis. This is maintained both in homogeneous phase and when supported on sMAO, showing that the supported system retains the benefits of homogeneous molecular catalysis. The production of UHMWaPP under ambient temperature conditions and moderate pressure is potentially of industrial significance.

4.2.1. The effect of reaction scale

Polymerisation activity was found to be highest at 30 °C and decreasing with increasing temperature, correlating with decreasing solubility of propylene in hexanes.[31] This suggests that in both homogeneous and supported regimes, the catalytic activity of complex **2**/MAO is limited principally by the availability of propylene in the system, with monomer diffusion being rate limiting. Further studies at higher pressures of propylene would be required to find the performance ceiling. The diffusion limited regime is evidenced by a 34% increase in activity of $\mathbf{2_{sMAO}}$/MAO, to 9800 $kg_{PP}\ mol_{Ti}^{-1}\ h^{-1}\ bar^{-1}$, when the solvent volume was increased to 250 mL in a larger reaction vessel. This leads to a more dilute, lower viscosity solution, more efficient stirring, and a reduced mass-transport barrier for the dissolution of propylene. In this large-scale regime, the quantity of MAO added was also increased five-fold to $[Al_{MAO}]/[Ti] = 5000$ in order to maintain a consistent initial concentration of aluminium, $[Al_{MAO}] = 14$ mM.

To explore this further, the effects of reaction scale were investigated with **2**/MAO, with higher catalyst dilutions leading to an increase in per-mole activity (Figure 4.3). Activity appears to be proportional to the reciprocal concentration of catalyst ($r^2 = 0.997$), increasing to a value of 12 000 $kg_{PP}\ mol_{Ti}^{-1}\ h^{-1}\ bar^{-1}$ at one eighth relative dilution ([Ti] = 1.8 μM). The mass of MAO cocatalyst added was not changed, maintaining a

concentration of [Al_{MAO}] = 14 mM. The weight-average molecular weight of the resulting polypropylenes was found to increase from 1.1 to 1.5 MDa at one eighth dilution, showing a trend towards higher molecular weights at higher dilutions, despite the increasing [Al]/[Ti] ratio.

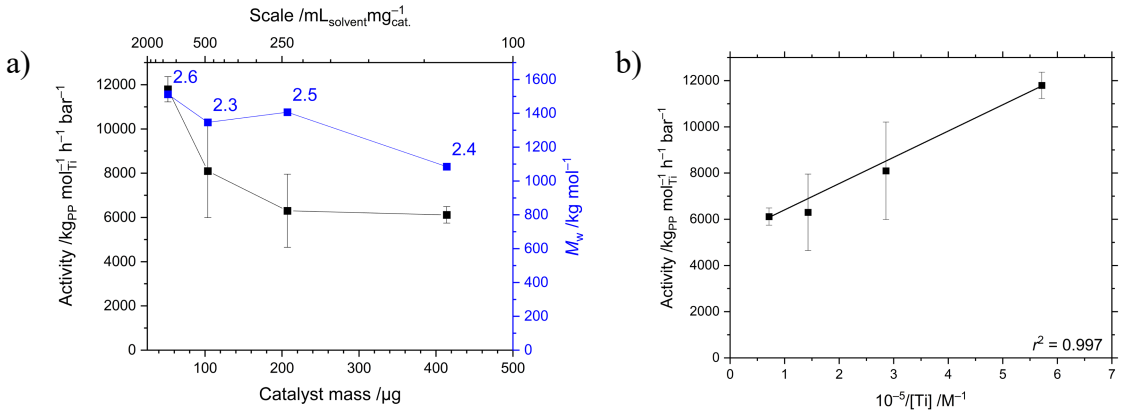

Figure 4.3 Mean propylene polymerisation activity and polypropylene molecular weight (PDIs (M_w/M_n) annotated) as a function of mass of complex ^{Me_2}SB(^{tBu_2}ArO,I*)TiCl$_2$ **2**/MAO. Polymerisation conditions: 2 bar propylene, 50 mL hexanes, 10 minutes, 30 °C, and 41.4 mg MAO. Error bars shown at one standard deviation.

Complex **2** was tested for solution-phase propylene polymerisation at SCG Chemicals PLC (Rayong, Thailand) on a large scale. The catalytic system (**2**/TIBA/MAO) consisted of **2** (1 mg, 1.7 µmol), TIBA (1 mmol, [Al_{TIBA}]/[Ti] = 588), and MAO ([Al_{MAO}]/[Ti] = 250) and polymerisation was performed in a 2 L steel reactor, containing 1 L hexanes, at 60 °C for 120 minutes under 8 bar propylene pressure. An activity of 4843 kg_{PP} mol_{Ti}^{-1} h^{-1} bar^{-1} was reported and a polymer molecular weight of 287 kDa (Đ = 2.7). The reported activity is slightly greater than the most comparable laboratory scale run at 30 minutes; accounting for the expected decrease in activity as a function of time, this suggests that much higher activities are seen under higher pressures. The decrease in molecular weight observed may be due to more chain transfer to TIBA than

MAO, or increased chain transfer to monomer, facilitated by the higher propylene concentration. Runs were attempted under the same conditions using **2**$_{\mathbf{sMAO}}$/TEA, with no polymer observed.

4.2.2. The effect of cocatalyst loading

The performance of both complex **2**/MAO and sMAO supported catalyst **2**$_{\mathbf{sMAO}}$/MAO was investigated at T_p = 30 °C as a function of the ratio [Al$_{MAO}$]/[Ti], ranging from 0 to 5000 (Figure 4.4). In the absence of an aluminium cocatalyst, activity was found to be moderate with **2**$_{\mathbf{sMAO}}$ and no activity was recorded with **2**. This demonstrates the dual-function nature of solid polymethylaluminoxane as an activating support.[32] Increasing the MAO loading resulted in increased polymerisation activities up to a maximum value at 2500 equivalents of 12 000 and 11 000 kg$_{PP}$ mol$_{Ti}^{-1}$ h^{-1} bar^{-1} respectively for **2**$_{\mathbf{sMAO}}$/MAO and **2**/MAO. This activity compares well with some of the most active polypropylene catalysts in literature: the $TiCl_4$–Al/Mg system reported by Rishina *et al.* and the fluorenyl zirconocene reported by Resconi *et al.* have activities of 22 000 and 29 000 kg$_{PP}$ mol$_{M}^{-1}$ h^{-1} respectively when used in liquid propylene,[7,33] a far greater concentration of monomer than the 2 bar pressure used in this work.[34] Runs were attempted using **2** and other alkyl aluminium cocatalysts – TMA, TEA, and TIBA – in place of MAO, but negligible activity was recorded in these cases. The catalyst system **2**$_{\mathbf{sMAO}}$/TIBA (*i.e.* without MAO) by contrast did show moderate polymerisation activity (279 kg$_{PP}$ mol$_{Ti}^{-1}$ h^{-1} bar^{-1} at 60 °C), further demonstrating the activating nature of the sMAO support.

As expected, M_w was found to decrease with increasing MAO loading (Figure 4.4) as a result of increased chain transfer to aluminium, with **2**$_{\mathbf{sMAO}}$/MAO and **2**/MAO having maxima at [Al$_{MAO}$]/[Ti] = 250 and 1000 respectively (1.4 and 1.1 MDa respectively).

Polymerisations at 4 and 22 °C were performed with **2**$_{\mathbf{sMAO}}$/MAO at [Al$_{MAO}$]/[Ti] = 500 as a balance between high M_w and high activities, and at 4 °C with **2**/MAO and [Al$_{MAO}$]/[Ti] = 1000 (Figure 4.2). Activities were comparatively much reduced in these lower temperature conditions, though still classed as "very high",[35] and molecular weight was found to increase still further, reaching 2.0 MDa at T_p = 4 °C with **2**$_{\mathbf{sMAO}}$/MAO. In homogeneous polymerisation with **2**/MAO, the increase in M_w at low temperature was less dramatic, reaching 1.3 MDa at 4 °C. The titanium phenoxy-imine and 2,2'-thiobis(6-*tert*-butyl-4-methylphenoxy) (TBP) complexes reported by Saito *et al.* and Miyatake *et al.* respectively were able to produce *a*PP with M_w > 8 MDa but with activities of only 48 kg$_{PP}$ mol$_{Ti}^{-1}$ h^{-1} bar^{-1} (20 °C, 1 bar) and 8900 kg$_{PP}$ mol$_{Ti}^{-1}$ h^{-1} (25 °C, liquid propylene) respectively,[13,14] significantly lower than **2**$_{\mathbf{sMAO}}$/MAO, reported in this work with activities up to 12 000 kg$_{PP}$ mol$_{Ti}^{-1}$ h^{-1} bar^{-1} (30 °C, 2 bar). Liquid propylene has a density of 613.9 kg m^{-3}, and therefore a molar concentration of 14.6 M; by contrast, at 40 °C and 2.4 bar, the equilibrium concentration of propylene in *n*-heptane was found to be 1.2 M.[31]

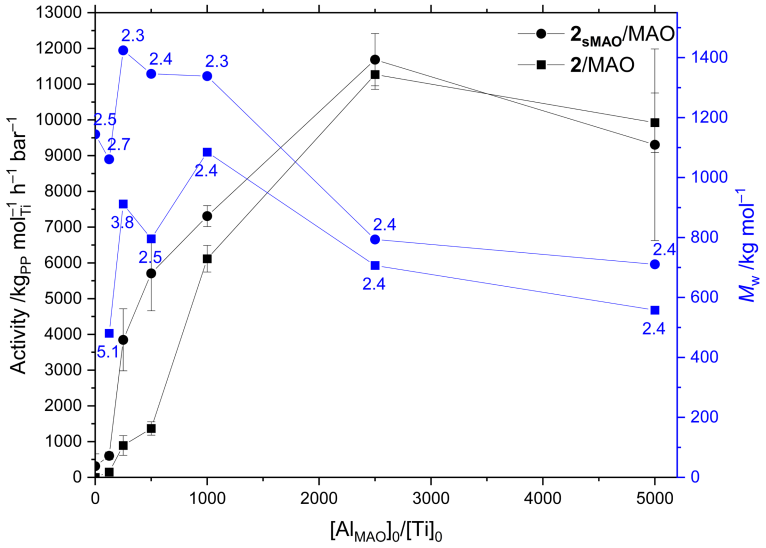

Figure 4.4 Mean propylene polymerisation activity and polypropylene molecular weight (dispersity values (PDI, Đ = Mw/Mn) annotated) as a function of $[Al_{MAO}]/[Ti]$ using homogeneous phase and sMAO-supported $^{Me2}SB(^{tBu2}ArO,I^*)TiCl_2$ (**2**, and **2**$_{sMAO}$ respectively). Polymerisation conditions: 0.714 μmol Ti (10 mg solid catalyst, or 414 μg complex), 2 bar propylene, 50 mL hexanes, 10 minutes, and 30 °C. Error bars shown at one standard deviation.

4.2.3. Thermal, optical, and mechanical properties of UHMWaPP

Thermogravimetric analysis (TGA) shows a single mass loss event at 490 °C under a nitrogen atmosphere, and at 382 °C in a synthetic air mixture (20% O_2 in N_2). Differential scanning calorimetry (DSC) confirmed the identity of the polymers as wholly amorphous *a*PP, with no melting endotherm observed. Crystallisation was not attained either by ageing at room temperature for a long time (several months), or by annealing above the glass transition for 200 minutes, which has previously been shown by Mansel *et al.* for largely atactic polypropylenes with a small degree of crystallinity.[36] Glass transitions were observed between –12 and –3 °C, with $\Delta C_{p,T_g}$ values in the region 0.4–0.6 J °C^{-1} g^{-1} (Figure 4.5), consistent with the values reported by Wilkinson *et al.* for *a*PP and the predictions of Hirai and Eyring that, for a perfectly amorphous polyolefin, $\Delta C_{p,T_g}$ should be 2.97 calories per degree per mole of chain atoms (corresponding to a value of

0.591 J °C^{-1} g^{-1} for PP).[37-39] The PP synthesised by the indenyl complex **14**$_{\mathbf{sMAO}}$ has a T_g of –12 °C, in perfect agreement with literature values for *a*PP.[37] The PHENI* complexes **1**$_{\mathbf{sMAO}}$, **2**$_{\mathbf{sMAO}}$, and **11**$_{\mathbf{sMAO}}$ produce PP with slightly elevated T_g values, presumably due to the higher molecular weights in these cases, according to the Flory-Fox equation $T_g = T_{g,\infty} - K/M_n$. From this model, $T_{g,\infty}$ is calculated as –2.85 ± 0.32 °C, and K as 196 ± 22 °C kg mol^{-1}. Measured T_g values close to that of $T_{g,\infty}$ indicates that the synthesised UHMWaPP is approaching the limiting behaviour of infinite molecular weight polymer.

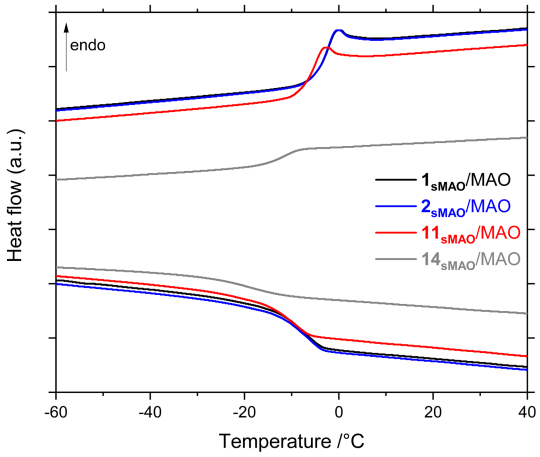

Figure 4.5 Differential scanning calorimetry plots (at 10 K min^{-1}, second heating and cooling shown) of *a*PP produced by **1**$_{\mathbf{sMAO}}$/MAO, **2**$_{\mathbf{sMAO}}$/MAO, **11**$_{\mathbf{sMAO}}$/MAO, and **14**$_{\mathbf{sMAO}}$/MAO. Polymerisation conditions: 10 mg catalyst, 2 bar propylene, 50 mL hexanes, [Al$_{MAO}$]/[Ti] = 1000, 30 minutes, and 60 °C.

^{13}C{^{1}H} Nuclear Magnetic Resonance (NMR) spectra were recorded at 298 K in chloroform-*d* and are characteristic for atactic polypropylene, assigned according to the analysis of Miyatake *et al.* (Figure 4.6).[40-43] The **C**H$_3$ resonances are at δ 19–22 ppm, the **C**H at δ 27–28 ppm, and the **C**H$_2$ between δ 45–48 pm. There was minimal evidence found for 2,1-insertion regioerrors in the ^{13}C{^{1}H} NMR spectra, particularly for *a*PP synthesised by **1**$_{\mathbf{sMAO}}$/MAO, **2**$_{\mathbf{sMAO}}$/MAO, and **2**/MAO.[44-46] This behaviour is typical for early transition metal post-metallocenes, where 2,1 regioerrors are usually <1 mol%.[47]

The presence of resonances at $\delta_{^{13}C}$ = 14–18 and 30–44 ppm in the NMR spectra of *a*PP synthesised by **11**$_{sMAO}$/MAO and **14**$_{sMAO}$/MAO (Figure 4.6c–d) indicate an increased degree of 2,1-insertions, and thus poorer regiocontrol, in these cases.

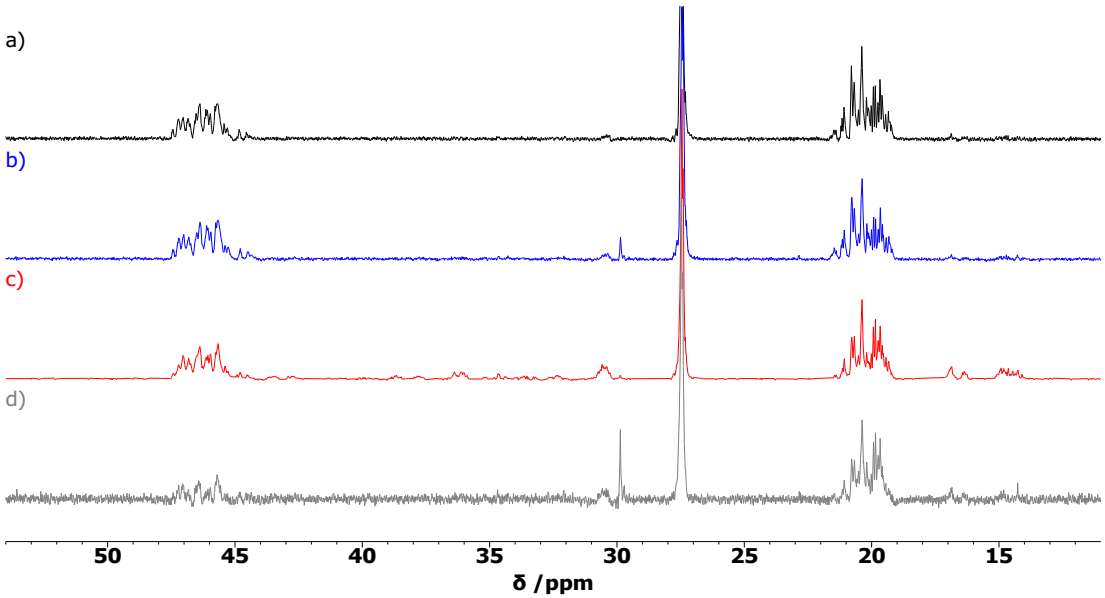

Figure 4.6 $^{13}C\{^{1}H\}$ NMR spectra (126 or 151 MHz, chloroform-*d*, 298 K, 55 ≤ δ ≤ 10) of polypropylene synthesised by a) **1**$_{sMAO}$/MAO, b) **2**$_{sMAO}$/MAO, c) **11**$_{sMAO}$/MAO, and d) **14**$_{sMAO}$/MAO. Polymerisation conditions: 10 mg catalyst, 2 bar propylene, 50 mL hexanes, [Al$_{MAO}$]/[Ti] = 1000, 30 minutes, and 60 °C.

The absence of Bragg reflections in the Wide-Angle X-ray Scattering (WAXS) pattern is also indicative of a fully amorphous material (Figure 4.7a).

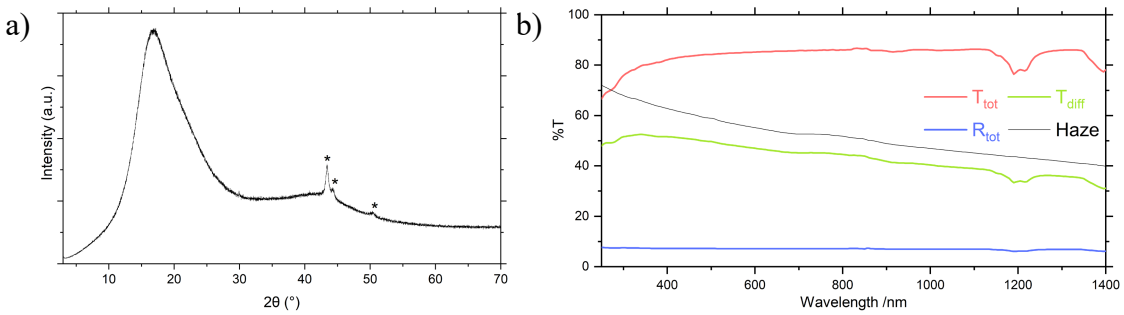

Figure 4.7 a) WAXS pattern, with asterisks (*) denoting reflections arising from the sample holder, and b) UV-Vis-NIR spectra of UHMWaPP.

To facilitate mechanical characterisation, a batch of 33 g UHMWaPP (M_w = 1.2 MDa, Đ = 2.7) was cryogenically milled to a powder-like material and pressed at 180–200 °C to form an optically transparent plate of 1 mm thickness. The bulk density was determined according to ISO1183, and was found to be 876 kg m^{-3}.[48] Optical transmissivity was found to be 85% across the visible light region (380–750 nm), approaching the values of more conventional transparent polyolefin block copolymers (Figure 4.7b, Figure 4.8).[49] Optical haze (T_{diff}/T_{tot}) is calculated to be 50–60%, and total reflection measured at 7%, indicative of a reasonably high clarity material, both quantities decreasing at longer wavelengths of incident light.



Figure 4.8 Image of pressed transparent disc of UHMWaPP, thickness 900 μm.

The mechanical properties of the polymer were analysed according to ISO527.5A (Figure 4.9) using type 5A test specimens.[50] The Young's modulus was found to be 2.05 MPa. The ultimate tensile strength was 1.08 MPa, at a strain of 184%, where a zero-slope condition is achieved demonstrating "yield-like" behaviour comparable to EPM copolymers (Figure 4.9a).[51]

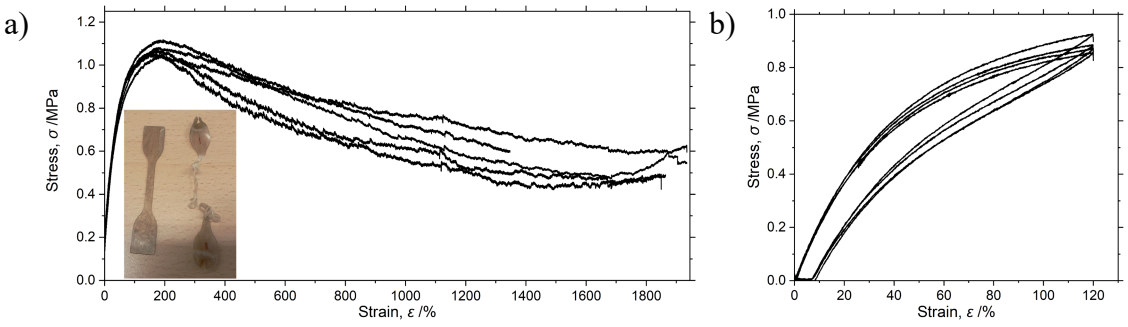

Figure 4.9 a) engineering stress-strain curves (inset: image of dog-bone samples before and after tensile testing), and b) stress-strain hysteresis curves obtained from UHMWaPP samples.

Break characteristics could not be determined; the elongation at break was higher than could be tested, but is at least 1900%, indicative of a tough, highly ductile material. Strain hardening was not observed. The "almost atactic" PP synthesised by Rishina *et al.* using $Ti(O^iPr)_4$ has M_w up to 98 kDa and exhibits an ultimate tensile strength of 2.3 MPa, and a strain at break of 550%; in this case, a yield point was not observed, with stress increasing nonlinearly to a limiting value.[52]

Elastic hysteresis curves were obtained by stress-relaxation from 120% strain (Figure 4.9b) according to the ASTM D638 protocol used by Rieger *et al.*.[20] Excellent elastic recovery is observed with a set value of 7–8%. This is much less than for lower molecular weight *a*PPs, which suffer from large set values resulting from irreversible deformation typical of low crystallinity thermoplastic polyolefins. Behaviour is comparable to that reported by Rieger *et al.*, who further noted the comparable performance with commercial thermoplastic elastomers such as the Kraton™ styrene-butadiene-styrene block copolymer.[20]

Ethylene-propylene copolymer rubbers are the most closely-related widely-studied materials, with the metallocene-catalysed materials produced by Faingol'd *et al.* having tensile strengths of 2.4–15.2 MPa and elongations at break up to 840% – slightly stronger

but substantially less ductile than UHMWaPP.[53] Unlike UHMWaPP, these polymers have a degree of crystallinity and exhibit mechanical strain hardening.

The elastomeric mechanical properties of UHMWaPP are postulated to be, at least in part, due to physical crosslinking made possible by the ultra-high molecular weights, which limits irreversible deformation by reducing chain mobility.[54-56]

These data compare favourably with commercial thermoplastic elastomers, such as the olefin block copolymers from Dow (e.g. INFUSE™ 9817), with a density of 877 kg m^{-3}, a Young's modulus of 2.31 MPa, an ultimate tensile strength of 7.00 MPa, an elongation at break of 1700%, and a compression set of 15%,[57] or the olefinic thermoplastic elastomers from DuPont (e.g. MULTIFLEX™ TPO 50 D 41 81171) with a density of 890 kg m^{-3}, and an elongation at break of 650%.[58] By comparison, the UHMWaPP reported in this work shows a stiffness of 2.05 MPa, elongation of >1900%, and a tension set of 7%. The initial mechanical properties of this UHMWaPP show highly promising results, suggesting that they may have to ability to encroach on the properties of more conventional materials. Such polymers, in particular UHMWaPP, warrant further study to determine commercial applicability.

4.3. Chiral PHENI* complexes towards stereospecific polymerisation

The mixed-bridge PHENI* complexes *rac*-^{Me,nPr}SB(^{tBu_2}ArO,I*)$TiCl_2$ (**12**) and *rac*- ^{Me,Ph}SB(^{tBu_2}ArO,I*)$TiCl_2$ (**13**), which are chiral at the bridging silicon atom, were investigated for propylene polymerisation as the chiral active site may be expected to induce stereospecific polymerisation (Figure 4.10). Leveraging catalyst symmetry to achieve control of polymer tacticity is a well understood strategy, codified as Ewen's Symmetry Rules.[59] Many strategies have been employed for the synthesis of chiral *ansa*

metallocenes,[60] including chiral bridges, which have proved to be stereoselective polymerisation catalysts.[61,62]

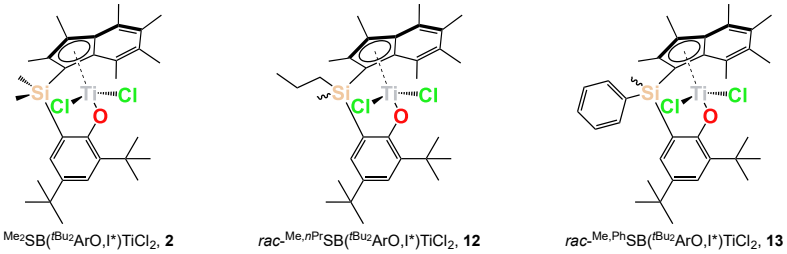

^{Me_2}SB(^{tBu_2}ArO,I*)TiCl$_2$, **2** *rac*-^{Me,nPr}SB(^{tBu_2}ArO,I*)TiCl$_2$, **12** *rac*-^{Me,Ph}SB(^{tBu_2}ArO,I*)TiCl$_2$, **13**

Figure 4.10 Complexes used in this section.

The chiral-at-silicon PHENI* complexes **12** and **13** were immobilised on sMAO ([Al$_{sMAO}$]/[Ti] = 200) and tested for propylene polymerisation using 10 mg supported catalyst, 50 mL hexanes, 2 bar propylene, MAO ([Al$_{MAO}$]/[Ti] = 1000), and 30 minutes (Figure 4.11).

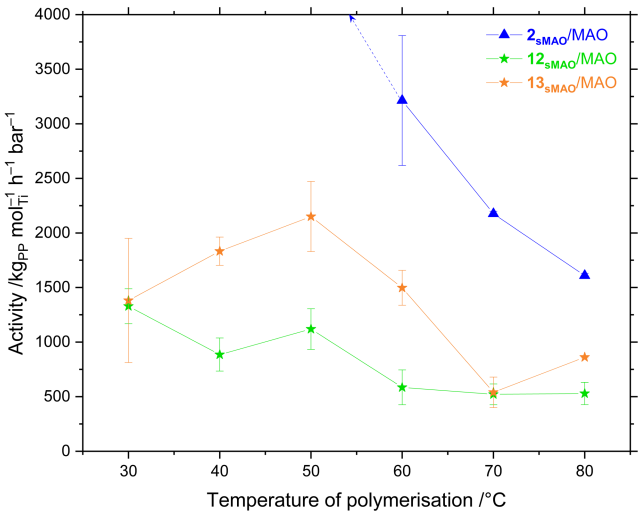

Figure 4.11 Mean Propylene polymerisation activity as a function of temperature of **2$_{sMAO}$**/MAO, **12$_{sMAO}$**/MAO, and **13$_{sMAO}$**/MAO. Polymerisation conditions: 10 mg catalyst, 2 bar propylene, 50 mL hexanes, 30 minutes, and MAO ([Al$_{MAO}$]/[Ti] = 1000). Error bars shown at one standard deviation.

Despite showing ethylene polymerisation activities comparable to that of the Me$_2$Si complex **2$_{sMAO}$** (Chapter 3.3.2), the mixed-bridge complexes **12$_{sMAO}$**/MAO and

13$_{sMAO}$/MAO (Me^{n}PrSi and MePhSi respectively) show relatively reduced activities in propylene polymerisation. Polymerisations using **12**$_{sMAO}$/MAO and **13**$_{sMAO}$/MAO could be conducted at $30 \leq T_p \leq 80$ °C for 30 minutes without solution viscosity being excessive. The Me^{n}PrSi system showed a minimal temperature dependence, while the MePhSi system had a peak activity of 2150 kg_{PP} mol_{Ti}^{-1} h^{-1} bar^{-1} at 50 °C. The additional steric bulk afforded by the *n*-propyl and phenyl groups pendant at the silane bridge results in an increased energetic barrier to monomer insertion leading to reduced activities, which is more pronounced at lower temperatures.

4.3.1. Polypropylene microstructure

The molecular weight and dispersity of polypropylenes synthesised by the mixed-bridge catalysts is broadly consistent with that of the dimethyl bridged complex, though with molecular weight following the general trend Me_2Si > Me^{n}PrSi > MePhSi (Figure 4.12).

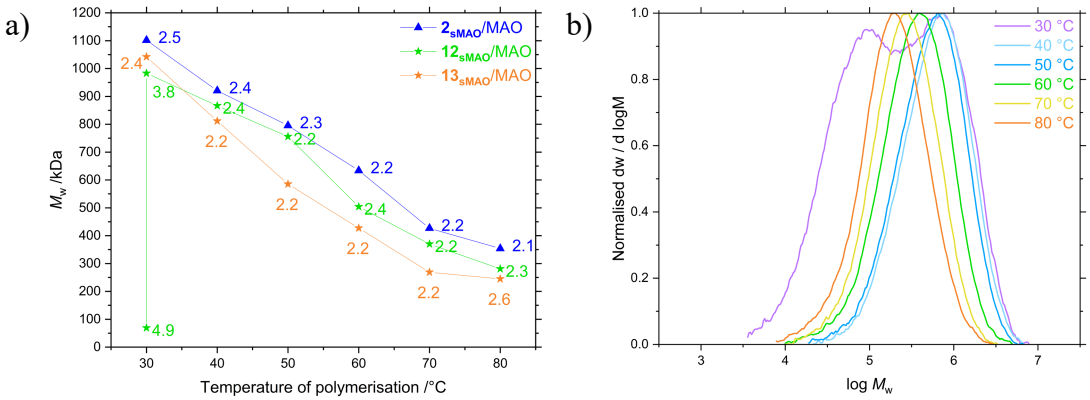

Figure 4.12 a) Weight-average molecular weight (M_w, PDIs annotated) as a function of polymerisation temperature of PP synthesised by **2**$_{sMAO}$/MAO, **12**$_{sMAO}$/MAO, and **13**$_{sMAO}$/MAO. b) Gel permeation chromatogram of PP synthesised by **12**$_{sMAO}$/MAO at $30 \leq T_p \leq 80$ °C. Polymerisation conditions: 10 mg catalyst, 2 bar propylene, 50 mL hexanes, 30 minutes, and MAO ([Al_{MAO}]/[Ti] = 1000).

Of particular note is the bimodal M_w distribution produced by the Me^{n}Pr complex **12**$_{sMAO}$ at a temperature of 30 °C (Figure 4.12b). This may indicate the presence of two distinct

active sites at low temperatures, one of which having a larger energetic barrier to monomer insertion and perhaps therefore greater enantioselectivity.

The polymers were analysed by solution-phase $^{13}C\{^{1}H\}$ NMR spectroscopy and differential scanning calorimetry. Both isotactic and syndiotactic PP are expected to be partially crystalline; *i*PP has a melting temperature of 190 °C, and *s*PP has a melting temperature of 160 °C. In DSC experiments, the PP synthesised by both **12**$_{\mathbf{sMAO}}$/MAO and **13**$_{\mathbf{sMAO}}$/MAO is essentially amorphous at all polymerisation temperatures. For PP synthesised by the Me^{n}PrSi complex **12**$_{\mathbf{sMAO}}$/MAO, very weak melting transitions at around 175 °C or cold crystallisations around 190 °C were observed on the first heating cycles for some samples, which may indicate a degree of crystallinity arising from a slightly isotactically enriched polymer. However, no transitions were detected on subsequent heating or cooling cycles, consistent with the formation of a stable amorphous phase.

This mirrors the findings of Senda *et al*., who synthesised a range of mixed-bridge Cp*–PHENICS complexes with MeEtSi, MeCySi, and MePhSi bridges (^{Me,R_a}SB($^{t Bu,Me}$ArO,Cp*)TiCl$_2$; R = Et, Cy, Ph).[63,64] In that study, it was found that the substituents at silicon (both symmetric and mixed) had a strong influence on molecular weight and regioselectivity, but not on stereoselectivity. When polymerised at 40 °C, under 2 bar of propylene pressure in 150 mL of toluene, and activated by TIBA/TB, it was found that the MePhSi complex gave *a*PP with M_w of 1.3 MDa and 11.5% of 2,1-regioerrors, while the MeCySi complex gave a polymer with M_w of 2.3 MDa, and 4.1% regioerrors. The [*mmmm*] pentad fractions of polymers synthesised by the mixed-bridge Cp*–PHENICS complexes showed no improvement over the symmetrically bridged complexes, with all polymers reported in the range 1.58–2.77%.

Solution-phase $^{13}C\{^{1}H\}$ NMR analysis, performed by Prof. Roberta Cipullo (Università Federico II, Naples), using a CM-*C*1 model,[65] determines the stereochemistry at the pentad level as [*mmmm*] fractions of 4.2% (**2$_{sMAO}$**/MAO), 8.7% (**12$_{sMAO}$**/MAO), and 4.2% (**13$_{sMAO}$**/MAO). The spectra are consistent with a chain migratory mechanism, with the complexes possessing two diastereotopic sites, one highly (S1) and one moderately (S2) enantioselective. After insertion at S1, the probability of insertion at S2 is $P_{12} > 0.9$, while the probability of subsequent insertion at S1 after S2 is $P_{21} << 0.5$, with a large tendency for chain back-skip – this leads to consecutive monomer insertion at the less stereoselective site S2.[66] The MePhSi complex shows no improvement in stereoselectivity compared with the achiral Me_2Si complex, whereas the Me^{n}PrSi complex is more than twice as isoselective, though insufficiently so to result in a stable degree of crystallinity.

4.4. Conclusions

Selective synthesis of UHMWaPP by an industrially viable high-yielding process has been described for the first time.

Ansa permethylindenyl-phenoxy (PHENI*) complexes have proven to be remarkably active catalysts for the polymerisation of propylene in both solution-phase and when supported on solid polymethylaluminoxane (sMAO). Activities up to 12 000 $kg_{PP}\ mol_{Ti}^{-1}\ h^{-1}\ bar^{-1}$ are reported at 2 bar propylene pressure, and this appears to be limited principally by reaction conditions. Furthermore, the product is a fully amorphous, ultra-high molecular weight, atactic, and regioregular polypropylene (UHMWaPP). Molecular weights were measured up to 2.0 MDa by GPC, among the highest values reported in the literature.

UHMWaPP demonstrates mechanical behaviour that is broadly comparable to EPM and other commercial thermoplastic elastomers, including remarkable extensibility with a strain at break of >1900%, and a low elastic set of 7% in elastic recovery hysteresis experiments.

This demonstrates the potential of PHENI* catalysts to synthesise homopolymeric UHMWaPP efficiently under mild conditions. The material properties of UHMWaPP are potentially competitive with commercial composite and copolymeric thermoplastic elastomers, with advantages in processability and recyclability, while offering optical transparency, comparable strength, and high ductility.

In addition, two mixed-bridge PHENI* complexes – chiral at silicon – were investigated as catalysts for propylene polymerisation. Both produced essentially atactic polymer, though *rac*-$^{Me,n Pr}$SB($^{t Bu_2}$ArO,I*)TiCl$_2$ showed a slight degree of stereoinduction by ^{13}C NMR with a [*mmmm*] pentad fraction double that of the parent complex.

4.5. References

1 A. C. Shamiri, M.H.; Jahan, S.; Hussain, M.A.; Kaminsky, W.; Aravind, P.V.; Yehye, W.A., *Materials*, 2014, **7**, 5069-5108.
2 P. Corradini, V. Barone, R. Fusco, G. Guerra, *Eur. Polym. J.*, 1979, **15**, 1133-1141.
3 N. Bahri-Laleh, A. Hanifpour, S. A. Mirmohammadi, A. Poater, M. Nekoomanesh-Haghighi, G. Talarico, L. Cavallo, *Prog. Polym. Sci.*, 2018, **84**, 89-114.
4 A. Shamiri, M. H. Chakrabarti, S. Jahan, M. A. Hussain, W. Kaminsky, P. V. Aravind, W. A. Yehye, *Materials*, 2014, **7**, 5069-5108.
5 Z. Zhang, R. Zhang, Y. Huang, J. Lei, Y. H. Chen, J. H. Tang, Z. M. Li, *Ind. Eng. Chem. Res.*, 2014, **53**, 10144-10154.
6 C. De Rosa, F. Auriemma, C. Spera, G. Talarico, O. Tarallo, *Macromolecules*, 2004, **37**, 1441-1454.
7 L. Resconi, R. L. Jones, A. L. Rheingold, G. P. A. Yap, *Organometallics*, 1996, **15**, 998-1005.
8 Q. Wu, Q. Su, L. Ye, G. Li, Y. Mu, *Dalton Trans.*, 2010, **39**, 2525-2535.
9 G. W. Coates, *Chem. Rev.*, 2000, **100**, 1223-1252.
10 L. Resconi, L. Cavallo, A. Fait, F. Piemontesi, *Chem. Rev.*, 2000, **100**, 1253-1346.
11 J. A. Ewen, *J. Am. Chem. Soc.*, 1984, **106**, 6355-6364.
12 W. Spaleck, M. Antberg, J. Rohrmann, A. Winter, B. Bachmann, P. Kiprof, J. Behm, W. A. Herrmann, *Angew. Chem. Int. Ed. Engl.*, 1992, **31**, 1347-1350.
13 J. Saito, M. Onda, S. Matsui, M. Mitani, R. Furuyama, H. Tanaka, T. Fujita, *Macromol. Rapid Commun.*, 2002, **23**, 1118-1123.
14 T. Miyatake, K. Mizunuma, Y. Seki, M. Kakugo, *Makromol. Chem., Rapid Commun.*, 1989, **10**, 349-352.
15 S. Segal, I. Goldberg, M. Kol, *Organometallics*, 2005, **24**, 200-202.

16 K. Nomura, S. Pengoubol, W. Apisuk, *Molecules*, 2019, **24**, 1634.
17 K. C. Jayaratne and L. R. Sita, *J. Am. Chem. Soc.*, 2000, **122**, 958-959.
18 M. Fujita, Y. Seki, T. Miyatake, *J. Polym. Sci., Part A: Polym. Chem.*, 2004, **42**, 1107-1111.
19 K. Nomura, S. Pengoubol, W. Apisuk, *RSC Adv.*, 2016, **6**, 16203-16207.
20 B. Rieger, C. Troll, J. Preuschen, *Macromolecules*, 2002, **35**, 5742-5743.
21 S. Basak, *J. Macromol. Sci. A*, 2021, **58**, 579-593.
22 D. Z. Pirityi and K. Pölöskei, *Polymers*, 2021, **13**, 1116.
23 G. van Doremaele, M. van Duin, M. Valla, A. Berthoud, *J. Polym. Sci., Part A: Polym. Chem.*, 2017, **55**, 2877-2891.
24 H. Braunschweig and F. M. Breitling, *Coord. Chem. Rev.*, 2006, **250**, 2691-2720.
25 T. J. Williams, J. C. Buffet, Z. R. Turner, D. O'Hare, *Catal. Sci. Technol.*, 2018, **8**, 5454-5461.
26 M. Nabika, H. Katayama, T. Watanabe, H. Kawamura-Kuribayashi, K. Yanagi, A. Imai, *Organometallics*, 2009, **28**, 3785-3792.
27 H. Hanaoka, T. Hino, M. Nabika, T. Kohno, K. Yanagi, Y. Oda, A. Imai, K. Mashima, *J. Organomet. Chem.*, 2007, **692**, 4717-4724.
28 T. Senda, H. Hanaoka, S. Nakahara, Y. Oda, H. Tsurugi, K. Mashima, *Macromolecules*, 2010, **43**, 2299-2306.
29 M. Eskelinen and J. V. Seppala, *Eur. Polym. J.*, 1996, **32**, 331-335.
30 M. A. Parvez, M. Rahaman, M. A. Suleiman, J. B. P. Soares, I. A. Hussein, *Int. J. Polym. Sci.*, 2014, **2014**, 549031.
31 A. Dashti, S. H. Mazloumi, A. Bakhshi Ani, A. Akbari, *J. Chem. Eng. Data*, 2014, **59**, 2258-2262.
32 A. F. R. Kilpatrick, J. C. Buffet, P. Nørby, N. H. Rees, N. P. Funnell, S. Sripothongnak, D. O'Hare, *Chem. Mater.*, 2016, **28**, 7444-7450.
33 L. A. Rishina, Y. V. Kissin, S. S. Lalayan, V. G. Krasheninnikov, *J. Appl. Polym. Sci.*, 2019, **136**.
34 J. T. M. Pater, G. Weickert, W. P. M. van Swaaij, *Chem. Eng. Sci.*, 2002, **57**, 3461-3477.
35 G. J. P. Britovsek, V. C. Gibson, D. F. Wass, *Angew. Chem. Int. Ed. Engl.*, 1999, **38**, 428-447.
36 S. Mansel, E. Pérez, R. Benavente, J. M. Pereña, A. Bello, W. Röll, R. Kirsten, S. Beck, H. H. Brintzinger, *Macromol. Chem. Phys.*, 1999, **200**, 1292-1297.
37 R. W. Wilkinson and M. Dole, *J. Polym. Sci.*, 1962, **58**, 1089-1106.
38 N. Hirai and H. Eyring, *J. Appl. Phys.*, 1958, **29**, 810-816.
39 N. Hirai and H. Eyring, *J. Polym. Sci.*, 1959, **37**, 51-70.
40 T. Miyatake, Y. Kawai, Y. Seki, M. Kakugo, K. Hikichi, *Polym. J.*, 1989, **21**, 809-814.
41 S. N. Zhu, X. Z. Yang, R. Chûjô, *Polym. J.*, 1983, **15**, 859-868.
42 V. Busico, R. Cipullo, G. Monaco, G. Talarico, M. Vacatello, J. C. Chadwick, A. L. Segre, O. Sudmeijer, *Macromolecules*, 1999, **32**, 4173-4182.
43 V. Busico, R. Cipullo, G. Monaco, M. Vacatello, A. L. Segre, *Macromolecules*, 1997, **30**, 6251-6263.
44 R. C. Klet, D. G. VanderVelde, J. A. Labinger, J. E. Bercaw, *Chem. Commun.*, 2012, **48**, 6657-6659.
45 T. Asakura, Y. Nishiyama, Y. Doi, *Macromolecules*, 1987, **20**, 616-620.
46 Z. Zhou, J. C. Stevens, J. Klosin, R. Kümmerle, X. Qiu, D. Redwine, R. Cong, A. Taha, J. Mason, B. Winniford, P. Chauvel, N. Montañez, *Macromolecules*, 2009, **42**, 2291-2294.
47 V. Busico, R. Cipullo, J. C. Chadwick, J. F. Modder, O. Sudmeijer, *Macromolecules*, 1994, **27**, 7538-7543.
48 ISO, *ISO 1183: Plastics – Methods for determining the density of non-cellular plastics*, 2019.
49 X. Song, L. Cao, R. Tanaka, T. Shiono, Z. Cai, *ACS Macro Lett.*, 2019, **8**, 299-303.
50 ISO, *ISO 527: Plastics – Determination of tensile properties*, 2019.
51 K. J. Wright and A. J. Lesser, *Macromolecules*, 2001, **34**, 3626-3633.
52 L. A. Rishina, Y. V. Kissin, S. S. Lalayan, V. G. Krasheninnikov, E. O. Perepelitsina, T. I. Medintseva, *Polym. Sci. Ser. B*, 2016, **58**, 152-162.
53 E. E. Faingol'd, S. L. Saratovskikh, A. N. Panin, O. N. Babkina, I. V. Zharkov, N. O. Garifullin, G. V. Shilov, N. M. Bravaya, *Polymer*, 2021, **220**, 123559.
54 C. Jourdan, J. Y. Cavaille, J. Perez, *J. Polym. Sci., Part B: Polym. Phys.*, 1989, **27**, 2361-2384.
55 P. Svoboda, R. Theravalappil, D. Svobodova, P. Mokrejs, K. Kolomaznik, K. Mori, T. Ougizawa, T. Inoue, *Polym. Test.*, 2010, **29**, 742-748.
56 M. Mihailov and L. Minkova, *Colloid. Polym. Sci.*, 1987, **265**, 681-685.
57 Dow Chemical Company, "INFUSE™ 9817 Olefin Block Copolymer", 400-00119899en, 29/09/2011.
58 DuPont de Nemours, Inc., "MULTIFLEX™ TPO 50 D 41 81171 Polyolefin Thermoplastic Elastomer", 08/11/2021.
59 J. A. Ewen, *J. Mol. Catal. A Chem.*, 1998, **128**, 103-109.
60 M. A. Bau, S. Wiesler, S. L. Younas, J. Streuff, *Chem. Eur. J.*, 2019, **25**, 10531-10545.

61 B. Rieger, G. Jany, R. Fawzi, M. Steimann, *Organometallics*, 1994, **13**, 647-653.
62 E. Kirillov, N. Marquet, M. Bader, A. Razavi, V. Belia, F. Hampel, T. Roisnel, J. A. Gladysz, J. F. Carpentier, *Organometallics*, 2011, **30**, 263-272.
63 T. Senda, H. Hanaoka, T. Hino, Y. Oda, H. Tsurugi, K. Mashima, *Macromolecules*, 2009, **42**, 8006-8009.
64 T. Senda, H. Hanaoka, T. Hino, Y. Oda, H. Tsurugi, K. Mashima, *Macromolecules*, 2010, **43**, 5162-5162.
65 V. Busico and R. Cipullo, *Prog. Polym. Sci.*, 2001, **26**, 443-533.
66 G. Guerra, L. Cavallo, G. Moscardi, M. Vacatello, P. Corradini, *Macromolecules*, 1996, **29**, 4834-4845.

Chapter 5 – Copolymerisation of linear α-olefins

5.1. Introduction

The incorporation of linear α-olefins (LAOs) into ethylene polymers allows for control over short-chain branching, enabling tuneability of the chemical and physical properties of the resulting linear low density polyethylene (LLDPE) polymers.[1-4] Propylene, 1-butene, 1-pentene, 1-hexene, 1-octene, and higher olefins up to at least 1-hexacosene have been studied as comonomers for ethylene polymerisation.[5-13] While less studied, copolymers of propylene with 1-butene, 1-hexene, 1-octene, and higher olefins up to 1-octadecene have been synthesised using a range of catalysts.[14-17]

Heterogeneous Ziegler-Natta catalysts have been used in the copolymerisation of ethylene with LAOs with high activities, but relatively limited comonomer incorporation.[18,19] Metallocenes such as Cp_2ZrCl_2, $(^nBuCp)_2ZrCl_2$, $EBIZrCl_2$, and $^{Me_2}SBCp_2ZrCl_2$, when activated with MAO, have shown good homogeneous catalytic activity towards E/LAO copolymerisation with a more uniform comonomer distribution than is possible with heterogeneous systems.[20-22] Quijada *et al.* showed that *ansa*-bridged metallocenes enabled higher LAO incorporation than unbridged analogues.[22]

With the development of post-metallocene catalysts such as the Constrained Geometry Complexes (CGCs),[23] it was shown that ligands with electron-donating substituents had increased activities and afforded copolymers with increased molecular weights, and high comonomer incorporations.[24,25]

Group four PHENICS complexes utilising Cp-,[26,27] Ind-,[28] and Flu-derived[29] apical ligands have demonstrated LAO incorporations of up to 35 mol%, reported with the

complex {Me_2C–(Cp)PhO}$TiCl_2$ in toluene, under 6 bar ethylene pressure and with 200 mM concentration of 1-hexene.[27] Compared to CGC, PHENICS complexes were found to result in greater E/C6 copolymerisation activities as well as high comonomer incorporation.[27,28]

Williams *et al.* have reported activity enhancements in E/C6 copolymerisation when using the permethylindenyl complex $^{Me_2}SB(^{t Bu}N,I^*)TiCl_2$ compared to the CGC $^{Me_2}SB(^{t Bu}N,Cp^*)TiCl_2$, though lower comonomer incorporations were reported for the CGCI* complex.[30,31]

Irwin *et al*. reported the complex $^{Me_2}SB(\eta^1\text{-}C_{29}H_{36},^{t Bu}N)ZrCl_2\cdot OEt_2$, based on a substituted fluorenyl apical ligand, which, in E/C8 copolymerisations, demonstrated activities and 1-octene incorporations proportional to comonomer concentration.[32] Activities as high as 81 000 kg mol_{Zr}^{-1} h^{-1} bar^{-1} and incorporations of 75 mol% were reported for reactions conducted in neat 1-octene, under 80 psi (5.5 bar) ethylene pressure at 75 °C. In this case an "unyielding comonomer effect" describes the phenomenon of linearly increasing activities with comonomer concentration. This is contrary to the behaviour of most olefin copolymerisation systems where, after an initial comonomer effect,[33] activities generally reduce with further increases in comonomer concentration.

Heterogenised single-site catalysts can be used in gas-phase and slurry-phase processes which overcome morphological constraints and reactor fouling. Organometallic complexes for olefin copolymerisations have been immobilised on a range of solid supports including silica,[34] sMAO,[30] LDH,[35,36] and (aminomethyl)polystyrene.[37]

5.1.1. Chapter synopsis

Following the synthesis of PHENI* catalysts in Chapter 2, and their application to ethylene and propylene homopolymerisation in Chapters 3 and 4, this chapter describes the application of the PHENI* complex ^{Me_2}SB(^{t}Bu$_2$ArO,I*)TiCl$_2$, supported on sMAO, in a wide range of olefinic copolymerisation regimes. Ethylene, propylene, 1-hexene, 1-octene, 1-dodecene, and 5-ethylidene-2-norbornene are used as monomers for the synthesis of ethylene-propylene rubber (EPM), linear low-density polyethylene (LLDPE), propylene-hexene copolymer (PPH), and ethylene-propylene-diene terpolymer (EPDM). Post-polymerisation modification of the unsaturated EPDM has been demonstrated using a model sulphur vulcanisation system. Finally, multivariate statistical tools are used on the PHENI* ethylene/LAO copolymerisation dataset, demonstrating the immense tunability of this copolymerisation system, and the analytical and predictive power of models derived from large datasets.

5.2. Copolymerisation of ethylene with propylene

Copolymers of ethylene and propylene (EPM) are an important class of elastic materials, with extensive research relating the physical properties to the composition and chain structure.[38] Vanadium-based catalysts dominate the industrial production of EPM,[39] though group four complexes have also been studied,[40] with the Keltan ACE™ titanium amidinate complexes used commercially.[41]

The effects of temperature, scavenger, and partial pressure of monomer have been studied using the catalyst sMAO-^{Me_2}SB(^{t}Bu$_2$ArO,I*)TiCl$_2$ (**2$_{sMAO}$**, [Al$_{sMAO}$]/[Ti] = 200), which demonstrated the greatest activity of the synthesised PHENI* complexes for the homopolymerisation of both ethylene and propylene. Copolymerisations were carried out in 150 mL Rotaflo® ampoules for 30 minutes in 50 mL hexanes, using 10 mg **2$_{sMAO}$** and

2 bar total pressure. A mixed gas feed of ethylene (E) and propylene (P) was used in a ratio of 25:75, 50:50, or 75:25. The temperature of polymerisation (T_p) was in the range $30 \leq T_p \leq 90$ °C. The resulting copolymer is referred to as EPM.

In the homopolymerisation of ethylene, **2**$_{\mathbf{sMAO}}$/TIBA showed the greatest catalytic activity, while in propylene homopolymerisation the highest activities were achieved with **2**$_{\mathbf{sMAO}}$/MAO. Therefore, E/P copolymerisations were performed using a 50:50 monomer feed mixture and either MAO or TIBA as scavenger (Figure 5.1). As a scavenger, TIBA displayed significantly higher copolymerisation activity than MAO, 3313 and 548 $kg_{EPM}\ mol_{Ti}^{-1}\ h^{-1}\ bar^{-1}$ respectively. It has previously been noted that TIBA can transalkylate with MAO, leading to *iso*-butyl substituted aluminoxanes that are almost inactive towards propylene polymerisation.[42] When using **2**$_{\mathbf{sMAO}}$/TIBA, E/P copolymerisation activity was comparable to that of ethylene homopolymerisation (3719 $kg_{PE}\ mol_{Ti}^{-1}\ h^{-1}\ bar^{-1}$), though in a highly dissimilar diffusion regime: while polyethylene was formed as well dispersed solid particles, EPM is hexane-soluble at all compositions studied, and forms as a gel instead. Copolymerisations were subsequently run using E:P ratios of 25:75 and 75:25 with **2**$_{\mathbf{sMAO}}$/TIBA as the catalyst system. In these cases, activity is approximately independent of monomer feed composition, being within 1 standard deviation of each other. The titanium half-sandwich complexes reported by Zhang *et al.*, which incorporate X-type anionic nitrogen-based donors, demonstrated activities of up to 2390 $kg_{EPM}\ mol_{Ti}^{-1}\ h^{-1}$.[43] In this case, an E/P ratio of 33:67 resulted in 38 mol% propylene incorporation, and a viscosity-average molecular weight, M_η, of 340 kDa. It was found that both activity and propylene incorporation increased with increasing TIBA/Ti ratio. The commercial Keltan ACE™ complexes have demonstrated

activities as high as 132 500 kg_{EPM} mol_{Ti}^{-1} h^{-1} bar^{-1}, molecular weights up to 1.7 MDa, and incorporations up to 61 wt% P from a feed containing 67% propylene.[41]

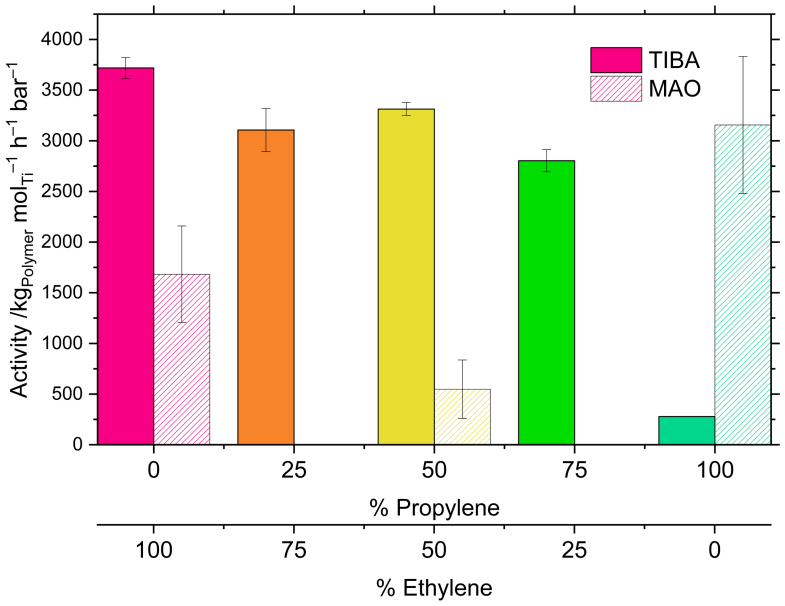

Figure 5.1 Mean polymerisation activity as a function of monomer feed composition for sMAO-^{Me2}SB(^{tBu2}ArO,I*)$TiCl_2$. Polymerisation conditions: 10 mg catalyst, 2 bar total pressure, 50 mL hexanes, either 150 mg TIBA or MAO ([Al_{MAO}]/[Ti] = 1000), 60 °C, and 30 minutes. Error bars shown at one standard deviation.

The resulting EPM copolymers were analysed by gel permeation chromatography (GPC), infrared (IR) and nuclear magnetic resonance (NMR) spectroscopy, and differential scanning calorimetry (DSC) techniques. All of the EPM synthesised in this chapter was found to be amorphous by DSC, with no melting, crystallisation, or glass transitions observed between 30–180 °C – consistent with the production of a random copolymer. Glass transitions would be expected to occur at temperatures below –30 °C and show a dependency on the copolymer composition.[44,45] Caballero *et al.* report amorphous copolymers in the composition range 21–59 mol% ethylene, with the crystallinity afforded by the ethylene and *i*PP segments observable only at the outer extremes of composition.[44]

Polymer molecular weight and distribution were estimated from GPC as well as short-chain branching (SCB) density and composition from an inline IR detector (Figure 5.2). Weight-average molecular weight (M_w) was found to be greater when the scavenger was MAO than TIBA, 290 and 150 kDa respectively, due to a high molecular weight shoulder in the chromatogram. This is reflected in a greater dispersity (PDI) of 3.1 when using MAO compared to 2.3 with TIBA.

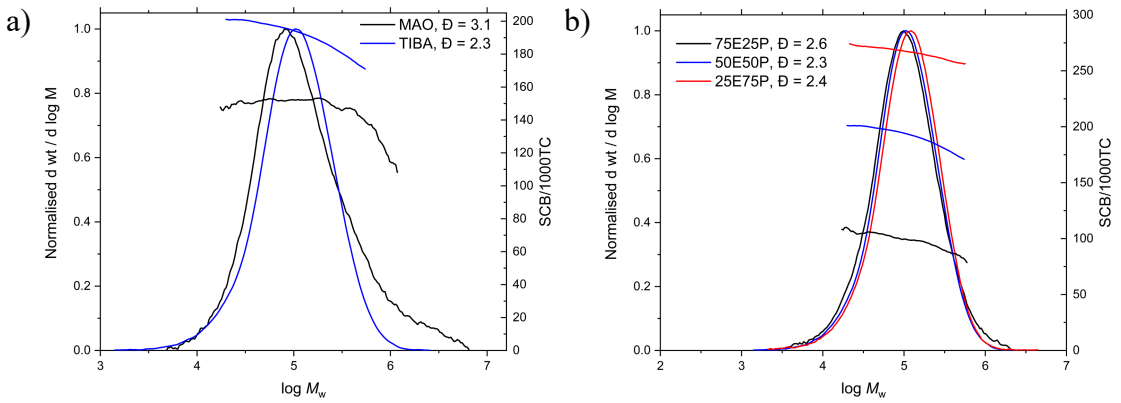

Figure 5.2 Gel permeation chromatograms with overlayed short chain branching density as a function of log(M_w) of EPM synthesised using $\mathbf{2}_{\mathbf{sMAO}}$. a) 50:50 E/P using either MAO or TIBA as scavenger, and b) using TIBA and an E/P ratio of either 25:75, 50:50, or 75:25. Theoretical branching densities: 2:1 copolymer (143 SCB/1000TC), 1:1 copolymer (200 SCB/1000TC), 1:2 copolymer (250 SCB/1000TC).

Both molecular weight and PDI were largely independent of feed composition, with M_w in the range 150–160 kDa from 25–75% propylene. The NHC-supported vanadium (V) complex reported by Zhang *et al.* copolymerises ethylene and propylene in a "quasi-living" manner resulting in molecular weights up to 1.6 MDa.[46]

Copolymer composition demonstrated precise tuneability, with the monomer ratio in the EPM corresponding almost exactly to that in the feed gas mixture. By GPC–IR, the EPM copolymers were found to contain 20, 42, and 71 wt% propylene; this was confirmed by quantitative solution-phase $^{13}C\{^1H\}$ NMR spectroscopy, which gave values of 26, 45, and 74 wt% propylene. Short chain branching per 1000 total carbon (SCB/1000TC) is

determined from GPC by the ratio of CH_3 and CH signals from an inline infrared spectrometer, which can be used to calculate comonomer incorporation. NMR spectra were recorded in 1,1,2,2-tetrachloroethane-d_2 at 403 K using an inverse-gated decoupling pulse sequence and assigned according to the analysis of Wang *et al.*.[38,47,48] A comparative study of comonomer incorporation determination using GPC-IR and ^{13}C NMR techniques has previously been reported by Suárez *et al.*, who note the utility of the IR output from routine GPC analysis and were able to achieve a 2% deviation between the two techniques.[49,50]

Such direct tuneability of the comonomer composition as an almost 1-to-1 function of the feed gas is an unusual feature of the PHENI* catalyst system. By contrast, the [O-NS] titanium complex used by Yao *et al.* produced EPM with up to 29.5 mol% propylene incorporation at 60 °C, even when the feed was 33:67 E/P. Whilst the incorporation was approximately linear over the composition regimes studies in this case, it was far from a 1-to-1 relationship.[51] The half-titanocene complexes synthesised by Zhang *et al.* could incorporate up to 44 mol% propylene at the same feed ratio at T_p = 80 °C.[43] Vanadium compounds dominate the commercial production of ethylene-propylene copolymers. The vanadium (III) NHC complexes reported by Zhang *et al.* were able to incorporate up to 39 mol% propylene under a 75:25 E/P monomer supply.[46] Caballero *et al.* used the catalyst ($SB^{2\text{-}Me}I$)$ZrCl_2$ to synthesise a complete range of EPM compositions, though the system preferentially polymerised ethylene, with a 3:97 E/P feed resulting in a polymer with 13 mol% ethylene.[44]

5.2.1. The effect of temperature on E/P copolymerisation

The effect of polymerisation temperature on E/P copolymerisation was determined using a monomer feed with 50:50 composition. Catalytic activity is shown in Figure 5.3,

alongside ethylene homopolymerisation activity under the same catalytic regime for comparison. Surprisingly, a virtually identical temperature profile is observed in both cases, suggestive of a common rate limiting process. The profile is similar to that of the half-titanocenes reported by Zhang *et al.* which show a peak at 60 °C, with propylene incorporation decreasing at higher polymerisation temperatures.[43]

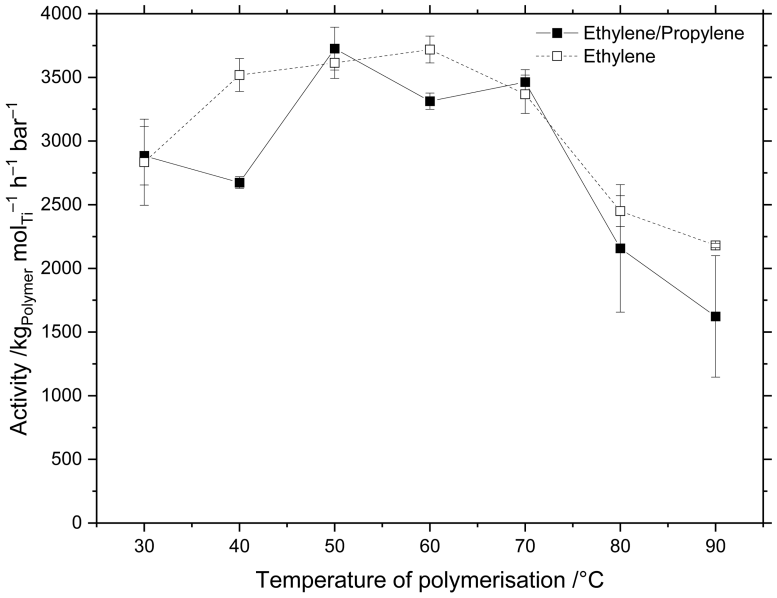

Figure 5.3 Mean polymerisation activity as a function of temperature of polymerisation using **2**$_{sMAO}$/TIBA. Polymerisation conditions: 10 mg catalyst, 2 bar total pressure (either ethylene or 50:50 ethylene/propylene), 50 mL hexanes, 150 mg TIBA, and 30 minutes. Error bars shown at one standard deviation.

The temperature dependence of incorporation is often studied as it gives an indication of the reactivity ratio of the catalyst towards ethylene insertion compared to propylene.[51]

M_w decreases with increasing temperature as is expected for all olefinic copolymerisations as the rate of chain termination increases relative to that of propagation (Figure 5.4). PDIs were consistent and relatively small, being in the range 2.3–2.6 for all temperatures. Remarkably, the polymer composition was not found to significantly depend on the temperature of polymerisation, being in the range 40–47 wt% and broadly

reflecting the 50:50 E/P composition of the feed gas. Yao *et al.* reported salicyaldiminato-based titanium complexes which show a maximum propylene incorporation at 60 °C, which relates to a minimum in the quantity r_{EP}*r_{PE}.[51]

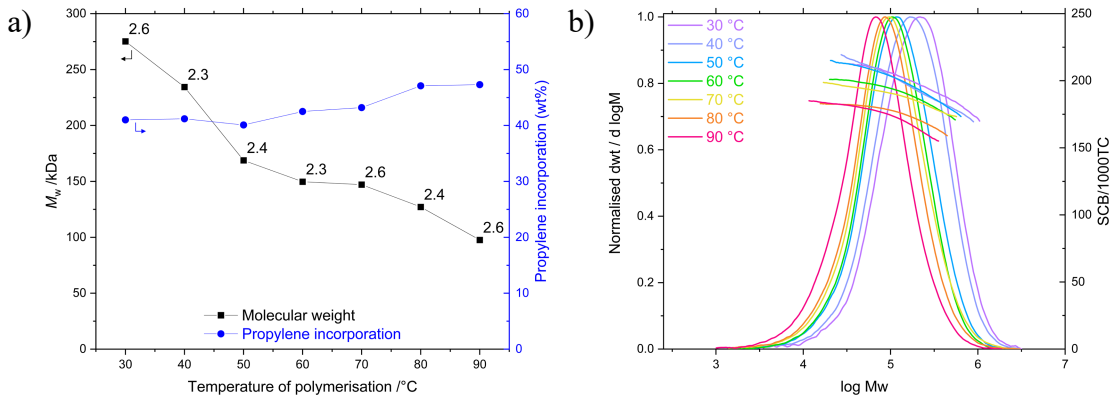

Figure 5.4 a) Weight-average molecular weight, with PDIs annotated, and propylene incorporation as a function of temperature, and b) gel permeation chromatograms with overlayed short chain branching density as a function of log(M_w) of EPM synthesised using **2$_{sMAO}$**/TIBA using 50:50 E/P and a temperature of polymerisation of 30–90 °C.

5.3. Terpolymerisation of ethylene, propylene, and a diene

Following the successful synthesis of EPM polymers at high activity and with tuneable composition, the catalytic system **2$_{sMAO}$**/TIBA was used in the terpolymerisation of ethylene, propylene, and 5-ethylidene-2-norbornene (E/P/ENB). Due to the toxicity and difficulty of handling butadiene, surrogates such as 5-ethylidene-2-norbornene (ENB), 4-vinylcyclohexene (VH), and 1,4-hexadiene (HD) are commonly used.[52] ENB is commonly used as a diene in multicomponent polymerisations, as only the internal norbornyl olefin participates in polymerisation, with the ethylidene providing pendant unsaturation to the polymer backbone which can then undergo post-polymerisation modifications such as crosslinking. EPDM is the most-produced non-tyre rubber, and is more resistant to oxygen, ozone, UV, and heat than commodity rubbers.[53]

As before, 10 mg **2**$_{sMAO}$, 150 mg TIBA, and 45 mL hexanes was charged into a Rotaflo® ampoule with ENB (up to 625 µL) and 5 mL hexanes charged into a side arm. The ampoule was stirred at 1000 rpm in a thermostatic oil bath, and the reaction was started by exposing the ampoule to 2 bar of an ethylene/propylene mix (50:50) while simultaneously opening the side arm. After 30 minutes, the ampoule was vented, the polymer was precipitated in acetone/water, and dried overnight in a vacuum oven.

After initially increasing by 56% to 5155 $kg_{EPDM}\ mol_{Ti}^{-1}\ h^{-1}\ bar^{-1}$ at 78 µL, terpolymerisation activity rapidly decreased as [ENB] increased, reaching 1065 $kg_{EPDM}\ mol_{Ti}^{-1}\ h^{-1}\ bar^{-1}$ at 625 µL (Figure 5.5).

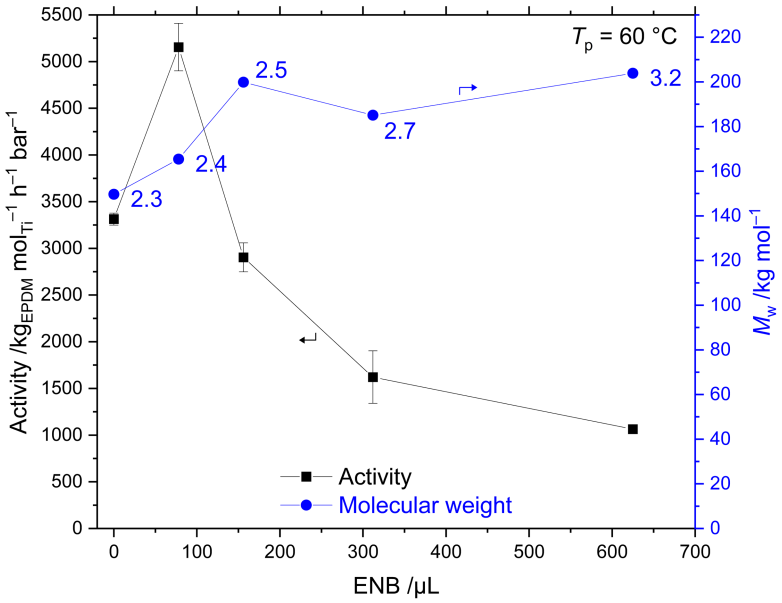

Figure 5.5 Mean terpolymerisation activity of **2**$_{sMAO}$/TIBA and EPDM molecular weight (M_w, with PDIs annotated) as a function of ENB loading ($0 \leq V \leq 625$ µL; $0 \leq c \leq 93$ mM). Polymerisation conditions: 10 mg catalyst, 2 bar ethylene/propylene (50:50), 50 mL hexanes, 150 mg TIBA, 60 °C, and 30 minutes. Error bars shown at one standard deviation.

5.3.1. Characterisation of EPDM

EPDM molecular weight was estimated by GPC. Contrary to the findings in E/LAO copolymerisation (*vide infra*), M_w increased slightly with increasing ENB loading,

reaching 204 kDa at 625 μL, 36% higher than the E/P copolymerisation in the absence of ENB, resulting from poor chain transfer to ENB.[54] Dispersities increase with increasing [ENB] from 2.3 in the copolymer to 3.2 at 625 μL, indicating a broadened molecular weight distribution, contrary to the findings of E/LAO copolymers which generally have narrower PDIs as comonomer loading increases.

The composition of the EPDM polymers was determined by solution-phase ^{1}H NMR spectroscopy, according to the peak assignments and integral analysis of Leone *et al.* (Figure 5.6).[53] In the ENB-free copolymer, an E/P mol% ratio of 0.79 shows a slight preference for propylene insertion; in terpolymerisations, the preference is for ethylene, with E/P ratios of 1.1–1.6. The proportion of ENB in the terpolymer increases with increasing [ENB] from 1.8 mol% at 78 μL (12 mM) to 13.4 mol% at 625 μL (93 mM). The complex EBIZrCl$_2$ studied by Ali *et al.* produced EPDM with composition 79.5/18.2/2.30 mol% (E/P/ENB) from an 80:20 E/P feed with 60 mM ENB at an activity of 3.55 x 10^6 kg$_{EPDM}$ mol$_{Zr}^{-1}$ h^{-1}.[54] Malmberg *et al.* used the same catalyst and achieved ENB incorporations of up to 16 mol% at a 600 mM concentration.[55] The vanadium (V) complexes studied by Leone *et al.* produced polymer with composition 80.3/6.5/13.2 mol% from an 18/73/9 feed at an activity of 3006 kg$_{EPDM}$ mol$_{V}^{-1}$ h^{-1}.[53]

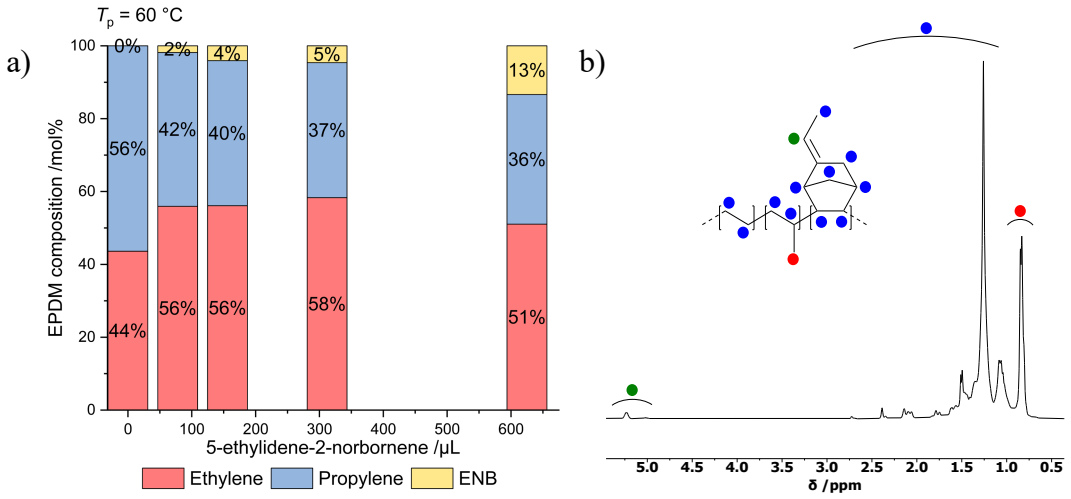

Figure 5.6 a) EPDM composition as a function of ENB loading, determined from ^{1}H NMR spectroscopy, and b) ^{1}H NMR spectrum (400 MHz, chloroform-*d*, 298 K) of EPDM, with assignments according to Leone *et al.*.[53]

5.3.2. Vulcanisation of EPDM

Systems for the crosslinking of unsaturated polymers, including Natural Rubber (NR) latexes, and EPDM terpolymers have been developed extensively in industry. Modern vulcanisation is a process involving dozens of additives and modifiers, such as silica and carbon black, in addition to peroxide- or sulphur-based crosslinking agents.[56] The purpose of the additional components is to optimise the vulcanisation kinetics and modify the physical and mechanical properties of the resulting rubbers.[57]

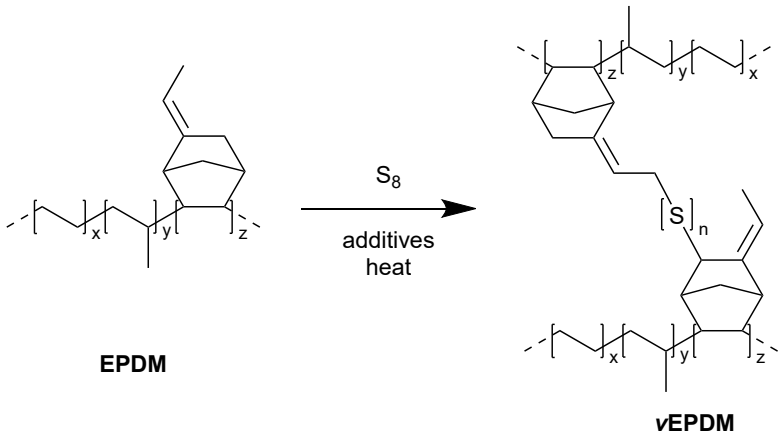

Equation 5.1 Reaction scheme for the sulphur vulcanisation of EPDM, adapted from the mechanism provided by Verbruggen *et al.*.[58]

In the interests of simplicity for this proof-of-concept study, a minimalist system comprising sulphur and the common accelerant 2-mercaptobenzothiazole ($C_6H_4(NH)SC{=}S$, MBT) was used to vulcanise EPDM. Relatively high loadings of S_8 (10 phr; parts per hundred rubber) and MBT (5 phr) were also used to ensure, in the absence of optimisations, sufficiently high conversion of ENB residues. Vulcanisations were performed in 50 μL DSC pans, and the reactions were followed by both dynamic and isothermal DSC protocols established through the work of Restrepo-Zapata *et al.*, who were able to fit simulated results and extract kinetic parameters.[56]

The polymer, sulphur, and MBT were combined in a toluene solution to ensure intimate mixing of the components, and the solvent was subsequently removed under vacuum. In the dynamic experiments, the samples were heated at a constant rate (2.5–20 °C min^{-1}) to 300 °C and then cooled to ambient temperature at the same rate. A second cycle was performed to obtain the baseline for the experiment. The isothermal experiments were performed by rapidly heating the samples to the desired temperature (180–200 °C), which was held for 3 hours, and then heated to 300 °C to ensure complete curing. The procedure was repeated to obtain a baseline for the experiment.

The thermograms resulting from the dynamic heating experiment show endothermic features corresponding to the melting points of sulphur (113 °C) and MBT (177–181 °C) (Figure 5.7). The exotherms between 180–230 °C are indicative of curing proceeding by sulphur crosslinking.

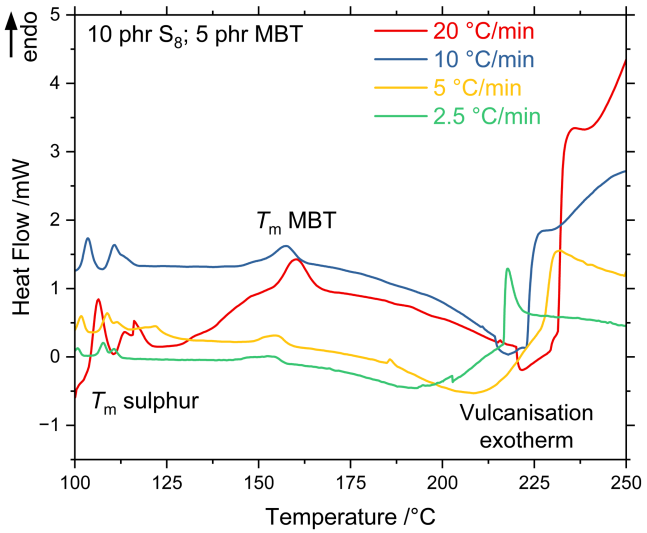

Figure 5.7 Differential scanning calorimetry thermograms for EPDM/S/MBT vulcanisation at heating rates of 2.5–20 °C min^{-1}.

These results demonstrate that copolymers containing unsaturation can be synthesised in high activities using the PHENI* catalyst platform with tuneable compositions. These polymers can then undergo industrially relevant post-polymerisation transformation reactions including cross-linking though conventional vulcanisation.

5.3.3. Characterisation of *v*EPDM

While EPDM is readily soluble in a range of organic solvents, *v*EPDM is not, losing less than 2% of its mass after several days in either boiling toluene or bromobenzene. This renders common solution-phase analysis impossible. The vulcanised rubbers were analysed by IR and ssNMR spectroscopy, and TGA (Figure 5.8).

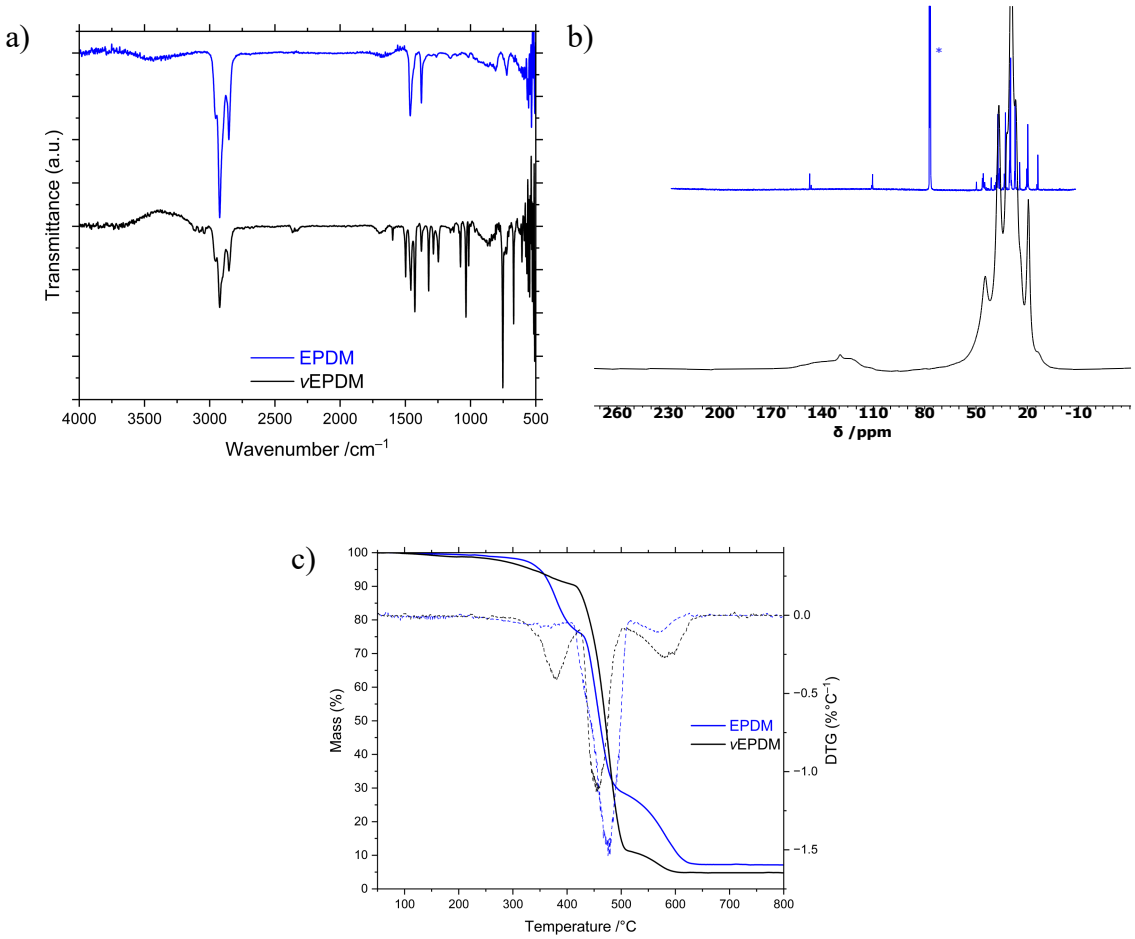

Figure 5.8 Characterisation of EPDM (blue) and *v*EPDM (black): a) IR spectroscopy, b) solution-phase (151 MHz, chloroform-*d*, 298 K, asterisk (*) denotes **C**DCl_3) and solid state (101 MHz, 10 kHz, 298 K) $^{13}C\{^1H\}$ NMR spectroscopy, and c) thermogravimetry.

In the infrared spectrum of *v*EPDM additional signals are observed compared to EPDM arising from C–H and C–C vibrations corresponding to the crosslinks,[59] and C–S vibrations are seen in the region 775–600 cm^{-1}.[60] Infrared S–S stretching transitions (510–450 cm^{-1}) were not observed in the wavenumber range studied. In ^{13}C NMR spectroscopy, the solid-state spectrum of *v*EPDM shows a broad resonance around 110–155 ppm, not present in the solution-phase spectrum of EPDM, and which corresponds to **C**–S resonances at the crosslink junctions α to the pendant olefin. Winters *et al.* showed that broad resonances in ssNMR spectra at δ 117 and 151 ppm arise from EPDM vulcanisation.[61] The TGA of EPDM and *v*EPDM both show a major mass-loss

event around 450–470 °C and a minor degradation at 580 °C which confirms that the main polymeric framework is preserved during vulcanisation. Furthermore, *v*EPDM has minor mass-loss events at 380 °C and a slightly higher residual char mass at 800 °C compared to EPDM – these features are attributed to the presence of vulcanisation additives and crosslinking.

5.4. Copolymerisation of propylene and 1-hexene

Propylene/LAO copolymers, such as poly(propylene-co-1-hexene) (PPH), are much less studied than their E/LAO counterparts, though *i*PP/LAO, *s*PP/LAO, and *a*PP/LAO copolymers have been reported and the comonomer shown to modify the physical properties of the polymers.[17,62]

The copolymerisation of propylene with 1-hexene (P/C6) was attempted using 10 mg **2$_{sMAO}$**, 50 mL hexanes, 2 bar propylene, at 60 °C and with either 150 mg TIBA or 40 mg MAO as cocatalyst and scavenger. With 625 μL C6, **2$_{sMAO}$**/TIBA had an activity of 254 $kg_{PPH}\ mol_{Ti}^{-1}\ h^{-1}\ bar^{-1}$, and **2$_{sMAO}$**/MAO displayed an activity of 1875 $kg_{PPH}\ mol_{Ti}^{-1}\ h^{-1}\ bar^{-1}$. This mirrors the homopolymerisation of propylene, where MAO resulted in much greater catalytic activities than TIBA. P/C6 copolymerisation was then investigated using **2$_{sMAO}$**/MAO as a function of comonomer loading (Figure 5.9). No positive comonomer effect was observed, and activities broadly decrease with increasing [C6]. Similarly, a positive comonomer effect was not found with the (^{ArMe_4}Cp)TiCl$_2$ODipp complexes reported by Wu *et al.*,[62] and of the complexes studied by Quijada *et al.*, only the isoselective SBIZrCl$_2$ catalyst showed a positive comonomer effect.[17]

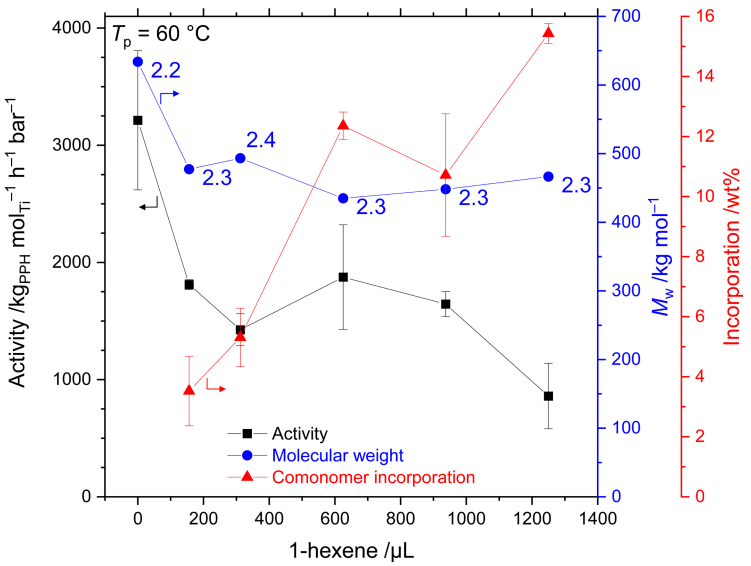

Figure 5.9 Mean copolymerisation activity of **2$_{sMAO}$**/MAO and the molecular weight (M_w, PDIs annotated) and mean C6 incorporation of PPH as a function of 1-hexene loading ($0 \leq V \leq 1250$ µL; $0 \leq c \leq 200$ mM). Polymerisation conditions: 10 mg catalyst, 2 bar propylene, 50 mL hexanes, 40 mg MAO ([Al$_{MAO}$]/[Ti] = 1000), 60 °C, and 30 minutes. Error bars shown at one standard deviation.

5.4.1. Characterisation of PPH

The resulting poly(propylene-co-1-hexene) (PPH) was analysed by GPC and NMR spectroscopy. Molecular weight was found to be 25% decreased in the copolymer compared to the propylene homopolymer, and remained approximately constant with increasing [C6] at 460 ± 20 kDa. The *a*PP/C6 reported by Wu *et al.* showed lower molecular weights (<200 kDa) which decreased with increasing incorporation.[62] Quijada *et al.* demonstrated that isoselective catalysts produced polymers whose M_w did not depend on comonomer concentration, while syndioselective complexes produced polymers where M_w decreased with increasing comonomer concentration.[17] Dispersities remained narrow, between 2.2 and 2.4. 1-Hexene incorporation was determined from quantitative ^{13}C NMR spectroscopy obtained from chloroform-*d* solution of the polymers: the relative integrals of the –CH$_2$CH(**C**H$_3$)– and –CH$_2$CH((CH$_2$)$_3$**C**H$_3$)– regions were used to calculate the mole fraction of C6. Incorporation increased

approximately proportionally to [C6] up to 15.4 mol% at 1250 μL (200 mM). Incorporations up to 10.1 mol% are reported by Wu *et al.* at [C6] of 500 mM,[62] and Arnold *et al.* used the complex EBIHfCl$_2$ to synthesise *i*PP/LAO copolymers over the complete composition range.[15] Uozumi *et al.* found that 1-hexene incorporation followed the trend aspecific < isospecific < syndiospecific.[63] Despite the PHENI* system being aspecific, **2$_{sMAO}$**/MAO is able to incorporate C6 more efficiently than these systems, with greater incorporations produced at lower comonomer concentrations.

5.5. Copolymerisation of ethylene with higher linear α-olefins

The catalyst system **2$_{sMAO}$**/TIBA was employed in the copolymerisation of ethylene with higher α-olefins, namely 1-hexene (H, C6), 1-octene (C8), and 1-dodecene (C12), and the effects of both polymerisation temperature and comonomer concentration were investigated. Copolymerisations were carried out in 150 mL Rotaflo® ampoules for 30 minutes in 50 mL hexanes (total volume), using 10 mg **2$_{sMAO}$** ([Al]/[Ti] = 200), 150 mg TIBA, and 2 bar pressure of ethylene. The comonomer (0–5000 μL) was added to a side arm and released into the reaction mixture simultaneously with the introduction of ethylene. The temperature of polymerisation (T_p) was in the range $30 \leq T_p \leq 90$ °C. The resulting copolymers are various grades of linear low-density polyethylene (LLDPE). A positive comonomer effect – the observed increase in activity upon addition of a comonomer relative to homopolymerisation – is common and several possible attributions have been proposed in the literature, including reduced activation energies, increased number of active sites, diffusion, accelerated fragmentation, and solubility.[33,64-67]

5.5.1. Copolymerisation of ethylene with 1-hexene

A positive comonomer effect was observed in ethylene-hexene (E/C6) copolymerisation, with a general increase in polymerisation activity with the concentration of comonomer (Figure 5.10). At 60 °C, activity with 50 mM 1-hexene was increased by 13% relative to homopolymerisation at 4218 $kg_{LLDPE}\ mol_{Ti}^{-1}\ h^{-1}\ bar^{-1}$.

Different behaviour was observed both at the extremes of temperature, and at high comonomer concentration. In the case of $T_p \leq 40$ °C, a drop in activity was observed upon initial addition of 1-hexene, and a positive comonomer effect was not observed until 100 mM. This is attributed to a larger energetic barrier for the coordination of 1-hexene compared to ethylene.

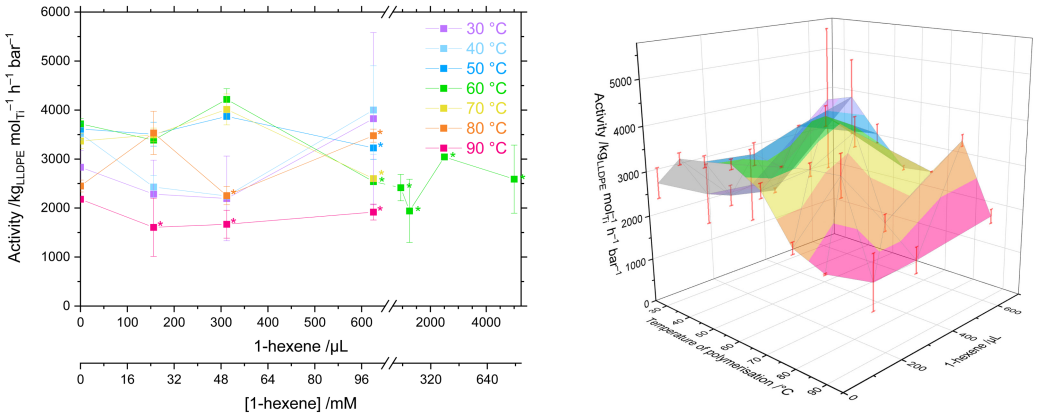

Figure 5.10 Mean copolymerisation activity of **2$_{sMAO}$** as a function of temperature of polymerisation ($30 \leq T_p \leq 90$ °C) and 1-hexene concentration ($0 \leq V \leq 5000$ µL; $0 \leq c \leq 800$ mM). Polymerisation conditions: 10 mg catalyst, 2 bar ethylene, 50 mL hexanes (total volume), 150 mg TIBA, and 30 minutes. Error bars shown at one standard deviation. Asterisk (*) denotes gel formation.

At either high temperatures or high comonomer concentrations, the LLDPE formed is of sufficiently low crystallinity that it is soluble in hexanes and forms as a gel rather than dispersed solid particles. These reactions therefore occur under a different mass-transport regime, where monomer diffusion is rate-limiting (denoted by an asterisk in Figure 5.10a). At 60 °C and with 1-hexene concentrations above 100 mM, activities

plateau, and do not further increase with increasing [C6] within error. Under these conditions, mass-transport limitations outweigh any further comonomer effect advantages.

5.5.2. Characterisation of LLDPE-C6

The resulting LLDPE-C6 has been characterised by GPC, IR, NMR and DSC techniques. Comonomer incorporation was determined by GPC–IR and, for polymers synthesised at 60 °C, additionally by high-temperature quantitative $^{13}C\{^{1}H\}$ NMR spectroscopy (Figure 5.11). The values calculated from GPC-IR and ^{13}C NMR are in excellent agreement for low comonomer incorporation, whilst GPC-IR consistently underestimated the incorporation at higher values. In general, an increased temperature of polymerisation results in increased comonomer incorporation for a given concentration, as a result of being better able to overcome the larger barrier to comonomer coordination. Of particular note, is the virtually linear dependence of incorporation on concentration, indicating – as was seen for E/P copolymerisation – that the rate of insertion of both monomers is greater than their rate of diffusion to the active site at 2 bar pressure. This is despite the mass-transport effects, which typically result in supported catalysts giving lower incorporation than homogeneous catalysts.[30,68,69] Such diffusional control allows for much greater comonomer incorporations than are commonly seen in the literature, up to 86 wt% C6 at 800 mM. In addition to this ability to incorporate very large quantities of comonomer, it also enables a very wide scope for facile tuneability of intermediate incorporations. This feature is desirable, as the short-chain branching density is directly linked to many of the physical properties of LLDPE.

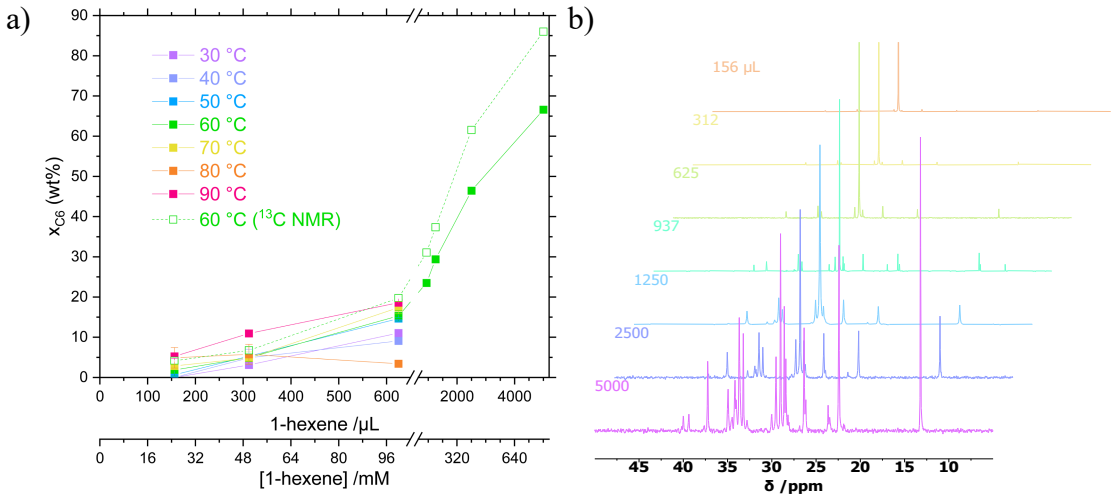

Figure 5.11 a) Mean comonomer incorporation, as a function of concentration of 1-hexene, of LLDPE-C6 synthesised by $\mathbf{2}_{\mathbf{sMAO}}$/TIBA, obtained from GPC-IR measurements. b) Quantitative $^{13}C\{^{1}H\}$ NMR spectra (151 MHz, 1,1,2,2-tetrachloroethane-d_2, 403 K, $50 \geq \delta \geq 5$ ppm) of LLDPE-C6 synthesised by $\mathbf{2}_{\mathbf{sMAO}}$/TIBA at 60 °C. Error bars shown at one standard deviation.

Molecular weights were estimated by GPC (Figure 5.12). In addition to the expected temperature dependence, where M_w decreases as a function of T_p, a strong dependence on comonomer concentration was observed, and M_w decreased with increasing concentration. This is because olefinic comonomers can act as chain transfer agents, higher concentrations of which increase the rate of transfer relative to propagation.[70] It has also been shown *in silico* that the copolymer has a lower energy barrier for β-elimination (4.7 kcal mol^{-1}) than the homopolymer (6.2 kcal mol^{-1}), resulting in depressed molecular weights.[67] At low polymerisation temperatures, ultra-high molecular weight LLDPE was observed: at 40 °C, M_w was reported as 1.53 MDa at a 1-hexene concentration of 50 mM, and 4.9 wt% incorporation. In addition to overall comonomer incorporation, the branching density, calculated from GPC–IR as SCB/1000TC, provides an insight into the distribution and uniformity of polymer composition as a function of molecular weight. In this case, the traces are consistent with uniform copolymer composition and sample homogeneity, typical of single-site molecular catalysts.[71,72]

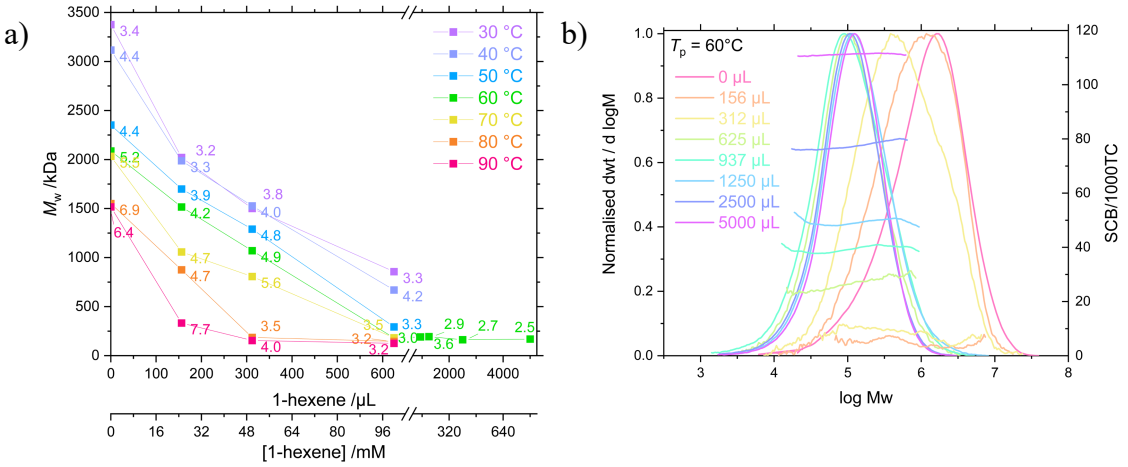

Figure 5.12 a) Weight-average molecular weight of LLDPE-C6 synthesised by $\mathbf{2}_{\mathbf{sMAO}}$/TIBA as a function of temperature of polymerisation and 1-hexene concentration, with PDIs annotated. b) Gel permeation chromatograms with overlayed short chain branching density as a function of log(M_w) of LLDPE-C6 synthesised at 60 °C. Theoretical branching densities: 1:1 copolymer (125 SCB/1000TC), 5:1 copolymer (63 SCB/1000TC), 10:1 copolymer (38 SCB/1000TC), 50:1 copolymer (9 SCB/1000TC).

The increase in short-chain branching density afforded by LAO incorporation is expected to reduce the efficiency with which the polymer chains can pack together, reducing crystallinity and decreasing the melting point of the LLDPE relative to HDPE.[73,74] The synthesised LLDPE-C6 polymers were analysed by DSC (Figure 5.13). It was found that as LAO incorporation increased – by increasing either comonomer concentration or the polymerisation temperature – both the melting point (T_m) and crystallinity (α) decreased. Polymer crystallinity is calculated as the ratio of the enthalpy of fusion of the polymer to that of perfectly crystalline HDPE.[75,76] The UHMWPE synthesised at 60 °C in the absence of comonomer had a T_m of 133 °C and α of 78%, which is reduced to 55 °C and 13% respectively at a C6 concentration of 200 mM, corresponding to an incorporation of 29.4 wt%. At still higher LAO incorporations, amorphous polymers were produced which entirely lack crystallinity and exhibit elastomeric or gel-like consistencies.

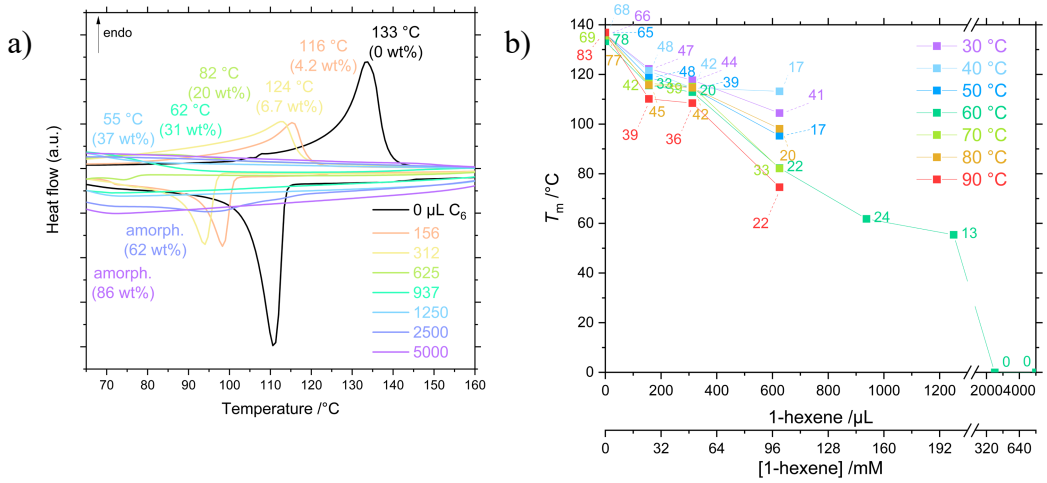

Figure 5.13 a) Differential scanning calorimetry plots (20 K min^{-1}, second heating and cooling shown, T_m and incorporation annotated; incorporations determined by ^{13}C NMR spectroscopy) of LLDPE-C6 synthesised by **2**$_{sMAO}$/TIBA at 60 °C as a function of 1-hexene concentration. b) Melting temperature (with crystallinity annotated) of LLDPE-C6 synthesised by **2**$_{sMAO}$/TIBA as a function of temperature of polymerisation and comonomer concentration.

Though beyond the scope of this study, the reduction in crystallinity and melting point is expected to have a profound effect on many other physical and mechanical properties of the polymers.[77,78] Therefore, the ability to access a wide range of incorporations and thermal characteristics from a single catalyst system is of significant industrial relevance.

5.5.3. Copolymerisation of ethylene with 1-octene

In addition to studying the effects of LAO incorporation and short-chain branching density, it was also decided to look at the effects of the length of the sidechains by investigating the copolymerisation of ethylene with 1-octene and 1-dodecene (5.5.5).

E/C8 copolymerisation were performed analogously to that of E/C6, with 0–5000 µL 1-octene in a concentration range of 0–637 mM (Figure 5.14). In comparison to E/C6 copolymerisation, an initial decease in activity was observed at all polymerisation temperatures, and a positive comonomer effect became apparent as the concentration of C8 increased, though less significantly so at higher temperatures. It is notable that the

plateauing behaviour observed at very high C6 loadings was not reproduced with C8, instead activity continued to increase to 5875 $kg_{LLDPE}\ mol_{Ti}^{-1}\ h^{-1}\ bar^{-1}$, a 58% increase compared with homopolymerisation at a C8 concentration of 637 mM.

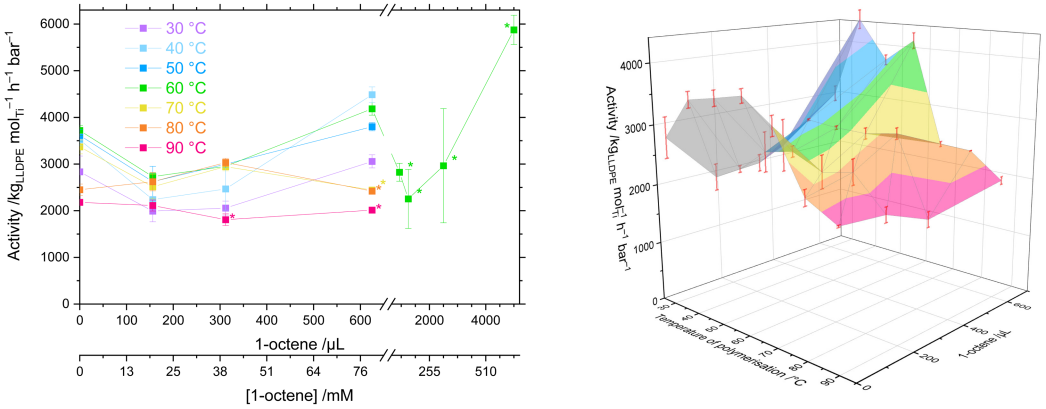

Figure 5.14 Mean copolymerisation activity of $\mathbf{2}_{sMAO}$/TIBA as a function of temperature of polymerisation ($30 \leq T_p \leq 90$ °C) and 1-octene concentration ($0 \leq V \leq 5000$ µL; $0 \leq c \leq 637$ mM). Polymerisation conditions: 10 mg catalyst, 2 bar ethylene, 50 mL hexanes (total volume), 150 mg TIBA, and 30 minutes. Error bars shown at one standard deviation. Asterisk (*) denotes gel formation.

5.5.4. Characterisation of LLDPE-C8

At elevated polymerisation temperatures, comonomer enchainment was found to be more efficient with C8 than was found with C6: at 625 µL and 90 °C, incorporation was 23.5 and 26 wt% respectively with C6 and C8. Similarly, the incorporation with 5000 µL at 60 °C was 70.1 wt% (measured by GPC–IR), 5% greater than for C6 under the same conditions. At reduced polymerisation temperatures, however, the inverse trend is observed: at 30 °C and 312 µL, for example, incorporation was 3.1 and 1.8 wt% respectively with C6 and C8. This behaviour suggests that the energy barrier for chain propagation with C8 is greater than for C6, which would be expected based on steric arguments.

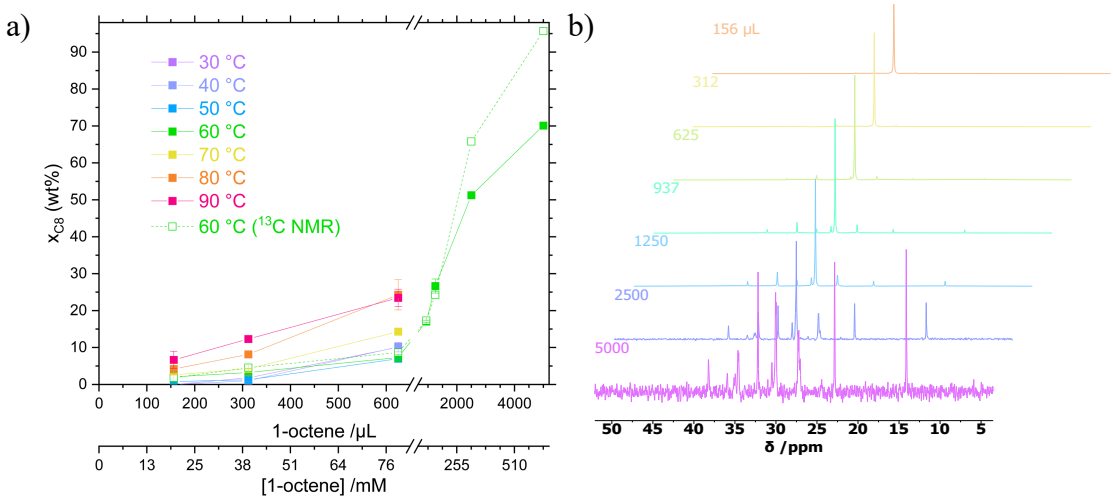

Figure 5.15 a) Mean comonomer incorporation, as a function of concentration of 1-octene, of LLDPE-C8 synthesised by **2**$_{sMAO}$/TIBA, obtained from GPC-IR measurements. b) Quantitative $^{13}C\{^{1}H\}$ NMR spectra (151 MHz, 1,1,2,2-tetrachloroethane-d_2, 403 K, $50 \geq \delta \geq 5$ ppm) of LLDPE-C8 synthesised by **2**$_{sMAO}$/TIBA at 60 °C. Error bars shown at one standard deviation.

As observed for E/C6 copolymerisation, the molecular weights of the resulting LLDPE-C8 decrease both with increasing polymerisation temperature and LAO concentration. Additionally, a greater spread of M_w values is seen. For example, at 312 µL C8 and 90 °C polymerisation temperature the value is 139 kDa, 9.7% less than for C6, whilst at 30 °C M_w = 2.33 MDa for the same C8 concentration, a 56% increase relative to C6. This effect may be related to the bulk incorporation; as previously noted, the incorporation is less for C8 than C6 at lower temperatures and greater as temperature increases. At both high T_p and LAO concentration, M_w appears to approach a limiting value, always above 130 kDa. Access is therefore granted both to ultra-high molecular weight LLDPE-C8, and to polymers with extremely high branching densities and comparatively high molecular weights.

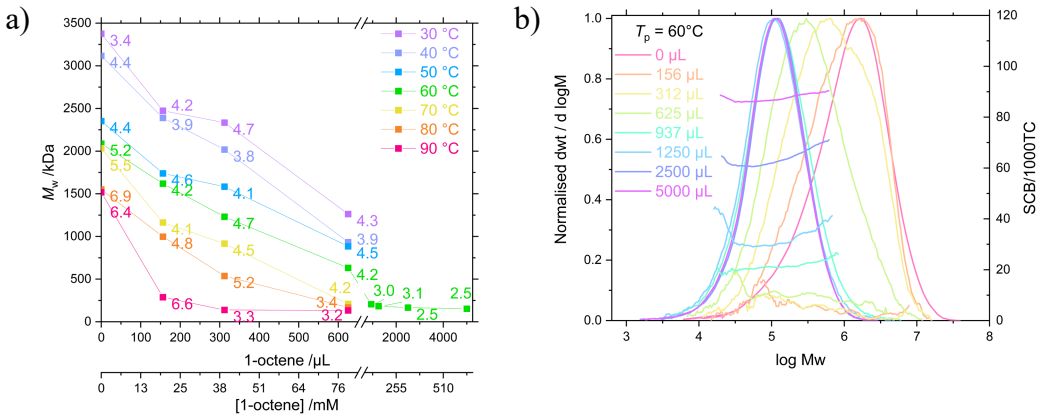

Figure 5.16 a) Weight-average molecular weight of LLDPE-C8 synthesised by **2**$_{sMAO}$/TIBA as a function of temperature of polymerisation and 1-octene concentration, with PDIs annotated. b) Gel permeation chromatograms with overlayed short chain branching density as a function of log(M_w) of LLDPE-C8 synthesised at 60 °C. Theoretical branching densities: 1:1 copolymer (100 SCB/1000TC), 5:1 copolymer (56 SCB/1000TC), 10:1 copolymer (36 SCB/1000TC), 50:1 copolymer (9 SCB/1000TC).

Both the melting point and crystallinity of LLDPE-C8 decrease as a function of comonomer incorporation, mirroring the trends in E/C6 copolymerisation. The physical properties of the copolymers are mostly a function of the overall incorporation rather than any one experimental factor. This allows independent control of otherwise highly coupled parameters such as M_w and T_m which both depend on T_p and [LAO]. As a result, exploiting the tunability of the copolymerisation system by simultaneously varying the temperature, the comonomer, and its concentration gains access to an expansive gamut of polymer property-space. This concept is further developed in the copolymerisation of ethylene with 1-dodecene, studied in section 5.5.5.

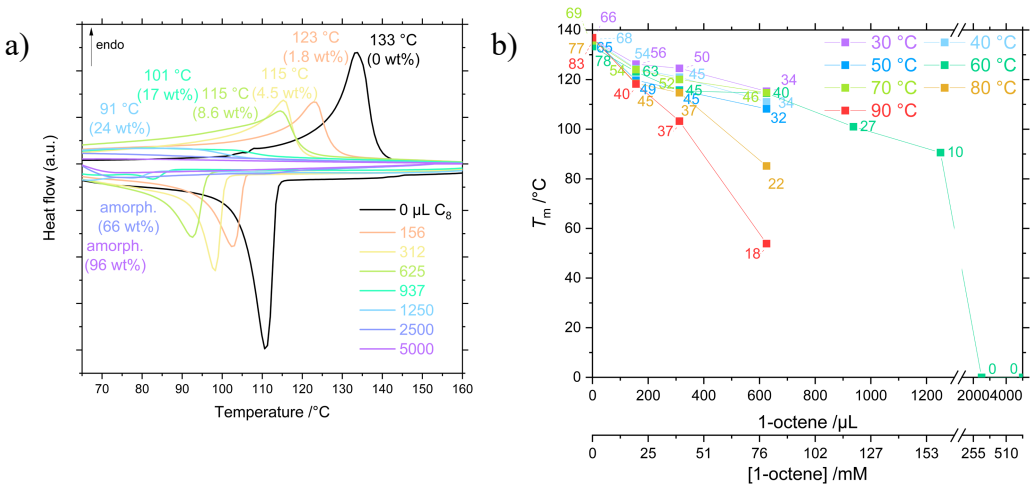

Figure 5.17 a) Differential scanning calorimetry plots (20 K min^{-1}, second heating and cooling shown, T_m and incorporation annotated; incorporations determined by ^{13}C NMR spectroscopy) of LLDPE-C8 synthesised by **2**$_{sMAO}$/TIBA at 60 °C as a function of 1-octene concentration. b) Melting temperature (with crystallinity annotated) of LLDPE-C8 synthesised by **2**$_{sMAO}$/TIBA as a function of temperature of polymerisation and comonomer concentration.

5.5.5. Copolymerisation of ethylene with 1-dodecene

The copolymerisations of ethylene with 1-dodecene were studied as before using the **2**$_{sMAO}$/TIBA catalyst system and 0–5000 µL of C12, corresponding to concentrations of up to 451 mM.

Two features of the temperature-concentration activity profile are notably distinct from the C6 and C8 cases. Firstly, the effects of T_p on copolymerisation activity is more significant than that of [C12] – at all temperatures, activity is largely constant up to 56 mM, with a positive comonomer effect only seen significantly at 60 °C. Secondly, the extent of the positive comonomer effect at very large LAO loadings is much higher: at 5000 µL and 60 °C, the respective activities for C6, C8, and C12 copolymerisation are 30, 58, and 113% higher compared to the homopolymerisation.

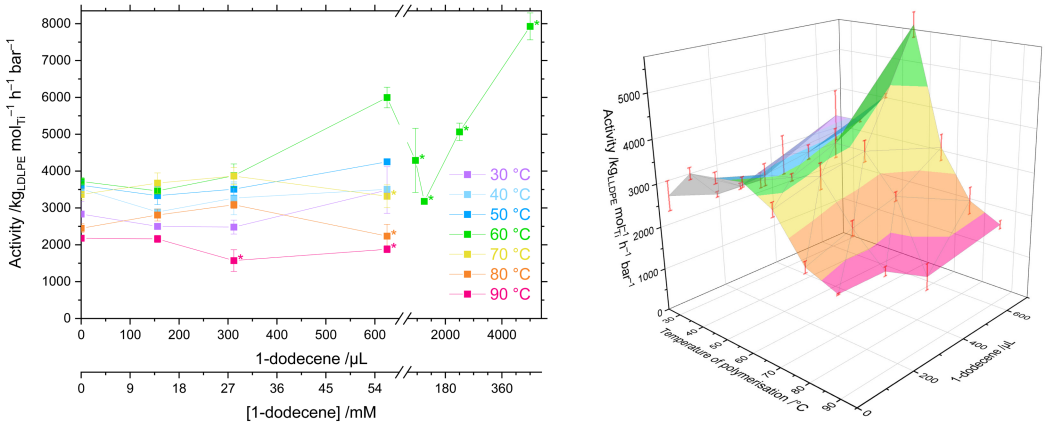

Figure 5.18 Mean copolymerisation activity of **2**$_{sMAO}$/TIBA as a function of temperature of polymerisation ($30 \leq T_p \leq 90$ °C) and 1-dodecene concentration ($0 \leq V \leq 5000$ μL; $0 \leq c \leq 451$ mM). Polymerisation conditions: 10 mg catalyst, 2 bar ethylene, 50 mL hexanes (total volume), 150 mg TIBA, and 30 minutes. Error bars shown at one standard deviation. Asterisk (*) denotes gel formation.

5.5.6. Characterisation of LLDPE-C12

Characterisation of the resulting LLDPE-C12 copolymers proceeded analogously to the C6 and C8 cases, by GPC–IR, NMR, and DSC techniques.

Comonomer incorporation was determined by GPC–IR and ^{13}C NMR. In general, lower incorporation was obtained with C12 than either C6 or C8, particularly so at lower polymerisation temperatures. Only trace incorporation could be detected at $T_p < 60$ °C, at least an order of magnitude less than for C6 copolymerisation. At higher temperatures, while reasonably high levels of enchainment were obtained (16.7 wt% at 90 °C and 625 μL), this is a 10 and 29% decrease respectively when compared with C6 and C8 copolymerisation at the same loading (by volume). Incorporations were also lower with respect to LAO concentration: 1.7 mol% at 60 °C and 56 mM C12 compared to 2.4 mol% at 60 °C and 50 mM C6.

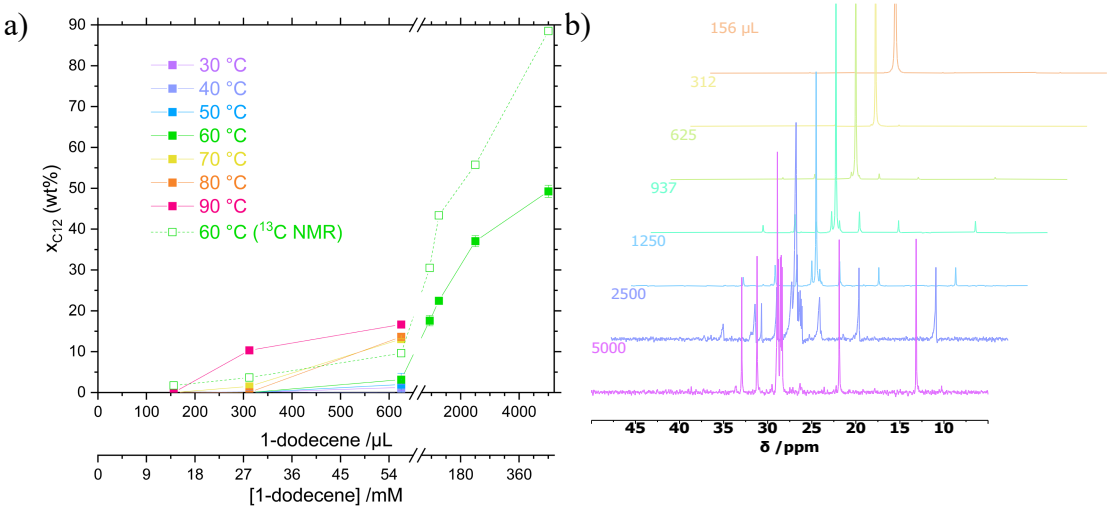

Figure 5.19 a) Mean comonomer incorporation, as a function of concentration of 1-dodecene, of LLDPE-C12 synthesised by **2**$_{sMAO}$/TIBA, obtained from GPC-IR measurements. b) Quantitative $^{13}C\{^{1}H\}$ NMR spectra (151 MHz, 1,1,2,2-tetrachloroethane-d_2, 403 K, 50 ≥ δ ≥ 5 ppm) of LLDPE-C12 synthesised by **2**$_{sMAO}$/TIBA at 60 °C. Error bars shown at one standard deviation.

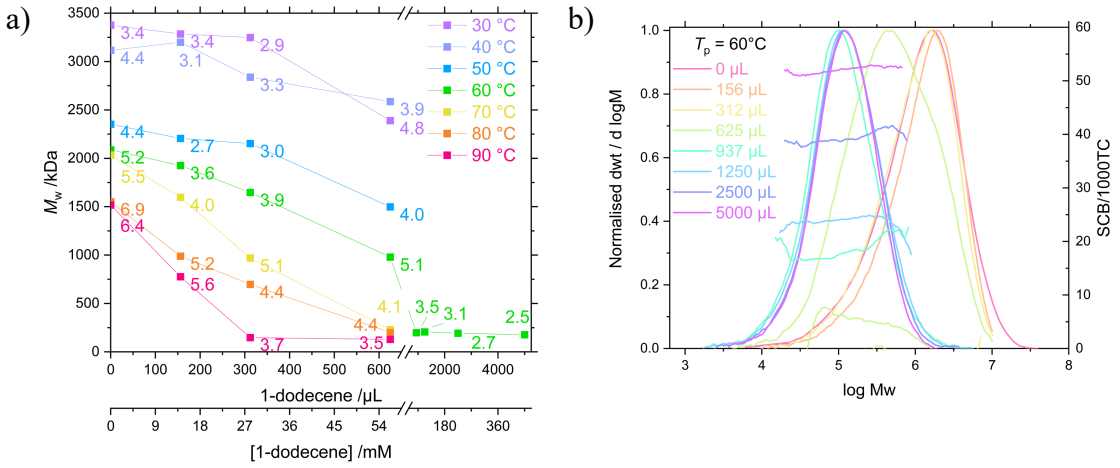

Figure 5.20 a) Weight-average molecular weight of LLDPE-C12 synthesised by **2**$_{sMAO}$/TIBA as a function of temperature of polymerisation and 1-dodecene concentration, with PDIs annotated. b) Gel permeation chromatograms with overlayed short chain branching density as a function of log(M_w) of LLDPE-C12 synthesised at 60 °C. Theoretical branching densities: 1:1 copolymer (71 SCB/1000TC), 5:1 copolymer (45 SCB/1000TC), 10:1 copolymer (31 SCB/1000TC), 50:1 copolymer (9 SCB/1000TC).

The less efficient enchainment seen in E/C12 copolymerisation is reflected in the molecular weights of LLDPE-C12. At low polymerisation temperatures, where very minimal C12 incorporation was observed, M_w is approximately invariant as a function of

[C12] over the range of study. As incorporation increases, both with increasing T_p and [C12], M_w decreases, although it remains above 128 kDa in all cases.

While fully amorphous LLDPE-C12 is produced at very high comonomer concentrations (above 113 mM), the less efficient copolymerisation under more moderate conditions results in polymers with higher T_m and crystallinity when compared with LLDPE-C8 and LLDPE-C6.

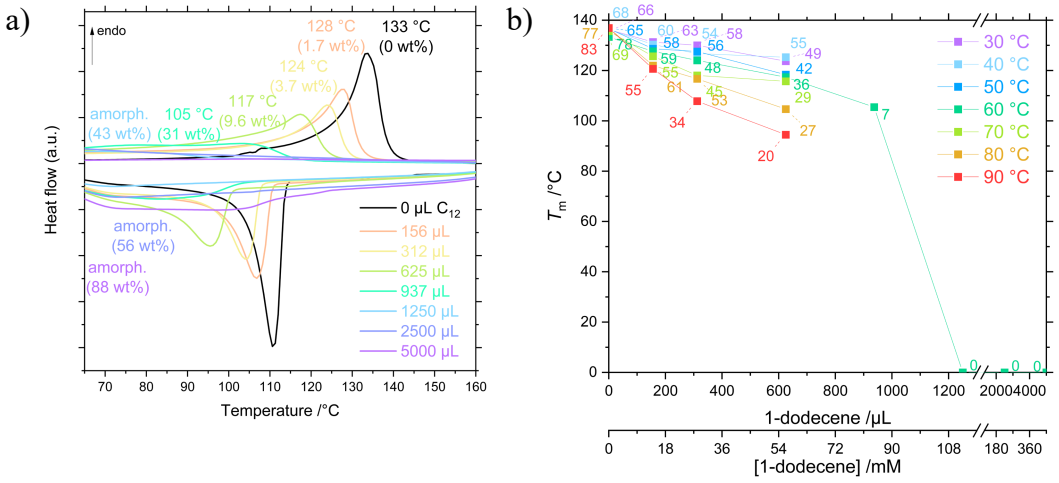

Figure 5.21 a) Differential scanning calorimetry plots (20 K min^{-1}, second heating and cooling shown, T_m and incorporation annotated; incorporations determined by ^{13}C NMR spectroscopy) of LLDPE-C12 synthesised by **2**$_{sMAO}$/TIBA at 60 °C as a function of 1-dodecene concentration. b) Melting temperature (with crystallinity annotated) of LLDPE-C12 synthesised by **2**$_{sMAO}$/TIBA as a function of temperature of polymerisation and comonomer concentration.

5.5.7. Summary of E/LAO copolymerisation

Notably, for a given incorporation, there appears to be little correlation between the thermal properties and the identity of the LAO comonomer (Figure 5.22), though the crystallinity of LLDPE-C8 is slightly higher than either LLDPE-C6 or LLDPE-C12 for a given incorporation. However, using different comonomers has been shown to give access to varying incorporations for a given set of experimental conditions, thus allowing independent control of molecular weight and incorporation. Effects such as side chain

crystallisation would be expected to become prominent for longer LAOs than studied in this chapter.

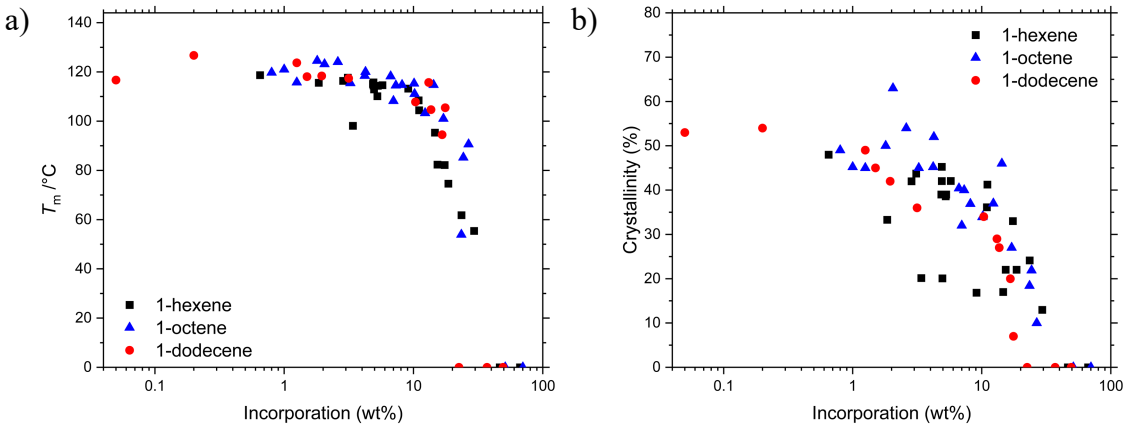

Figure 5.22 a) Melting point and b) crystallinity of LLDPE as a function of comonomer incorporation. Synthesised by $\mathbf{2}_{\mathbf{sMAO}}$/TIBA using C6, C8, and C12 at $30 \leq T_p \leq 90$ °C and 156–5000 μL LAO.

By utilising C6, C8, and C12 in copolymerisations with ethylene, a diverse system of behaviours has been studied. Of the three monomers, C8 is incorporated the most efficiently under PHENI* catalysis, while C12 results in the highest activities. C6 offers intermediate capabilities and, taken together, the PHENI*/E/LAO system offers virtually unprecedented access to an extremely wide scope of LLDPEs of varying chemical, thermal, and physical properties. Studying the mechanical properties of these LLDPEs as a function of composition would be an interesting avenue of future research, with particular focus on industrially relevant parameters. Furthermore, monomers from C4 though to C18 and beyond are routinely used in olefinic copolymerisations and may offer further scope for polymerisations using the PHENI* system.

5.6. Multivariate analysis of copolymerisation system

5.6.1. Introduction

With the advent of "big data", computational chemistry, and data-led discovery, interest is rapidly growing in the application of advanced computer models to complex and

chaotic chemical systems.[79,80] Much of this research is focussed on data-driven drug discovery[81] and organic synthesis.[82] While inorganic chemistry is often informed by *ab initio* quantum mechanical calculations, these are computationally expensive and so empirical and semi-empirical models based on large datasets are increasingly common.[83-85]

Modelling of ethylene polymerisation systems generally focuses on quantitative structure-activity relationships (QSAR) informed by density functional theory (DFT) calculations on the precatalysts.[86-88] This can give useful chemical and mechanistic insights, and inform future catalyst development.[89] Beyond fundamental chemical research, the ultimate goal of such methodology is to construct a model that is able to predict experimental parameters to tune polymerisation properties. In real-world systems, a large number of factors beyond precatalyst QSAR are significant, such as morphology, shear forces, diffusion, mixing, impurities, scavengers and cocatalysts. Furthermore, the structure of components such as MAO and sMAO is not fully elucidated,[90,91] and even the oxidation state of the active species is debated.[92] Recently, models using multiple linear regression have been used in combination with large datasets obtained by high-throughput experimentation with reasonably explanatory and predictive abilities.[93]

Multivariate data analysis was carried out on the PHENI* E/LAO copolymerisation system, with the aim of establishing a predictive model for the synthesis of designer polymers.

5.6.2. Multivariate analysis

When attempting to analyse the various LAO copolymerisation systems simultaneously, all of the relevant variables must first be identified. The explanatory variables are

identified as the temperature of polymerisation (T_p), the identity of the comonomer (enumerated as the number of carbon atoms in the LAO, n), and the comonomer concentration (c). Other factors such as pressure, solvent, scale, scavenger, catalyst ligand, and stirring speed have been held constant in these studies but are likely to have an influence over the polymer properties. In particular, the ethylene pressure is expected to have a dramatic influence – at sufficiently high values, it is anticipated that the observed diffusion-controlled regime would be replaced by a kinetic regime in which the reactivity ratios of the catalyst to the two monomers becomes the dominating factor. The response variables are then identified as catalytic activity (A), polymer melting point (T_m), crystallinity (α), molecular weight (M_w), dispersity (PDI, Đ) and comonomer incorporation (x). Taken together, this 9-dimenstional dataset ($N = 75$) encompasses all of the reaction-space explored in the slurry-phase copolymerisation of ethylene with α-olefins using the PHENI* catalyst $\mathbf{2_{sMAO}}$/TIBA.

From an inspection of the scatterplot matrix (Figure 5.23), it is immediately clear that some of these factors are more strongly correlated than others. As would be expected, the physical properties of the polymers depend strongly on comonomer incorporation, which is in turn strongly correlated with comonomer concentration. While it has been shown that LAO incorporation is also influenced heavily both by the polymerisation temperature and the identity of the comonomer (*vide supra*), the bivariate plots do not show a strong correlation, though incorporation does increase slightly with T_p. This is consistent with the interdependency of these two variables and is itself strong motivation for pursuing further multivariate analysis. Of the polymer properties, T_m shows a strong linear correlation decreasing with increasing incorporation, while α, M_w, and PDI all show decreasing but non-linear correlations.

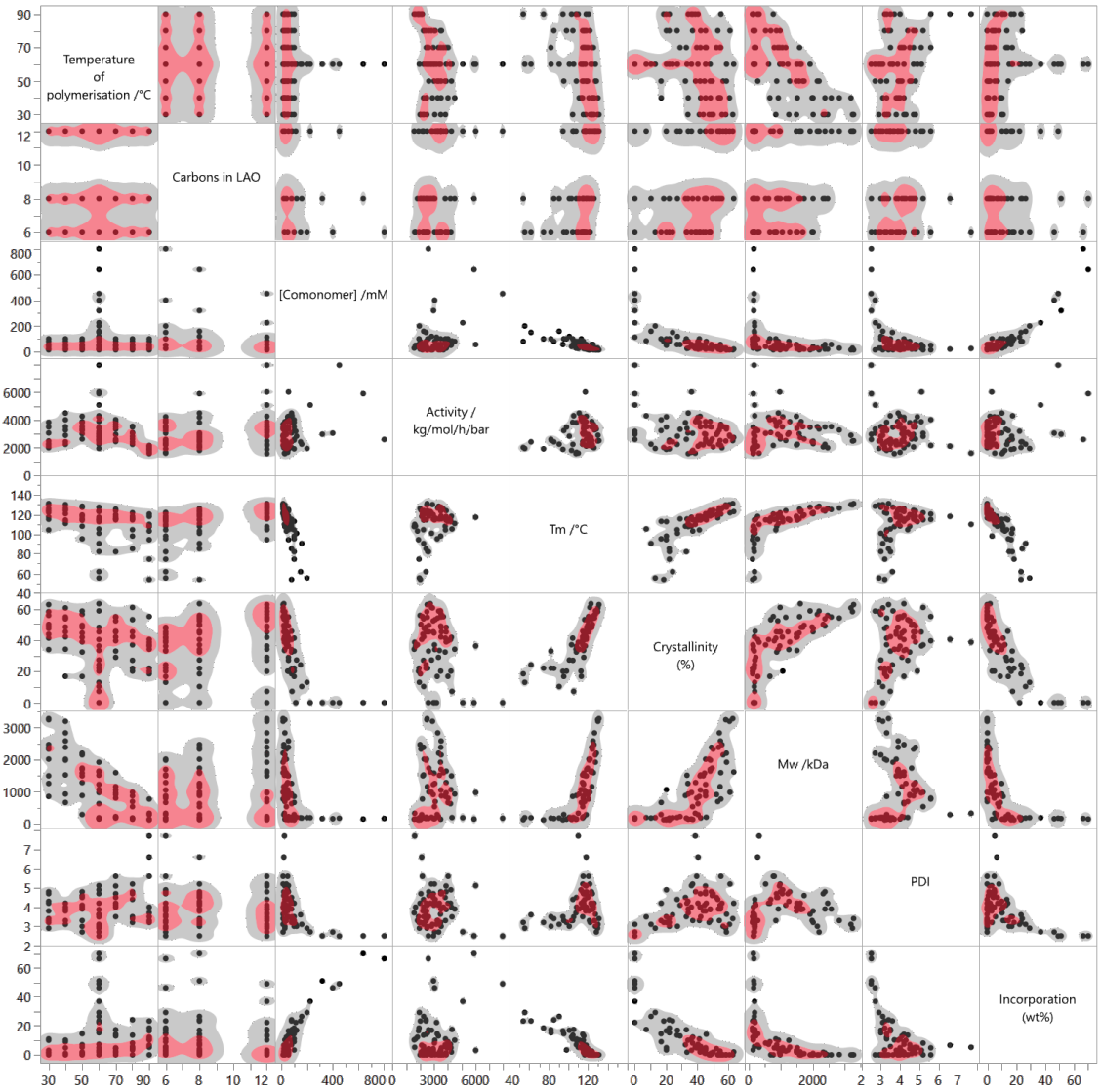

Figure 5.23 Scatterplot matrix of the PHENI*/E/LAO dataset, showing 2-dimensional scatter plots as functions of pairs of experimental variables. Shaded nonparametric density contours shown at the 50% and 90% quantiles. $N = 75$.

5.6.3. Multivariate linear regression modelling

As the relationships plotted in Figure 5.23 are generally nonlinear, multivariable regression was performed using polynomial combinations of the explanatory variables, up to quadratic terms (T_p, c, n, T_p^2, c^2, n^2, $T_p n$, $T_p c$, cn). This resulted in a nonlinear model (model 1, M1) after least squares regression was applied to the dataset. This model allows for a detailed statistical analysis of regression, in particular the coupling of the explanatory variables to each other and the strength of their influence on the response

variables. On the basis of likelihood ratio tests, T_p and c explain much of the variation of M1, with $-\log_{10}(p\text{-values})$ of 33.0 and 24.9 respectively, and all of the polynomial terms apart from n^2 have significant relationships at the .01 level of hypothesis testing. The model is predictive with R^2 values of: A (0.65), T_m (0.85), α (0.81), M_w (0.96), PDI (0.50), x (0.85). Linear regression models assume linearity, homoscedasticity, and residual normality. In this dataset, visual inspection of the distribution of the residuals, confirms that these assumptions approximately hold. Linear models are unable to fit limiting behaviour, and so the empirical lower bounds, particular of M_w, are likely to be poorly accounted for.

F ratios are a measure of signal-to-noise and are defined as the ratio between the partial variation explained by the model, relating to each predictor, and the unexplained variation. Larger values indicate a stronger relationship between a predictor and a response, and a value close to unity indicates no statistically significant effect. Activity is determined mostly by T_p and T_p^2 (F ratio 16.6 and 53.2), with the quadratic term reflecting the maxima around 60 °C (Table 5.1). Other key factors are T_pc and c^2 (F ratio 13.3 and 14.4) which highlight the temperature-concentration coupling that was observed qualitatively in Chapter 5.3. The quadratic concentration term goes some way to account for the initial decrease in activity before a positive comonomer effect becomes apparent at higher concentrations. Concentration effects are confounded by the change in diffusion regime from the formation of free-flowing polymer particles to soluble gels at higher concentrations which lead to a reduction in activity associated with mass-transport processes.

Table 5.1 Summary of partial effect tests in model M1: F ratios and *p*-values for each predictor on each response. Predictors composed of T_p (temperature of polymerisation), *n* (chain length of LAO), and *c* (LAO concentration). $N = 75$.

	F ratio, *p*-value											
Predictor	**Activity**		M_w		**PDI**		T_m		**α**		***x***	
T_p	16.62	.0001	678.26	<.0001	3.16	.0808	66.60	<.0001	25.51	<.0001	49.52	<.0001
n	1.05	.3105	13.15	.0006	0.54	.4658	5.80	.0193	1.15	.2876	3.42	.0696
c	8.55	.0049	330.29	<.0001	6.59	.0129	86.03	<.0001	136.24	<.0001	139.76	<.0001
$T_p n$	3.59	.0631	44.90	<.0001	2.31	.1340	4.19	.0453	5.03	.0287	2.48	.1208
$T_p c$	13.29	.0006	20.01	<.0001	24.23	<.0001	16.47	.0001	1.09	.3020	4.02	.0497
nc	0.19	.6679	5.17	.0267	3.38	.0710	1.35	.2508	14.51	.0003	3.16	.0807
T_p^2	53.17	<.0001	0.69	.4090	0.58	.8111	5.19	.0264	0.23	.6304	6.29	.0150
n^2	6.29	.0150	0.11	.7457	0.11	.7430	0.09	.7717	6.49	.0135	2.16	.1474
c^2	14.41	.0004	26.99	<.0001	0.65	.4232	0.02	.8864	1.25	.2677	0.76	.3877

The cross term $T_p c$ (24.2) is the principal controlling predictor for PDI, which also has moderate contributions to both M_w (20.0) and T_m (16.5). The anticipated dependency of M_w on both T_p and c is reflected in large F ratios for these predictors, 678.3 and 330.3 respectively. Interestingly, of the cross terms, $T_p n$ (44.9) had the largest F ratio, showing that temperature-chain length coupling is a more important factor than concentration-chain length. This is suggestive of a mechanistic interpretation, with larger energy barriers associated with larger monomers interacting with the thermal energy in the system; since polymer molecular weight is ultimately governed by the ratio of chain propagation to termination rate, such a phenomenon is to be expected.

Incorporation is determined almost linearly by concentration, with c being the dominant predictor, alongside a contribution from T_p. The thermal properties of the polymer – T_m and α – depend largely on T_p and c, and therefore secondarily on x. The regression analysis reveals that while T_m is determined principally by the temperature-concentration couple, crystallinity depends more strongly on the side chain length, with the predictors nc, n^2 and $T_p n$ all having statistically significant contributions. This is consistent with physical expectations: increased comonomer concentration (and therefore, incorporation) increases the degree of branching, which reduces the intermolecular forces between polymer chains and lowers the melting point.[94] The branches are generally excluded from the crystalline lamellae, disrupt chain folding and lead to defective crystallisation,[95] with the length of the side chain controlling crystallinity.[96]

Through this analysis, it is possible to quantify many of the features of this system that were observed qualitatively in Chapter 5.5. That the relatively simple regression model M1 captures so much of the chemical and physical behaviour of this highly non-trivial reaction system demonstrates not only the power of large datasets for the delineation of

interrelated variables, but also the potential ability to leverage the tuneability of the PHENI* catalyst system towards parameter-space optimisation.

5.6.4. Towards the synthesis of designer copolymers

In addition to the statistical insight afforded by this highly multidimensional analysis, the real power of statistical models is predictive. Given the immense tuneability afforded by the PHENI* catalyst platform in olefinic copolymerisations, it would be highly desirable to be able to exploit control over the reaction conditions to synthesise polymers with predefined properties. To explore this, three sets of LLDPE properties were devised and translated into desirability functions corresponding to M1, consisting of unimodal functions maximised at the desired value (Figure 5.24).

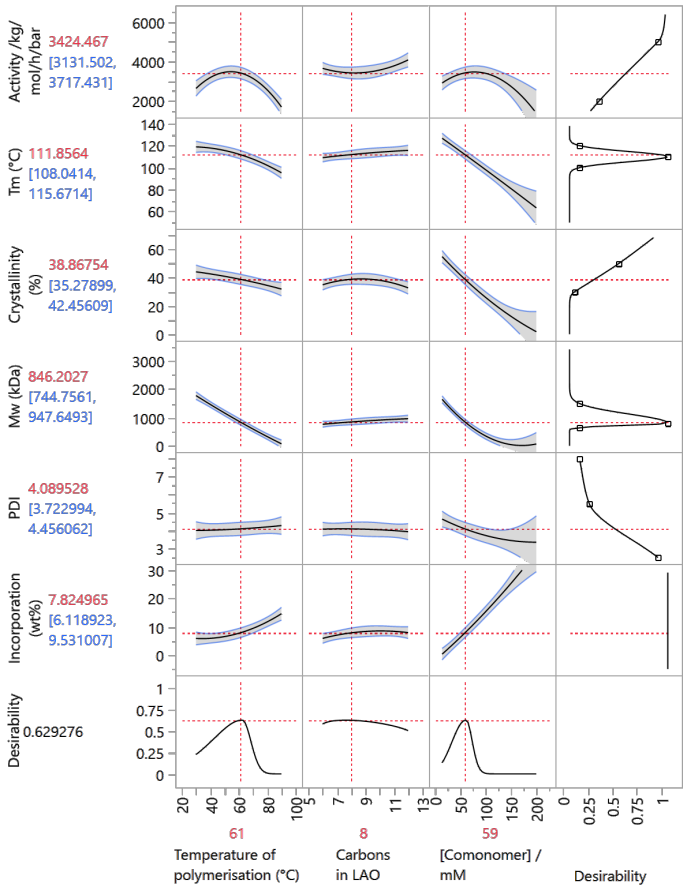

Figure 5.24 Prediction profiler plots with desirability functions optimised for sample P1: T_m = 110 °C, M_w = 1 MDa, maximised activity and crystallinity, and minimised PDI.

Following multivariate optimisation of total desirability, the calculated values for T_p, C*n*, and [LAO] were rounded to an experimentally relevant degree. The expected values of the predicted output properties were found with a 95% confidence interval based on the covariance matrices. These copolymerisations were then performed with otherwise identical conditions to those used throughout Chapter 5.3: 50 mL hexanes, 150 mg TIBA, 2 bar ethylene, and 30 minutes (Figure 5.25).

Sample P1 was optimised to a relatively unconstrained high M_w (1 MDa) high T_m (110 °C) LLDPE copolymer, the likes of which have already been synthesised *vide supra*. Additionally, the activity and crystallinity were maximised and the PDI minimised. The model M1 converged on a set of conditions (T_p = 61 °C, n = 8, c = 55.5 mM) consistent with the optimised properties and with relatively narrow 95% confidence intervals (T_m = 112 °C; M_w = 846 kDa). Experimentally, the copolymer melting point and molecular weight (112 ± 3 °C; 606 ± 281 kDa) showed a close qualitative fit with the predictions of M1. The relatively large standard deviation in experimental M_w results from the reaction being at the boundary of the insoluble and soluble regimes, with poor reproducibility between runs. This morphological variation has been noted in Chapter 5.5, and is not explicitly included in M1. Furthermore, the predictions for activity (M1 3424 $kg_{LLDPE}\ mol_{Ti}^{-1}\ h^{-1}\ bar^{-1}$; expt. 3175 ± 271 $kg_{LLDPE}\ mol_{Ti}^{-1}\ h^{-1}\ bar^{-1}$), crystallinity (M1 39 %; expt. 40 ± 7 %), and PDI (M1 4.1; expt. 4.1 ± 0.4) were also closely aligned with M1.

Incorporation, x, (M1 7.8 %; expt. 37.8 ± 4.7 %) showed a large discrepancy between the prediction of M1 and the experimental result. This is surprising both because incorporation as a function of T_p, n, and c is one of the best-defined aspects of M1 and because x determines many of the other well-predicted properties such as T_m and α. The

generally excellent agreement between the desired, predicted, and experimental values highlights the power and utility of a large dataset and statistical modelling in the production of polymers with designer properties.

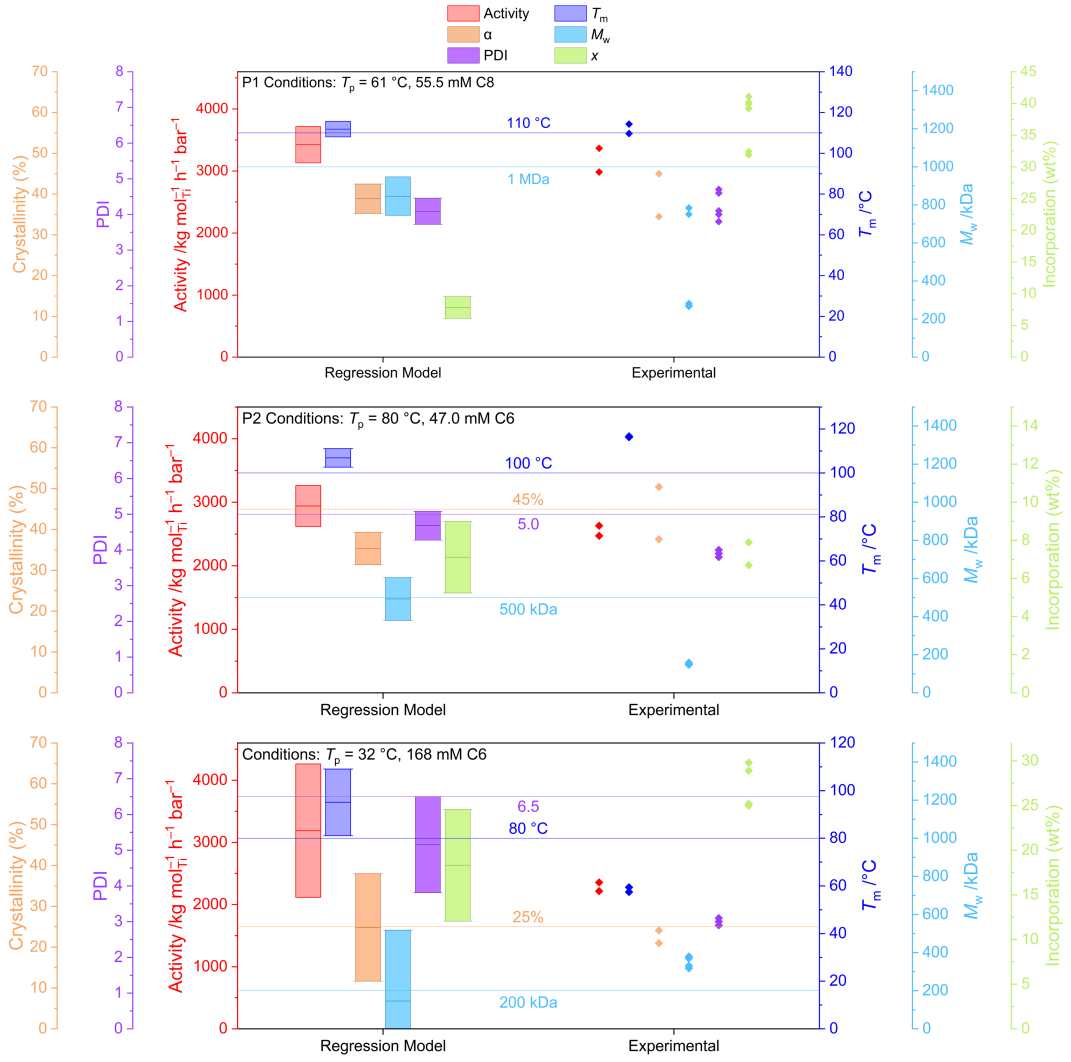

Figure 5.25 Polymerisation parameters of P1–P3 predicted by the regression model M1 (95% confidence intervals shown) and experimental results. Horizontal lines indicated the target values which determined the optimisation functions for calculating experimental conditions. Polymerisation conditions: 50 mL hexanes, 150 mg TIBA, 2 bar ethylene, and 30 minutes.

Samples P2 and P3 were optimised in a more constrained fashion with four variables determined simultaneously. P2 (M_w = 500 kDa; PDI = 5.0; T_m = 100 °C; α = 45%) was interpolated within the scope of previously synthesised copolymers. For P3

(M_w = 200 kDa; PDI = 6.5; T_m = 80 °C; α = 25%), the combination of high incorporation – required for the low crystallinity and melting point – and large PDI is unlike any E/LAO copolymer previously synthesised within this work. As before, in both cases, activity was maximised, and incorporation was unconstrained. Simultaneous quadruplex optimisation resulted in a poorer match between the desired properties and those predicted by the optimised reaction conditions. In particular, the extrapolated properties desired for P3 resulted in poor agreement and large 95% confidence intervals for the predicted values.

P2 was synthesised at T_p = 80 °C, with [C6] = 47.0 mM. The experimental melting point (116.5 ± 0.3 °C) is both larger than the desired value and that predicted by M1. The molecular weight (153 ± 7 kDa) is much less than the desired and predicted values. Otherwise, there is good agreement between M1 and experimentation. The generally good agreement between the predicted and experimental data further demonstrates the power of M1, but the poorer match with the desired properties compared to P1 shows the limits of this methodology for simultaneous optimisation of many intercorrelated parameters.

P3 was synthesised at T_p = 32 °C, with [C6] = 168 mM. The desirability functions were poorly optimised, with the desired values of T_m and PDI (80 °C; 6.5) falling outside the 95% confidence interval of the predicted values of T_m and PDI (95 °C; 5.1). This reflects the lack of data for copolymers having both high incorporation and a high PDI, and perhaps suggests that $\mathbf{2}_{\mathbf{sMAO}}$/TIBA cannot produce such polymers under these conditions. Polymer melting temperature and dispersity (58 ± 2 °C; 3.0 ± 0.1) were substantially lower than both the target and predicted value, and M_w (355 ± 35 kDa) was found to be increased compared with the desired and predicted values. Only crystallinity (23 ± 2%) was well optimised and predicted. In addition to the relatively poor desirability

optimisation and low-confidence predictions, this clearly demonstrates the limitations of extrapolating to property-space much beyond the data used to construct the model.

Despite the obvious limitations, the potential of synthesising designer polyolefins using a single catalyst on the basis of a statistical model has been demonstrated in principle, and is of potentially enormous industrial significance. Parallelised high-throughput reaction platforms would enable more time- and resource-efficient dataset collection and including additional experimental parameters such as pressure would allow finer control and increase the accuracy of simultaneous multiplex optimisations. Incorporating mechanical and material characterisation into the modelling would further enable a dramatically expanded scope of tunability and control, with the ultimate goal of entirely application-directed synthesis.

5.7. Conclusions

In this chapter, the PHENI* catalyst sMAO-^{Me_2}SB(^{tBu_2}ArO,I*)$TiCl_2$/TIBA has demonstrated excellent catalytic performance across a range of olefinic copolymerisations involving ethylene, propylene, 1-hexene, 1-octene, 1-dodecene, and 5-ethylidene-2-norbornene. The synthesis of EPM and EPDM is reported with high activities, and the resulting polymers have high molecular weights and tuneable composition. These materials are amorphous elastomers, and EPDM undergoes post-polymerisation sulphur vulcanisation to synthesise a cross-linked rubber. P/LAO copolymerisation has also been demonstrated, and the resulting PPH polymer displays high molecular weight, efficient comonomer incorporation, and tuneable composition. E/LAO copolymerisations using C6, C8, and C12 demonstrate the versatility of this catalyst platform, which facilitates the synthesis of high and ultra-high molecular weight LLDPE with tuneable short chain branching densities, which translates into the physical

properties of the polymers. Multidimensional statistical techniques have been used to delineate the relationships between polymerisation conditions and polymer properties. The resulting model was used to optimise the experimental conditions for a set of three designer polyolefins. Good agreements between predicted and experimental results are measured, with promising indications that this methodology could be used to synthesise a wide range of polyolefin copolymers with designable properties.

In all cases, copolymer composition can be determined simply by the concentration of comonomer in the reactor, approaching the "unyielding comonomer effect" behaviour described by Irwin *et al*.

In addition to the recently reported PHENI* solution-phase copolymerisation of ethylene with the polar comonomers 10-undecen-1-ol and 11-bromo-1-undecene,[97] this work demonstrates the extreme versatility of the PHENI* catalyst platform towards polyolefins. As a result, this catalyst system is anticipated to be attractive in terms of industrial viability.

5.8. References

1 K. Shirayama, S. I. Kita, H. Watabe, *Makromol. Chem.*, 1972, **151**, 97-120.
2 P. Starck and B. Löfgren, *Eur. Polym. J.*, 2002, **38**, 97-107.
3 F. J. Stadler and H. Münstedt, *J. Rheol.*, 2008, **52**, 697-712.
4 Y. S. Kim, C. I. Chung, S. Y. Lai, K. S. Hyun, *J. Appl. Polym. Sci.*, 1996, **59**, 125-137.
5 W. Kaminsky, *Macromol. Chem. Phys.*, 1996, **197**, 3907-3945.
6 W. Kaminsky and M. Schlobohm, *Makromol. Chem. Macromol. Symp.*, 1986, **4**, 103-118.
7 A. Rossi, J. Zhang, G. Odian, *Macromolecules*, 1996, **29**, 2331-2338.
8 S. Ohta, Y. Kasai, T. Toda, K. Nishii, M. Okazaki, *Polym. J.*, 2019, **51**, 345-349.
9 S. Kitphaitun, Q. Yan, K. Nomura, *ChemistryOpen*, 2021, **10**, 867-876.
10 K. Nomura, S. Pengoubol, W. Apisuk, *Molecules*, 2019, **24**, 1634.
11 S. Kitphaitun, H. Takeshita, K. Nomura, *ACS Omega*, 2022, **7**, 6900-6910.
12 J. Li, H. Li, Y. Zhang, Y. Mu, *J. Appl. Polym. Sci.*, 2011, **120**, 1514-1519.
13 W. Kaminsky, C. Piel, K. Scharlach, *Macromol. Symp.*, 2005, **226**, 25-34.
14 B. Poon, M. Rogunova, A. Hiltner, E. Baer, S. P. Chum, A. Galeski, E. Piorkowska, *Macromolecules*, 2005, **38**, 1232-1243.
15 M. Arnold, O. Henschke, J. Knorr, *Macromol. Chem. Phys.*, 1996, **197**, 563-573.
16 S. Rulhoff and W. Kaminsky, *Macromol. Chem. Phys.*, 2006, **207**, 1450-1460.
17 R. Quijada, J. L. Guevara, G. B. Galland, F. M. Rabagliati, J. M. Lopez-Majada, *Polymer*, 2005, **46**, 1567-1574.

18 T. E. Nowlin, Y. V. Kissin, K. P. Wagner, *J. Polym. Sci., Part A: Polym. Chem.*, 1988, **26**, 755-764.
19 Y. V. Kissin, R. I. Mink, T. E. Nowlin, A. J. Brandolini, *Top. Catal.*, 1999, **7**, 69-88.
20 H. S. Cho, J. S. Chung, J. H. Han, Y. G. Ko, W. Y. Lee, *J. Appl. Polym. Sci.*, 1998, **70**, 1707-1715.
21 B. Paredes, R. v. Grieken, A. Carrero, I. Suarez, J. B. P. Soares, *Macromol. Chem. Phys.*, 2011, **212**, 1590-1599.
22 R. Quijada, J. Dupont, M. S. L. Miranda, R. B. Scipioni, G. B. Galland, *Macromol. Chem. Phys.*, 1995, **196**, 3991-4000.
23 A. L. McKnight and R. M. Waymouth, *Chem. Rev.*, 1998, **98**, 2587-2598.
24 J. Klosin, W. J. Kruper, P. N. Nickias, G. R. Roof, P. De Waele, K. A. Abboud, *Organometallics*, 2001, **20**, 2663-2665.
25 J. Klosin, P. P. Fontaine, R. Figueroa, *Acc. Chem. Res.*, 2015, **48**, 2004-2016.
26 H. Hanaoka, T. Hino, M. Nabika, T. Kohno, K. Yanagi, Y. Oda, A. Imai, K. Mashima, *J. Organomet. Chem.*, 2007, **692**, 4717-4724.
27 M. Nabika, H. Katayama, T. Watanabe, H. Kawamura-Kuribayashi, K. Yanagi, A. Imai, *Organometallics*, 2009, **28**, 3785-3792.
28 H. Hanaoka, T. Hino, H. Souda, K. Yanagi, Y. Oda, A. Imai, *J. Organomet. Chem.*, 2007, **692**, 4059-4066.
29 T. Senda, H. Hanaoka, S. Nakahara, Y. Oda, H. Tsurugi, K. Mashima, *Macromolecules*, 2010, **43**, 2299-2306.
30 T. J. Williams, J. V. Lamb, J. C. Buffet, T. Khamnaen, D. O'Hare, *RSC Adv.*, 2021, **11**, 5644-5650.
31 T. J. Williams, *Olefin polymerisation using group 4 permethylindenyl complexes*, D.Phil. Thesis, *University of Oxford*, 2020.
32 L. J. Irwin, J. H. Reibenspies, S. A. Miller, *J. Am. Chem. Soc.*, 2004, **126**, 16716-16717.
33 J. C. W. Chien and T. Nozaki, *J. Polym. Sci., Part A: Polym. Chem.*, 1993, **31**, 227-237.
34 G. B. Galland, M. Seferin, R. Guimarães, J. A. Rohrmann, F. C. Stedile, J. H. Z. dos Santos, *J. Mol. Catal. A Chem.*, 2002, **189**, 233-240.
35 J. C. Buffet, N. Wanna, T. A. Q. Arnold, E. K. Gibson, P. P. Wells, Q. Wang, J. Tantirungrotechai, D. O'Hare, *Chem. Mater.*, 2015, **27**, 1495-1501.
36 M. Daud, F. Shehzad, M. A. Al-Harthi, *Arab. J. Sci. Eng.*, 2018, **43**, 6021-6032.
37 R. M. Kasi and E. B. Coughlin, *Organometallics*, 2003, **22**, 1534-1539.
38 W. J. Wang and S. Zhu, *Macromolecules*, 2000, **33**, 1157-1162.
39 A. M. F. Phillips, H. Suo, M. d. F. C. Guedes da Silva, A. J. L. Pombeiro, W. H. Sun, *Coord. Chem. Rev.*, 2020, **416**, 213332.
40 R. Kravchenko and R. M. Waymouth, *Macromolecules*, 1998, **31**, 1-6.
41 G. van Doremaele, M. van Duin, M. Valla, A. Berthoud, *J. Polym. Sci., Part A: Polym. Chem.*, 2017, **55**, 2877-2891.
42 H. Kurokawa and T. Sugano, *Macromol. Symp.*, 1995, **97**, 143-149.
43 Z. Q. Zhang, J. T. Qu, S. Zhang, Q. P. Miao, Y. X. Wu, *Polym. Chem.*, 2018, **9**, 48-59.
44 M. J. Caballero, I. Suarez, B. Coto, R. Van Grieken, B. Monrabal, *Macromol. Symp.*, 2007, **257**, 122-130.
45 N. Tanaka, *Thermochim. Acta*, 2001, **374**, 1-5.
46 S. Zhang, W. C. Zhang, D. D. Shang, Y. X. Wu, *J. Polym. Sci., Part A: Polym. Chem.*, 2019, **57**, 553-561.
47 M. Kakugo, Y. Naito, K. Mizunuma, T. Miyatake, *Macromolecules*, 1982, **15**, 1150-1152.
48 H. N. Cheng, *Macromolecules*, 1984, **17**, 1950-1955.
49 I. Suárez, M. J. Caballero, B. Coto, *Eur. Polym. J.*, 2011, **47**, 171-178.
50 I. Suárez, M. J. Caballero, B. Coto, *Polym. Eng. Sci.*, 2011, **51**, 317-322.
51 Z. Yao, D. F. Ma, Z. x. Xiao, W. l. Yang, Y. X. Tu, K. Cao, *RSC Adv.*, 2017, **7**, 10175-10182.
52 A. Ali, M. A. Akram, Y. T. Guo, H. F. Wu, W. C. Liu, A. Khan, X. Y. Liu, Z. S. Fu, Z. Q. Fan, *J. Macromol. Sci. A*, 2020, **57**, 156-164.
53 G. Leone, G. Zanchin, R. Di Girolamo, F. De Stefano, C. Lorber, C. De Rosa, G. Ricci, F. Bertini, *Macromolecules*, 2020, **53**, 5881-5894.
54 A. Ali, M. K. Tufail, M. I. Jamil, W. Yaseen, N. Iqbal, M. Hussain, A. Ali, T. Aziz, Z. Fan, L. Guo, *Molecules*, 2021, **26**, 2037.
55 A. Malmberg and B. Löfgren, *J. Appl. Polym. Sci.*, 1997, **66**, 35-44.
56 N. C. Restrepo-Zapata, T. A. Osswald, J. P. Hernández-Ortiz, *Polym. Eng. Sci.*, 2015, **55**, 2073-2088.
57 N. Sanches, S. Cassu, M. Diniz, R. Lazzarini Dutra, *Polímeros*, 2014, **24**, 269-275.
58 M. A. L. Verbruggen, L. van der Does, J. W. M. Noordermeer, M. van Duin, *J. Appl. Polym. Sci.*, 2008, **109**, 976-986.

59 F. J. Linnig and J. E. Stewart, *Rubber Chem. Technol.*, 1958, **31**, 719-736.
60 G. Socrates, *Infrared and Raman Characteristic Group Frequencies*, 3rd edn., John Wiley & Sons Ltd.
61 R. Winters, W. Heinen, M. A. L. Verbruggen, J. Lugtenburg, M. van Duin, H. J. M. de Groot, *Macromolecules*, 2002, **35**, 1958-1966.
62 Q. Wu, Q. Su, L. Ye, G. Li, Y. Mu, *Dalton Trans.*, 2010, **39**, 2525-2535.
63 T. Uozumi and K. Soga, *Makromol. Chem.*, 1992, **193**, 823-831.
64 V. V. Sukulova, A. A. Barabanov, M. A. Matsko, V. A. Zakharov, T. B. Mikenas, *J. Catal.*, 2019, **369**, 276-282.
65 B. Jiang, X. Liu, Y. Weng, Z. Fu, A. He, Z. Fan, *J. Catal.*, 2019, **369**, 324-334.
66 J. A. M. Awudza and P. J. T. Tait, *J. Polym. Sci., Part A: Polym. Chem.*, 2008, **46**, 267-277.
67 V. L. Cruz, A. Muñoz–Escalona, J. Martinez–Salazar, *J. Polym. Sci., Part A: Polym. Chem.*, 1998, **36**, 1157-1167.
68 L. A. Williams and T. J. Marks, *Organometallics*, 2009, **28**, 2053-2061.
69 K. Czaja, L. A. Novokshonova, N. J. Kovaleva, *Macromol. Chem. Phys.*, 1999, **200**, 983-988.
70 N. Herfert, P. Montag, G. Fink, *Makromol. Chem.*, 1993, **194**, 3167-3182.
71 A. Ortín, J. Montesinos, E. López, P. del Hierro, B. Monrabal, J. R. Torres-Lapasió, M. C. García-Álvarez-Coque, *Macromol. Symp.*, 2013, **330**, 63-80.
72 C. Piel, E. Jannesson, Å. Qvist, *Macromol. Symp.*, 2009, **282**, 41-49.
73 S. Hosoda, Y. Nozue, Y. Kawashima, K. Suita, S. Seno, T. Nagamatsu, K. B. Wagener, B. Inci, F. Zuluaga, G. Rojas, J. K. Leonard, *Macromolecules*, 2011, **44**, 313-319.
74 G. Rojas, B. Inci, Y. Wei, K. B. Wagener, *J. Am. Chem. Soc.*, 2009, **131**, 17376-17386.
75 F. M. Mirabella and A. Bafna, *J. Polym. Sci., Part B: Polym. Phys.*, 2002, **40**, 1637-1643.
76 D. R. Burfield, *Macromolecules*, 1987, **20**, 3020-3023.
77 C. Li Pi Shan, J. B. P. Soares, A. Penlidis, *Polymer*, 2002, **43**, 767-773.
78 H. Miyata, M. Yamaguchi, M. Akashi, *Polymer*, 2001, **42**, 5763-5769.
79 J. P. Janet, F. Liu, A. Nandy, C. Duan, T. Yang, S. Lin, H. J. Kulik, *Inorg. Chem.*, 2019, **58**, 10592-10606.
80 G. R. Schleder, A. C. M. Padilha, A. Reily Rocha, G. M. Dalpian, A. Fazzio, *J. Chem. Inf. Model.*, 2020, **60**, 452-459.
81 L. Zhao, H. L. Ciallella, L. M. Aleksunes, H. Zhu, *Drug Discov.*, 2020, **25**, 1624-1638.
82 V. H. Nair, P. Schwaller, T. Laino, *Chimia*, 2019, **73**, 997.
83 C. Bo and F. Maseras, *Dalton Trans.*, 2008, 2911-2919.
84 J. P. Janet, T. Z. H. Gani, A. H. Steeves, E. I. Ioannidis, H. J. Kulik, *Ind. Eng. Chem. Res.*, 2017, **56**, 4898-4910.
85 C. Chen and S. P. Ong, *Nat. Comput. Sci.*, 2022, **2**, 718-728.
86 R. Parveen, T. R. Cundari, J. M. Younker, G. Rodriguez, L. McCullough, *ACS Catal.*, 2019, **9**, 9339-9349.
87 V. Cruz, J. Ramos, A. Muñoz-Escalona, P. Lafuente, B. Peña, J. Martinez-Salazar, *Polymer*, 2004, **45**, 2061-2072.
88 V. L. Cruz, S. Martinez, J. Martinez-Salazar, D. Polo-Cerón, S. Gómez-Ruiz, M. Fajardo, S. Prashar, *Polymer*, 2007, **48**, 4663-4674.
89 D. J. Durand and N. Fey, *Chem. Rev.*, 2019, **119**, 6561-6594.
90 M. Linnolahti and S. Collins, *ChemPhysChem*, 2017, **18**, 3369-3374.
91 A. F. R. Kilpatrick, J. C. Buffet, P. Nørby, N. H. Rees, N. P. Funnell, S. Sripothongnak, D. O'Hare, *Chem. Mater.*, 2016, **28**, 7444-7450.
92 D. Fregonese, S. Mortara, S. Bresadola, *J. Mol. Catal. A Chem.*, 2001, **172**, 89-95.
93 P. Chammingkwan, *High-throughput approach for establishing structure-performance relationship in Ziegler-Natta catalyzed olefin polymerization*, http://hdl.handle.net/10119/16739.
94 F. J. Stadler, C. Gabriel, H. Münstedt, *Macromol. Chem. Phys.*, 2007, **208**, 2449-2454.
95 S. Watanabe, N. Sano, I. Noda, Y. Ozaki, *J. Phys. Chem. B*, 2009, **113**, 3385-3394.
96 X. b. Zhang, Z. s. Li, H. Yang, C. C. Sun, *Macromolecules*, 2004, **37**, 7393-7400.
97 A. Hawkins, *Synthesis of next-generation functional polymers: exploration of PHENI* transition metal complexes*, M.Chem. Part II Thesis, *University of Oxford*, 2022.

Chapter 6 – Experimental details

6.1. General details and instrumentation

6.1.1. General procedures

Air- and moisture-sensitive compounds were manipulated under an inert atmosphere of nitrogen, using standard Schlenk line techniques[1] on a dual manifold vacuum/nitrogen line or in an MBraun Labmaster 100 glovebox.

Pentane, hexane, toluene, and benzene were dried using an MBraun SPS 800 solvent purification system, stored over a potassium mirror, and degassed under partial vacuum before use. Anhydrous dichloromethane, dimethylformamide, and acetonitrile were dried using an MBraun SPS 800 system, stored over pre-activated 3 Å molecular sieves and degassed under partial vacuum before use. Tetrahydrofuran was distilled from sodium/benzophenone, stored over pre-activated 3 Å molecular sieves and degassed under partial vacuum before use. Diethyl ether was distilled from NaK, stored over a potassium mirror, and degassed under partial vacuum before use. Acetone was used as received. Dioxane was distilled from sodium, stored over pre-activated 3 Å molecular sieves and degassed under partial vacuum before use.

Deuterated solvents were dried over potassium metal (benzene-d_6, and toluene-d_8) or CaH_2 (chloroform-*d*, dichloromethane-d_2, acetonitrile-d_3, bromobenzene-d_5, pyridine-d_5, and tetrahydrofuran-d_8) and refluxed under reduced pressure, distilled under static vacuum, freeze-pump-thaw degassed three times and stored over pre-activated 3 or 4 Å molecular sieves. Chloroform-*d* and 1,1,2,2-tetrachloroethane-d_2 were used as supplied for samples which were not air- and moisture-sensitive.

6.1.2. Solution NMR spectroscopy

NMR spectra were recorded on either a Bruker Avance III HD NanoBay NMR (9.4 T, 400.2 MHz), a Bruker Avance III NMR (11.75 T, 499.9 MHz), a Bruker Avance NMR (11.75 T, 500.3 MHz) with a ^{13}C-detect cryoprobe, or a Bruker NEO 600 (14.1 T, 600.4 MHz) with a broadband helium cryoprobe. Spectra were recorded at 298 K unless otherwise stated and referenced internally to the residual *protio* solvent resonance. Chemical shifts, δ, are reported in parts per million (ppm) relative to tetramethylsilane (δ = 0 ppm). Air-sensitive samples were prepared in a glovebox under an inert atmosphere of nitrogen, using dried deuterated solvents and sealed in 5 mm J. Young's tap NMR tubes.

For polyethylene samples, NMR spectra were recorded in 1,1,2,2-tetrachloroethane-d_2 at 393–403 K with chromium (III) acetylacetonate as a T_1 relaxation agent (0.5 wt%).

6.1.3. Solid-state NMR spectroscopy

Solid-state NMR spectra were recorded by Dr Nicholas Rees (University of Oxford) on a Bruker Avance III HD NanoBay solid-state NMR spectrometer (9.4 T, 399.9 MHz) or by Dr Dinu Iuga (University of Warwick, UK High-Field Solid-State NMR Facility) on a Bruker WB US^2 solid-state NMR spectrometer (20.0 T, 850.2 MHz). Samples were spun at the magic angle at spin rates of 10, 12, 20, or 60 kHz. ^{13}C NMR spectra were referenced to adamantane, ^{27}Al to aluminium nitrate, and ^{29}Si to kaolinite.

6.1.4. X-ray crystallography

Single-crystal X-ray diffraction data collection and structure determination were performed by Dr Zoë R. Turner (University of Oxford) or the author. Crystals were mounted on MiTeGen MicroMounts using perfluoropolyether oil and rapidly transferred

to a goniometer head on a diffractometer fitted with an Oxford Cryosystems Cryostream open-flow nitrogen cooling device.[2] Data collections were carried out at 100 or 150 K on an Oxford Diffraction Supernova or XtalLAB Synergy R DW diffractometer using mirror-monochromated Cu Kα radiation (λ = 1.54178 Å) and data were processed using CryAlisPro.[3] The structures were solved using direct methods (SIR-92)[4] or a charge flipping algorithm (SUPERFLIP)[5] and refined by full-matrix least-squares using either the Win-GX or CRYSTALS software suites.[6,7] Molecular bond lengths and angles were calculated, where required, using PLATON.[8] Illustrations of the solid state molecular structures were created using ORTEP.[9] Thermal ellipsoids were shown at 30% probability unless otherwise specified.

6.1.5. Wide-angle X-ray scattering

X-ray scattering experiments were performed by Dr. Philip Kenyon (University of Oxford) on a PANalytical X'Pert Pro diffractometer in reflection mode, using copper Kα radiation ($\lambda_{\alpha1}$ = 1.540598 Å, $\lambda_{\alpha2}$ = 1.544426 Å, α_1/α_2 = 0.5) at 40 kV and 40 mA. Samples were mounted on stainless steel sample holders, and scans were recorded from $2° \leq 2\theta \leq 70°$.

6.1.6. Elemental analysis

Samples were prepared in a glovebox under a nitrogen atmosphere and sealed in glass vials. CHN analyses were carried out in duplicate by Ms Orla McCullough (London Metropolitan University).

6.1.7. Infrared spectroscopy

Fourier-transform infrared (FTIR) spectra were measured using a ThermoScientific Nicolet iS 5 FTIR spectrometer, and either the iD1 Transmission, or germanium iD3

Attenuated Total Reflection accessories. A background spectrum was run prior to the samples and subtracted from the sample spectra. Air-sensitive samples were prepared in a glove box, ground with anhydrous potassium bromide, and pressed into discs.

6.1.8. Scanning electron microscopy

Scanning electron microscopy (SEM) images were collected on a JEOL JSM-6010LV scanning electron microscope. Samples were prepared on carbon tape and coated with platinum using a Quorum Technologies SC7620 sputter coater to reduce charge build-up and improve image quality.

6.1.9. Gel permeation chromatography

Gel permeation chromatography (GPC) was performed by Ms. Liv Thobru, Ms. Sara Herum, and Ms. Rita Jenssen (Norner AS, Norway) on a high temperature gel permeation chromatograph with an IR5 infrared detector (GPC-IR5). Samples were prepared by dissolution in 1,2,4-trichlorobenzene (TCB) containing 300 ppm of 3,5-di-*tert*-butyl-4-hydroxytoluene (BHT) at 160 °C for 90 minutes and then filtered with a 10 μm SS filter before being passed through the GPC column. The samples were run under a flow rate of 0.5 mL min^{-1} using TCB containing 300 ppm of BHT as mobile phase with 1 mg mL^{-1} BHT added as a flow rate marker. The GPC column and detector temperature were set at 145 and 160 °C respectively.

6.1.10. Differential scanning calorimetry

Differential scanning calorimetry was performed on a Perkin Elmer DSC 4000 System within a temperature range of 30–180 °C at a rate of 20 K min^{-1}. Polymer samples were sealed in 100 μL aluminium crucibles. An empty crucible was used as a reference, and the DSC was calibrated using indium and zinc.

Low temperature runs were performed on a TA Instruments DSC 25, with a Refrigerated Cooling System 90 within a temperature range of –80–200 °C at a rate of 10 K min^{-1}. Samples were sealed in TA Instrument TZero pans, and an empty pan was used as a reference.

6.1.11. Thermogravimetry

Thermogravimetric analysis was performed by Mr. Alexander Evans (University of Oxford) on a Perkin Elmer TGA 8000 thermogravimetric analyser within a temperature range of 50–800 °C. Polymer samples were loaded into pre-weighed ceramic pans and heated at a rate of 20 K min^{-1}. A purge gas of either dry nitrogen or synthetic air (20% O_2 in N_2) was used.

6.1.12. Mechanical analysis

Mechanical testing was performed by Ms. Thea Høibjerg Glittum, and Ms. Heidi Nornes Bryntesen (Norner AS, Norway). The UHMWaPP sample was cut up and milled to a powder-like material using a cooling unit (liquid nitrogen). A thermal stabiliser (BHT) was added, and the sample was pressed into plates (80 x 60 x 1 mm) at either 200 or 180 °C. Samples pressed at 200 and 180 °C gave the same results. Density was measured at room temperature (23 °C) according to ISO1183-1 (2012) on a Mettler Toledo XS204 instrument. Measurement was repeated three times. Tensile properties were determined at room temperature (23 °C) according to ISO527-1/2 using type 5A test specimens, on a Zwick Z010 instrument with a 5 kN load cell. The gauge length was L_0 = 20 mm, and the gripping distance was L = 50 mm. Testing speed was 50 mm min^{-1}. Samples were stopped at 1900%. Measurements were repeated 5 times.

6.1.13. Optical measurements

Optical characterisation was performed using a PerkinElmer LAMBDA 1050+ UV/Vis/NIR Spectrophotometer with a 150 mm InGaAs Integrating Sphere using tungsten-halogen and deuterium-arc sources within a wavelength range of 250–1400 nm.

6.1.14. Microcompounding

Microcompounding was performed by Dr. Giovanni Santagiuliana (Queen Mary University, Nanforce Technology Ltd.). UHMWPE was blended with either LDPE or HDPE inside the DSM Xplore 15cc micro-compounder in recirculation mode for about 5 min using a screw speed of 100 rpm and argon atmosphere to avoid material oxidation/degradation. The temperature was set separately for the three zones of the micro-compounder: top part (beginning of the screws/feeding area) 150–200 °C, middle region 150–200 °C, and bottom part (tip of the screws/die area) 150–205 °C. After blending, the samples were collected in a ribbon shape using a flat film die attached to the microcompounder and a dedicated take-off system. The take-off system consisted of an air blade positioned close to the die used for a fast cooling to avoid or limit any lateral shrinkage of the extruded material; a speed-controlled collection roll; and a torque-controlled winding roll.

6.1.15. Dynamic mechanical thermal analysis

Dynamic mechanical thermal analysis was performed with the assistance of Mr. Nicholas Hawkins (University of Oxford) on a TA Instruments Q800 DMA equipped with a TA Instruments ACS-3 chiller system. Rectangular samples were cut from extruded ribbons with a width of approx. 7 mm with thickness 50–500 μm, and sample length of approx. 10 mm. Samples were fixed in a film clamp with 5 psi clamping force and subjected to a heating protocol from –100 to 125 °C at 3 °C min^{-1} and a 1 Hz sinusoidal displacement

applied at 0.1% strain. Force ramps were performed at room temperature on samples with width approx. 4 mm, from 0 to 18 N, at a rate of 0.25 N min^{-1} (for 50 μm thick films), with the rate scaled proportionally to the sample thickness to maintain a stress rate of approximately 1 MPa min^{-1}.

6.2. Commercially supplied materials

^{n}BuLi (1.6 or 2.5 M in hexanes), MeLi (1.6 M in diethyl ether), $PhCH_2MgCl$ (2.0 M in THF), 4-methyl-2-*tert*-butylphenol, bromine, sulphur, 2-mercaptobenzothiazole, 2-bromophenol, titanium tetrachloride, trimethylaluminium, triethylaluminium, tri*iso*butylaluminium, 2,6-di*iso*propylphenol, iodine, potassium hydroxide, sodium hydroxide, sodium carbonate, methyl iodide, 2,4-dimethylphenol, 4-methyl-2-*tert*-butylphenol, platinum(0)-1,3-divinyl-1,1,3,3-tetramethyldisiloxane (2 wt% Pt in xylene), LDPE, triphenylmethylium tetrakis(pentafluorophenyl)borate, sulphuric acid, and sodium ethoxide were purchased from Sigma Aldrich and used as received.

2,3,4,5,6,7-hexamethylindene, and HDPE (SCG Chemicals PLC), 6-bromo-2,4-di-*tert*-butylphenol, and 2,5-dibromohydroquinone (Alfa Aesar), 2-bromo-4,6-difluorophenol (Fluorochem), magnesium turnings, and magnesium sulphate (Fisher Scientific) were all used a received.

1,5-hexadiene, 1-hexene, 1-dodecene, and 5-ethylidene-2-norbornene (Sigma Aldrich) and 1-octene (Alfa Aesar) were dried over CaH_2, distilled under static vacuum, freeze-pump-thaw degassed three times and stored over pre-activated 3 or 4 Å molecular sieves. TMSI and TMSBr (Sigma Aldrich) were stored over pre-activated 3 Å molecular sieves and metallic copper. *N,N*-dimethylanilinium tetrakis(pentafluorophenyl(borate)

was recrystallised from DCM and dried under vacuum before use. Et_3N was dried over KOH, distilled under static vacuum and freeze-pump-thaw degassed before use. 2,4-bis(*α*,*α*-dimethylbenzyl)phenol (Sigma Aldrich) was recrystallized from hot ethanol before use. $MeCl_2SiH$, Me_2SiCl_2, $Me^nPrSiCl_2$, and $MePhSiCl_2$ (Sigma Aldrich) were dried over pre-activated 3 Å molecular sieves before use. $Me^tBuSiCl_2$ (ABCR (UK) Ltd.) was sublimed under vacuum before use. Allyl bromide (Sigma Aldrich) was washed with $NaHCO_3$ followed by distilled water and dried over $MgSO_4$. Ethylene, propylene (N2.5), hydrogen, ethylene/propylene, and ethylene/hydrogen were supplied by BOC Ltd., CK Special Gases Ltd., CK Isotopes Ltd., or Buse Gasses Ltd. and used as received. Ethylene was passed through pre-activated molecular sieves before use. Solid polymethylaluminoxane (sMAO, third generation) was supplied by SGC Chemicals PLC as a slurry in toluene which was dried under vacuum before use. MAO was supplied by Chemtura Corporation as a slurry in toluene which was dried under vacuum before use.

6.3. Literature preparations

The indenyl-PHENICS complex ^{Me2}SB(^{tBu,Me}ArO,Ind)$TiCl_2$ (**14**) was synthesised according to a modified literature procedure.[10] Potassium benzyl was synthesised by Dr. Nichabhat Blake (University of Oxford) according to a literature procedure.[11] (2,3,4,5,6,7-hexamethyl-1*H*-inden-1-yl)lithium,[12,13] $TiCl_4$·2THF,[14] I*Me_2SiCl,[13,15] KODipp,[16] $Cl_2Si(Me)$-$(CH_2)_6$-$(Me)SiCl_2$,[17] and 1,4-dibromo-2,5-di(allyloxy)benzene[18] were synthesised according to literature procedures or modified literature procedures. Silica (PQES70X) was supplied by PQ Corporation (USA) and was calcined by Dr. Philip Kenyon (University of Oxford). 1-hexanol modified Mg_3Al-CO_3 AMO-LDH was synthesised by Ms. Katherine Laney (University of Oxford) according to modified literature procedures.[19,20]

6.4. Experimental details for Chapter Two

6.4.1. Synthesis of PHENI* ligands

Substituted phenol, ^{R_1R_2}ArOH (1 equivalent), was dissolved in dichloromethane in a round-bottomed flask. To this, Br_2 (1 eq.) was added dropwise. The reaction was stirred for 90 minutes, after which the crude mixture was washed with distilled water. The organic portion was dried over $MgSO_4$, filtered, and the solvent removed under vacuum to yield the monobrominated product quantitatively as a thick oil.

The bromophenol ^{Br,R_1R_2}ArOH and allyl bromide (CH_2CHCH_2Br, 1.5 eq.) were then dissolved in acetone in a round-bottomed flask. This solution was then added dropwise to a 10% aqueous solution of NaOH (1.5 eq.) and stirred for 4 hours. The reaction mixture was neutralised with 5% aqueous H_2SO_4 and the volatiles removed under vacuum. The product, ^{Br,R_1R_2}ArOAllyl, was extracted in toluene, dried over $MgSO_4$ and the solvent removed under vacuum to give the desired products in quantitative yields as off-white solids.

The allylphenol ^{Br,R_1R_2}ArOAllyl was dissolved in toluene in a Schlenk flask. To this was added dropwise at –70 °C 1.3 eq. of ^{n}BuLi solution (1.6 M in hexanes) and the reaction was allowed to warm to –20 °C. This mixture was then dropwise added to a toluene solution of 3 eq. $R_aR_bSiCl_2$ at –20 °C. The reaction was allowed to warm to room temperature and stirred for 18 h. The solid byproducts were removed by filtration, and the volatiles removed under vacuum, leaving the chlorosilyl product, ^{R_aR_bSiCl,R_1R_2}ArOAllyl, as a pale yellow to colourless oil. This was then combined with 1.1 equivalents of (2,3,4,5,6,7-hexamethyl-1*H*-inden-1-yl)lithium (Ind$^{\#}$Li) and dissolved in THF at 0 °C. The reaction was allowed to warm to room temperature and stirred for 18 h, after which it was dried under vacuum; the product was extracted in pentane and

the solvent removed under vacuum to yield the proligand ^{R_aR_b}SB(^{R_1R_2}ArOAllyl,I*)H. The proligand was then redissolved in toluene. 3.5 equivalents of triethylamine were added, and the mixture cooled to –78 °C. 2.25 eq. of ^{n}BuLi solution (1.6 M in hexanes) was added dropwise. The reaction was allowed to warm to room temperature and stirred for 3–18 h, during which the solution gradually darkens. In the stepwise process, removal of the volatiles under vacuum yielded the ligands as dilithium salts, ^{R_aR_b}SB(^{R_1R_2}ArO,I*)Li$_2$, as bright orange powders in approximately quantitative yields. The crude products were used to synthesise group 4 complexes without further purification.

6.4.1.1. ^{Me_2}SB(^{tBu,Me}ArOAllyl,I)H (1e)*

^{1}H NMR (400 MHz, benzene-d_6, 298 K): δ 7.24 (d, $^4J_{H–H}$ = 2.2 Hz, 1H, 3,5-C$_6$**H**$_2$), 7.03 (d, $^4J_{H–H}$ = 2.3 Hz, 1H, 3,5-C$_6$**H**$_2$), 5.87 (ddt, $^3J_{H–H}$ = 17.2 Hz, $^3J_{H–H}$ = 10.8 Hz, $^3J_{H–2H}$ = 4.0 Hz, 1H, OCH$_2$C**H**CH$_2$), 5.57 (app. dq, $^3J_{H–H}$ = 17.2 Hz, $^2J_{H–H}$ = $^4J_{H–2H}$ = 2.1 Hz, 1H, OCH$_2$CHC**H**$_2$), 5.16 (app. dq, $^3J_{H–H}$ = 10.8 Hz, $^2J_{H–H}$ = $^4J_{H–2H}$ = 1.9 Hz, 1H, OCH$_2$CHC**H**$_2$), 4.47 (ddt, $^2J_{H–H}$ = 14.1 Hz, $^3J_{H–H}$ = 4.0 Hz, $^4J_{H–2H}$ = 2.0 Hz, 1H, OC**H**$_2$CHCH$_2$), 4.26 (ddt, $^2J_{H–H}$ = 14.1 Hz, $^3J_{H–H}$ = 4.1 Hz, $^4J_{H–2H}$ = 2.0 Hz, 1H, OC**H**$_2$CHCH$_2$), 4.00 (s, 1H, I***H**), 2.53 (s, 3H, I***Me**), 2.21 (s, 6H, I***Me**), 2.19 (s, 3H, I***Me**), 2.17 (s, 6H, I***Me** and Ph**Me**), 1.85 (s, 3H, I***Me**), 1.49 (s, 9H, C**Me**$_3$), 0.29 (s, 3H, Si**Me**), and 0.07 (s, 3H, Si**Me**) ppm.

^{13}C{^{1}H} NMR (126 MHz, benzene-d_6, 298 K): δ 161.43 (1-**C**$_6$H$_2$), 142.06 (**Ar**), 141.96 (**Ar**), 141.65 (**Ar**), 139.38 (**I***), 135.12 (3,5-**C**$_6$H$_2$), 133.80 (OCH$_2$**C**HCH$_2$), 132.54 (**I***),132.48 (**I***),132.14 (**I***),131.74 (**Ar**), 130.01 (3,5-**C**$_6$H$_2$), 129.31 (**Ar**), 127.98 (**Ar**), 127.09 (**Ar**), 125.72 (**I***),115.57 (OCH$_2$CH**C**H$_2$), 75.82 (O**C**H$_2$CHCH$_2$), 47.71 (**I***Si), 35.03 (**C**Me$_3$), 31.05 (C**Me**$_3$), 20.81 (C$_6$H$_2$**Me**), 18.74 16.10 16.04 16.03 14.87 14.57 (I***Me**), 0.32 and −3.12 (Si**Me**) ppm.

6.4.1.2. ^{Me2}SB(^{tBu2}ArOAllyl,I)H (2e)*

^{1}H NMR (400 MHz, benzene-d_6, 298 K): δ 7.59 (d, $^{4}J_{H–H}$ = 2.5 Hz, 1H, 3,5-C$_6$**H**$_2$), 7.37 (d, $^{4}J_{H–H}$ = 2.5 Hz, 1H, 3,5-C$_6$**H**$_2$), 5.87 (ddt, $^{3}J_{H–H}$ = 17.2 Hz, $^{3}J_{H–H}$ = 10.8 Hz, $^{3}J_{H–2H}$ = 4.0 Hz, 1H, OCH$_2$C**H**CH$_2$), 5.56 (app. dq, $^{3}J_{H–H}$ = 17.2 Hz, $^{2}J_{H–H}$ = $^{4}J_{H–2H}$ = 2.0 Hz, 1H, OCH$_2$CHC**H**$_2$), 5.16 (app. dq, $^{3}J_{H–H}$ = 10.8 Hz, $^{2}J_{H–H}$ = $^{4}J_{H–2H}$ = 1.9 Hz, 1H, OCH$_2$CHC**H$_2$**), 4.47 (ddt, $^{2}J_{H–H}$ = 14.1 Hz, $^{3}J_{H–H}$ = 4.1 Hz, $^{4}J_{H–2H}$ = 2.0 Hz, 1H, OC**H**$_2$CHCH$_2$), 4.26 (ddt, $^{2}J_{H–H}$ = 14.4 Hz, $^{3}J_{H–H}$ = 4.3 Hz, $^{4}J_{H–2H}$ = 2.1 Hz, 1H, OC**H**$_2$CHCH$_2$), 3.98 (s, 1H, I***H**), 2.53 (s, 3H, I***Me**), 2.24 (s, 3H, I***Me**), 2.21 (s, 3H, I***Me**), 2.18 (s, 3H, I***Me**), 2.14 (s, 3H, I***Me**), 1.86 (s, 3H, I***Me**), 1.53 (s, 9H, C**Me**$_3$), 1.30 (s, 9H, C**Me**$_3$), 0.28 (s, 3H, Si**Me**), and 0.17 (s, 3H, Si**Me**$_3$) ppm.

^{13}C{^{1}H} NMR (126 MHz, benzene-d_6, 298 K): δ 161.70 (1-**C**$_6$H$_2$), 145.45 (2,4-**C**$_6$H$_2$), 142.51 (**I***), 142.29 (**I***), 141.58 (2,4-**C**$_6$H$_2$), 139.74 (**I***), 134.21 (OCH$_2$**C**HCH$_2$), 132.96 (**I***), 132.31 (6-**C**$_6$H$_2$), 132.17 (**I***), 132.03 (3,5-**C**$_6$H$_2$), 129.67 (**I***), 127.45 (**I***), 126.51 (3,5-**C**$_6$H$_2$), 126.12 (**I***), 115.91 (OCH$_2$CH**C**H$_2$), 76.00 (O**C**H$_2$CHCH$_2$), 48.45 (**I***Si), 35.76 34.65 (**C**Me$_3$), 31.69 31.46 (C**Me**$_3$), 19.10 16.51 16.43 16.39 15.27 15.05 (I***Me**), 0.20 and −2.32 (Si**Me**) ppm.

6.4.1.3. ^{Me2}SB(^{Cumyl2}ArOAllyl,I)H (11e)*

^{1}H NMR (400 MHz, benzene-d_6, 298 K): δ 7.63 (d, $^{4}J_{H–H}$ = 2.5 Hz, 1H, 3,5-C$_6$**H**$_2$), 7.35−7.28 (m, 5H, CMe$_2$Ph**H** and 3,5-C$_6$**H**$_2$), 7.23−6.97 (m, 6H, CMe$_2$Ph**H**), 5.49 (ddt, $^{3}J_{H–H}$ = 17.4 Hz, $^{3}J_{H–H}$ = 10.7 Hz, $^{3}J_{H–2H}$ = 4.4 Hz, 1H, OCH$_2$C**H**CH$_2$), 5.15 (dd, $^{3}J_{H–H}$ = 17.3 Hz, $^{2}J_{H–H}$ = 2.0 Hz, 1H, OCH$_2$CHC**H**$_2$), 4.96 (dd, $^{3}J_{H–H}$ = 10.8 Hz, $^{2}J_{H–H}$ = 1.9 Hz, 1H, OCH$_2$CHC**H**$_2$), 3.83 (I***H**), 3.49 (ddt, $^{2}J_{H–H}$ = 13.2 Hz, $^{3}J_{H–H}$ = 4.2 Hz, $^{4}J_{H–2H}$ = 1.9 Hz, 1H, OC**H**$_2$CHCH$_2$), 3.26 (ddt, $^{2}J_{H–H}$ = 13.2 Hz, $^{3}J_{H–H}$ = 4.1 Hz, $^{4}J_{H–2H}$ = 1.9 Hz, 1H, OC**H**$_2$CHCH$_2$), {2.50 (3H) 2.21 (3H) 2.17 (6H) 2.04

(3H) 1.78 (3H) 1.75 (3H) 1.71 (3H) 1.70 (3H) 1.67 (3H) (s, I*Me and CMe$_2$Ph)}, 0.14 (s, 3H, SiMe), and 0.02 (s, 3H, SiMe) ppm.

^{13}C{^{1}H} NMR (126 MHz, benzene-d_6, 298 K): δ 161.12 (OAr), 151.80 (CMe$_2$Ph), 151.05 (CMe$_2$Ph), 145.28 (Ar), 142.45 (I*), 142.17 (I*), 142.04 (Ar), 139.57 (I*), 134.97 (OCH$_2$CHCH$_2$), 134.34 (OAr), 132.93 (I*), 132.78 (I*), 132.10 (I*), 129.61 (I*), 128.38 (CMe$_2$Ph), 128.35 (CMe$_2$Ph), 128.16 (Ar), 128.12 (Ar), 127.97 (OAr), 127.35 (Ar), 127.17 (Ar), 126.62 (Ar), 126.07 (I*), 126.04 (CMe$_2$Ph), 125.62 (CMe$_2$Ph), 114.95 (OCH$_2$CHCH$_2$), 74.34 (OCH$_2$CHCH$_2$), 48.41 (I*Si), 43.11 (CMe$_2$Ph), 42.85 (CMe$_2$Ph), 31.15 (CMe$_2$Ph), 31.08 (CMe$_2$Ph), 30.88 (CMe$_2$Ph), 30.59 (CMe$_2$Ph), 19.11 (I*Me), 16.54 (I*Me), 16.39 (I*Me), 16.36 (I*Me), 15.25 (I*Me), 15.08 (I*Me), –0.39 (SiMe), and –2.29 (SiMe) ppm. Two additional aromatic resonances were expected but not detected.

6.4.1.4. ^{Me2}SB(^{H2}ArOAllyl,I)H (19e)*

^{1}H NMR (400 MHz, chloroform-*d*, 298 K): δ 7.36 (ddd, $^3J_{H–H}$ = 8.2 Hz, $^3J_{H–H}$ = 7.3 Hz, $^4J_{H–H}$ = 1.8 Hz, 1H, 3-ArH), 7.26 (dd, $^3J_{H–H}$ = 7.2 Hz, $^4J_{H–H}$ = 1.8 Hz, 1H, 5-ArH), 6.94 (ddd, $^3J_{H–H}$ = 7.3 Hz, $^3J_{H–H}$ = 7.3 Hz, $^4J_{H–H}$ = 0.9 Hz, 1H, 4-ArH), 6.87 (dd, $^3J_{H–H}$ = 8.3 Hz, $^4J_{H–H}$ = 0.9 Hz, 1H 2-ArH), 6.15 (ddt, $^3J_{H–H}$ = 17.3 Hz, $^3J_{H–H}$ = 10.4 Hz, $^3J_{H–H}$ = 5.6 Hz, 1H, OCH$_2$CHCH$_2$), 5.43 (app. dq, $^3J_{H–H}$ = 17.2 Hz, $^2J_{H–H}$ = $^4J_{H–H}$ = 1.5 Hz, 1H, OCH$_2$CHCH$_2$), 5.31 (app. dq, $^3J_{H–H}$ = 10.4 Hz, $^2J_{H–H}$ = $^4J_{H–H}$ = 1.3 Hz, 1H, OCH$_2$CHCH$_2$), 4.63 (dt, $^3J_{H–H}$ = 5.6 Hz, $^4J_{H–H}$ = 1.4 Hz, 2H, OCH$_2$CHCH$_2$), 3.95 (s, 1H, I*H), 2.53 (s, 3H, I*Me), 2.23 (s, 3H, I*Me), 2.18 (s, 3H, I*Me), 2.08 (s, 3H, I*Me), 1.72 (s, 3H, I*Me), 0.08 (s, 3H, SiMe), and –0.15 (s, 3H, SiMe) ppm.

6.4.1.5. ^{Me2}SB(^{tBu2}ArO,I)Li$_2$ (2f)*

^{1}H NMR (400 MHz, pyridene-d_5, 298 K): δ 7.72 (d, $^4J_{H–H}$ = 2.8 Hz, 1H, *m*Ar**H**), 7.43 (d, $^4J_{H–H}$ = 2.8 Hz, 1H, *m*Ar**H**), 2.80 (s, 3H, I***Me**), 2.71 (s, 3H, I***Me**), 2.68 (s, 3H, I***Me**), 2.52 (s, 3H, I***Me**), 2.32 (s, 3H, I***Me**), 2.14 (s, 3H, I***Me**), 1.70 (s, 9H, C**Me**$_3$), 1.39 (s, 9H, C**Me**$_3$), and 0.88 (br, 6H, Si**Me**$_2$) ppm.

6.4.1.6. ^{Me2}SB(^{Cumyl2}ArO,I)Li$_2$ (11f)*

^{1}H NMR (400 MHz, pyridine-d_5, 298 K): δ 7.91 (d, $^4J_{H–H}$ = 2.5 Hz, 1H, *m*Ar**H**), 7.76 (d *J* = 8.0 Hz, 2H, CMe$_2$**Ph**), 7.66 (d, *J* = 7.8 Hz, 3H, CMe$_2$**Ph**), 7.57 (d, $^4J_{H–H}$ = 2.4 Hz, 1H, *m*Ar**H**), 7.36 (td, *J* = 7.9, 2.2 Hz, 2H, CMe$_2$**Ph**), 7.19 (dd, *J* = 10.0, 4.7 Hz, 3H, CMe$_2$**Ph**), 2.89 (s, 6H, I***Me**), 2.88 (s, 3H, I***Me**), 2.66 (s, 3H, I***Me**), 2.47 (s, 3H, I***Me**), 2.38 (s, 3H, I***Me**), 1.99 (s, 6H, C**Me**$_2$Ph), 1.98(s, 6H, C**Me**$_2$Ph), and 0.97 (br, 6H, Si**Me**$_2$) ppm.

^{13}C{^{1}H} NMR (101 MHz, pyridine-d_5, 298 K): δ 155.14 (Ar), 134.15 (Ar), 132.83 (Ar), 132.14 (Ar), 131.65 (Ar), 129.88 (**I***), 129.14 (Ar), 128.36 (CMe$_2$**Ph**), 128.19 (CMe$_2$**Ph**), 127.98 (CMe$_2$**Ph**), 127.38 (CMe$_2$**Ph**), 126.66 (Ar), 126.23 (**Ar**O), 125.48 (CMe$_2$**Ph**), 124.76 (**I***), 122.72 (Ar), 120.26 (Ar), 119.69 (**I***), 105.71 (Ar), 89.38 (Si**I***), 43.59 (**C**Me$_2$Ph), 43.34 (**C**Me$_2$Ph), 32.75 (C**Me**$_2$Ph), 31.24 (C**Me**$_2$Ph), 23.09 (I***Me**), 18.38 (I***Me**), 17.92 (I***Me**), 17.83 (I***Me**), 17.12 (I***Me**), 16.44 (I***Me**), and 6.22 (Si**Me**$_2$) ppm. Additional aromatic resonances were expected but not observed.

^{29}Si NMR (^{1}H-observed HMBC, 80 MHz, pyridine-d_5, 298 K): δ –21 ppm.

6.4.1.7. rac-^{Me,nPr}SB(^{tBu2}ArO,I)Li$_2$ (12f)*

^{1}H NMR (400 MHz, pyridine-d_5, 298 K): δ 7.91 (d, $^4J_{H–H}$ = 2.8 Hz, 1H, *m*Ar**H**), 7.61 (d, $^4J_{H–H}$ = 2.8 Hz, 1H, *m*Ar**H**), 2.95 (s, 6H, I***Me**), 2.89 (s, 3H, I***Me**), 2.74 (s, 3H, I***Me**),

2.51 (s, 3H, I***Me**), 2.43 (d, *J* = 7.2 Hz, 2H, SiC**H**$_2$CH$_3$), 2.39 (s, 3H, I***Me**), 1.89 (s, 9H, C**Me**$_3$), 1.59 (s. 9H, C**Me**$_3$), 0.97 (t, *J* = 7.1 Hz, 3H, SiC**H**$_3$), and 0.80 (t, *J* = 7.3 Hz, 3H, SiCH$_2$C**H**$_3$) ppm.

^{7}Li NMR (155 MHz, pyridine-d_5, 298 K): δ 1.99, and 1.68 ppm.

^{29}Si NMR (^{1}H-observed HMBC, 80 MHz, pyridine-d_5, 298 K): δ –13 ppm.

6.4.1.8. rac-^{Me,Ph}SB(^{tBu2}ArO,I)Li$_2$ (13f)*

^{1}H NMR (400 MHz, pyridine-d_5, 298 K): δ 8.46 (br, 1H, *m*Ar**H**), 8.13 (dt, *J* = 6.1, 1.6 Hz, 1H *m*Ar**H**), 7.48–7.26 (m, 5H, SiC$_6$**H**$_5$), 3.12 (s, 3H, I***Me**), 2.97 (s, 3H, I***Me**), 2.88 (s, 3H, I***Me**), 2.73 (s, 3H, I***Me**), 2.71 (s, 3H, I***Me**), 2.48 (s, 3H, I***Me**), 1.92 (s, 9H, C**Me**$_3$), 1.43 (s, 9H, C**Me**$_3$), and 0.96 (Si**Me**) ppm.

^{7}Li NMR (156 MHz, pyridine-d_5, 298 K): δ 2.6, and –1.4 ppm.

^{29}Si NMR (^{1}H-observed HMBC, 80 MHz, pyridine-d_5, 298 K): δ –15 ppm.

6.4.2. Synthesis of group four PHENI* dichloride complexes

The stepwise process is continued as follows: to one equivalent of ligand, and 1.5 eq. of TiCl$_4$·2THF was added toluene, and the reaction stirred for 18 h during which the solution became dark red. Alternatively, in the *in situ* process, to a toluene solution of the proligand and 4 equivalents of triethylamine cooled to –78 °C, 2.25 equivalents of ^{n}BuLi (1.6 M in hexanes) was added dropwise. The reaction was allowed to warm to 23 °C and stirred for 3 h, during which the solution gradually darkens. To this was then added 1.5 equivalents of TiCl$_4$·2THF as a slurry in toluene, the resulting mixture was heated to 90 °C and stirred for 4 h during which the reaction turned dark red.

The insoluble materials were removed by filtration and the volatiles were removed from the filtrate under vacuum. The resulting brick-red solid was washed with pentane to afford the titanium dichloro complexes, ^{R_aR_b}SB(^{R1R2}ArO,I*)TiCl$_2$.

6.4.2.1. ^{Me2}SB(^{tBu,Me}ArO,I)TiCl$_2$ (1)*

430 mg (18%) yield. Crystals suitable for X-ray diffraction were grown from slow evaporation of a diethyl ether solution at –30 °C.

^{1}H NMR (400 MHz, benzene-d_6, 298 K): δ 7.22 (d, $^4J_{H–H}$ = 1.9 Hz, 1H, *m*Ph**H**), 7.19 (d, $^4J_{H–H}$ = 2.0 Hz, 1H, *m*Ph**H**), 2.66 (s, 3H, I***Me**), 2.56 (s, 3H, I***Me**), 2.27 (s, 3H, Ph**Me**), 2.14 (s, 3H, I***Me**), 2.03 (s, 3H, I***Me**), 2.02 (s, 3H, I***Me**), 1.98 (s, 3H, I***Me**), 1.46 (s, 9H, C**Me**$_3$), 0.68 (s, 3H, Si**Me**), and 0.66 (s, 3H, Si**Me**) ppm.

^{13}C{^{1}H} NMR (126 MHz, benzene-d_6, 298 K): δ 167.79 (***i***ArO), 144.68 (**I***), 138.03 (**I***), 136.99 (***o***ArO), 136.95 (**I***), 136.51 (**I***), 134.04 (Si**Ar**O), 133.98 (***p***ArO), 132.50 (**I***), 131.98 (**I***), 131.37 (***m***ArO), 131.22 (**I***), 131.01 (**I***), 129.04 (***m***ArO), 110.75 (Si**I***),35.12 (**C**Me$_3$), 30.05 (C**Me**$_3$), 21.81 (I***Me**), 21.44 (4-**Me**-ArO), 17.46 (I***Me**), 17.26 (I***Me**), 16.66 (I***Me**), 16.50 (I***Me**), 15.69 (I***Me**), 3.62 (Si**Me**), and 1.49 (Si**Me**) ppm.

6.4.2.2. ^{Me2}SB(^{tBu2}ArO,I)TiCl$_2$ (2)*

961 mg (29%) and 2.13 g (19%) yields. Crystals suitable for X-ray diffraction were grown from a saturated pentane solution at –30 °C.

^{1}H NMR (400 MHz, benzene-d_6, 298 K): δ 7.58 (d, $^4J_{H–H}$ = 2.4 Hz, 1H, *m*Ar**H**), 7.56 (d, $^4J_{H–H}$ = 2.4 Hz, 1H, *m*Ar**H**), 2.65 (s, 3H, I***Me**), 2.55 (s, 3H, I***Me**), 2.12 (s, 3H, I***Me**),

2.05 (s, 3H, I*$\mathbf{Me}$), 2.02 (s, 3H, I*$\mathbf{Me}$), 1.96 (s, 3H, I*$\mathbf{Me}$), 1.50 (s, 9H, C$\mathbf{Me}_3$), 1.38 (s, 9H, C$\mathbf{Me}_3$), and 0.72 (s, 6H, Si$\mathbf{Me}$) ppm.

^{13}C{^{1}H} NMR (126 MHz, benzene-d_6, 298 K): δ 167.32 (***i***ArO), 146.91 (***o,p***ArO), 144.39 (**I***), 137.60 (**I***), 136.61 (**I***), 136.15 (**I***), 136.10 (***o,p***ArO), 133.14 (Si**Ar**O), 132.24 (**I***), 131.61 (**I***), 130.85 (**I***), 130.62 (**I***), 127.07 (***m***ArO), 124.87 (***m***ArO), 110.40 (Si**I***), 35.11 (**C**Me_3), 34.61 (**C**Me_3), 31.44 (C$\mathbf{Me}_3$), 29.73 (C$\mathbf{Me}_3$), 21.37 (I*$\mathbf{Me}$), 17.11 (I*$\mathbf{Me}$), 16.88 (I*$\mathbf{Me}$), 16.29 (I*$\mathbf{Me}$), 16.12 (I*$\mathbf{Me}$), 15.47 (I*$\mathbf{Me}$), 3.35 (Si$\mathbf{Me}$), and 1.44 (Si$\mathbf{Me}$) ppm.

^{29}Si NMR (80 MHz, benzene-d_6, 298 K): δ –12.6 ppm.

CHN analysis (%): Expected C 64.25, H 7.65; observed C 64.57, H 7.86.

6.4.2.3. ^{Me2}SB(^{Cumyl2}ArO,I)TiCl$_2$ (11)*

388 mg (12%) yield. Crystals suitable for X-ray diffraction were grown from slow evaporation of a diethyl ether solution at –30 °C.

^{1}H NMR (400 MHz, benzene-d_6, 298 K): δ 7.51 (d, $^4J_{H–H}$ = 2.4 Hz, 1H, 3,5-C$_6\mathbf{H}_2$), 7.46 (d, $^4J_{H–H}$ = 2.4 Hz, 1H, 3,5-C$_6\mathbf{H}_2$), 7.37–7.17 (m, 8H, CMe$_2$**Ph**), 7.13–7.07 (m, 1H, CMe$_2$**Ph**), 7.06–7.00 (m, 1H, CMe$_2$**Ph**), 2.62 (s, 3H, I*$\mathbf{Me}$), 2.42 (s, 3H, I*$\mathbf{Me}$), 2.09 (s, 3H, I*$\mathbf{Me}$), 2.00 (s, 3H, I*$\mathbf{Me}$), 1.98 (s, 3H, I*$\mathbf{Me}$), 1.90 (s, 3H, I*$\mathbf{Me}$), 1.73 (s, 6H, C$\mathbf{Me}_2$Ph), 1.70 (s, 3H, C$\mathbf{Me}_2$Ph), 1.67 (s, 3H, C$\mathbf{Me}_2$Ph), 0.60 (s, 3H, Si$\mathbf{Me}$), and 0.59 (s, 3H, Si$\mathbf{Me}$) ppm.

^{13}C{^{1}H} NMR (126 MHz, benzene-d_6, 298 K): δ 166.74 (**Ar**), 151.09 (**Ar**), 169.81 (**Ar**), 146.72 (**Ar**), 144.62 (**Ar**), 137.54 (**Ar**), 136.74 (**Ar**), 136.51 (**Ar**), 136.28 (**Ar**), 133.84 (6-**C**$_6\mathrm{H}_2$), 132.43 (**Ar**), 131.65 (**Ar**), 130.97 (**Ar**), 130.74 (**Ar**), 129.83

(3,5-**C**$_6$H$_2$), 128.46 (CMe$_2$**Ph**), 128.35 (CMe$_2$**Ph**), 128.32 (CMe$_2$**Ph**), 128.16 (CMe$_2$**Ph**), 127.97 (CMe$_2$**Ph**), 127.68 (3,5-**C**$_6$H$_2$), 127.13 (CMe$_2$**Ph**), 126.39 (CMe$_2$**Ph**), 126.19 (CMe$_2$**Ph**), 125.58 (CMe$_2$**Ph**), 110.69 (**I***Si), 43.34, and 42.92 (**C**Me$_2$Ph), 31.26, 31.23, 30.60 and 29.00 (C**Me**$_2$Ph), 21.65, 17.44, 17.31, 16.65, 16.39, and 15.66 (I***Me**), 3.93, and 1.41 (Si**Me**) ppm. An additional aromatic resonance was expected but not observed.

CHN analysis (%): Expected C 69.98, H 6.88; observed C 71.33, H 7.65.

6.4.2.4. ^{Me2}SB(^{H2}ArO,I)TiCl$_2$ (19)*

^{1}H NMR (400 MHz, benzene-d_6, 297 K): δ 7.39–7.27 (m, 1H, Ar**H**), 7.03–6.91 (m, 3H, Ar**H**), 6.73–6.63 (m, 1H, Ar**H**), 2.65 (s, 3H, I***Me**), 2.53 (s, 3H, I***Me**), 2.09 (s, 3H, I***Me**), 2.04 (s, 3H, I***Me**), 1.91 (s, 3H, I***Me**), 1.85 (s, 3H, I***Me**), 0.60 (s, 3H, Si**Me**), and 0.57 (s, 3H, Si**Me**) ppm.

6.4.2.5. rac-^{Me,nPr}SB(^{tBu2}ArO,I)TiCl$_2$ (12)*

288 mg (6%) yield. Crystals suitable for X-ray diffraction were grown from slow evaporation of a diethyl ether solution at –30 °C.

^{1}H NMR (600 MHz, benzene-d_6, 298 K): δ 7.57 (d, $^4J_{H–H}$ = 2.4 Hz, 1H, *m*Ar**H**), 7.54 (d, $^4J_{H–H}$ = 2.4 Hz, 1H, *m*Ar**H**), 2.63 (s, 3H, I***Me**), 2.58 (s, 3H, I***Me**), 2.23 (s, 3H, I***Me**), 2.09 (s, 3H, I***Me**), 2.01 (s, 3H, I***Me**), 1.88 (s, 3H, I***Me**), 1.47 (s, 9H, C**Me**$_3$), 1.38 (s, 9H, C**Me**$_3$), 0.74 (t, $^3J_{H–H}$ = 7.0 Hz, 3H, SiCH$_2$CH$_2$C**H**$_3$), and 0.73 (s, 3H, Si**Me**) ppm.

Additional ^{1}H resonances were observed in ^{1}H–^{13}C HSQC at δ 1.43 and 1.37 ppm corresponding to SiC**H**$_2$CH$_2$CH$_3$ and SiCH$_2$C**H**$_2$CH$_3$.

^{13}C{^{1}H} NMR (151 MHz, benzene-d_6, 298 K): δ 168.15 (1-**Ar**O), 147.06 (2,4-**Ar**O), 145.65 (**I***), 137.98 (**I***), 136.79 (**I***), 136.39 (2,4-**Ar**O), 136.32 (**I***), 133.21 (Si**Ar**O),

132.93 (**I***), 132.09 (**I***), 131.43 (**I***), 130.59 (**I***), 128.35 (3,5-**Ar**O), 125.05 (3,5-**Ar**O), 109.41 (Si**I***), 35.43 (**C**Me$_3$), 34.94 (**C**Me$_3$), 31.82 (C**Me**$_3$), 30.07 (C**Me**$_3$), 21.84 (I***Me**), 20.66 (I***Me**), 18.66 (I***Me**), 18.45 (I***Me**), 17.74 (I***Me**), 17.27 (I***Me**), 16.93 (Si**C**H$_2$CH$_2$Me), 16.62 (SiCH$_2$**C**H$_2$Me), 16.56 (SiCH$_2$CH$_2$**Me**), and 1.67 (Si**Me**) ppm.

^{29}Si NMR (^{1}H-observed HMBC, 80 MHz, benzene-d_6, 298 K): δ –11.2 ppm.

CHN analysis (%): Expected C 65.23, H 7.96; observed C 65.26, H 7.89.

6.4.2.6. rac-^{Me,Ph}SB(^{tBu2}ArO,I)TiCl$_2$ (13)*

81 mg (3%) yield. Crystals suitable for X-ray diffraction were grown from a saturated pentane solution at –30 °C.

^{1}H NMR (600 MHz, benzene-d_6, 298 K): δ 7.82–7.78 (m, 2H, SiC$_6$**H**$_5$), 7.59 (d, $^4J_{H–H}$ = 2.4 Hz, 1H, *m*Ar**H**), 7.48 (d, $^4J_{H–H}$ = 2.4 Hz, 1H, *m*Ar**H**), 7.32–7.23 (m, 3H, SiC$_6$**H**$_5$), 2.68 (s, 3H, I***Me**), 2.57 (s, 3H, I***Me**), 2.17 (s, 3H, I***Me**), 2.03 (s, 3H, I***Me**), 1.98 (s, 3H, I***Me**), 1.94 (s, 3H, I***Me**), 1.60 (s, 9H, C**Me**$_3$), 1.24 (s, 9H, C**Me**$_3$), and 1.04 (s, 3H, Si**Me**) ppm.

^{13}C{^{1}H} NMR (126 MHz, benzene-d_6, 298 K): δ 168.06 (1-**Ar**O), 147.32 (2,4-**Ar**O), 144.38 (**I***), 138.94 (**I***), 138.03 (**I***), 136.95 (**I***), 136.58 (2,4-**Ar**O), 136.01 (Si**Ar**O), 135.87 (Si**Ar**), 132.56 (**I***), 132.13 (**I***), 131.90 (**I***), 131.58 (**I***), 131.36 (**I***), 130.42 (Si**Ar**), 128.82 (3,5-**Ar**O), 128.72 (Si**Ar**), 128.35 (Si**Ar**), 125.63 (3,5-**Ar**O), 110.05, 35.57 (**C**Me$_3$), 34.95 (**C**Me$_3$), 31.66 (C**Me**$_3$), 30.26 (C**Me**$_3$), 21.66 (I***Me**), 17.17 (I***Me**), 17.09 (I***Me**), 16.69 (I***Me**), 16.66 (I***Me**), 14.97 (I***Me**), and 4.08 (Si**Me**) ppm. Two additional aromatic resonances were expected but not observed.

^{29}Si NMR (^{1}H-observed HMBC, 80 MHz, benzene-d_6, 298 K): δ –16.0 ppm.

CHN analysis (%): Expected C 67.39, H 7.23; observed C 67.50, H 7.24.

6.4.2.7. ^{Me2}SB(^{tBu2}ArO,I)ZrCl$_2$ (15)*

The zirconium complex **15** was synthesised by Dr. Nichabhat Blake (University of Oxford). The proligand, ^{Me_2}SB(^{t}Bu$_2$ArOAllyl,I*)H (7.4 g, 15 mmol), and triethylamine (8.2 mL, 59 mmol) were dissolved in toluene and cooled to –78 °C. 2.25 equivalents of ^{n}BuLi (33 mmol, 1.6 M in hexanes) was added dropwise. The reaction was allowed to warm to room temperature and stirred for 18 hours, after which the solution was added dropwise to a toluene slurry of $ZrCl_4$ (5.2 g, 22 mmol) and stirred for a further 18 hours. The reaction mixture was filtered, the volatiles were removed from the filtrate under vacuum, and the resulting solid was washed with pentane at 23 °C to yield the desired product ^{Me_2}SB(^{t}Bu$_2$ArO,I*)$ZrCl_2$ as a dark brown powder (2.0 g). A further crop was isolated as a precipitate from the pentane washings stored at –30 °C, to give a total 2.98 g (32%) yield. Crystals suitable for single-crystal X-ray diffraction were grown from slow evaporation of a benzene solution at 23 °C.

^{1}H NMR (500 MHz, benzene-d_6, 298 K): δ 7.58 (d, $^4J_{H–H}$ = 2.4 Hz, 1H, *m*Ar**H**), 7.56 (d, $^4J_{H–H}$ = 2.5 Hz, 1H, *m*Ar**H**), 2.56 (s, 3H, I***Me**), 2.49 (s, 3H, I***Me**), 2.13 (s, 3H, I***Me**), 2.12 (s, 3H, I***Me**), 2.02 (s, 3H, I***Me**), 1.90 (s, 3H, I***Me**), 1.47 (s, 9H, C**Me**$_3$), 1.39 (s, 9H, C**Me**$_3$), 0.75 (s, 3H, Si**Me**$_2$), and 0.70 (s, 3H, Si**Me**$_2$) ppm.

^{13}C{^{1}H} NMR (126 MHz, benzene-d_6, 298 K): δ 162.80 (1-**Ar**O), 145.78 (2,4-**Ar**O), 142.93 (**I***), 136.81 (2,4-**Ar**O), 135.68 (**I***), 135.10 (**I***), 135.08 (**I***), 131.12 (Si**Ar**O), 130.42 (**I***), 130.20 (**I***), 129.73 (**I***), 127.41 (3,5-**Ar**O), 125.57 (3,5-**Ar**O), 123.72 (**I***), 99.06 (Si**I***), 35.28 (**C**Me$_3$), 34.83 (**C**Me$_3$), 31.89 (C**Me**$_3$), 30.15 (C**Me**$_3$), 21.62 (I***Me**),

17.39 (I*Me), 17.16 (I*Me), 16.53 (I*Me), 15.88 (I*Me), 15.10 (I*Me), 3.12 (SiMe$_2$), and 3.04 (SiMe$_2$) ppm.

6.4.2.8. ^{Me2}SB(^{tBu2}ArO,I)HfCl$_2$ (16)*

The hafnium complex **16** was prepared by combining **11f** and $HfCl_4$ in a Schlenk and slurrying in toluene at 60 °C for 96 hours. The product was extracted in toluene, dried and recrystallised from pentane at –80 °C. 15 mg (1%) yield. Crystals suitable for X-ray diffraction were grown from slow evaporation of a diethyl ether solution at –30 °C.

^{1}H NMR (600 MHz, benzene-d_6, 298 K): δ 7.59 (s, 2H, *m*ArH), 2.56 (s, 3H, I*Me), 2.52 (s, 3H, I*Me), 2.23 (s, 3H, I*Me), 2.13 (s, 3H, I*Me), 2.04 (s, 3H, I*Me), 1.92 (s, 3H, I*Me), 1.47 (s, 9H, CMe$_3$), 1.39 (s, 9H, CMe$_3$), 0.76 (s, 3H, SiMe$_2$), and 0.70 (s, 3H, SiMe$_2$) ppm.

^{13}C{^{1}H} NMR (151 MHz, benzene-d_6, 298 K): 162.24 (1-ArO), 145.49 (2,4-ArO), 141.82 (I*), 137.40 (2,4-ArO), 135.34 (I*), 134.68 (I*), 133.88 (I*), 131.29 (SiArO), 130.03 (I*), 129.52 (I*), 129.31 (I*), 127.35 (3,5-ArO), 125.63 (3,5-ArO), 120.72 (I*), 96.18 (SiI*), 35.21 (CMe$_3$), 34.78 (CMe$_3$), 31.93 (CMe$_3$), 30.14 (CMe$_3$), 21.66 (I*Me), 17.38 (I*Me), 17.07 (I*Me), 16.45 (I*Me), 15.78 (I*Me), 14.78 (I*Me), 3.41 (SiMe), and 3.19 (SiMe) ppm.

^{29}Si NMR (^{1}H-observed HMBC, 80 MHz, benzene-d_6, 298 K): δ –13.8 ppm.

6.4.3. Synthesis of ^{Me2}SB(^{tBu,Me}ArO,I*)TiX$_2$

To a solution of **1** in either benzene or benzene-d_6 was added 2–3 equivalents of MeLi (1.6 M in Et_2O), or $LiCH_2SiMe_3$

6.4.3.1. ^{Me2}SB(^{tBu,Me}ArO,I)TiMe$_2$ (17)*

13 mg (14%) yield.

^{1}H NMR (500 MHz, benzene-d_6, 298 K): δ 7.26 (d, $^4J_{H–H}$ = 2.2 Hz, 1H, *m*Ar**H**), 7.23 (d, $^4J_{H–H}$ = 2.2 Hz, 1H, *m*Ar**H**), 2.61 (s, 3H I***Me**), 2.48 (s, 3H I***Me**), 2.31 (s, 3H I***Me**), 2.13 (s, 3H I***Me**), 2.09 (s, 3H I***Me**), 1.97 (s, 3H I***Me**), 1.76 (s, 3H 4-**Me**-ArO), 1.67 (s, 9H C**Me**$_3$), 0.87 (s, 3H Ti**Me**), 0.61 (s, 3H Si**Me**), 0.57 (s, 3H Si**Me**), and 0.15 (s, 3H Ti**Me**) ppm.

^{13}C{^{1}H} NMR (126 MHz, benzene-d_6, 298 K): δ 165.07 (**Ar**O), 138.26 (**I***), 136.00 (**Ar**O), 134.41 (**Ar**O), 133.82 (**Ar**O), 133.16 (**I***), 133.03 (**I***), 131.41 (**Ar**O), 131.29 (**I***), 130.30 (**I***), 130.05 (**I***), 129.52 (**I***), 128.94 (**Ar**O), 120.56 (**I***), 98.96 (Si**I***), 56.85 (Ti**Me**), 55.14 (Ti**Me**), 35.15 (**C**Me$_3$), 30.14 (C**Me**$_3$), 21.77 (I***Me**), 21.40 (I***Me**), 17.41 (I***Me**), 16.97 (I***Me**), 16.44 (I***Me**), 15.40 (I***Me**), 14.52 (4-**Me**-ArO), 3.90 (Si**Me**), and 1.81 (Si**Me**) ppm.

6.4.3.2. ^{Me2}SB(^{tBu,Me}ArO,I)Ti(CH$_2$SiMe$_3$)$_2$ (18)*

100 mg scale, quantitative by ^{1}H NMR spectroscopy.

^{1}H NMR (400 MHz, benzene-d_6, 298 K): δ 7.25 (d, $^4J_{H–H}$ = 2.3 Hz, 1H, *m*Ar**H**), 7.22 (d, $^4J_{H–H}$ = 2.2 Hz, 1H, *m*Ar**H**), 2.67 (s, 3H, I***Me**), 2.66 (s, 3H, I***Me**), 2.24 (s, 3H, I***Me**), 2.15 (s, 3H, I***Me**), 2.08 (s, 3H, I***Me**), 2.06 (s, 3H, I***Me**), 1.92 (d, $^2J_{H–H}$ = 11 Hz, 1H, C**H**$_2$SiMe$_3$), 1.88 (s, 3H, 4-**Me**-ArO), 1.70 (s, 9H, C**Me**$_3$), 0.97 (d, $^2J_{H–H}$ = 12 Hz, 1H, C**H**$_2$SiMe$_3$), 0.94 (d, $^2J_{H–H}$ = 11 Hz, 1H, C**H**$_2$SiMe$_3$), 0.69 (s, 3H, Si**Me**), 0.64 (s, 3H, Si**Me**), 0.17 (s, 9H, CH$_2$Si**Me**$_3$), 0.13 (s, 9H, CH$_2$Si**Me**$_3$), –0.90 (d, $^2J_{H–H}$ = 12 Hz, 1H, C**H**$_2$SiMe$_3$) ppm.

6.4.4. Synthesis of ^{Me2}SB(^{tBu2}ArO,I*)TiX$_2$

To a solution of **2** in either benzene or benzene-d_6 was added 2–3 equivalents of one of Me_3SiBr, Me_3SiI, MeLi (1.6 M in Et_2O), $LiCH_2SiMe_3$, $PhCH_2MgCl$ (2.0 M in THF), $LiNMe_2$, NaOEt, or KODipp. The mixtures were either left at 23 °C or heated at 60–80 °C until conversion was judged to be complete by ^{1}H NMR spectroscopy.

6.4.4.1. ^{Me2}SB(^{tBu2}ArO,I)TiBr$_2$ (3)*

6 hours heating at 80 °C. 50 mg scale, quantitative by ^{1}H NMR spectroscopy. The volatiles were removed under vacuum to yield the desired complex. Crystals suitable for single-crystal X-ray diffraction were obtained from storage of the reaction mixture NMR tube at 4 °C.

^{1}H NMR (500 MHz, benzene-d_6, 298 K): δ 7.58 (d, $^4J_{H–H}$ = 2.4 Hz, 1H, *m*Ar**H**), 7.57 (d, $^4J_{H–H}$ = 2.1 Hz, 1H, *m*Ar**H**), 2.71 (s, 3H, I***Me**), 2.62 (s, 3H, I***Me**), 2.13 (s, 3H, I***Me**), 2.04 (s, 3H, I***Me**), 2.03 (s, 3H, I***Me**), 1.97 (s, 3H, I***Me**), 1.58 (s, 9H, C**Me**$_3$), 1.38 (s, 9H, C**Me**$_3$), 0.71 (s, 3H, Si**Me**), and 0.70 (s, 3H, Si**Me**) ppm.

^{13}C{^{1}H} NMR (126 MHz, benzene-d_6, 298 K): δ 168.03 (***i***ArO), 147.45 (***o,p***ArO), 144.77 (**I***), 137.87 (**I***), 137.11 (**I***), 136.77 (**I***), 136.47 (***o,p***ArO), 134.18 (Si**Ar**O), 133.24 (**I***), 132.54 (**I***), 131.95 (**I***), 131.66 (**I***), 127.53 (***m***ArO), 125.33 (***m***ArO), 112.04 (Si**I***), 35.64 (**C**Me$_3$), 35.01 (**C**Me$_3$), 31.78 (C**Me**$_3$), 30.34 (C**Me**$_3$), 21.72 (I***Me**), 17.69 (I***Me**), 17.55 (I***Me**), 17.26 (I***Me**), 16.74 (I***Me**), 16.11 (I***Me**), 4.58 (Si**Me**), and 1.73 (Si**Me**) ppm.

^{29}Si NMR (80 MHz, benzene-d_6, 298 K): δ –12.5 ppm.

6.4.4.2. ^{Me2}SB(^{tBu2}ArO,I)TiI$_2$ (4)*

1.75 hours heating at 80 °C. 50 mg scale, quantitative by ^{1}H NMR spectroscopy. The volatiles were removed under vacuum to yield the desired complex. Crystals suitable for single-crystal X-ray diffraction were grown from slow evaporation of a diethyl ether solution at –30 °C.

^{1}H NMR (500 MHz, benzene-d_6, 298 K): δ 7.60 (d, $^4J_{H–H}$ = 2.4 Hz, 1H, *m*Ar**H**), 7.55 (d, $^4J_{H–H}$ = 2.4 Hz, 1H, *m*Ar**H**), 2.80 (s, 3H, I***Me**), 2.76 (s, 3H, I***Me**), 2.10 (s, 3H, I***Me**), 2.04 (s, 3H, I***Me**), 2.03 (s, 3H, I***Me**), 1.94 (s, 3H, I***Me**), 1.70 (s, 9H, C**Me**$_3$), 1.37 (s, 9H, C**Me**$_3$), 0.69 (s, 3H, Si**Me**), and 0.66 (s, 3H, Si**Me**) ppm.

^{13}C{^{1}H} NMR (126 MHz, benzene-d_6, 298 K): δ 168.47 (***i***ArO), 147.57 (***o,p***ArO), 144.65 (**I***), 137.60 (**I***), 137.20 (**I***), 137.01 (**I***), 136.37 (***o,p***ArO), 135.04 (Si**Ar**O), 134.29 (**I***), 133.31 (**I***), 132.82 (**I***), 132.26 (**I***), 127.70 (***m***ArO), 125.45 (***m***ArO), 113.12 (Si**I***), 35.91 (**C**Me$_3$), 35.04 (**C**Me$_3$), 31.74 (C**Me**$_3$), 30.88 (C**Me**$_3$), 21.70 (I***Me**), 19.56 (I***Me**), 18.24 (I***Me**), 17.28 (I***Me**), 16.94 (I***Me**), 16.89 (I***Me**), 5.52 (Si**Me**), and 1.91 (Si**Me**) ppm.

^{29}Si NMR (80 MHz, benzene-d_6, 298 K): δ –12.5 ppm.

6.4.4.3. ^{Me2}SB(^{tBu2}ArO,I)TiMe$_2$ (5)*

Rapid reaction at room temperature. Solid by-products were removed by filtration, and volatiles were removed under vacuum. 171 mg (92%) isolated yield. Crystals suitable for single-crystal X-ray diffraction were grown from slow evaporation of a pentane solution at –30 °C.

^{1}H NMR (400 MHz, benzene-d_6, 298 K): δ 7.61 (d, $^{4}J_{H–H}$ = 2.4 Hz, 1H, *m*Ar**H**), 7.55 (d, $^{4}J_{H–H}$ = 2.5 Hz, 1H, *m*Ar**H**), 2.61 (s, 3H, I***Me**), 2.48 (s, 3H, I***Me**), 2.12 (s, 3H, I***Me**), 2.08 (s, 3H, I***Me**), 1.95 (s, 3H, I***Me**), 1.78 (s, 3H, I***Me**), 1.71 (s, 9H, C**Me**$_3$), 1.40 (s, 9H, C**Me**$_3$), 0.87 (s, 3H, Ti**Me**), 0.67 (s, 3H, Si**Me**), 0.61 (s, 3H, Si**Me**), and 0.16 (s, 3H, Ti**Me**) ppm.

^{13}C{^{1}H} NMR (126 MHz, benzene-d_6, 298 K): δ 165.01 (1-**Ar**O), 144.58 (2,4-**Ar**O), 138.24 (**I***), 135.46 (2,4-**Ar**O), 133.88 (**I***), 133.79 (**I***), 133.15 (**I***), 133.02 (Si**Ar**O), 130.26 (**I***), 130.05 (**I***), 129.51 (**I***), 127.44 (3,5-**Ar**O), 125.05 (3,5-**Ar**O), 120.75 (**I***), 98.96 (Si**I***), 56.92 (Ti**Me**), 55.21 (Ti**Me**), 35.51 (**C**Me$_3$), 34.79 (**C**Me$_3$), 31.98 (C**Me**$_3$), 30.20 (C**Me**$_3$), 21.70 (I***Me**), 17.43 (I***Me**), 16.97 (I***Me**), 16.44 (I***Me**), 15.43 (I***Me**), 14.64 (I***Me**), 4.04 (Si**Me**), and 2.16 (Si**Me**) ppm.

^{29}Si NMR (^{1}H-observed HMBC, 80 MHz, benzene-d_6, 298 K): δ –13.8 ppm.

IR (KBr): 746, 766, 778, 812, 829, 879, 923, 983, 1120, 1183, 1198, 1234, 1306, 1414, and 2954 cm^{-1}.

CHN analysis (%): Expected C 73.58, H 9.36; observed C 66.71, H 8.42.

6.4.4.4. ^{Me2}SB(^{tBu2}ArO,I)Ti(CH$_2$SiMe$_3$)$_2$ (6)*

50 mg scale, rapid reaction at room temperature, judged quantitative by ^{1}H NMR spectroscopy. Solid by-products were removed by filtration, and volatiles were removed under vacuum. Crystals suitable for single-crystal X-ray diffraction were grown from slow evaporation of a pentane solution at –30 °C.

^{1}H NMR (400 MHz, benzene-d_6, 297 K): δ 7.60 (d, $^{4}J_{H–H}$ = 2.5 Hz, 1H, *m*Ar**H**), 7.54 (d, $^{4}J_{H–H}$ = 2.5 Hz, 1H, *m*Ar**H**), 2.67 (s, 3H, I***Me**), 2.65 (s, 3H, I***Me**), 2.15 (s, 3H, I***Me**),

2.08 (s, 3H, I*Me), 2.04 (s, 3H, I*Me), 1.90 (s, 1H, CH$_2$SiMe$_3$), 1.87 (s, 3H, I*Me), 1.75 (s, 9H, CMe$_3$), 1.36 (s, 9H, CMe$_3$), 0.96 (dd, J = 11.3, 5.8 Hz, 2H, CH$_2$SiMe$_3$), 0.76 (s, 3H, SiMe), 0.69 (s, 3H, SiMe), 0.15 (s, 9H, CH$_2$SiMe$_3$), 0.12 (s, 9H, CH$_2$SiMe$_3$), and –0.88 (d, J = 11.9 Hz, 1H, CH$_2$SiMe$_3$) ppm.

^{13}C{^{1}H} NMR (101 MHz, benzene-d_6, 298 K): δ 166.04 (1-ArO), 144.22 (2,4-ArO), 136.84 (I*), 135.32 (2,4-ArO), 134.26 (I*), 133.36 (SiArO), 132.99 (I*), 132.12 (I*), 131.95 (I*), 130.47 (I*), 128.83 (I*), 128.16 (3,5-ArO), 125.38 (3,5-ArO), 122.39 (I*), 98.12 (SiI*), 84.11 (TiCH$_2$SiMe$_3$), 70.66 (TiCH$_2$SiMe$_3$), 35.83 (CMe$_3$), 34.68 (CMe$_3$), 31.86 (CMe$_3$), 31.30 (CMe$_3$), 21.39 (I*Me), 17.76 (I*Me), 16.92 (I*Me), 16.58 (I*Me), 16.50 (I*Me), 16.34 (I*Me), 4.87 (SiMe), 4.71 (SiMe), 3.72 (CH$_2$SiMe$_3$), and 2.71 (CH$_2$SiMe$_3$) ppm.

^{29}Si NMR (80 MHz, benzene-d_6, 298 K): δ 0.3 (CH$_2$SiMe$_3$), 0.0 (CH$_2$SiMe$_3$), –0.5 (CH$_2$SiMe$_3$), and –14.8 (SiMe$_2$) ppm.

CHN analysis (%): Expected C 68.58, H 9.76; observed C 67.26, H 9.53.

6.4.4.5. ^{Me2}SB(^{tBu2}ArO,I)Ti(NMe$_2$)$_2$ (8)*

50 mg scale, 42 hours heating at 80 °C, judged quantitative by ^{1}H NMR spectroscopy. Solid by-products were removed by filtration, and volatiles were removed under vacuum. Crystals suitable for single-crystal X-ray diffraction were grown from slow evaporation of a pentane solution at –30 °C.

^{1}H NMR (500 MHz, benzene-d_6, 298 K): δ 7.67 (d, $^4J_{H–H}$ = 2.5 Hz, 1H, *m*ArH), 7.61 (d, $^4J_{H–H}$ = 2.6 Hz, 1H, *m*ArH), 3.00 (s, 6H, NMe$_2$), 2.60 (s, 6H, NMe$_2$), 2.58 (s, 3H, I*Me), 2.47 (s, 3H, I*Me), 2.15 (s, 3H, I*Me), 2.08 (s, 3H, I*Me), 2.06 (s, 3H, I*Me), 1.91 (s,

3H, I*Me), 1.51 (s, 9H, CMe$_3$), 1.44 (s, 9H, CMe$_3$), 0.88 (s, 3H, SiMe), and 0.72 (s, 3H, SiMe) ppm.

^{13}C{^{1}H} NMR (126 MHz, benzene-d_6, 298 K): δ 166.75 (1-ArO), 142.86 (2,4-ArO), 139.30 (I*), 136.43 (2,4-ArO), 133.11 (SiArO), 132.22 (I*), 131.39 (I*), 130.27 (I*), 129.92 (I*), 129.56 (I*), 128.35 (I*), 127.61 (3,5-ArO), 124.68 (3,5-ArO), 116.42 (I*), 94.88 (SiI*), 47.98 (NMe$_2$), 47.67 (NMe$_2$), 35.41 (CMe$_3$), 34.71 (CMe$_3$), 32.12 (CMe$_3$), 30.48 (CMe$_3$), 21.35 (I*Me), 17.69 (I*Me), 16.96 (I*Me), 16.56 (I*Me), 15.85 (I*Me), 15.23 (I*Me), 5.64 (SiMe), and 2.99 (SiMe) ppm.

^{29}Si NMR (^{1}H-observed HMBC, 80 MHz, benzene-d_6, 298 K): δ –14.6 ppm.

6.4.4.6. ^{Me2}SB(^{tBu2}ArO,I)Ti(OEt)$_2$ (9)*

50 mg scale, 137 hours heating at 80 °C, judged quantitative by ^{1}H NMR spectroscopy. Solid by-products were removed by filtration, and volatiles were removed under vacuum.

^{1}H NMR (500 MHz, benzene-d_6, 298 K): δ 7.62 (d, $^4J_{H–H}$ = 2.5 Hz, 1H, *m*ArH), 7.54 (d, $^4J_{H–H}$ = 2.5 Hz, 1H, *m*ArH), 4.42 (qd, $^3J_{H–H}$ = 6.9 Hz, $^4J_{H–H}$ = 0.9 Hz, 2H, OCH$_2$CH$_3$), 3.98–30.80 (m, 2H, OCH$_2$CH$_3$), 2.58 (s, 3H, I*Me), 2.51 (s, 3H, I*Me), 2.31 (s, 3H, I*Me), 2.05 (s, 3H, I*Me), 1.98 (s, 3H, I*Me), 1.89 (s, 3H, I*Me), 1.45 (s, 9H, CMe$_3$), 1.42 (s, 9H, CMe$_3$), 1.18 (t, $^3J_{H–H}$ = 6.9 Hz, 3H, OCH$_2$CH$_3$), 1.01 (t, $^3J_{H–H}$ = 6.9 Hz, 3H, OCH$_2$CH$_3$), 0.88 (s, 3H, SiMe), and 0.83 (s, 3H, SiMe) ppm.

^{13}C{^{1}H} NMR (126 MHz, benzene-d_6, 298 K): δ 167.16 (1-ArO), 143.05 (2,4-ArO), 142.14 (I*), 135.75 (2,4-ArO), 133.55 (SiArO), 132.57 (I*), 132.37 (I*), 129.75 (I*), 129.15 (I*), 128.66 (I*), 127.56 (I*), 127.14 (3,5-ArO), 124.49 (3,5-ArO), 119.98 (I*), 100.20 (SiI*), 71.50 (OCH$_2$Me), 68.70 (OCH$_2$Me), 35.25 (CMe$_3$), 34.72 (CMe$_3$), 32.13

(C**Me**$_3$), 29.83 (C**Me**$_3$), 21.89 (OCH$_2$**Me**), 19.75 (OCH$_2$**Me**), 19.73 (I***Me**), 17.66 (I***Me**), 17.01 (I***Me**), 16.31 (I***Me**), 16.20 (I***Me**), 15.05 (I***Me**), 4.06 (Si**Me**), and 1.75 (Si**Me**) ppm.

^{29}Si NMR (^{1}H-observed HMBC, 80 MHz, benzene-d_6, 298 K): δ –13.7 ppm.

6.4.4.7. ^{Me2}SB(^{tBu2}ArO,I)Ti(ODipp)$_2$ (10)*

50 mg scale, 24 hours heating at 60 °C, judged quantitative by ^{1}H NMR spectroscopy. Solid by-products were removed by filtration, and volatiles were removed under vacuum. Crystals suitable for single-crystal X-ray diffraction were grown from slow evaporation of a benzene solution at 23 °C.

^{1}H NMR (500 MHz, benzene-d_6, 298 K): δ 7.56 (d, $^4J_{H–H}$ = 2.6 Hz, 1H, *m*Ar**H**), 7.53 (d, $^4J_{H–H}$ = 2.5 Hz, 1H, *m*Ar**H**), 7.09–6.87 (m, 6H, O(^{i}Pr$_2$)C$_6$**H**$_3$), 3.52 (hept, $^3J_{H–H}$ = 6.9 Hz, 2H, C**H**(CH$_3$)$_2$), 3.14 (hept, $^3J_{H–H}$ = 6.9 Hz, 2H, C**H**(CH$_3$)$_2$), 2.37 (s, 3H, I***Me**), 2.31 (s, 3H, I***Me**), 2.24 (s, 3H, I***Me**), 2.06 (s, 3H, I***Me**), 2.04 (s, 3H, I***Me**), 1.92 (s, 3H, I***Me**), 1.56 (s, 9H, C**Me**$_3$), 1.38 (s, 9H, C**Me**$_3$), 1.20 (d, $^3J_{H–H}$ = 6.7 Hz, 6H, CH(C**H**$_3$)$_2$), 1.16 (d, $^3J_{H–H}$ = 6.7 Hz, 6H, CH(C**H**$_3$)$_2$), 0.98 (d, $^3J_{H–H}$ = 6.7 Hz, 6H, CH(C**H**$_3$)$_2$), 0.89 (d, $^3J_{H–H}$ = 6.7 Hz, 6H, CH(C**H**$_3$)$_2$), 0.70 (s, 3H, Si**Me**), and 0.70 (s, 3H, Si**Me**) ppm.

^{13}C{^{1}H} NMR (126 MHz, benzene-d_6, 298 K): δ 168.70 (1-**Ar**O), 162.23, 161.76, 144.82, 143.82 (2,4-**Ar**O), 138.99, 138.94, 138.45, 135.28 (2,4-**Ar**O), 134.49, 133.62, 133.23, 132.37, 129.73, 128.99, 128.62 (3,5-**Ar**O), 128.56, 128.35, 127.97, 127.53, 125.17, 125.01 (3,5-**Ar**O), 123.63 (**Ar**^{Dipp}), 123.09 (**Ar**^{Dipp}), 122.52 (**Ar**^{Dipp}), 122.28 (**Ar**^{Dipp}), 106.10 (Si**I***), 35.76 (**C**Me$_3$), 34.61 (**C**Me$_3$), 31.85 (C**Me**$_3$), 30.90 (C**Me**$_3$), 26.78 (Ar**C**HMe$_2$), 26.73(Ar**C**HMe$_2$), 25.39 (ArCH**Me**$_2$), 24.90 (ArCH**Me**$_2$), 24.40

(ArCH**Me**$_2$), 21.59 (I***Me**), 17.70 (I***Me**), 17.20 (I***Me**), 17.10 (I***Me**), 16.59 (I***Me**), 15.20 (I***Me**), 4.15 (Si**Me**), and 3.54 (Si**Me**) ppm.

^{29}Si NMR (^{1}H-observed HMBC, 80 MHz, benzene-d_6, 298 K): δ –13.1 ppm.

CHN analysis (%): Expected C 76.53, H 9.11; observed C 72.99, H 8.76.

6.4.4.8. ^{Me2}SB(^{tBu2}ArO,I)Ti(CH$_2$Ph)$_2$ (7)*

To a solution of **2** (200 mg, 0.34 mmol) in benzene in a Schlenk flask was added three equivalents of PhCH$_2$MgCl (2 M in THF, 0.52 mL), resulting in a dark red solution. The mixture was stirred at 23 °C for 20 hours during which the solution changed to a dark orange. The volatiles were removed under vacuum, and the product was extracted in toluene (with ~5 mL dioxane to aid precipitation of MgCl$_2$) to yield the desired product as a bright orange solid (180 mg, 76%).

^{1}H NMR (600 MHz, benzene-d_6, 298 K): δ 7.62 (d, $^4J_{H–H}$ = 2.5 Hz, 1H, *m*Ar**H**), 7.55 (d, $^4J_{H–H}$ = 2.5 Hz, 1H, *m*Ar**H**), 7.07–7.01 (m, 4H, CH$_2$C$_6$**H**$_5$), 6.93 (ddd, J = 10.9, 8.2, 1.4 Hz, 4H, CH$_2$C$_6$**H**$_5$), 6.86 (qt, J = 7.4, 1.3 Hz, 2H, CH$_2$C$_6$**H**$_5$), 2.74 (d, $^2J_{H–H}$ = 10.7 Hz, 1H, C**H**$_2$C$_6$H$_5$), 2.66 (d, $^2J_{H–H}$ = 10.7 Hz, 1H, C**H**$_2$C$_6$H$_5$), 2.39 (s, 3H, I***Me**), 2.14 (s, 3H, I***Me**), 2.12 (d, $^2J_{H–H}$ = 11.1 Hz, 1H, C**H**$_2$Ph), 2.10 (s, 3H, I***Me**), 2.04 (s, 3H, I***Me**), 1.96 (s, 3H, I***Me**), 1.74 (s, 3H, I***Me**), 1.55 (s, 9H, C**Me**$_3$), 1.37 (s, 9H, C**Me**$_3$), 1.31 (d, $^2J_{H–H}$ = 10.8 Hz, 1H, C**H**$_2$Ph), 0.65 (s, 3H, Si**Me**), and 0.64 (s, 3H, Si**Me**) ppm.

^{13}C{^{1}H} NMR (151 MHz, benzene-d_6, 298 K): δ 165.50 (1-**Ar**O), 149.58, 149.01, 144.93 (2,4-**Ar**O), 138.56, 135.85, 134.47, 133.57, 133.44, 133.21, 131.56, 130.15, 129.67, 128.81, 128.61, 128.38, 128.35, 127.82 (3,5-**Ar**O), 127.56 (2,4-**Ar**O), 126.22, 125.30 (3,5-**Ar**O), 123.01, 122.82 (CH$_2$**Ph**), 122.38 (CH$_2$**Ph**), 101.12 (Si**I***), 86.23 (Ti**C**H$_2$Ph),

86.03 (Ti**C**H_2Ph), 35.51 (**C**Me_3), 34.76 (**C**Me_3), 31.89 (C**Me**$_3$), 30.76 (C**Me**$_3$), 21.70 (I***Me**), 17.35 (I***Me**), 17.10 (I***Me**), 16.62 (I***Me**), 15.02 (I***Me**), 14.76 (I***Me**), 4.68 (Si**Me**), and 3.17 (Si**Me**) ppm. Two additional aromatic resonances were expected but not observed.

^{29}Si NMR (^{1}H-observed HMBC, 99 MHz, benzene-d_6, 298 K): δ –13.8 ppm.

CHN analysis (%): Expected C 78.23, H 8.46; observed C 69.46, H 8.04.

6.4.5. Synthesis of cationic intermediates

A J. Young's tap NMR tube was charged with approximately 10 mg of either **2** or **5** and dissolved in approximately 0.6 mL of perdeuterated solvent. Equivalents of one of TB, AB, or MAO were added and the reactions were monitored by ^{1}H NMR spectroscopy.

6.4.6. Synthesis of solid catalysts

The quantity of catalyst immobilised on the surface of the support is given in terms of the Al:Ti ratio of the methylaluminoxane (MAO) component to the organometallic complex. In the case of SSMAO and LDHMAO, 40wt% MAO was used to activate the surface of each support. SSMAO and LDHMAO are prepared by weighing out silica or LDH and MAO into a Schlenk in a glovebox and then adding toluene (40 mL) to the mixture, heating at 80 °C for 2 h with regular swirling and then drying under vacuum (1×10^{-2} mbar) at room temperature for at least 4 h to ensure all the solvent was removed. The finished solid catalysts were synthesised according to the following method: in a glove box the inorganic support (SSMAO, LDHMAO or sMAO) and the desired complex were weighed into a Schlenk in a [Al_{MAO}]:[$Ti_{complex}$] ratio of 200:1. Then toluene (40 mL) was added and the slurry was heated at 60 °C with regular swirling for 1 h or until the supernatant solution had discoloured. The coloured solid was allowed to settle, then the

supernatant was decanted (or filtered), and the product dried under vacuum (1×10^{-2} mbar) at room temperature for at least 4 h to ensure all the solvent was removed.

sMAO-^{Me2}SB(^{tBu,Me}ArO,I*)TiCl$_2$ ($\mathbf{1}_{sMAO}$): 234 mg (90%) isolated yield.

sMAO-^{Me2}SB(^{tBu2}ArO,I*)TiCl$_2$ ($\mathbf{2}_{sMAO}$): 1.11 g (96%) isolated yield.

^{1}H zgbs NMR (850.2 MHz, 60 kHz): δ 7.0, 3.4, 1.9, 1.3, –0.9 ppm.

^{13}C CPMAS NMR (100.6 MHz, 10 kHz)**:** δ –8 (AlO**Me**), 18 (Ar**Me**) 30 (C**Me**$_3$), 50 (Ti**Me**), 128 (**Ar**) ppm.

^{13}C CPMAS NMR (213.8 MHz, 60 kHz)**:** δ –2, 22, 26, 30, 36, 40, 56, 58, 134, 183, 189 ppm.

^{27}Al Hahn echo NMR (104.2 MHz, 20 kHz)**:** δ 426, 244, 64, –95, –349, –484 ppm.

^{27}Al DFS NMR (221.6 MHz, 60 kHz)**:** δ 95, 91, 38 ppm.

^{29}Si CPMAS NMR (79.4 MHz, 10 kHz)**:** δ –13 (**Si**Me$_2$) ppm.

^{29}Si CPMAS NMR (168.9 MHz, 12 kHz)**:** δ –13 (**Si**Me$_2$) ppm.

IR (KBr): 1026, 1086, 1219, 1259 1384, 1442, 1500, 1534, 1599, and 2947 (b) cm^{-1}.

SSMAO-^{Me2}SB(^{tBu2}ArO,I*)TiCl$_2$ ($\mathbf{2}_{SSMAO}$): 220 mg (77%) isolated yield.

^{1}H zgbs NMR (399.9 MHz, 20 kHz): δ 6.8, 3.4, 2.0, 1.5, 0.9, 0.5, –0.2, –0.4, –1.1 ppm.

^{13}C CPMAS NMR (100.6 MHz, 10 kHz): δ –10 (AlO**Me**), 31 (C**Me**), 50 (Ti**Me**), 128 (**Ar**) ppm.

^{27}Al Hahn echo NMR (104.2 MHz, 20 kHz): δ 392, 259, 200, 33, –60, –132, –318 ppm.

^{29}Si CPMAS NMR (79.4 MHz, 10 kHz): δ –13 (**Si**Me_2), –107 (**Si**O_2) ppm.

LDHMAO-^{Me2}SB(^{tBu2}ArO,I*)TiCl$_2$ (2_{LDHMAO}): 170 mg (61%) isolated yield.

^{1}H zgbs NMR (399.9 MHz, 20 kHz): δ 7.0, 6.8, 3.3, 2.0, 1.0, 0.5, –0.3, –0.4, –0.7 ppm.

^{13}C CPMAS NMR (100.6 MHz, 10 kHz): δ –9, 12, 22, 26, 32, 35, 50, 62, 128, 164 ppm.

^{27}Al Hahn echo NMR (104.2 MHz, 20 kHz): δ 596, 354, 231, 216, 86, 56, 28, –34, –154, –412, –571, –763 (**Al** in MAO) ppm.

^{27}Al DPMAS NMR (104.2 MHz, 20 kHz): δ 67, 7 (Mg_3**Al** LDH) ppm.

^{29}Si CPMAS NMR (79.4 MHz, 10 kHz): δ –14 (**Si**Me_2), –25, –102 ppm.

sMAO-^{Me2}SB(^{tBu2}ArO,I*)TiBr$_2$ (3_{sMAO}): 157 mg (60%) isolated yield.

sMAO-^{Me2}SB(^{tBu2}ArO,I*)TiI$_2$ (4_{sMAO}): 175 mg (66%) isolated yield.

sMAO-^{Me2}SB(^{tBu2}ArO,I*)TiMe$_2$ (5_{sMAO}): 280 mg (93%) isolated yield.

^{1}H zgbs NMR (850.2 MHz, 60 kHz): δ 7.7, 6.7, 3.2, 1.9, 1.0, –0.9 ppm.

^{13}C CPMAS NMR (213.8 MHz, 60 kHz)**:** δ –2, 21, 26, 36, 55, 78, 134, 188 ppm.

^{27}Al DFS NMR (221.6 MHz, 60 kHz)**:** δ 93 ppm.

sMAO-^{Me2}SB(^{tBu2}ArO,I*)Ti(CH_2SiMe_3)$_2$ (6_{sMAO}): 420 mg (80%) isolated yield.

sMAO-^{Me2}SB(^{tBu2}ArO,I*)Ti(CH_2Ph)$_2$ (7_{sMAO}): 247 mg (94%) isolated yield.

sMAO-^{Me2}SB(^{tBu2}ArO,I*)Ti(NMe$_2$)$_2$ (8$_{sMAO}$): 187 mg (72%) isolated yield.

sMAO-^{Me2}SB(^{tBu2}ArO,I*)Ti)(OEt)$_2$ (9$_{sMAO}$): 191 mg (73%) isolated yield.

sMAO-^{Me2}SB(^{tBu2}ArO,I*)Ti(O$^{2,6\text{-}iPr2}$Ar)$_2$ (10$_{sMAO}$): 180 mg (68%) isolated yield.

sMAO-^{Me2}SB(^{Cumyl2}ArO,I*)TiCl$_2$ (11$_{sMAO}$): 239 mg (91%) isolated yield.

^{1}H zgbs NMR (399.9 MHz, 20 kHz)**:** δ 7.6, 6.5, 1.7, 0.7, 0.3, –1.0 ppm.

^{13}C CPMAS NMR (100.6 MHz, 10 kHz)**:** δ –8, 16, 20, 29, 32, 42, 127, 131, 135, 149, 176 ppm.

^{27}Al Hahn echo NMR (104.2 MHz, 20 kHz)**:** δ 565, 436, 252, 64, –119, –352, –486, –678 ppm.

^{29}Si CPMAS NMR (79.4 MHz, 10 kHz)**:** δ –13 (**Si**Me$_2$) ppm.

sMAO-*rac*-^{Me,nPr}SB(^{tBu2}ArO,I*)TiCl$_2$ (12$_{sMAO}$): 289 mg (79%) isolated yield.

sMAO-*rac*-^{Me,Ph}SB(^{tBu2}ArO,I*)TiCl$_2$ (13$_{sMAO}$): 288 mg (79%) isolated yield.

sMAO-^{Me2}SB(^{tBu,Me}ArO,Ind)TiCl$_2$ (14$_{sMAO}$): 199 mg (77%) isolated yield.

sMAO-^{Me2}SB(^{tBu2}ArO,I*)ZrCl$_2$ (15$_{sMAO}$): 224 mg (86%) isolated yield.

sMAO-^{Me2}SB(^{tBu2}ArO,I*)HfCl$_2$ (16$_{sMAO}$): 166 mg (81%) isolated yield.

6.5. Experimental details for Chapter Three

6.5.1. Solution-phase ethylene polymerisation studies

A typical solution-phase polymerisation procedure is as follows. A stock solution of a complex in toluene was prepared at a concentration of 713 μM. 1000 equivalents MAO were added to a 150 mL Rotaflo® ampoule and washed in with 49 mL hexanes, and 1 mL stock solution (713 nmol) was added to the ampoule along with a further 40 mL hexanes. The ampoule was sealed, cycled onto a Schlenk line, and degassed under reduced pressure. It was cycled a further two times using ethylene as a purge gas while the vessel was brought to temperature in a thermostatic oil bath with the stirring set at 1000 rpm. The stopcock was opened to ethylene at a pressure of 2 bar and the timer was started. On completion of the run (after 5 minutes, or when stirring became impeded by reactor fouling), the vessel was degassed under partial vacuum, then filtered on a sintered glass frit (porosity 3) and washed with 2 x 25 mL pentane. The polyethylene was dried under vacuum until constant weight. All runs were carried out at least in duplicate to ensure reproducibility.

6.5.2. Slurry-phase ethylene polymerisation studies

A typical slurry-phase laboratory polymerisation run was performed as follows. 150 mg triisobutylaluminium (TIBA) was added into a vial and 10 mL of hexanes was added. This mixture was introduced into a 150 mL Rotaflo® ampoule containing a stirrer bar and swirled around the glassware. 10 mg supported catalyst was added to the ampoule and washed in with a further 40 mL hexanes. The run was then continued as for the homogeneous polymerisations.

6.5.3. High-throughput screening (Xplore, University of Naples Federico II)

Polymerisation experiments were conducted in a FreeSlate Parallel Pressure Reactor (PPR) platform consisting of 48 reaction cells contained within a MBraun LabMaster Glovebox. The cells (geometric volume ~23 mL, working volume 5 mL) were individually controlled with temperature and pressure monitoring. Slurry-phase polymerisations were run in semi continuous mode. Two Vortex stir plates fitted with 6 x 8 racks held the catalyst system components (pre-catalyst and scavenger). The injection system consisted of a dual arm robot with specialised needles and injectors. Liquid solvents, diluents, and monomers were fed through syringe pumps, with gaseous monomers and diluents fed through direct lines with solenoid valves to individual cells.[21]

Heptane solvent (5 mL) and TIBA scavenger (10 μmol) were added to the PPRs *via* robotic syringes which were then heated to the required temperature and pressurised to 120 psi (8.3 bar) with ethylene. Pre-catalyst (0.05–0.80 mg in heptane slurry) and 1-hexene (where required) were injected with robotic syringes. The reactions were run for 1 hour or until a certain ethylene uptake was reached, after which the reactions were quenched with an excess of dry air. The polymer samples were transferred to a Genevac EZ-Plus centrifugal evaporator to remove the volatiles and then dried under vacuum overnight.

The polymers were characterised by high-temperature $^{13}C\{^{1}H\}$ NMR spectroscopy, gel permeation chromatography, and crystallisation elution fractionation (CEF). $^{13}C\{^{1}H\}$ NMR spectra were run at 393 K in 1,1,2,2-tetrachloroethane-d_2 on a 400 MHz Bruker Avance III spectrometer equipped with a 5 mm high-temperature cryoprobe. GPC curves were recorded with a FreeSlate GPC setup, equipped with a set of two mixed-bed Agilent PLgel 10 μm columns and a Polymer Char IR4 detector. CEF curves were collected with

a Polymer Char CEF setup, equipped with a 42-well auto sampler, and IR5 detector and a dual-capillary viscometer detector. The formation of UHMWPE and the resulting highly viscous solutions made some of the characterisation techniques impractical.

6.5.4. Large-scale polymerisation (SCG Chemicals PLC; Rayong, Thailand)

A 2.5 L steel reactor was charged with hexane (850 mL), either TEA scavenger (1.0 mmol L^{-1}) or TIBA (0.5 mmol L^{-1}) and MAO (13 g), and saturated with ethylene gas (2 bar). The reactor was heated to temperature and a mixture of pre-catalyst (0.05–0.10 g) in hexane (20 mL) was added and washed in with a further 130 mL hexane. The ethylene pressure was set to 1–8 bar and the polymerisations were run for 2 hours. On completion the polymer was decanted and dried in an oven overnight.

6.6. Experimental details for Chapter Four

6.6.1. Propylene polymerisation studies using supported catalysts

A typical laboratory polymerisation run was performed as follows. 1000 equivalents methylaluminoxane (MAO) was introduced into a 150 mL Rotaflo® ampoule containing a stirrer bar. 10 mg supported catalyst was added to the ampoule and washed in with 50 mL hexanes. The vessel was sealed and was pumped onto a vacuum line and degassed under reduced pressure. It was cycled once more using a propylene purge while the reaction was brought to temperature in an oil bath or water/ice bath with the stirring set at 1000 rpm. The stopcock was opened to propylene at a pressure of 2 bar and the timer was started. On completion of the run, the vessel was closed to propylene and degassed. The mixture was rinsed out with fresh hexane and decanted into a 500 mL round-bottomed flask containing dilute aqueous hydrochloric acid. The organic solvents were removed by rotary evaporation. The polymer was manually separated from the

aqueous phase and dried in a vacuum oven until constant weight. All polymerisation runs were carried out at least in duplicate to ensure reproducibility.

6.6.2. Solution-phase propylene polymerisation studies

A typical solution-phase polymerisation run was performed as follows. 1000 equivalents methylaluminoxane (MAO) was introduced to a 150 mL Rotaflo ampoule containing a stirrer bar, and washed in with 49 mL hexanes. To this was added 1 mL of a pre-prepared stock solution of complex in toluene (0.714 μmol mL^{-1}). The polymerisation was then continued as for the polymerisations using supported catalysts described above.

6.6.3. Large-scale polymerisation (SCG Chemicals PLC; Rayong, Thailand)

A 2.5 L steel reactor was charged with hexane (850 mL), TIBA scavenger (0.5 mmol L^{-1}), and MAO (2.7 g), and saturated with propylene gas (2 bar). The reactor was heated to temperature and a mixture of pre-catalyst (0.01 g) in hexane (20 mL) was added and washed in with a further 130 mL hexane. The propylene pressure was set to 8 bar and the polymerisations were run for 1 hour. On completion the polymer was decanted and dried in an oven overnight.

6.7. Experimental details for Chapter Five

6.7.1. Copolymerisation of ethylene and propylene

1000 equivalents methylaluminoxane (MAO) was introduced into a 150 mL Rotaflo® ampoule containing a stirrer bar. 10 mg supported catalyst was added to the ampoule and washed in with 50 mL hexanes. The vessel was sealed and was pumped onto a vacuum line and degassed under reduced pressure. It was cycled once more using an ethylene/propylene purge while the reaction was brought to temperature in an oil bath with the stirring set at 1000 rpm. The stopcock was opened to a mixed ethylene/propylene

at a given monomer ration (25:75, 50:50, or 75:25) and a total pressure of 2 bar, and the timer was started. On completion of the run, the vessel was closed to monomer and degassed. The mixture was rinsed out with fresh hexane and decanted into a 500 mL round-bottomed flask containing dilute aqueous hydrochloric acid. The organic solvents were removed by rotary evaporation. The polymer was manually separated from the aqueous phase and dried in a vacuum oven until constant weight. All polymerisation runs were carried out at least in duplicate to ensure reproducibility.

^{1}H NMR (600 MHz, 1,1,2,2-tetrachloroethane-d_2, 403 K): δ 1.51, 1.42, 1.31, 1.14, 0.89, and 0.88 ppm.

^{13}C{^{1}H} NMR (151 MHz, 1,1,2,2-tetrachloroethane-d_2, 403 K): δ 45.85, 45.63, 38.40, 37.94, 37.56, 33.26, 30.94, 30.74, 30.35, 29.96, 27.42, 24.86, 20.78, and 20.08 ppm.

6.7.2. Terpolymerisation of ethylene, propylene, and ethylidenenorbornene

1000 equivalents methylaluminoxane (MAO) was introduced into a 150 mL Rotaflo® ampoule containing a stirrer bar. 10 mg supported catalyst was added to the ampoule and washed in with 45 mL hexanes. In a sidearm, the desired amount of 5-ethylidene-2-norbornene (ENB) was added and washed in with 5 mL hexanes. The vessel was sealed and was pumped onto a vacuum line and degassed under reduced pressure. It was cycled once more using an ethylene/propylene purge while the reaction was brought to temperature in an oil bath with the stirring set at 1000 rpm. The stopcock was opened to a mixed ethylene/propylene (50:50) at a total pressure of 2 bar, and the timer was started. On completion of the run, the vessel was closed to monomer and degassed. The mixture was rinsed out with fresh hexane and decanted into a 500 mL round-bottomed flask containing dilute aqueous hydrochloric acid. The organic solvents

were removed by rotary evaporation. The polymer was manually separated from the aqueous phase and dried in a vacuum oven until constant weight. All polymerisation runs were carried out at least in duplicate to ensure reproducibility.

^{1}H NMR (400 MHz, chloroform-*d*, 298 K): δ 7.26, 5.24, 5.01, 2.73, 2.69, 2.39, 2.35, 2.14, 2.10, 2.06, 1.83, 1.79, 1.75, 1.61, 1.56, 1.51, 1.49, 1.47, 1.41, 1.35, 1.26, 1.09, 0.85, and 0.83 ppm.

^{13}C{^{1}H} NMR (151 MHz, chloroform-*d*, 298 K): δ 147.42, 146.56, 111.23, 110.64, 49.90, 46.41, 45.91, 45.73, 45.42, 45.17, 45.11, 41.23, 39.45, 38.50, 38.37, 38.20, 38.03, 37.63, 37.59, 37.37, 37.30, 37.08, 36.30, 33.62, 33.31, 32.95, 30.57, 30.24, 29.94, 29.90, 27.63, 27.55, 27.50, 27.29, 27.12, 24.66, 24.47, 20.49, 19.93, 19.90, 19.87, 19.77, 19.72, 19.69, 14.53, and 14.01 ppm.

IR: 2955, 2922, 2852, 1461, 1377, 1260, 1153, 1018, 806, and 718 cm^{-1}.

6.7.3. Vulcanisation of EPDM

To a vial containing a magnetic stirrer bar was added 100 mg EPDM (synthesised using [ENB] = 58 mM; 5 mol% incorporation), and 10 mg (10 phr; parts per hundred rubber) elemental sulphur (S_8), and 5 mg (5 phr) 2-mercaptobenzothiazole (MBT). The components were dissolved in toluene to ensure thorough mixing. The toluene was then removed in a vacuum oven overnight. To a 50 µL aluminium DSC pan, approximately 6–8 mg of EPDM/S/MBT was added, and the pan was subjected to a DSC heating protocol. Under the Dynamic Vulcanisation protocol, the reaction is heated to 300 °C at a rate of 2.5–20 °C min^{-1}. Under the Isothermal Vulcanisation protocol, the reaction is heated to 180–200 °C, held for 3 hours, then heated to 300 °C. In both cases the protocol is repeated to obtain a baseline.

^{13}C CPMAS ssNMR (101 MHz, 10 kHz, 298 K): δ 129.44 (br), 44.79, 36.83, 32.27, 29.47, 26.59, 23.78, and 19.39 ppm.

IR: 3112, 3079, 3039, 2955, 2922, 2849, 2365, 2329, 1695 (br), 1596, 1494, 1461, 1424, 1477, 1322, 1282, 1249, 1080, 1033, 1011, 864 (br), 751, 670, and 604 cm^{-1}.

6.7.4. Copolymerisation of propylene with 1-hexene

1000 equivalents methylaluminoxane (MAO) was introduced into a 150 mL Rotaflo® ampoule containing a stirrer bar. 10 mg supported catalyst was added to the ampoule and washed in with 45 mL hexanes. In a sidearm, the desired amount of 1-hexene was added and washed in with 5 mL hexanes. The vessel was sealed and was pumped onto a vacuum line and degassed under reduced pressure. It was cycled once more using a propylene purge while the reaction was brought to temperature in an oil bath with the stirring set at 1000 rpm. The stopcock was opened to propylene (2 bar) and the timer was started. On completion of the run, the vessel was closed to monomer and degassed. The mixture was rinsed out with fresh hexane and decanted into a 500 mL round-bottomed flask containing dilute aqueous hydrochloric acid. The organic solvents were removed by rotary evaporation. The polymer was manually separated from the aqueous phase and dried in a vacuum oven until constant weight. All polymerisation runs were carried out at least in duplicate to ensure reproducibility.

^{1}H NMR (600 MHz, chloroform-*d*, 298 K): δ 58, 1.45, 1.28, 1.21, 1.16, 1.10, 1.06, 1.03, 1.01, 1.00, 0.95, 0.91, 0.90, 0.88, 0.82, 0.81, 0.76, and 0.74 ppm.

^{13}C{^{1}H} NMR (151 MHz, chloroform-*d*, 298 K): δ 47.46, 47.23, 47.07, 46.85, 46.41, 46.10, 45.70, 45.42, 44.84, 44.56, 43.76, 43.45, 42.99, 42.75, 32.16, 30.48, 28.76, 27.49,

23.44, 23.37, 23.31, 21.48, 21.09, 20.80, 20.69, 20.39, 20.17, 20.02, 19.94, 19.86, 19.76, 19.67, 19.59, 19.46, 19.33, and 14.36 ppm.

6.7.5. Copolymerisation of ethylene with linear α-olefins

150 mg triisobutylaluminium (TIBA) was added into a vial and 10 mL of hexanes was added. This mixture was introduced into a 150 mL Rotaflo® ampoule containing a stirrer bar and swirled around the glassware. 10 mg supported catalyst was added to the ampoule and washed in with a further 35 mL hexanes. To a sidearm the desired amount of comonomer was added and washed in with sufficient hexanes to keep the total reaction volume at 50 mL. The ampoule was sealed, cycled onto a Schlenk line, and degassed under reduced pressure. It was cycled a further two times using ethylene as a purge gas while the vessel was brough to temperature in a thermostatic oil bath with the stirring set at 1000 rpm. The stopcock was opened to ethylene at a pressure of 2 bar at the timer was started. On completion of the run, the vessel was degassed under partial vacuum, then either filtered on a sintered glass frit (porosity 3) and washed with 2 x 25 mL pentane or precipitated by decanting decanted into a 500 mL round-bottomed flask containing dilute aqueous hydrochloric acid and rotary evaporation of solvent. The polyethylene was dried under vacuum until constant weight. All runs were carried out at least in duplicate to ensure reproducibility.

Ethylene/1-hexene copolymer.

$^{13}C\{^{1}H\}$ NMR (151 MHz, 1,1,2,2-tetrachloroethane-d_2, 403 K): δ 38.20, 34.60, 34.21, 30.45, 29.95, 29.56, 27.29, 23.37, and 14.18 ppm.

Ethylene/1-octene copolymer.

$^{13}C\{^1H\}$ NMR (151 MHz, 1,1,2,2-tetrachloroethane-d_2, 403 K): δ 38.21, 34.59, 32.20, 30.45, 29.95, 27.28, 22.87, and 14.15. ppm.

Ethylene/1-dodecene copolymer.

$^{13}C\{^1H\}$ NMR (151 MHz, 1,1,2,2-tetrachloroethane-d_2, 403 K): δ 38.23, 34.60, 32.19, 30.45, 29.96, 29.56, 27.29, 22.86, and 14.14 ppm.

6.7.6. Multivariate regression analysis

Data analysis and prediction was performed using the JMP® Pro software suite.[22] A standard full factorial least squares model was used to construct models of A, T_m, α, M_w, PDI, x against T_p, c, n, T_p^2, c^2, n^2, T_pn, T_pc, and cn. Analysis of variance (ANOVA) tests the assumptions of homoscedasticity and normality of residuals. Effect test analysis shows which predictors are significant. Full ANOVA is included in Appendix B.

The prediction profiler was used with desirability functions define by three points to determine the experimental conditions for a predetermined set of copolymer properties (Table A.16–A.17).

6.8. References

1 D. F. Shriver and M. A. Drezdon, *The Manipulation of Air-Sensitive Compounds*, 2 edn., Wiley, 1986.
2 J. Cosier and A. M. Glazer, *J. Appl. Crystallogr.*, 1986, **19**, 105-107.
3 U. K. L. Oxford Diffraction Agilent Technologies, Yarnton, England.
4 A. Altomare, G. Cascarano, C. Giacovazzo, A. Guagliardi, *J. Appl. Crystallogr.*, 1993, **26**, 343-350.
5 L. Palatinus and G. Chapuis, *J. Appl. Crystallogr.*, 2007, **40**, 786-790.
6 L. Farrugia, *J. Appl. Crystallogr.*, 1999, **32**, 837-838.
7 P. W. Betteridge, J. R. Carruthers, R. I. Cooper, K. Prout, D. J. Watkin, *J. Appl. Crystallogr.*, 2003, **36**, 1487-1487.
8 A. L. Spek, *J. Appl. Crystallogr.*, 2003, **36**, 7-13.
9 L. J. Farrugia, *J. Appl. Crystallogr.*, 2012, **45**, 849-854.
10 H. Hanaoka, T. Hino, H. Souda, K. Yanagi, Y. Oda, A. Imai, *J. Organomet. Chem.*, 2007, **692**, 4059-4066.
11 P. J. Bailey, R. A. Coxall, C. M. Dick, S. Fabre, L. C. Henderson, C. Herber, S. T. Liddle, D. Loroño-González, A. Parkin, S. Parsons, *Chem. Eur. J.*, 2003, **9**, 4820-4828.

12 F. M. Alías, S. Barlow, J. S. Tudor, D. O'Hare, R. T. Perry, J. M. Nelson, I. Manners, *J. Organomet. Chem.*, 1997, **528**, 47-58.
13 J. Tudor, S. Barlow, B. R. Payne, D. O'Hare, P. Nguyen, C. E. B. Evans, I. Manners, *Organometallics*, 1999, **18**, 2281-2284.
14 C. Görl, E. Betthausen, H. G. Alt, *Polyhedron*, 2016, **118**, 37-51.
15 J. V. Lamb, J. C. Buffet, J. E. Matley, C. M. R. Wright, Z. R. Turner, D. O'Hare, *Dalton Trans.*, 2019, **48**, 2510-2520.
16 M. J. Monreal, R. K. Thomson, T. Cantat, N. E. Travia, B. L. Scott, J. L. Kiplinger, *Organometallics*, 2011, **30**, 2031-2038.
17 S. M. Bae, S. M. Jeong, J. W. Baek, H. J. Lee, H. Kim, Y. Yoon, S. C. Chung, B. Y. Lee, *Eur. Polym. J.*, 2021, **144**, 110243.
18 S. Ma, B. Ni, S. Lin, Z. Liang, *J. Organomet. Chem.*, 2005, **690**, 5389-5395.
19 C. P. Chen, M. S. Yang, Q. Wang, J. C. Buffet, D. O'Hare, *J. Mater. Chem. A*, 2014, **2**, 15102-15110.
20 D. Romano, N. Tops, E. Andablo-Reyes, S. Ronca, S. Rastogi, *Macromolecules*, 2014, **47**, 4750-4760.
21 V. Busico, R. Cipullo, A. Mingione, L. Rongo, *Ind. Eng. Chem. Res.*, 2016, **55**, 2686-2695.
22 A. Kamardin, M. N. B. Derman, A. Rahmat, W. Z. A. W. Muhamad, *AIP Conf. Proc.*, 2018, **2013**, 020002.

Conclusions and outlook

The research discussed in this thesis broadly covers three topics: firstly the development of a permethylindenyl-phenoxy ligand system and the synthesis of post-metallocene complexes. Subsequently these PHENI* complexes were explored as polymerisation catalysts for the homopolymerisation of olefins with unique properties, and for the highly tuneable copolymerisation of olefinic monomers.

i) Novel permethylindenyl-phenoxy (PHENI*) post-metallocene complexes

A new class of *ansa*-bridged permethylindenyl-phenoxy ligands have been developed with a simple, efficient, and modular synthesis from cost-effective starting materials. The ability to utilise a variety of substitution patterns at the silane bridge and the phenoxide was explored with the synthesis of five distinct ligand frameworks. In total eighteen group four complexes were isolated, with thirteen characterised by single crystal X-ray diffraction, with complexes appearing to fall into a dichotomous conformational classification. While direct structure-activity relationships in supported catalysis is a notable challenge, it would be of interest to study the effects of the ligand on complex conformation and catalytic activity in more detail, including through computational simulation. Further optimisations to reagents and synthetic conditions would certainly improve overall yields. There remains plenty of scope for further modifications of the ligand, for example using carbon-based *ansa* bridges, and expanding the range of phenoxy substituents including modifications to sterics and electronics, and the incorporation of pendant neutral donors.

The reactions between PHENI* complexes and catalyst activators were studied by NMR spectroscopy, revealing the formation of monoalkylated cationic species which are

catalytically reactive towards ethylene. The complexes were heterogenised on inorganic solid supports (sMAO, SSMAO, and LDHMAO) for use in slurry-phase polymerisations.

ii) Ultra-high molecular weight homopolymers of ethylene and propylene

When applied to ethylene polymerisation, PHENI* complexes of titanium are highly efficient catalysts. Excellent control over polymer morphology was achieved with heterogenised catalysts in slurry-phase, with sMAO-*rac*-^{Me,nPr}SB(^{tBu2}ArO,I*)TiCl$_2$/TIBA having the highest activities. A twenty-two-fold increase in activity is observed when sMAO-^{Me2}SB(^{tBu,Me}ArO,I*)TiCl$_2$/TIBA is compared with the indenyl analogue sMAO-^{Me2}SB(^{tBu,Me}ArO,Ind)TiCl$_2$/TIBA (3231 and 144 kg_{PE} mol_{Ti}^{-1} h^{-1} bar^{-1} respectively). The activity seems to be principally limited by the solubility of ethylene in hexanes at 2 bar, with experiments conducted at 8.3 bar resulting in activities up to 6001 kg_{PE} mol_{Ti}^{-1} h^{-1} bar^{-1}. No evidence was found for significant catalyst decomposition, and higher pressures and reaction scales would likely result in increased activities. The synthesis of substantially disentangled ultra-high molecular weight polyethylene is reported (up to 4.2 MDa, double that of indenyl-PHENICS catalysts) which exhibited excellent mechanical properties comparable to commercial materials and was able to reinforce blends with HDPE effectively.

In the polymerisation of propylene, diffusion-limited kinetics are observed, with activities up to 12 000 kg_{PP} mol_{Ti}^{-1} h^{-1} bar^{-1}, a twenty-five-fold improvement relative to indenyl analogues. Of most interest was the formation of random atactic regioregular polypropylene with ultra-high molecular weights, up to 2 MDa. PHENI* is among the highest activity catalysts for the production of *a*PP in the literature, and the first to produce UHMWaPP in high yields under mild conditions. This transparent, amorphous,

thermoplastic material exhibits excellent elasticity, with an extensibility of over 1900%, and an elastic recovery of 93%. Mechanically it is competitive with the properties of commercial block copolymer elastomers such as styrene-butadiene-styrene while being a homopolymer gives advantages in terms of cost, compatibility, processability, and recyclability. Polymerisations at increased pressures and with mechanical stirring would be expected to overcome some of the diffusional limitations and would further increase activity. It would be interesting to assess the performance of PHENI* catalysts in liquid monomer, which is a common regime for the industrial polymerisation of propylene.

iii) PHENI* as a platform technology for the copolymerisation of olefins

Finally, the scope of copolymerisation using PHENI* catalysts was assessed with a range of monomers and conditions – ethylene, propylene, 1-hexene, 1-octene, 1-dodecene, and 5-ethylidene-2-norbornene. The production of EPM, EPDM, PPH, and LLDPE is reported, and in all cases, high activities and molecular weights were reported. Unusually, copolymer composition could be controlled by comonomer concentration, incorporations up to 96 wt% are recorded with 1-octene at 2 bar ethylene pressure. PHENI* catalysts are sufficiently active that, under mild reaction conditions, high yields of copolymer are obtained under diffusion-controlled kinetics. This monomer-agnostic behaviour results in random copolymers with composition tuneable as a function of monomer concentration. This makes PHENI* an attractive platform technology, with a single catalyst able to produce a wide scope of olefin copolymers. With sufficiently large datasets and sufficiently sophisticated statistical models, the production of application-driven designer copolymers by programmed synthesis is an extremely desirable industrial goal.